

Utilizing Salt-Coated Polypropylene Fabrics in Face Masks and  
Covers to Combat Respiratory Disease Transmission

by

Sumin Han

A thesis submitted in partial fulfillment of the requirements for the degree of

Doctor of Philosophy

in

Chemical Engineering

Department of Chemical and Materials Engineering  
University of Alberta

© Sumin Han, 2024

# Abstract

Infections in the respiratory system not only cause individual illness but can also spread to others and potentially develop into pandemics or epidemics. Various types of vaccines have been used to control the spread of pathogens. However, vaccine development has limitations due to time-consuming processes and costs. Therefore, surgical masks and respirators are widely used as the first means of protection once an outbreak begins or symptoms are identified. Yet, conventional masks have limitations such as single-use restriction, risk of contact transmission via contaminated surfaces, and concerns over biohazardous waste. Besides, attempts to decontaminate and reuse masks during shortages can significantly degrade their effectiveness. This situation necessitates the development of antimicrobial masks. Therefore, we have developed salt-coated fabrics that rapidly inactivate pathogens through non-specific mechanisms. Our research aims to assess the optimal stacking sequence of salt-coated fabrics, identify main mechanism behind the pathogen inactivation of salt-coated fabrics, demonstrate the pathogen inactivation efficiency against resilient pathogens, and analyze contact-based transmission of salt-coated fabrics compared to bare fabrics.

First, the optimal stacking sequence and the effects of wetness on both salt-coated and bare fabrics have been assessed. Diverse mask configurations, including those with salt-coated fabric and bare fabric as covers and outer layers of 3-ply surgical masks or N95 respirators, were subjected to filtration efficiency and breathability tests. Additionally, DI water was sprayed on the fabrics at varying levels of wetness (1, 6, and 12 mg/cm<sup>2</sup>), followed by further tests on filtration efficiency and breathability. It should be noted that when tested with 5% NaCl, the salt-coated fabric alone exhibited lower filtration efficiency compared to conditions

with only bare fabric, due to the lack of electrostatic attraction between the fabric and ions in 5% NaCl aerosols. However, when salt-coated and bare fabrics were used as either a cover or an outer layer, they showed similar trends in filtration efficiency and breathability, due to high filtration efficiency of middle layer. After water exposure, salt-coated fabric exhibited enhancing filtration efficiency with water amount, while bare fabrics showed opposite trends. This was attributed to the hydrophilicity of salt-coated fabrics, which enables them to form a water film around fibers. In contrast, the low filtration efficiency of bare fabrics was mainly due to the degradation of electrets upon water exposure. This finding suggests that salt-coated fabrics can offer pathogen inactivation effects while also ensuring high filtration efficiency when utilized as a cover or outer layer of 3-ply masks.

Second, the mechanism study for pathogen inactivation on salt-coated fabrics was performed using salt powders, saline solutions, and salt-coated fabrics of three different types of salts (NaCl, KCl, and K<sub>2</sub>SO<sub>4</sub>). The time-dependent salt recrystallization behavior of salt powder and salt-coated fabrics was characterized by X-ray diffraction (XRD) and monitored using optical microscopy and scanning electron microscopy (SEM). In parallel, time-dependent pathogen inactivation tests were conducted using colony-forming units (CFU) and bicinchoninic acid (BCA) assay for the viability analysis of *Klebsiella pneumoniae*, and plaque-forming units (PFU) and hemagglutinin (HA) titer for A/PR8/34 H1N1 analysis. Notably, the salt-recrystallization pattern was consistent with the pathogen inactivation pattern, showing active salt recrystallization (i.e., the formation of salt crystals and sharp edges) and active pathogen inactivation in 3-5 minutes for NaCl- and KCl-coated fabrics and 5-15 minutes for K<sub>2</sub>SO<sub>4</sub>-coated fabrics. Furthermore, the pathogen inactivation efficiency of osmotic pressure and ionic effects was not significant, demonstrating that the main pathogen inactivation mechanism is salt recrystallization. In addition to the tests, the antimicrobial

efficiency of pathogens in two different media (DI water and artificial saliva) was tested using two different transmission modes (droplets (5  $\mu$ L) and aerosols (2.5–4  $\mu$ m in diameter)), which demonstrated significant pathogen inactivation efficiency.

The demonstration of pathogen inactivation efficiency against resilient pathogens was performed using *K. pneumoniae* (a non-spore-forming bacterium), *Clostridium difficile* (a spore-forming bacterium), A/California/04/2009 (an enveloped virus), and HRV 16 (a non-enveloped virus). Their inactivation upon exposure to NaCl-, KCl-, and K<sub>2</sub>SO<sub>4</sub>-coated fabrics, with varying salt amounts (5, 9, and 13 mg/cm<sup>2</sup>), was evaluated and compared. As expected, resilient pathogens (spore-forming bacteria and non-enveloped viruses) showed lower pathogen inactivation efficiency compared to non-spore-forming bacteria and enveloped viruses; however, significant inactivation was still observed in spore-forming bacteria and non-enveloped viruses. Moreover, the potential for contact-based transmission through salt-coated and bare fabrics was tested using fluorescent dyes (sulforhodamine B and calcofluor white), *K. pneumoniae*, and A/Puerto Rico/8/34. When sprayed on both salt-coated and bare fabrics, the salt-coated fabrics significantly reduced the percentage of translocation from fabrics to hands compared to bare fabrics. The findings demonstrate that the efficiency of salt-coated fabrics can significantly contribute to enhancing the control of pathogen spread during pandemics/epidemics, and their pathogen non-specific inactivation mechanism will allow for an instant response to novel pathogens.

Overall, this thesis has proven the effectiveness of salt-coated fabrics in inactivating pathogens and preventing their spread, and it has suggested the optimal stacking sequence to maximize their efficiency. Ultimately, the thesis proposes a novel system to combat respiratory pathogens and enhance global health.

## Preface

Section 1.2 of this thesis was derived from the journal article published as S. Han, P. Lee, and H.-J. Choi, “Non-Invasive Vaccines: Challenges in Formulation and Vaccine Adjuvants”, *Pharmaceutics*, vol. 15, issue 8, 2114 (2023). I contributed as the first author and was responsible for literature review and writing the manuscript. P. Lee assisted with writing the manuscript. H.-J. Choi was the corresponding author and assisted in writing the manuscript.

Section 1.3.3, 1.3.4, 1.3.6, 1.3.7, 2.2, and 2.3 of this thesis were published as S. Han, E. Oh, E. Keltie, J.-S. Kim, and H.-J. Choi, “Engineering of Materials for Respiratory Protection: Salt-Coated Antimicrobial Fabrics for Their Application in Respiratory Devices”, *Accounts of Materials Research*, vol. 3, issue 3, 297-308 (2022). I contributed as the first author and was responsible for literature review, experiments, data analysis, and manuscript writing. E. Oh, E. Keltie, and J.-S. Kim assisted with literature review and /or experiments and/or manuscript writing. H.-J. Choi was the corresponding author, was involved with conceiving and designing the experiments, and assisted with performing experiments, data analysis, and writing the manuscript.

Chapter 3 of this thesis is being prepared for publication in *ACS Applied Polymer Materials* as S. Han, C. Maliksi, S. Kumaran, E. Oh, Y. Kim, D. -H. Ko, and H.-J. Choi, “Exploring the Influence of Antimicrobial Coating Types on Mask Performance”. I contributed as the first author and was responsible for literature review, experiments, data analysis, statistical analysis, and manuscript writing. C. Maliksi, S. Kumaran, E. Oh, Y. Kim assisted with performing experiments and/or data analysis and /or writing the manuscript. D. -H. Ko was involved in designing the experiment, provided resources, and editing the manuscript. H.-J. Choi was the corresponding author, was involved with conceiving and designing the experiments, and assisted with performing experiments, data analysis, and writing the

manuscript.

Chapter 4 of this thesis was based on the manuscript published as I. Rubino, S. Han, E. Oh, S. Kumaran, M. Lawson, Y.-J. Jung, K.-H. Kim, N. Bhatnagar, S.-H. Lee, H.-J. Kang, D.-H. Lee, K.-B. Chu, S.-M. Kang, F.-S. Quan, and H.-J. Choi, “Study of the pathogen inactivation mechanism in salt-coated filters”. I contributed as co-first author and was responsible for performing experiments (investigation of pathogen inactivation efficiency and the effect of vacuum application on salt-coated fabrics), data analysis, and writing the manuscript. I. Rubino as a co-first author performed experiments (investigation of pathogen inactivation efficiency and salt recrystallization pattern), data analysis, and manuscript writing. E. Oh, S. Kumaran, M. Lawson, Y.-J. Jung, K.-H. Kim, N. Bhatnagar, S.-H. Lee, H.-J. Kang, D.-H. Lee, K.-B. Chu, and S.-M. Kang assisted with performing the experiments, data analysis, and/or manuscript editing. F.-S. Quan and H.-J. Choi were the corresponding authors, were involved with conceiving and designing the experiments, and assisted with performing experiments, data analysis, and writing the manuscript.

Chapter 5 of this thesis was adapted from the manuscript under review (ACS Applied Bio Materials) as S. Han, E. Oh, H. Shin, S. Kumaran, D.-H. Ko, and H.-J. Choi, “Antimicrobial Face Masks and Mask Covers with a Salt-Coated Stacked Spunbond Polypropylene Fabric: Efficient Inactivation of Resilient Pathogens and Prevention of Contact Transmission”. I contributed as the first author and was responsible for performing experiments, data analysis, and writing the manuscript. E. Oh assisted with performing experiments, statistical analysis, and manuscript editing. H. Shin, S. Kumaran, and D.-H. Ko assisted with performing the experiments and/or manuscript editing. H.-J. Choi was the corresponding author, was involved with conceiving and designing the experiments, and assisted with performing experiments, data analysis, and writing the manuscript.

# Acknowledgments

I am deeply thankful to my supervisor, Dr. Hyo-Jick Choi, for his exceptional guidance throughout my research journey. Dr. Choi consistently committed his time to guiding my research and manuscripts. His supervision had a profound influence on my growth as a researcher. I am also grateful to my supervisory committee members, Dr. Anthony Yeung and Dr. Chun Il Kim, for their invaluable advice and encouragement, which have been crucial to my academic progress.

My thanks also go to my current and former groupmates, Euna, Surjith, Ilaria, Manika, and Harish. Their support and assistance have been a cornerstone of my experience, and getting to know them has been a rewarding part of my journey. I extend my gratitude to our volunteer undergraduate students, David, Caitlyn, and Young-Jin. Their contributions have greatly enriched our work.

A special acknowledgment is reserved for my family, whose constant love, understanding, and support have been the bedrock of my academic path. To my fiancé, Kanghee Ryu, your unwavering support and strength, both physically and mentally, have been a source of immense comfort and motivation.

This journey would have been much more challenging without these remarkable individuals by my side. Their collective belief in my abilities and their constant support have uplifted me, enabling me to reach new heights in my academic pursuits.

# Table of Contents

1 Introduction .....	1
1.1 Infection of respiratory system .....	2
1.1.1 Respiratory pathogens.....	2
1.1.2 Resistance of respiratory pathogens.....	6
1.1.3 Size dependent infection mechanism of pathogens.....	9
1.1.4 Target molecules of pathogens in the host.....	11
1.2 Vaccines and their limitations.....	13
1.2.1 Types of vaccines and immune responses .....	13
1.2.2 Limitations in invasive administration .....	15
1.2.3 Limitations in non-invasive administration .....	17
1.2.3.1 Oral administration .....	18
1.2.3.2 Intranasal administration.....	20
1.2.3.3 Transcutaneous administration .....	21
1.3 Respiratory protective system.....	24
1.3.1 Types of respiratory protection system.....	24
1.3.2 Efficiency of using masks in preventing the spread of pathogens .....	25
1.3.3 Structure and limitations of conventional masks.....	27
1.3.4 Mask decontamination methods and technical challenges .....	29
1.3.5 Conventional antimicrobial substance and the limitations in the application to surgical masks.....	33
1.3.6 Requirements for antimicrobial masks and respirators.....	37
1.3.7 Application methods of antimicrobial coatings on mask fabrics.....	37
1.3.8 Standards for filtration efficiency and breathability tests .....	40
2 Novel approach in airborne disease control.....	44
2.1 Goal and hypothesis .....	44
2.2 Formulation of salt coating .....	46
2.3 Salt coating process.....	47
2.4 Methodology .....	49

2.4.1 RNA extraction, cDNA synthesis, and qPCR.....	49
2.4.2 CFU and PFU.....	50
2.4.3 BCA assay .....	50
2.4.4 TCID50 assay .....	51
2.4.5 HA assay .....	51
3 Investigation on the Impact of Salt Coating on Mask Performance .....	52
3.1 Background .....	53
3.2 Methods.....	56
3.2.1 Preparation of salt-coated fabrics.....	56
3.2.2 Wetness test.....	57
3.2.3 Filtration efficiency and breathability tests .....	58
3.2.4 Statistical analysis .....	59
3.3 Results and discussion .....	59
3.3.1 Filter performance of bare fabrics.....	59
3.3.2 Performance of salt-coated staked spunbond (SB) fabrics .....	66
3.3.3 Application of stacked salt-coated SB fabrics to a mask cover and outer layer of a mask for antimicrobial face masks .....	72
3.3.4 Filter performance of three stacked salt-coated SB fabrics in wet conditions .....	77
3.3.5 Filter performance of N95 respirators only and when combined with I×3 and I <sub>NaCl</sub> ×3 <sub>9</sub> as a cover .....	85
3.4 Conclusion .....	87
4 Mechanistic study of pathogen inactivation on salt-coated filters.....	88
4.1 Background .....	89
4.2 Methods.....	91
4.2.1 Filter preparation.....	91
4.2.2 Bacteria and influenza virus preparation .....	92
4.2.3 Test of pathogen stability change on salt powders .....	93
4.2.4 Test of pathogen stability change due to osmotic pressure.....	94
4.2.5 Test of pathogen stability change on filters .....	95
4.2.6 X-ray diffraction (XRD) analysis .....	97
4.2.7 Microscope analysis .....	97

4.2.8 Statistical analysis .....	98
4.3 Results and discussion .....	98
4.3.1 Characterization of the salt powder recrystallization.....	98
4.3.2 Pathogen inactivation on the salt powders.....	105
4.3.3 Characterization of the salt filter recrystallization.....	112
4.3.4 Pathogen inactivation on the salt filters .....	118
4.3.5 Effect of salt amount and coating process on the salt coating morphology.....	122
4.3.6 Effect of droplet size and composition on pathogen inactivation .....	129
4.4 Conclusion.....	132
5 Efficient inactivation of resilient pathogens and prevention of contact transmission using salt-coated filters.....	133
5.1 Background.....	134
5.2 Method.....	139
5.2.1 Preparation of salt-coated fabrics.....	139
5.2.2 Bacteria preparation .....	140
5.2.3 Virus preparation .....	141
5.2.4 Antimicrobial activity test on salt-coated fabrics .....	143
5.2.5 Filtration efficiency and breathability tests.....	143
5.2.6 Contact transmission test .....	146
5.2.7 Finger pressing measurement .....	148
5.2.8 Microscope analysis.....	149
5.2.9 Statistical analysis .....	149
5.3 Results .....	150
5.3.1 Antimicrobial activity of salt-coated stacked spunbond (SB) fabrics against resilient pathogens .....	150
5.3.2 Particle filtration efficiency and breathability: evaluating the effectiveness of salt-coated stacked SB fabrics as an outer layer and a cover for conventional mask.....	157
5.3.3 Contact transmission test through simulated biocontamination .....	167
5.3.4 A stack of salt-coated SB fabrics: preventing contact transmission of bacterial droplets .....	177
5.3.5 A stack of salt-coated SB fabrics: preventing contact transmission of viral droplets..	181
5.4 Conclusions.....	185

6 Conclusions and future work ..... 186  
    6.1 Conclusions..... 186  
    6.2 Future work..... 189  
Bibliography ..... 191

## List of Tables

Table 1.1. Decontamination methods tested for face masks/medical masks/respirators under investigation. Abbreviations: surgical mask (SM), N95 respirator (N95), cloth mask (CM), filtering facepiece (FFP)Physical characteristics of surgical mask .....	30
Table 1.2. Standards for particulate filtration efficiency (PFE) of respirators and surgical/medical masks.....	41
Table 1.3. Standards for bacterial filtration efficiency (BFE) of respirators and surgical/medical masks.....	42
Table 1.4. Standards for breath resistance of respirators and surgical/medical masks.....	43
Table 2.1. Properties of salts.....	47
Table 4.1. Salt and sucrose solution conditions used for tests of the osmotic pressure effect on bacteria and viruses during aerosol drying .....	94

# List of Figures

Figure 1.1. Schematic illustration of immune responses upon vaccine administration.....	15
Figure 1.2. Schematic illustration of limitations in invasive vaccines .....	16
Figure 1.3. Representation of immune responses of intestinal M cell .....	19
Figure 1.4. Implications of respiratory protection for pandemic/epidemic preparedness. The development of pathogen inactivating respiratory devices can contribute to narrowing the gap between contamination/infrastructure and pandemic readiness with regards to personal protection, health care system, and governance .....	37
Figure 1.5. Antimicrobial functionalization strategies for mask fibers .....	39
Figure 2.1. Production of salt-coated filters. Fabrication of salt-coated filters by drying pre-wet (via dip- or spray-coating) filters (A; i: schematic, ii: scanning electron microscope (SEM) images of spunbond PP fabrics), drying pre-wet spunbond PP fabrics in a coating formulation (B; i: schematic, ii: pre-wet+600 $\mu$ L, iii: pre-wet+1200 $\mu$ L), and application of vacuum to pre-wet PP fabrics followed by drying (C; i: schematic, ii: SEM images). (A-ii, B-ii,iii, and C-ii) Reproduced (Adapted) with permission from reference. Copyright 2021 ACS. ....	48
Figure 3.1. Filter performance of bare fabrics. Filtration efficiency was performed according to NIOSH 42CFR84 standard. (a) Overall filtration efficiency of bare fabrics tested with 5% NaCl aerosol (i) and DOP aerosol (ii). (b,c) Particle size-dependent filtration efficiency tested with 5% NaCl aerosols (b) and DOP aerosols (c) (i: filtration efficiency of bare fabrics and ii: zoomed-in filtration efficiency of the bare fabrics). (n = 7–21 for b and 9–24 for c, mean $\pm$ SD) .....	63
Figure 3.2. Particle size-dependent filtration efficiency of single bare fabrics. (a–b) 5% NaCl aerosol (i) and DOP aerosol (ii) used to measure the filtration efficiency of fabrics: (a) M $\times$ 1 and (b) O $\times$ 1. (n = 7–15 for a and n = 9–19 for b, mean $\pm$ SD)) .....	64
Figure 3.3. Breathability of bare fabrics with different staking sequences. Breathability was performed according to ASTM F2100–19e1 standard. (n = 9–12, mean $\pm$ SD) .....	65
Figure 3.4. Filter performance of salt-coated fabrics. Filtration efficiency was performed according to NIOSH 42CFR84. (a,b) Overall filtration efficiency (a) and particle size-dependent filtration efficiency (b) of salt-coated fabrics tested with 5% NaCl aerosol (i) and DOP aerosol (ii). (n = 13–23 for a(i), n = 12–22 for a(ii), n = 9–21 for b(i), and n = 8–24 for b(ii) mean $\pm$ SD) .....	68
Figure 3.5. Particle size-dependent filtration efficiency of salt-coated fabric only conditions tested. (a–d) 5% NaCl aerosol used to measure the filtration efficiency of different salt coating conditions: (a) I <sub>T20</sub> $\times$ 3	

( $n = 6-24$ , mean  $\pm$  SD), (b)  $I_{KCl} \times 3_5$  ( $n = 7-24$ , mean  $\pm$  SD), (c)  $I_{KCl} \times 3_9$  ( $n = 7-24$ , mean  $\pm$  SD), and (d)  $I_{K_2SO_4} \times 3_5$  ( $n = 7-24$ , mean  $\pm$  SD) ..... 69

Figure 3.6. Particle size-dependent filtration efficiency of salt-coated fabric only conditions tested. (a-d) DOP aerosol used to measure the filtration efficiency of different salt coating conditions: (a)  $I_{T20} \times 3$  ( $n = 6-24$ , mean  $\pm$  SD), (b)  $I_{KCl} \times 3_5$  ( $n = 7-24$ , mean  $\pm$  SD), (c)  $I_{KCl} \times 3_9$  ( $n = 7-24$ , mean  $\pm$  SD), and (d)  $I_{K_2SO_4} \times 3_5$  ( $n = 7-24$ , mean  $\pm$  SD) ..... 70

Figure 3.7. Breathability of salt-coated fabrics with different staking sequences. Breathability was performed according to ASTM F2100-19e1 standard. ( $n = 10-15$ , mean  $\pm$  SD) ..... 71

Figure 3.8. Filter performance of bare and salt-coated fabrics with different staking sequences. Filtration efficiency and breathability were performed according to NIOSH 42CFR84 and ASTM F2100-19e1 standards, respectively. (a) Overall filtration efficiency of  $I \times 3$  and  $I_{NaCl} \times 3$  as a cover of the 3-ply mask (i: 5% NaCl aerosol and ii: DOP aerosol). ( $n = 10-20$  for a(i) and  $n = 10-15$  for a(ii), mean  $\pm$  SD) (b,c) Particle size-dependent filtration efficiency of  $I \times 3$  and  $I_{NaCl} \times 3$  as cover of the 3-ply mask, tested with 5% NaCl aerosol (b) and DOP aerosol (c) (i: filtration efficiency of stacked fabrics and ii: zoomed-in filtration efficiency of the stacked fabrics). ( $n = 10-20$  for b and  $n = 10-15$  for c, mean  $\pm$  SD) ..... 74

Figure 3.9. Filter performance of bare and salt-coated fabrics with different staking sequences. Filtration efficiency and breathability were performed according to NIOSH 42CFR84 and ASTM F2100-19e1 standards, respectively. (a) Overall filtration efficiency of  $I \times 3$  and  $I_{NaCl} \times 3$  as an outer of the 3-ply mask (i: 5% NaCl aerosol and ii: DOP aerosol). ( $n = 12-19$  for a(i) and  $n = 11-16$  for a(ii), mean  $\pm$  SD) (b,c) Particle size-dependent filtration efficiency of  $I \times 3$  and  $I_{NaCl} \times 3$  as an outer of the 3-ply mask, tested with 5% NaCl aerosol (b) and DOP aerosol (c) (i: filtration efficiency of stacked fabrics and ii: zoomed-in filtration efficiency of the stacked fabrics). ( $n = 12-19$  for b and  $n = 7-16$  for c, mean  $\pm$  SD). (c) Breathability of  $I \times 3$  and  $I_{NaCl} \times 3$  used as an outer. ( $n = 9-12$ , mean  $\pm$  SD) ..... 75

Figure 3.10. Breathability of  $I \times 3$  and  $I_{NaCl} \times 3$  used as an outer (a) and cover (b). Breathability was performed according to ASTM F2100-19e1 standard. ( $n = 9-12$ , mean  $\pm$  SD) ..... 76

Figure 3.11. Characterization of  $I_{NaCl} \times 3_9$  fabrics after spraying DI water for the measurement of effects of wetness on filtration efficiency. Sulforhodamine B (SRB) was used to visualize the wetness of fabrics in the images; however, for filtration efficiency tests and breathability tests, DI water was used. (a-d) different amount of SRB was sprayed: (a) 0 mg/cm<sup>2</sup>, (b) 1 mg/cm<sup>2</sup>, (c) 6 mg/cm<sup>2</sup>, and (d) 12 mg/cm<sup>2</sup> ..... 79

Figure 3.12. Filter performance of bare and salt-coated fabrics with different wetness. See Figure 3.9 for the optical microscope images of wet fabrics. The wetness of the samples was measured by weighting the samples before and after water spray, followed by dividing the values by mask surface area. Filtration efficiency was performed according to NIOSH 42CFR84 standard. (a) Overall filtration efficiency tested with 5% NaCl (i) and DOP aerosols (ii). ( $n = 13-30$ , mean  $\pm$  SD). (b,c) particle size-dependent filtration efficiency of wet  $I \times 3$  and wet  $I_{NaCl} \times 3_9$ , tested with 5% NaCl (b) and DOP (c) aerosols (i: filtration efficiency of fabrics and ii: zoomed-in filtration efficiency of the fabrics). ( $n = 7-29$  for b and 6-29 for c, mean  $\pm$  SD) ..... 80

Figure 3.13. Particle size–dependent filtration efficiency of I×3 (a) and I<sub>NaCl</sub>×3<sub>9</sub> (b) tested with DOP aerosols (i: filtration efficiency of fabrics and ii: zoomed–in filtration efficiency of the fabrics). (n = 12–29, mean ± SD) ..... 81

Figure 3.14. Filtration efficiency of wet I×3 and I<sub>NaCl</sub> ×3 as a cover and an outer of the 3-ply mask, tested with 5% NaCl aerosol according to NIOSH 42CFR84. (a,b) Overall filtration efficiency of I×3 and I<sub>NaCl</sub>×3<sub>9</sub> fabrics used as a cover (a) and an outer layer (b). (n = 9–20, mean ± SD) ..... 82

Figure 3.15. Filtration efficiency of wet I×3 and I<sub>NaCl</sub> ×3 as a cover and an outer of the 3-ply mask, tested with 5% NaCl aerosol according to NIOSH 42CFR84. (a–c) I×3 and I<sub>NaCl</sub>×3<sub>9</sub> fabrics used as a cover (i) and an outer layer (ii): (a) 1 mg/cm<sup>2</sup> of water (n = 10–13, mean ± SD), (b) 6 mg/cm<sup>2</sup> of water (n = 9–13, mean ± SD), and (c) 12 mg/cm<sup>2</sup> of water (n = 10–11, mean ± SD) ..... 83

Figure 3.16. Breathability of bare and salt–coated fabrics with different wetness. Breathability was performed according to ASTM F2100–19e1 standard. (n = 9–14, mean ± SD) ..... 84

Figure 3.17. Filter performance of N95 respirators. Filtration efficiency and breathability were performed according to NIOSH 42CFR84. (a,b) N95 respirators alone, and with I×3 and I<sub>NaCl</sub> ×3<sub>9</sub> as a cover of N95. (a: breathability and b: overall filtration efficiency) (n = 10–15 for and n = 11–18 for b, mean ± SD). (c) Particle size–dependent filtration efficiency tested with 5% NaCl aerosols (i) and DOP aerosols (n = 15–19 for i and n = 10–18 for ii, mean ± SD) (ii) ..... 86

Figure 4.1. Salt powder size. Histogram of NaCl (a), K<sub>2</sub>SO<sub>4</sub> (b), and KCl (c) powder size (n = 100 for (a), n = 181 for (b), n = 123 for (c))..... 101

Figure 4.2. Characterization of the salt powder recrystallization. (a–c) Relevant XRD peaks of NaCl (a), K<sub>2</sub>SO<sub>4</sub> (b), and KCl (c) powders before aerosol exposure (No aerosol), right after aerosol exposure (0 min), and at 5, 15 and 30 min. Miller indices of relevant peaks corresponding to NaCl, K<sub>2</sub>SO<sub>4</sub> and KCl crystals, respectively, are shown in each XRD spectrum for phase/plane identification (i: scanning range 20–60°, ii: zoomed-in XRD patterns after curve fitting). Inserted numbers are Miller indices. Scan time was set to 3 min per XRD spectrum acquisition at each incubation time..... 102

Figure 4.3. Morphological changes due to salt powder recrystallization. Optical microscope images of NaCl (top), K<sub>2</sub>SO<sub>4</sub> (middle) and KCl (bottom) before aerosol exposure (i.e., No aerosol), and at 3, 5, 15 and 30 min after exposure, showing the morphological changes during the evaporation-induced salt recrystallization ..... 103

Figure 4.4. Morphological changes due to salt powder recrystallization. (a-c) SEM images of NaCl (a), K<sub>2</sub>SO<sub>4</sub> (b), and KCl (c) before (L: left) and after (R: right; >60-min incubation) aerosol exposure ((i): low magnification, (ii): high magnification), showing the morphological changes due to the evaporation-induced salt recrystallization..... 104

Figure 4.5. Pathogen inactivation on salt powders. (a) CFU change showing the effect of

incubation time on *K. pneumoniae* exposed to NaCl, K<sub>2</sub>SO<sub>4</sub> and KCl powders (n = 4–20, mean ± SD). (b) TEM images of *K. pneumoniae* aerosolized control (i), and following incubation on NaCl (ii), K<sub>2</sub>SO<sub>4</sub> (iii) and KCl (iv) powders for 30 min..... 106

Figure 4.6. Bacteria incubation in dissolved salt powders. CFU change showing the effect of incubation time on *K. pneumoniae* exposed to dissolved salt powders during the experiments (n = 4–20, mean ± SD) ..... 106

Figure 4.7. Effect of osmotic pressure on pathogens. (a) CFU change showing the effect of incubation time on *K. pneumoniae* exposed to NaCl, K<sub>2</sub>SO<sub>4</sub>, and KCl solutions at varying osmotic pressure levels (n = 3–30, mean ± SD) (b) TEM images of *K. pneumoniae* following incubation in NaCl 29 w/v % (i), K<sub>2</sub>SO<sub>4</sub> 10 w/v % (ii), and KCl 26 w/v % (iii) solutions for 30 min ..... 107

Figure 4.8. Effect of osmotic pressure on pathogens. (a) HA titer showing the effect of incubation time on the PR/34 virus exposed to NaCl, K<sub>2</sub>SO<sub>4</sub>, and KCl powders (n = 8, mean ± SD). (b) TEM images of the PR/34 virus control (i) and following incubation on NaCl (ii), K<sub>2</sub>SO<sub>4</sub> (iii), and KCl (iv) powders for 30 min. (c) HA titer showing the effect of incubation time on the PR/34 virus exposed to NaCl 29 w/v %, K<sub>2</sub>SO<sub>4</sub> 10 w/v %, and KCl 26 w/v % solutions (n = 12–13, mean ± SD) ..... 110

Figure 4.9. Effect of osmotic pressure on pathogens. (a) TEM images of PR/34 virus following incubation in NaCl 29 w/v% solution for 30 min. (b) HA titer showing the effect of incubation time on PR/34 virus exposed to sucrose 200 w/v% solution (n = 8, mean ± SD) ..... 111

Figure 4.10. Characterization of salt-coated filters. Plan-view (T: top) and cross-sectional (B: bottom) EDX mapping images of salt-functionalized filters, showing the salt coating on the surface of the filter fibers. (a) NaCl filter (combination of Na (red) and Cl (green) mapping images), (b) K<sub>2</sub>SO<sub>4</sub> filter (combination of K (red) and S (green)), (c) KCl filter (combination of K (red) and Cl (green)) ..... 114

Figure 4.11. Plan-view (T: top) and cross-sectional (B: bottom) SEM images NaCl (a), K<sub>2</sub>SO<sub>4</sub> (b) and KCl (c) filters ..... 115

Figure 4.12. Characterization of the salt recrystallization on the salt-coated filters. (a-c) Relevant XRD peaks of NaCl 600 (a), K<sub>2</sub>SO<sub>4</sub> 600 (b), and KCl 600 (c) before aerosol exposure (No aerosol), right after aerosol exposure (0 min), and at 5, 15 and 30 min. Miller indices of relevant peaks corresponding to NaCl, K<sub>2</sub>SO<sub>4</sub> and KCl crystals, respectively, are shown in each XRD spectra for phase/plane identification. Scan time was set to 3 min per XRD spectrum acquisition at each incubation time ..... 116

Figure 4.13. XRD spectra of bare membrane before aerosol exposure (No aerosol), right after aerosol exposure (0 min), and at 5, 15 and 30 min ..... 117

Figure 4.14. Pathogen inactivation on salt-coated filters. (a) TEM images of *K. pneumoniae*

following 30-min incubation on NaCl, K<sub>2</sub>SO<sub>4</sub> and KCl filters. (b,c) Relative HA activity (b) and virus titer (c) showing the effect of incubation time on PR/34 virus exposed to Bare, NaCl 600, K<sub>2</sub>SO<sub>4</sub> 600 and KCl 600 (n = 8–53 for (a), n = 4–33 for (b), mean ± SD). Relative: with respect to 0 min. §: below detection limit. (d) TEM images of PR/34 virus following 30-min incubation on NaCl 600, K<sub>2</sub>SO<sub>4</sub> 600 and KCl 600 ..... 120

Figure 4.15. Virus incubation in dissolved salt-functionalized filters. HA titer (a) and virus titer (b) showing the effect of osmotic pressure on PR/34 virus exposed to dissolved Bare, NaCl 600, K<sub>2</sub>SO<sub>4</sub> 600 and KCl 600 for 60 min (n = 8–53 for (c), n = 5–33 for (d), mean ± SD). Relative: with respect to 0 min. Mem: membrane ..... 121

Figure 4.16. Characterization of filters prepared with different amounts of coated salt. (a) Plan-view SEM images of NaCl, K<sub>2</sub>SO<sub>4</sub> and KCl filters, showing the morphology of the salt coatings at different amounts of coated salt. (b) Cross-sectional SEM images of NaCl 0, NaCl 300, NaCl 600, NaCl 900 and NaCl 1200, showing the morphology of the salt coatings at different amounts of coated salt..... 123

Figure 4.17. (a) Low-magnification SEM images of filters functionalized with NaCl (left), K<sub>2</sub>SO<sub>4</sub> (center) and KCl (right), showing the morphology of the salt coatings at different amounts of coated salt. (b) Low-magnification, cross-sectional SEM images of NaCl-functionalized filters, showing the morphology of the salt coatings at different amounts of coated salt..... 124

Figure 4.18. (a,b) Cross-sectional SEM images of K<sub>2</sub>SO<sub>4</sub> (a) and KCl (b) functionalized filters, showing the distribution of the salt coatings at different amounts of coated salt (i: low magnification, ii: high magnification) ..... 125

Figure 4.19. Production of salt-coated filters with vacuum application. Relationship between level of vacuum applied during salt coating (V) and amount of salt coated on the filters (W<sub>salt</sub>) (n = 6–15, mean ± SD). Linear fit equations are shown (P < 0.001) ..... 126

Figure 4.20. Characterization and pathogen inactivation on salt-coated filters prepared with vacuum process. (a) SEM images of filters functionalized with NaCl (left), K<sub>2</sub>SO<sub>4</sub> (center) and KCl (right), showing the morphology of the salt coatings at different levels of vacuum applied during coating. (b) Cross-sectional EDX mapping (combination of Na (red) and Cl (green) mapping images) (i), and SEM (ii, iii) images of NaCl-functionalized filters, showing the distribution of the salt coatings at different levels of vacuum applied during coating ..... 127

Figure 4.21. Production of salt-coated filters with vacuum application. Low-magnification SEM images of filters functionalized with NaCl (left), K<sub>2</sub>SO<sub>4</sub> (center) and KCl (right), showing the morphology of the salt coatings at different levels of vacuum applied during coating ..... 128

Figure 4.22. CFU change showing the effect of incubation time and dispersed medium (DI water and artificial saliva) on *K. pneumoniae* exposed to NaCl15 inHg in the form of aerosols (a) and droplets (b) (n = 5 for (a), n = 3 for (b), mean ± SD) ..... 131

Figure 5.1. Schematic presentation of antimicrobial face mask and mask covering based on salt coated stacked spunbond polypropylene (PP) fabric. (a) Schematic representation of a 3-ply face mask (top) and mask structure (bottom; SB: spunbond fabric, MB: meltblown fabric; I: inner layer, M: middle layer, O: outer layer). (b) Schematic representation of salt-coated stacked SB fabric (top) and salt-coated three-stacked SB fabric (bottom). (c) The proposed design and architecture of antimicrobial face mask (i) and mask covering (ii). The fabrics were labeled FabricSalt×#Amount, where Fabric is the PP fabric type (SB or MB), Salt the type of salt (NaCl, KCl, or K<sub>2</sub>SO<sub>4</sub>), # the number of stacked fabrics (1 or 3), and Amount the quantity of salt coating (5, 9, or 13 mg/cm<sup>2</sup>). Bare fabrics are labelled Fabric×#. For the fabrication of stacked SB fabrics in (b), SB PP fabric used as the inner layer of a conventional 3-ply mask (i.e., SB(I) in (a)) have been utilized..... 137

Figure 5.2. Spray test setup and spray droplet size distribution. (a) Spry system setup and (b) size distribution of the sprayed droplets. n=460. To measure the droplet size, droplets were sprayed onto a non-porous polypropylene sheet, and measurements of individual droplets were performed using MOTIC 2.0 software under an optical microscope ..... 145

Figure 5.3. Time-dependent pathogen inactivation efficiency of salt-coated spunbond (SB) PP fabrics. Bacterial viability change showing the effect of incubation time on *K. pneumoniae* (a) and *C. difficile* (b) exposed to NaCl, KCl, and K<sub>2</sub>SO<sub>4</sub>-coated SB fabrics (in a, i: 5 mg/cm<sup>2</sup>, ii: 9 mg/cm<sup>2</sup>, and iii: 13 mg/cm<sup>2</sup>; in b, i: 9 mg/cm<sup>2</sup> and ii: 13 mg/cm<sup>2</sup>) for 30 min. (n =3, mean ± SD). Relative: with respect to 0 min. §: below detection limit. (c) TEM images of *K. pneumoniae* (i) and *C. difficile* (ii) after 30 min incubation on SBsaltx39, a stack of three SB fabrics w/ 9 mg/cm<sup>2</sup> of salt coating..... 152

Figure 5.4. Viability reduction in CA/09 viruses using different salt-coated filters (a: NaCl-coated filters, b: KCl-coated filters, and c: K<sub>2</sub>SO<sub>4</sub>-coated filters). (d) TEM images of CA/09 after 30 min of exposure on NaCl-, KCl-, and K<sub>2</sub>SO<sub>4</sub>-coated filters (i.e., SBsaltx39: a stack of three SB fabrics w/ 9 mg/cm<sup>2</sup> of salt coating, SBx1: a bare SB fabric) ..... 155

Figure 5.5. Virus titer showing the effect of incubation time on the viability of HRV 16 upon exposure to salt-coated filters (a: NaCl-coated filters, b: KCl-coated filters, and c: K<sub>2</sub>SO<sub>4</sub>-coated filters) with different salt amount (i: 5 mg/cm<sup>2</sup> and ii: 9 mg/cm<sup>2</sup>, and iii: 13 mg/cm<sup>2</sup>). (n =3, mean ± SD). §: below detection limit. For all panels: ns: P > 0.05; \*P < 0.05; \*\*P < 0.01; \*\*\*P < 0.001; \*\*\*\*P < 0.0001, by one-way ANOVA ..... 156

Figure 5.6. Breathability of salt-coated fabrics. Left: Differential pressure of each layer, i.e. spunbond fabrics (inner layer: SB×1, outer layer: SB×1), meltblown fabrics (middle layer: MB×1), a stack of 3 spunbond fabrics (3-inner PP fabric stack: SB×3), and a stack of salt-coated spunbond fabrics (3-inner PP fabric stack, coated with 9 mg/cm<sup>2</sup> NaCl: SB<sub>NaCl</sub>×3<sub>9</sub>). Right: Differential pressure of the bare or salt-coated spunbond fabrics when used as an outer layer of the 3-ply mask (SB<sub>NaCl</sub>×3<sub>9</sub>/middle/inner) or cover on top of a mask (SB<sub>NaCl</sub>×3<sub>9</sub>/whole mask). (n =10-11, mean ± SD) ..... 159

Figure 5.7. Particle capturing efficiency measurement of each layer of a surgical mask. (a, b) A 3-

ply mask (stacking sequence: SB×1 (O)/MB×1 (M)/SB×1 (I)) underwent 1.5 mg/cm<sup>2</sup> of droplet spraying (a, 352 ± 207 μm in diameter) and 0.3 mg/cm<sup>2</sup> aerosol exposure (b, 2.5-4 μm in diameter) without airflow, followed by the separation of each layer and measurement of fluorescent intensity (i). (ii) Optical microscope images of SB×1 (O), MB×1 (M), and SB×1 (I) tested as aforementioned. (n = 3, mean ± SD). §: below detection limit. For all panels: ns: P > 0.05; \*P < 0.05; \*\*P < 0.01; \*\*\*P < 0.001; \*\*\*\*P < 0.0001, by one-way ANOVA ..... 163

Figure 5.8. Particle size-dependent filtration efficiency of each layers of surgical masks. (i) Filtration efficiency of outer (a), middle (b), and inner (c) layers. (ii) Relationship between particle size (P) and filtration efficiency (FE) examined within the particle size range of 1 to 4 μm (n= 9-24, mean ± SD). Fitting equations are shown (R<sup>2</sup>=0.75 (a), 0.77 (b), and 0.9 (c)). The filtration efficiency values at 3.5 and 4 μm particle size were calculated using the fitting equations. These values were then employed to estimate the average filtration efficiency of particles within the range of 2.5 to 4 μm under specific airflow conditions. This estimation was compared to dye-based aerosol experiments conducted under conditions of no significant airflow ..... 164

Figure 5.9. Particle capturing efficiency of individual layer of a surgical mask. (a) Conventional 3-ply mask (stacking sequence: SB×1(O)/MB×1(M)/SB×1(I)). (b) 3-ply mask (stacking sequence: SB×1(I)/MB×1(M)/SB×1(I)). (n = 12-14, mean ± SD). In this work, due to the higher filtration efficiency of the inner SB fabric of a conventional 3-ply mask compared to that of outer SB fabric, the stacked SB PP fabrics with and without salt coating (SB×# or SB<sub>Salt</sub>×#<sub>Amount</sub>), which are main focus of this study, have been fabricated for their application to the outer layer of a 3-ply mask or mask covering. This was achieved by utilizing the inner SB fabrics for their application to the outer layer of a conventional 3-ply mask and mask covering. The particle capturing efficiency (PCE) of each layer in a 3-ply mask was calculated based on the average particle filtration efficiency (PFE) measurements at 3 μm particle size (Figure S5). Specifically, the capturing efficiency of the first layer (PCE<sub>1st-layer</sub>) is equal to the filtration efficiency of the first layer (i.e., PFE<sub>1st-layer</sub>). The capturing efficiency of the second layer (PCE<sub>2nd-layer</sub>) is calculated as ((100-PCE<sub>1st-layer</sub>)×PFE<sub>2nd-layer</sub>/100), and the capturing efficiency of the third layer (PCE<sub>3rd-layer</sub>) is calculated as ((100-PCE<sub>1st-layer</sub>-PCE<sub>2nd-layer</sub>)×PFE<sub>3rd-layer</sub>/100) ..... 165

Figure 5.10. Particle size-dependent filtration efficiency of SB×3 and SB<sub>NaCl</sub>×3<sub>9</sub> fabrics. Each layer is subjected to a filtration efficiency test with airflow (85 LPM) using the PALAS PMFT 1000. (n =7-13 for (i) and n=8-19 for (ii), mean ± SD) ..... 166

Figure 5.11. Filtration efficiency of SB×3 (i) and SB<sub>NaCl</sub>×3<sub>9</sub> (ii), measured using spray droplets (d) or aerosol (e), when they were used as a mask cover (stacking sequence: SB×3 and SB<sub>NaCl</sub>×3<sub>9</sub> on top of a 3-ply mask) and outer layer of a 3-ply mask (stacking sequence: SB×3/middle/inner or SB<sub>NaCl</sub>×3<sub>9</sub>/middle/inner). (n =3 for c and d, mean ± SD). §: below detection limit. For all panels: ns: P > 0.05; \*P < 0.05; \*\*P < 0.01; \*\*\*P < 0.001; \*\*\*\*P < 0.0001, by one-way ANOVA ..... 166

Figure 5.12. Bare and salt-coated filters before (control) and after spraying 1.5 mg/cm<sup>2</sup> of calcofluor white (CW) or sulforhodamine B (SRB) over the course of incubation time ..... 169

Figure 5.13. Characterization of gloves after strong/gentle pressing with a gloved thumb on various architecture containing calcofluor white (CW)-contaminated MB fabric and/or sulforhodamin B (SRB)-contaminated SB fabrics (w/ and w/o NaCl coating) after 1, 5, and 10 min of incubation at room temperature. Optical micrographs represent the transferred contaminants from mask fabrics to gloved thumbs..... 170

Figure 5.14. Optical microscopy analysis to investigate the role of individual mask layer of a 3-ply mask and the effects of mask architecture/salt coating on the contact transmission behavior using fluorescent dye-contaminated mask fabrics. Characterization of gloves after strong/gentle pressing with a gloved thumb on various architecture containing calcofluor white (CW)-contaminated MB fabric and/or sulforhodamin B (SRB)-contaminated SB fabrics (w/ and w/o NaCl coating) after 15, 20, and 30 min of incubation at room temperature. Optical micrographs represent the transferred contaminants from mask fabrics to gloved thumbs ..... 171

Figure 5.15. Contact transmission of calcofluor white (CW)-sprayed mask. Translocation of CW associated with a finger pressing from CW-contaminated meltblown (MB) middle layer (i.e., (a) CW-MB×1 and (b) SB×1/CW-MB×1) to thumb (i) and index finger (ii) pressing. The amount of the translocated CW was analyzed using fluorometer (excitation/emission: 350/432 nm). (n = 3, mean ± SD). §: below detection limit. (c) Fluorescent microscope images of thumb gloves after the contact with the CW-contaminated fabrics at 1, 5, and 10 min after CW spray..... 174

Figure 5.16. Contact transmission of sulforhodamine B (SRB)-sprayed mask. Translocation of SRB associated with a finger pressing from SRB-contaminated outermost layer (i.e., (a) SRB-SB×1, (b) SRB-SB×3 and (c) SRB-SB<sub>NaCl</sub>×3<sub>9</sub>) to thumb (i) and index finger (ii) pressing. The amount of the translocated SRB was analyzed using fluorometer (excitation/emission: 565/586 nm). (n = 3, mean ± SD). §: below detection limit ..... 175

Figure 5.17. Fluorescent microscope images of gloves after the contact with the SRB-contaminated fabrics at 1, 5, and 10 min after SRB spray..... 176

Figure 5.18. Bacterial translocation to fingers. Translocation of *K. pneumoniae* associated with a finger pressing from (a) contaminated outermost layer of a mask or mask cover (i.e., a stack of three SB fabrics w/ and w/o salt coating) and (b) contaminated MB layer (i.e., MB only, SB/MB, and salt-coated SB stack/MB) to a finger. (i) Strong and (ii) gentle pressing with the gloved thumb; the amount of the translocated bacteria was analyzed by comparing the number of sprayed *K. pneumoniae* on mask fabrics and translocated bacteria to gloves using CFU. (n = 3, mean ± SD). Relative: with respect to bacteria (CFU/mL) sprayed on thumb sized fabric. Bold text indicates the contaminated layer. §: below detection limit..... 180

Figure 5.19. Viral translocation to fingers. Translocation of PR/34 associated with a finger pressing from (a) contaminated outermost layer (i.e., a stack of three SB fabrics w/ and w/o salt coating) and (b) contaminated MB middle layer (i.e., MB only, SB/MB, and salt-coated SB stack/MB) to a finger. (i) Strong and (ii) gentle pressing with the gloved thumb; the amount of the translocated virus was analyzed using real-time PCR targeting the HA gene. (n = 3, mean ± SD). Relative: with respect to gene copy number of viruses sprayed on thumb sized fabric. Bold text

indicates the contaminated layer. §: below detection limit..... 184

# 1 Introduction

For centuries, pathogens have been a persistent threat to human health. Despite various strategies to limit their spread, each approach has its shortcomings. Vaccines, for instance, have significantly reduced pathogen transmission, but their development is time-consuming due to various factors and necessitate extensive testing. As a result, masks have become the first means of protection against pathogens, reducing transmission before vaccines are developed. However, the limitations of masks, such as their lack of antimicrobial properties and issues with single-use and contact-based transmission, cannot be overlooked. To effectively mitigate the spread of pathogens, there is an urgent need to develop antimicrobial masks that can more competently control pathogens. This chapter begins by exploring the nature of pathogens and their transmission, followed by a discussion on the development of antimicrobial resistance in these pathogens. It then addresses the limitations in vaccine development, including those of invasive, non-invasive, and minimally invasive vaccines. Finally, the chapter introduces the limitations of conventional masks and their decontamination procedures, along with methods for mask functionalization with antimicrobial materials.

### 1.1.1 Infection of respiratory system

Respiratory diseases have been a persistent challenge throughout human history, varying in severity and requiring different treatments. Despite various efforts to control pathogens, mutations that lead to resistance often reduce the effectiveness of treatments. Therefore, the development of innovative systems or strategies capable of targeting a range of pathogens is essential.

### 1.1.2 Respiratory pathogens

Respiratory infections are caused by a variety of pathogens, including bacteria, viruses, and fungi. Among the bacterial causes, *Bordetella pertussis*, *Chlamydomphila pneumoniae*, *Corynebacterium diphtheriae*, *Haemophilus influenzae*, *Mycoplasma pneumoniae*, and *Streptococcus pneumoniae* are notable [1]. *Bordetella pertussis*, the bacterium responsible for whooping cough, has a notable history of causing outbreaks. The disease was first recognized in the Middle Ages, with various epidemics described over the centuries. Notably, the first written records of outbreaks date back to the 16th century, as documented by Guillaume de Baillou in France [2, 3]. The infection can be particularly deadly for infants and can lead to complications like bacterial pneumonia, neurological issues, and dehydration [2, 3]. *Chlamydomphila pneumoniae* is known to cause mild or asymptomatic infections, making it challenging to determine the exact number of cases each year. The disease can occur at any time of the year, without a specific season of heightened prevalence. Even though the acute illness it causes is typically mild, *C. pneumoniae* has been involved in several chronic diseases, including atherosclerosis and asthma [4]. *Haemophilus influenzae*, often referred to as Hib, is a bacterium that can cause various severe infections, especially in young children. Hib is known to cause several types of invasive diseases (e.g., meningitis, pneumonia, cellulitis, septic arthritis, and epiglottitis). Before the introduction of the Hib vaccine, meningitis was the most common Hib-

induced invasive disease, leading to severe complications like permanent hearing impairment or other neurological conditions in a significant percentage of patients who survived it [5].

*Mycoplasma pneumoniae* is a bacteria that cause upper respiratory tract infection and pneumonia. The number of infections varies over time, with disease peaks observed every 3 to 7 years. An estimated 2 million cases of *M. pneumoniae* infections occur each year in the United States, but the actual number might be higher as many infections go undiagnosed. This illness can occur any time of the year but may be more common in summer and early fall [6, 7].

*Streptococcus pneumoniae*, a Gram-positive bacterial pathogen, has been responsible for numerous outbreaks since its discovery in the 1880s. A study revealed 94 *S. pneumoniae* outbreaks occurring between 1916 to 2017 worldwide and *S. pneumoniae* leads to 450,000 hospitalizations per year in the United States. These outbreaks were predominantly respiratory infection that spread through airborne droplets [8, 9].

For respiratory viruses, notable examples include various coronaviruses such as SARS-CoV (2002), MERS-CoV (2012), and SARS-CoV-2 (2019); influenza viruses such as the Spanish flu (H1N1; 1918), Asian flu (H2N2; 1957), Hong Kong flu (H3N2; 1968), Russian flu (H1N1; 1977), and swine flu (H1N1; 2009); as well as human metapneumovirus, measles, mumps, and rhinoviruses [1, 10, 11]. Among various respiratory disease, MERS-CoV has the highest mortality rate at 34%, followed by SARS-CoV with 10% and the Spanish flu with 2.5% mortality rate [12-14]. However, the transmission rate should also be considered when determining the severity of viruses. The basic reproduction number ( $R_0$ ) is commonly used to estimate the number of people who are infected by a single infected individual in a population with no immunity and no interventions in place. Research indicates that the  $R_0$  values for SARS-CoV, MERS-CoV, and SARS-CoV-2 are 2-4, <1, and 1.9-6.49, respectively [15, 16]. For influenza viruses, the  $R_0$  values for the Spanish, Asian, Hong Kong influenza are 2.4-4.3, 1.8,

and 1.06-2.06, respectively [17-19]. In contrast to the viruses, measles, despite the availability of vaccines, has the highest  $R_0$  ranging from 12-18 [20]. The high infectivity of measles viruses can be attributed to factors such as airborne transmission, environmental stability, and the ability to initiate infection from 4 days before the onset of recognizable symptoms [21]. Respiratory diseases are typically characterized by a range of symptoms affecting the respiratory system. Common symptoms include coughing, shortness of breath, and increased production of sputum. In more severe cases, individuals may experience respiratory distress. The specific symptoms can vary depending on the type of respiratory disease. For instance, SARS-CoV and MERS-CoV tend to have a higher fatality rate and more severe respiratory symptoms, whereas SARS-CoV-2 has a broader range of clinical manifestations from asymptomatic cases to anosmia and gastrointestinal symptoms [22]. The influenza viruses (i.e., Spanish flu, Asian flu, Hong Kong flu, Russian flu, and swine flu) share similar symptoms. In milder cases, the illness is limited to the upper respiratory tract, exhibiting symptoms such as fever, sore throat, nasal congestion, coughing, headache, muscle aches, and fatigue. However, in more severe cases, the virus can cause pneumonia, which can be a direct consequence of the influenza virus or a result of a secondary bacterial infection in the lower respiratory tract. These severe cases of pneumonia can occasionally lead to fatal outcomes [23]. Human metapneumovirus, a relatively recently discovered virus, is associated with upper and lower respiratory tract infections, especially in children, the elderly, and immunocompromised individuals. Its symptoms are similar to those of other respiratory viruses, including cough, fever, and nasal congestion [24, 25]. Measles is characterized by a high fever, inflamed eyes, and a distinctive red rash that usually starts on the face and then spreads to the rest of the body [26, 27]. Mumps primarily presents with swollen salivary glands, causing puffy cheeks and a tender, swollen jaw, in addition to fever, headache, muscle aches, fatigue, and loss of appetite [28, 29]. Rhinoviruses, which are the most common

viral infectious agents in humans and the predominant cause of the common cold, present symptoms such as sore throat, runny nose, cough, sneezing, and sometimes a mild fever [30, 31].

Fungi primarily infecting the respiratory system includes *Blastomyces dermatitidis*, *Coccidioides* spp., *Cryptococcus gattii*, *Histoplasma capsulatum*, *Paracoccidioides* spp., and *Talaromyces marneffeii* [1]. These fungi led to localized outbreaks but were not developed to pandemics/epidemics. *Blastomyces dermatitidis*, the cause of blastomycosis, often presents as a lung infection but can spread to skin and bones. *Blastomyces dermatitidis* outbreaks particularly occurs near North American waterways, often linked to soil-disturbing activities [32]. *Coccidioides* spp. causes coccidioidomycosis or "Valley fever," endemic to desert regions of the southwestern United States, parts of Mexico, Central and South America, with symptoms ranging from mild to severe pulmonary issues [33]. *Cryptococcus gattii*, responsible for cryptococcosis, can lead to pneumonia and potentially disseminate to the central nervous system, particularly causing meningitis. It occurs in subtropical and tropical regions, as well as the Pacific Northwest of the United States [34]. *Histoplasma capsulatum* leads to histoplasmosis, commonly identified in areas such as the Ohio and Mississippi River valleys. Outbreaks have been linked to activities disturbing bird or bat droppings in endemic areas. Infection can range from mild respiratory symptoms to severe, disseminated disease [35]. *Paracoccidioides* spp. cause paracoccidioidomycosis, primarily found in Central and South America. The fungus typically infects individuals through inhalation of airborne spores from the environment, often linked to agricultural activities where soil disturbance can release fungal spores into the air. It often affects the lungs but can also involve mucous membranes and other organs [36]. *Talaromyces marneffeii*, previously known as *Penicillium marneffeii*, causes talaromycosis. It is endemic to tropical climates of Southeast Asia and is particularly severe in immunocompromised individuals. The fungus is often associated with bamboo rats as rodents'

burrows, found in the soil of forested areas, provide a suitable habitat for the fungus [37].

### 1.1.1 Resistance of respiratory pathogens

To combat respiratory pathogens, diverse antimicrobial agents including antibiotics, antivirals, and antifungals have been developed. However, a significant challenge is the ability of these pathogens to evolve and develop resistance mechanisms against these treatments, thereby diminishing the effectiveness of the antimicrobial agents. A notable example of this is seen in *Mycobacterium tuberculosis*. Mismanagement of antibiotic treatments, such as incorrect dosages or treatment durations, has led to the emergence of multidrug-resistant (MDR) tuberculosis. MDR tuberculosis strains have resistance to isoniazid and rifampicin, the first-line drugs that have proven their effectiveness [38]. The development of resistance can often be traced back to specific genetic mutations in the TB bacteria. For instance, resistance to isoniazid is frequently linked to alterations in the *katG* gene, responsible for producing the enzyme needed to activate isoniazid [39]. Similarly, rifampicin resistance is commonly associated with mutations in the *rpoB* gene, which encodes the beta subunit of RNA polymerase, affecting the binding efficacy of drugs [40]. Treatment regimens for these forms of *M. tuberculosis* are more complex and protracted, often extending for 18-24 months and necessitating the use of second-line drugs. These alternatives tend to be more costly, have greater side effects, and are less effective compared to the first-line drugs [41]. *Pseudomonas aeruginosa*, as another example, has acquired multi-drug resistance due to alternation in the quinolone resistance-determining regions (QRDR), which are responsible for DNA gyrase and topoisomerase IV. Besides, four efflux systems of the resistance nodulation division (RND) family, (i.e., MexAB-OprM, MexEF-OprN, MexCD-OprJ, and MexXY-OprM) have been reported to significantly contribute to the acquisition of antimicrobial resistance [42]. Treating multi-drug resistant *Pseudomonas*

*aeruginosa* infections presents a complex challenge due to the emergent resistance of the pathogen and the limited options for antibiotics. As such, such infections would result in increased length of treatment, higher readmission rates, and escalating costs [43].

Antiviral resistance in viruses can significantly impact human health, particularly in treating viral infections. The development of resistance to antiviral drugs can lead to treatment failure, prolonged illness, increased risk of spreading resistant viruses, and a need for alternative treatments that may be less effective or more toxic [44]. This resistance often arises from genetic changes in the virus. An example is the influenza virus, which can develop resistance against various drugs, including amantadine, rimantadine, laninamivir, oseltamivir, peramivir, and zanamivir [45]. These drugs mainly target the M2 ion channel and neuraminidase (NA) inhibitors. The M2 ion channel controls proton influx into viral particles and can be inhibited by specific drugs [46]. For instance, mutations at any of five key sites (positions 26, 27, 30, 31, or 34) in the M2 protein can lead to loss of effectiveness of these inhibitors[47]. Resistance also occurs in the NA inhibitors. The NA is involved in the final step of virus infection by cleaving sialic acid from cell surface and facilitating virus release from infected cells[48]. NA inhibitors produced based on analogue of the NA substrate sialic acid binds to NA proteins and inhibit the enzymatic activities. For instance, mutations such as Arg292Lys (a change from arginine to lysine at position 292) and Glu119Val (a change from glutamine to valine at position 119) have been linked to resistance against NA inhibitors such as oseltamivir [47]. Along with influenza viruses, diverse drugs are in development to against SARS-CoV-2 and there have been concern over drug resistance. Currently, there are three FDA-approved drugs: Veklury (remdesivir), Paxlovid (nirmatrelvir and ritonavir), and Lagevrio (molnupiravir) [49-51]. Remdesivir, the first FDA-approved antiviral for SARS-CoV-2, inhibits viral RNA synthesis. However, SARS-CoV-2 mutations, such as Ser759Ala (a change from serine to alanine at position 759) and Val792Ile

(a change from valine to isoleucine at position 792) in the RNA polymerase, have been reported to alter the structure of RNA polymerase and reduce the affinity of remdesivir [52]. Nirmatrelvir targets the main protease ( $M^{pro}$ ) of the virus but is less effective against strains with the Glu166Val (a change from glutamic acid to valine at position 166) mutation in the protease due to alterations in the  $M^{pro}$  structure. These mutations have already been identified in real-world cases [53, 54]. Molnupiravir acts as an analogue of cytosine (one of the four nucleotide bases) and induces random mutations during viral replication. To date, no resistance to molnupiravir treatment has been reported [55, 56].

Drug resistance in fungi is also a growing concern. To treat *Aspergillus fumigatus*, azole antifungals are commonly used as the first line of treatment. The azole antifungals inhibit the enzyme called lanosterol 14- $\alpha$ -demethylase, which converts lanosterol to ergosterol. The depletion of ergosterol impacts the integrity and functionality of the cell membrane, eventually leading to fungal cell death [57]. However, about 19% of *Aspergillus fumigatus* is resistant to azole antifungals, which is linked to increase in mortality by 25% [58, 59]. This high mutation is attributed to point mutations in *cyp51A*, which leads to reduction in the affinity of azoles to target protein. For instance, presence of 34-base pair tandem repeat ( $TR_{34}$ ) in the promoter region of *cyp51A* and Leu38His (a change from leucine to histidine at position 38) mutation are reported to be responsible for the drug resistance [58, 60]. Also, presence of 46-base pair tandem repeat ( $TR_{46}$ ) and two substitutions, Tyr121Phe (a change from tyrosine to phenylalanine at position 121) and Thr289Ala (a change from threonine to alanine at position 289) in the promoter region led to resistance to azole antifungals [58, 60]. *Candida auris* is another example of fungi that achieve resistance to antifungals. The typical first-line treatment for *Candida auris* infections involves echinocandin drugs such as anidulafungin, caspofungin, or micafungin [61]. These drugs inhibit the enzyme complex 1,3- $\beta$ -D-glucan synthase, crucial for maintaining the

cell wall structure of *Candida auris*. However, mutations in the *FKS1* gene of *Candida auris*, resulting in the S639Y (a change from serine to tyrosine at position 639) and R1354H (a change from arginine to histidine at position 1354) mutations, can enhance glucan synthase activity, thereby reducing the effectiveness of echinocandin [62, 63].

Drug resistance in pathogens, including bacteria, viruses, and fungi poses a significant threat to human health. It leads to reduced effectiveness of standard treatments, making infections harder to cure and increasing the risk of disease spread, severe illness, and death. Therefore, there is an urgent need to develop novel systems and strategies to combat drug-resistant infections.

### **1.1.2 Size dependent infection mechanism of pathogens**

The main pathogen transmission routes can be categorized into aerosol ( $< 5 \mu\text{m}$ ), droplets ( $< 100 \mu\text{m}$ ), and splash ( $> 100 \mu\text{m}$ ) [64]. Aerosols in respiratory systems are mostly generated by three mechanisms: bronchiole fluid film burst (BFFB), shear force applied to bronchiole, and laryngeal fluid film burst. BFFB is the mechanism where aerosols are generated in bronchiole by the process of exhalation and inhalation. During exhalation, alveolus shrinks, forming small airway ‘fluid’ closure, which bursts during inspiration as alveolus is expanded [65]. Besides, shear forces applied to bronchial fluid can be another source of aerosol generation, which is generated by coughing and sneezing of high flow rate ( $< 50 \text{ m/sec}$ ). Aerosols are also generated in laryngeal by vocal fold vibration and closure and reopening cycles of laryngeal [65]. Compared to aerosol generation, droplet and splash generation have more sources to cause such as closing and reopening of the mouth, vocal folds, small airways, and pores of Kohn. The droplets can be further shattered to small sizes by vibrational breakup, bag breakup, bag-and-stamen breakup, sheet-thinning breakup, and catastrophic breakup [66]. Vibrational breakup occurs when oscillations or vibrations within a liquid droplet become so pronounced that they lead to the disintegration of the liquid mass into smaller droplets [67]. Bag breakup is a phenomenon observed in droplets subjected to an aerodynamic field. As a droplet moves through a gas, it flattens and forms a bag-

like structure due to aerodynamic forces. The thin liquid "bag" expands until it can no longer sustain its structure and breaks up into smaller droplets [68]. The bag-and-stamen breakup is an extension of the bag breakup mode and occurs under specific conditions that allow for even greater relative velocities between the liquid and the surrounding gas. Following the initial formation of the bag, a central jet-like structure, known as the "stamen," emerges and disintegrates into droplets [69]. Sheet-thinning breakup involves the disintegration of a liquid sheet into droplets. This process occurs as the liquid sheet becomes unstable and thins out due to surface tension forces. Variations in the sheet's velocity and pressure lead to the formation of holes, which expand and fragment the sheet into droplets [70]. Catastrophic breakup occurs under extreme conditions, leading to the rapid and complete disintegration of the liquid mass into a fine mist of droplets [71].

Bacteria are mainly transmitted through droplets rather than aerosols (e.g., *Streptococcus pneumoniae*, *Haemophilus influenzae*, and *Neisseria meningitidis*), whereas viruses can utilize both transmission routes [5, 8, 72]. This distinction can be influenced by the larger size of bacterial particles and their environmental susceptibility, often requiring more moisture to remain viable. In contrast, viruses, especially those that are non-enveloped, can be more stable in dry environments and are capable of aerosol transmission over longer distances [73-75]. However, it does not indicate that bacteria only transmit through droplets and there are also many bacteria that they are transmitted mainly through aerosols as their main transmission route such as *Mycobacterium tuberculosis* [39]. *M. tuberculosis* has high durability as it contains thick waxy coat that makes *M. tuberculosis* relatively resistant to drying and allows it to survive in the air longer than many other bacteria [76].

For viruses, the distinction between droplet and aerosol transmission is not always clear-cut, and many viruses can be transmitted through both droplets and aerosols, depending on factors (e.g., viral load in respiratory secretions, temperature, and humidity) [77]. For influenza A viruses and rhinoviruses, decrease in temperature and humidity is reported to be related to increase in transmissibility as coldness decreases activity of protease in the host and dryness inhibit the mucociliary clearance that disrupt the virus binding [77, 78]. In contrast, enteroviruses (e.g., polioviruses, coxsackieviruses, and echoviruses) often peak in warmer months, particularly in temperate climates, which is opposite to the trend observed

with influenza and common cold viruses. The discrepancy was due to increased outdoor activities and school reopening, which enable the transmission of enteroviruses that are transmitted using respiratory droplets and the fecal-oral route [79, 80].

### 1.1.3 Target molecules of pathogens in the host

Pathogens often target different molecules for infection, a strategy that enables them to infect specific cell types or species. The nature of these target molecules varies widely among pathogens (such as viruses, bacteria, fungi, and parasites) and depends on the infection mechanism and specificity of the pathogen.

Bacteria have evolved various mechanisms to target specific molecules on host cells, facilitating their attachment, invasion, or the delivery of toxins. Certain strains of *Escherichia coli*, such as those causing urinary tract infections (UTIs), possess fimbriae (hair-like structures) that allow them to attach to the urinary tract's epithelial cells. For instance, uropathogenic *E. coli* (UPEC) can bind to mannosylated proteins on the surface of bladder cells using its FimH adhesin at the tip of its type 1 fimbriae [81]. *Staphylococcus aureus* uses fibronectin-binding proteins to attach to fibronectin, a molecule found in the extracellular matrix and on the surface of cells. This interaction facilitates the bacteria's adherence to and invasion of host tissues [82]. *Helicobacter pylori*, known for causing stomach ulcers and gastritis, adheres to gastric epithelial cells by binding to blood group antigen-binding adhesin (BabA) and sialic acid-binding adhesin (SabA). BabA recognizes various Lewis antigens, while SabA interacts with sialylated Lewis antigens on the gastric mucosal tissue. These interactions facilitate a strong attachment, enabling the bacteria to persist in the harsh acidic environment of the stomach [83]. *Neisseria gonorrhoeae* uses Neisserial type IV pili for initial binding and colony opacity-associated (Opa) proteins for tight interaction with epithelial cells of the mucosal surfaces. It specifically targets the CEACAM (carcinoembryonic antigen-related cell adhesion molecule) on the surface of human cells for attachment [84].

Viruses are highly specific in their interactions with host cells, largely due to the need to bind to

precise receptor molecules on the surface of these cells to initiate infection. This specificity is a cornerstone of viral tropism, determining which cells, tissues, or even species a virus can infect [85]. Influenza viruses target the respiratory tract and bind to sialic acid residues present on the surface of epithelial cells in the nose, throat, and lungs. The hemagglutinin (HA) proteins on the surface of the influenza viruses mediate this binding, allowing the virus to attach to and subsequently enter host cells. There are several subtypes of influenza viruses (e.g., H1N1, H3N2, and H5N1) that vary in their specific HA proteins and thus in their precise receptor specificity and infection patterns [86]. For instance, H1N1 and H3N2 influenza viruses mainly bind to sialic acids linked to galactose by an alpha-2,6 linkage while H5N1 influenza viruses bind to sialic acids linked to galactose by an alpha-2,3 linkage [87]. Human immunodeficiency viruses target immune cells, specifically CD4+ T cells, macrophages, and dendritic cells. The virus binds to the CD4 receptor on these cells in conjunction with a co-receptor, either CCR5 or CXCR4. The gp120 protein on the surface of HIV facilitates this binding. The specific interaction with these receptors is critical for the ability to infect immune cells, leading to the immune system deterioration observed in acquired immunodeficiency syndrome (AIDS) [88]. Rabies Viruses infect nerve cells (neurons) and initially bind to the nicotinic acetylcholine receptor (nAChR) on muscle cells using glycoproteins on rabies viruses. The viruses then bind to other receptors such as the neural cell adhesion molecule (NCAM) and p75 neurotrophin receptor (p75NTR). This targeting mechanism explains the neurotropism of rabies virus and its ability to travel along the nervous system to the brain [89].

Similar to viruses targeting receptors on host cells, fungi also have mechanisms to recognize and bind to certain sites or receptors on the surface of host cells to facilitate infection. This specificity is crucial for the adherence, colonization, and eventual invasion of host tissues by the fungi. However, compared to the well-documented receptor-ligand interactions seen in viral infections, the mechanisms of fungal adherence and specificity can be more varied and complex, often involving various binding sites [90-93]. *Candida albicans* for example, adheres to epithelial and endothelial cells through a variety of adhesin proteins that recognize specific molecules on the host cell surface [90, 91]. The Als (agglutinin-like sequence) family of proteins on *Candida albicans* can bind to various peptide ligands on host cells with differing binding affinities, facilitating adherence and invasion. These interactions are critical for the

establishment of candidiasis in various parts of the body [90, 91]. *Cryptococcus neoformans* has a capsule composed mainly of glucuronoxylomannan (GXM). The capsule not only protects the fungus from the host's immune system but also interacts with specific receptors on the host cell surface, facilitating adherence and invasion. For instance, GXM can bind to CD14, CD11/CD18 heterodimers, TLR2, and TLR4, promoting phagocytosis while also exploiting the process to survive and replicate within host cells [92]. *Aspergillus fumigatus* which causes aspergillosis, primarily affects the respiratory system. It produces various surface proteins that mediate adherence to host cells and extracellular matrix components. One such example is galactosaminogalactan, a cationic polysaccharide that facilitates adhesion to host cells and biofilm formation through electrostatic attraction with anionic cells [93].

## **1.2 Vaccines and their limitations**

While vaccines are highly efficient in controlling disease spread, their development is inherently time-consuming, involving a lengthy process from pre-clinical stages to clinical trials. It is reported that vaccinating within two months of an outbreak's onset can significantly curb pathogen spread [64]. However, the typical vaccine development timeline spans 10-15 years. The SARS-CoV-2 vaccine set a record for speed, developed in 12 months [94]. Despite this accelerated pace, producing vaccines within two months, while adhering to all regulatory guidelines and ensuring safety and efficacy, remains unfeasible.

### **1.2.1 Types of vaccines and immune responses**

Since Louis Pasteur's groundbreaking conceptualization of vaccination, significant advancements have been made in the development of vaccines in terms of their stability and effectiveness [95]. To date, seven types of vaccines have been developed: live-attenuated, inactivated, replicating viral vector, non-replicating viral vector, DNA, RNA, and subunit vaccines. Each vaccine type leverages distinct immunological mechanisms to trigger adaptive immunity upon administration [96]. Replicable vaccines, including live-attenuated vaccines,

replicating viral vector vaccines, and replicating nucleic acid vaccines, enter host cells and replicate virulent molecules, which are subsequently taken up by dendritic cells (DCs). In contrast, non-replicable vaccines, such as non-replicating viral vector vaccines, inactivated vaccines, subunit vaccines and non-replicating nucleic acid vaccines, are directly phagocytosed by DCs [96, 97]. Replicable vaccines are characterized by prolonged immunogenicity compared to non-replicable vaccines due to their ability to replicate. Whole particle-based vaccines, such as live-attenuated and inactivated vaccines, exhibit the highest immunogenicity compared to other types of vaccines due to the presence of immunostimulant molecules within the particles, effectively inducing immunity similar to that of natural infections [98-102].

Following the phagocytosis, DCs carrying vaccine particles migrate to the draining lymph node, where they present peptides derived from the vaccine antigens on the major histocompatibility complex (MHC) class II or MHC class I molecules. MHC II activation stimulates CD4<sup>+</sup> T cells (T helper cells), including T helper (Th) 1 cells and Th2 cells [103]. Th1 cells play a role in cell-mediated immunity by secreting interferon-gamma (IFN- $\gamma$ ), a proinflammatory cytokine that eliminates external pathogenic particles [104, 105]. Th1 cells also activate CD8<sup>+</sup> T cells (cytotoxic T cells) by interacting with MHC I [106]. This interaction leads to the production of granzymes, which induce apoptosis, and the pore-forming protein perforin, which physically damages the target cell membrane, allowing granzymes to enter the cell [107]. In contrast, Th2 cells initiate humoral immunity by producing interleukin-4 (IL-4), IL-5, and IL-13, which promote the proliferation and maturation of B cells. Additionally, Th2 cells produce anti-inflammatory IL-10, which modulates the inflammatory responses of Th1 cells (Figure 1.1) [104, 105].

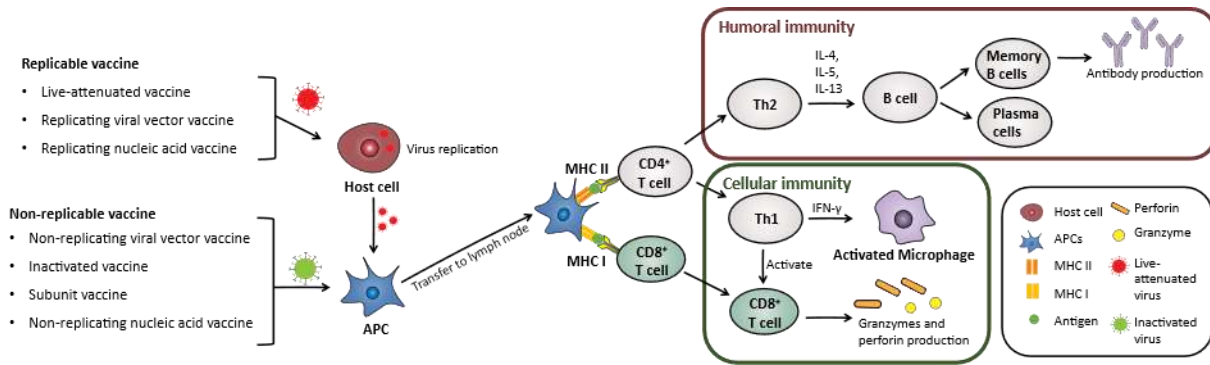


**Figure 1.1.** Schematic illustration of immune responses upon vaccine administration.

### 1.2.2 Limitation in invasive administration

Vaccine administration methods can be broadly categorized into invasive, minimally invasive and non-invasive administration, and conventional vaccine administration primarily relies on invasive administration (e.g., intramuscular, subcutaneous, and intradermal) to maximize vaccine bioavailability through site-specific administration. However, such methods of administration possess inherent limitations that compromise their utility (Figure 1.2). Firstly, liquid formulations used in these methods necessitate a cold chain system, making them susceptible to accidental freezing [108, 109]. Certain temperature ranges can drastically reduce the shelf life of vaccines, with examples including Pfizer-BioNTech (< 6 months at -60 to -90 °C and < 2 hrs at 8–30 °C), ModernaTX (< 30 days at 2-8 °C and < 12 hrs at 8–25 °C), and Oxford-AstraZeneca (< 6 months at 2-8 °C and < 2 hrs at 8–25 °C) SARS-CoV-2 vaccines [110]. Especially, mRNA vaccines are easily affected by changes in liquid formulation (i.e., pH, buffers, temperature, amount of oxygen, etc.), which can lead to the degradation of the vaccines through hydrolysis [111].

Second, the use of needle-based delivery of liquid vaccines also presents technical and

safety concerns. The variability in adipose tissue thickness among individuals necessitates adjusting the needle length based on body weight and sex. For instance, a needle length of 1 inch is recommended for individuals weighing less than 70 kg, 1-1.25 inches for men weighing 70-118 kg and women weighing 70-90 kg, and 1.5 inches for men weighing over 118 kg and women weighing over 90 kg [109, 112]. Achieving accurate administration requires specialized personnel and proper setups, posing challenges for vaccination in isolated communities and developing countries with limited resources and personnel. Furthermore, needle-based administration carries the risk of needlestick injuries and the transmission of bloodborne pathogens to the injection site (e.g., hepatitis B, hepatitis C, and human immunodeficiency virus (HIV)) [113].

Third, invasive vaccines primarily elicit systemic immune responses in the lower respiratory tract, unlike natural infections that stimulate robust, both systemic and mucosal immunities [114, 115]. While systemic immune responses can provide disease-attenuating or disease-preventing immunity through the production of immunoglobulin G (IgG) [114], the limited mucosal immunity in the lower respiratory tract can hinder the elimination of pathogens in the early stages, potentially exacerbating disease severity. On the other hand, minimally invasive and non-invasive vaccines can achieve mucosal vaccination that initiates both robust systemic and mucosal immunities, thereby efficiently preventing pathogens from developing severe disease [116, 117].

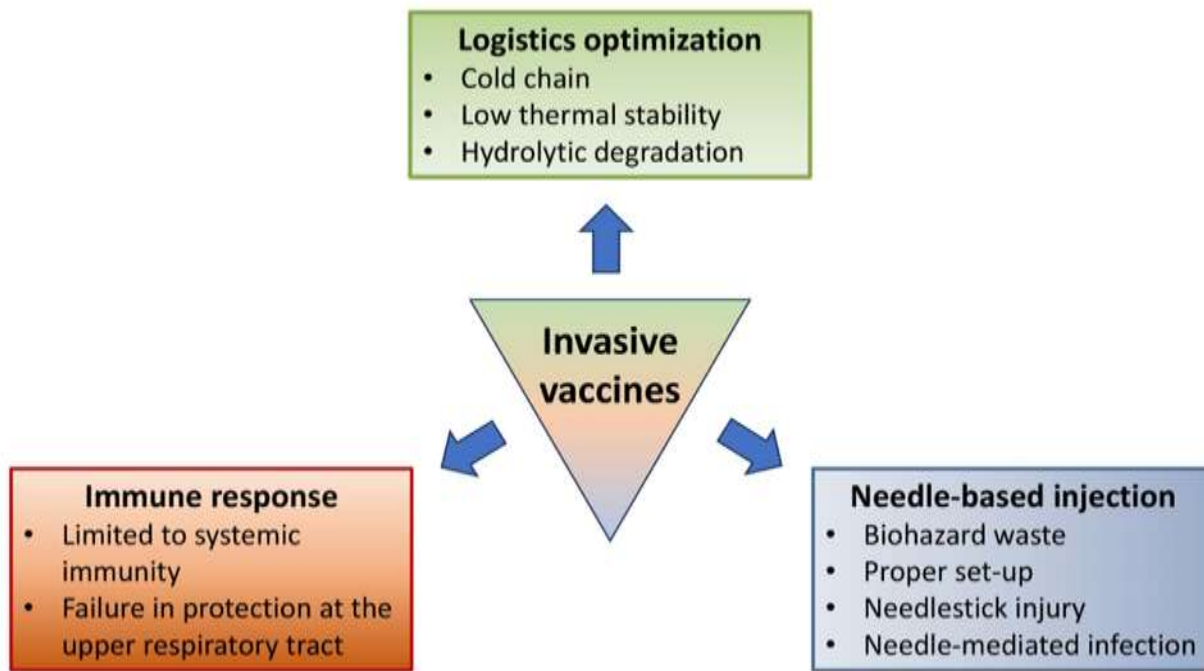


**Figure 1.2.** Schematic illustration of limitations in invasive vaccines.

### 1.2.3 Limitation in non-invasive administration

Non-invasive vaccines have gained significant recognition due to the drawbacks associated with conventional needle- and liquid-based invasive vaccines, such as the need for cold chain storage, challenges in self-administration, issues with thermal and long-term stability, risks of needle-mediated infections, and needlestick injuries. Among the major non-invasive vaccine systems, oral, intranasal, and transcutaneous administration have been extensively investigated. These non-invasive approaches offer solutions to various limitations of invasive vaccines. However, the effectiveness of non-invasive vaccines is hindered by their limited bioavailability, as biological barriers prevent their efficient absorption into the body. To

overcome this issue and enhance the bioavailability of non-invasive vaccines, diverse formulations tailored to specific administration routes are under development.

### **1.2.3.1 Oral administration**

Oral administration is one of the non-invasive administrations that are under development. The immune responses of oral vaccinations are mainly initiated in the intestine, where the majority of vaccine uptake and drug absorption occur [118, 119]. The intestine consists of several layers, including the mucus layer, water layer, epithelial layer, basement membrane/Peyer's patches, and lymph nodes [120]. The epithelial layer is composed of enterocytes, goblet cells, and microfold cells (M-cells), which are joined together by tight junctions that prevent the movement of molecules through paracellular and transcellular routes [120-122]. Enterocytes, the most abundant cells in the intestinal epithelium (constituting up to 80% of the local cell population), transport antibodies through transcytosis using the neonatal Fc receptor (FcRn) and form antibody-antigen complexes [123, 124]. Goblet cells produce mucin, the main component of the mucus layer, which provides physical protection against the uptake of pathogenic particles.[125] M-cells play a crucial role in initiating immune responses by phagocytosing large particles and endocytosing small particles through specialized receptors like pattern recognition receptors (PRRs) [121, 122]. Pathogen particles phagocytosed by M-cells are subsequently taken up by dendritic cells (DC cells) in Peyer's patches, leading to the activation of cellular and humoral immunity through the differentiation of T cells and B cells (Figure 1.3) [126].

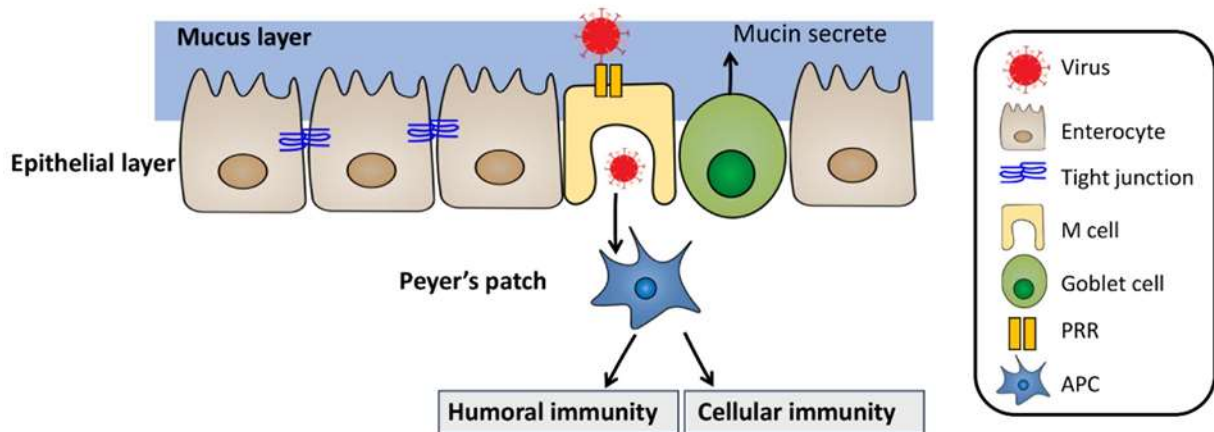


**Figure 1.3.** Representation of immune responses of intestinal M cell.

Despite the advantageous characteristics of oral immunization, (e.g., stability, independence from cold chain requirements, ease of administration and storage), there are technical challenges in controlling the behavior of orally administered vaccines. Factors such as the varying pH levels of gastrointestinal fluids (e.g., stomach: 0.8-5, duodenum:  $\sim 7$ , jejunum:  $\geq 7$ , ileum:  $\geq 7$ , and colon: 7-8), osmolality, surface tension, viscosity, temperature, volume, hydrodynamics, composition, gastric emptying rate and force, intestinal transit time, and flow rate can impact the performance of orally administered vaccines [118, 127]. Additionally, the presence of mucosal barriers and biomolecules, such as digestive enzymes, limits the bioavailability and immunogenicity of oral vaccines [128]. This low efficiency necessitates higher vaccine doses, which can eventually lead to immune tolerance in the host. Moreover, the primary approach for oral vaccines involves the use of heat-killed or attenuated pathogens, which makes it difficult to effectively activate the immune system due to poor penetration of the mucus layer. There is also a risk of attenuated pathogens regaining their toxicity, as exemplified by the oral polio vaccine (OPV) outbreak that occurred in several countries in 2000, including

Egypt, Haiti, the Philippines, and the Dominican Republic. Extensive research has been conducted to address these limitations and optimize the administration of oral vaccines [129].

### **1.2.3.2 Intranasal administration**

Intranasal vaccination offers several advantages, including easy accessibility, the potential for herd immunization, and the ability to initiate both mucosal and systemic immune responses, making it a favorable administration route for vaccines [130]. Similar to the Peyer's patches in the intestinal tract, the nasal-associated lymphoid tissues (NALTs) play a significant role in inducing immunity through intranasal vaccination in rodents. NALTs are regions rich in immune cells (such as T cells, B cells, dendritic cells, macrophages, and M-cells) where active immune responses occur [131]. The key difference between the Peyer's patches and NALTs is that the formation of NALT is triggered after exposure to pathogens, whereas Peyer's patches develop before birth. Similar to NALTs of rodents, Waldeyer's rings play a major role in human immune responses upon intranasal administration. The Waldeyer's rings, including the pharyngeal tonsil, tubal tonsils, palatine tonsils, and lingual tonsils, firstly transfer pathogens to DC cells, initiating mucosal immunity through the differentiation and proliferation of T cells [131, 132]. Similar to oral vaccination, intranasal vaccination faces challenges from the mucus layer, which can result in mucociliary clearance of vaccine particles and hinder the vaccination process. Therefore, numerous methods are under development to enhance the immune response during intranasal vaccination, such as improving mucoadhesive interaction and intestinal permeability, as well as incorporating adjuvants.

Intranasal vaccines, typically delivered in liquid form, are designed to uniformly disperse key components such as adjuvants and stabilizers, thereby facilitating enhanced penetration into cells [133]. However, similar to other liquid vaccines, they are not exempt from common

challenges associated with conventional liquid vaccines (e.g., osmolarity, pH, viscosity, and surface tension). In terms of osmolarity, isotonic solutions (~290 osmol/L) are commonly used to achieve optimal osmolarity, as hypotonic solutions are poorly absorbed and hypertonic solutions can cause cell shrinkage upon diffusion [133]. The pH of liquid formulations should be maintained between 4.5 and 6.5 to avoid irritation, considering that the nasal mucus layer has a pH of 5.5-6.5; it has also been observed that lysozymes in the intranasal system are inactivated at neutral pH, which can increase the risk of microbial infection [134, 135]. Increasing the viscosity of nasal mucus is another approach to enhance the immunogenicity of vaccines by prolonging their retention time in the nasal cavity and increasing the dosing volume of the nasal spray over conventional dosing volume (50-140  $\mu$ l) [136-138]. However, it must be noted that high mucosal viscosity may impede effective diffusion and spreading of the vaccines. Surface tension is another critical factor affecting the behavior of liquid vaccines. Most intranasal vaccines have lower surface tension (30.3–44.9 dynes/cm) than the nasal mucus layer (< 56 dynes/cm) [139]. The low surface tension of vaccines primarily facilitates better bioavailability by maximizing their spread within the nasal cavity [140].

Due to complexity in designing vaccines and physical hinderances, currently, there is only one FDA-approved intranasal vaccine, FluMist [141]. Diverse intranasal vaccines are still under development to combat various pathogens [131].

### **1.2.3.3 Transcutaneous administration**

Transcutaneous immunization (TCI) is a topical vaccination strategy that primarily stimulates systemic immunity, also inducing a moderate level of mucosal immunity with the assistance of an adjuvant [142]. TCI specifically targets epidermal cells, located in the middle layer of the skin, which also includes keratinocytes (KCs) and Langerhans cells (LCs). KCs are

the predominant cells in the epidermis and play a role in recognizing pathogens through Toll-like receptors (TLRs), triggering innate and adaptive immune responses. LCs, a type of dendritic cells, capture a significant portion of TCI particles and recognize them through the major histocompatibility complex (MHC), activating adaptive immune responses [143]. However, for TCI to be effective, it is necessary to penetrate the stratum corneum, the outer layer of the skin consisting of 10-20 layers of dead skin cells that act as a barrier against external substances [144]. Due to the limitation, there is currently no transcutaneous vaccine developed. Consequently, research has focused on exploring physical and chemical methods to enhance the penetration of the stratum corneum in order to achieve successful TCI.

Among the available transcutaneous immunization (TCI) methods, microneedles have gained acceptance due to their ease of use, accessibility, and independence from patches. Microneedles are minimally invasive and pain-free, involving small needles that penetrate the stratum corneum [145]. There are five categories of microneedles based on their structures: solid, coated, hollow, dissolving, and hydrogel-forming microneedles [146-148]. Solid microneedles are used to create microchannels in the skin, allowing for vaccine penetration [149]. To date, a variety of materials have been considered candidates for the production of solid microneedles (e.g., silicon, polysilicon, silicon dioxide, silicon nitride, PGA) [150]. While solid microneedles offer easy manufacturing and high dose delivery, they are hindered by a slower rate of diffusion when compared to other types of microneedles [151, 152].

Coated microneedles contain vaccines applied to the needle, enabling diffusion into the epidermis upon injection. However, one limitation is that the coating may cause coated particle loss during manufacturing and handling [145, 153]. As another option, hollow microneedles resemble conventional needle injection-based vaccination, with vaccines contained in the bore of the needle. These microneedles also provide the highest level of particle delivery but can

experience blockage by tissues upon contact, although repositioning the bore to the side can address this issue [145, 148].

Dissolving microneedles are made of water-soluble materials that penetrate and dissolve in the skin simultaneously. For these microneedles, vaccines and the microneedle matrix undergo a mixing process upon manufacturing. Among various candidates for the matrix of dissolving needles (e.g., sodium carboxymethylcellulose, poly(vinylalcohol), poly(vinylpyrrolidone), methylvinylether-co-maleic anhydride), sodium hyaluronate is most commonly used due to its biodegradability and mechanical strength [154, 155]. Remarkably, dissolving microneedles have shown high diffusion efficiency within a patch-wearing time of just several minutes, while it could be up to several hours for solid microneedles [151].

Lastly, hydrogel-forming microneedles have emerged as a promising option for their biocompatibility and controllable degradability [156]. These microneedles are equipped with hydrogel, capitalizing on its three-dimensional structure that allows for a significant capacity to carry vaccines; however, there is a possibility that vaccines can become trapped within the patch and they require a longer diffusion time up to several hours [151, 157, 158]. The mechanism of hydrogel-forming microneedles relies on the absorption of interstitial skin fluid, which causes the hydrogel to swell and burst, triggering the release of the vaccines from the microneedle [158, 159]. The vaccine-release behavior of the hydrogel is directly influenced by the swelling property of the matrix polymer and can be modulated by adjusting the amount of crosslinkers; increasing the percentage of crosslinkers results in a reduced swelling rate in the skin [156, 158]. Last but not least, achieving optimal performance with hydrogel-forming microneedles requires maintaining their hardness in a dry state, while ensuring rapid swelling in the skin [159].

## **1.3 Respiratory protection system**

While conventional masks are effective in mitigating pathogen transmission, they have inherent limitations. First, their single-use nature can lead to supply shortages during pandemics or epidemics and contribute to environmental pollution. Besides, the lack of antimicrobial properties in these masks means that contaminated surfaces can facilitate contact-based transmission, posing risks particularly to immunocompromised patients in healthcare settings and potentially triggering new outbreak waves. As such, exploring alternative methods or technologies to replace conventional masks is essential for better infection control and environmental sustainability.

### **1.3.1 Types of respiratory protection system**

Respiratory protection systems against pathogens can be broadly divided into cloth masks, surgical masks, and respirators. Cloth masks were a popular choice to use by the general public throughout the pandemic as they were widely available masks with low costs needed to purchase [160]. Although the cloth masks provided the most basic respiratory protection, they had the unique advantage of being consistently reusable while accommodating various face sizes, such as children and adults with little difficulty [160]. This advantage, with the benefit of higher comfort levels when wearing the mask made it an ideal choice for individuals not in the healthcare field.

Surgical masks originally took prominence in the healthcare field, where healthcare officials would utilize them to minimize the transmission of airborne pathogens to individuals who may be particularly vulnerable. However, with the Coronavirus pandemic, surgical masks were worn by the wider population as they could block coarse and fine aerosols released by nasal and oral orifices [161]. Although the wider population now utilized surgical masks, they

remained one of the most commonly used respiratory protection masks in hospital settings [162]. Surgical masks are a unique respiratory protection system as it is one of the most financially affordable due to their mass production. Compared to the N95 masks, surgical masks can be produced at a tenth of the price, making them ideal for those looking for basic respiratory protection at a minimal cost [162]. However, the limitations of the surgical mask lie in the fact that it provides a unidirectional sense of protection. This unidirectional protection stems from the surgical mask catching airborne particles released by the individual while providing minimal protection against pathogens for the user. There was minimal protection for the wearer as the surgical masks do not provide a sealed system [163].

The N95 respirator took dominance during the pandemic as it is a repository protection device, specialized for filtration of airborne particles. Due to the N95 respirator providing a bidirectional protection to the individual and to those around them, they were sought after by many. The unique aspect of bidirectional protection, elevated the respiratory protection the mask provided compared to surgical masks. The name N95 stems from the fact that the mask can remove up to 95% of all 0.3  $\mu\text{m}$  sized polydisperse [163]. As the N95 respirators had a higher cost of manufacturing, they were limited to the healthcare workers during the Coronavirus pandemic. A disadvantage of the N95 respirators was that they no longer provided bidirectional protection the moment they lost the seal on the face [164]. Currently the majority of N95 respirators are being utilized by healthcare workers who are in routine care of patients to prevent aerosol generation and infection of immunologically vulnerable individuals [165].

### **1.3.2 Efficiency of using masks in preventing the spread of pathogens**

Wearing masks has demonstrated its efficiency in controlling the spread of pathogens, as droplet spraying, considered a major infection pathway, contributes to 60-86% of cases, while

contact-based transmission through contaminated surfaces accounts for 9-32% of infection cases [166]. When  $10^2$ - $10^4$  PFU/ml of viruses in saliva were exposed in a healthcare setting face masks, face shields, and wearing both face masks and face shields reduced the relative risk of infection by 63%, 97%, and 99.9%, respectively [166]. Besides, modeling tests were performed to estimate the efficiency of mask-wearing, showing a reduction of 2-9% in the mortality rate in a New York setting and a 24-65% reduction in a Washington setting when 80% of the population wears a mask [167].

Recognizing the efficiency of mask-wearing, governments initiated regulations on mask use, which played a pivotal role in controlling the spread of pathogens. These regulations affect both directly (e.g., increased mask use compliance, reduction in community transmission, and protection for high-risk populations) and indirectly (e.g., normalization of mask-wearing, public awareness and education, and improvement in preparedness and response). It has been reported that after three weeks of implementing mask mandates across the US, the hospitalization growth rates were reduced by 5.6% in adults aged 18-64 years, compared to the growth rates observed in the four weeks prior to the enactment of the mandate [168]. Another study has shown that mask mandates contribute to a decrease in new SARS-CoV-2 cases by 3.55 per 100,000 people, a reduction in mortality rate by 0.13 per 100,000 people, and a decrease in hospital admissions by 2.38 per 100,000 people, after 40 days of mask mandates [169].

The data not only underscores the critical importance of mask usage in reducing transmission rates and protecting public health but also highlights the dynamic interplay between policy, public behavior, and health outcomes. As mask mandates have shown to significantly decrease the rate of new infections, hospital admissions, and mortality, it becomes clear that such preventative measures constitute a multifaceted approach to managing and eventually overcoming the pandemic.

### 1.3.3 Structure and limitations of conventional masks

Approved surgical/medical masks and respirators generally made of polymers (e.g., polypropylene, polyurethane, polyacrylonitrile, polystyrene, polycarbonate, polyethylene, and polyester). They usually consist of 3 (outer/middle (filter)/inner) or 4 layers (outer/support/middle (filter)/inner) [170]. The inner and outer layers protect the middle filter layer from physical damages. Common fabrics used in masks are made of hydrophobic fibers such as polypropylene, polyethylene, modacrylic, cellulose, and polyester, serving as a barrier to hydrophilic contaminants such as moisture and salivary droplets. As such, wearing a mask for an extended time can lead to the condensation of water and moisture retention, increasing breathing resistance. In addition to its economical advantage and chemical stability, polypropylene (PP) has been mainly used in outer/middle/inner layers for its compelling physical properties including a low melting point (160-166 °C), low density (0.91-0.94 g/cm<sup>3</sup>), and high tensile strength (3,200-5,000 psi) [171, 172]. Each layer of a mask is manufactured in a unique way, as the outer/inner and middle (filter) layers of masks are produced with high strength spunbond filaments (15-40 μm in diameter) and meltblown filaments (2-10 μm in diameter) with smaller pores, respectively [173-175]. Meltblown filters are often electrically charged (i.e., 10<sup>-5</sup>-10<sup>-6</sup> C/m<sup>2</sup>) to enhance the filtration efficiency by interacting with charged and non-charged contaminants through electrophoresis or dielectrophoresis [173]. However, the charge of electret fibers can be attenuated over time and significantly impacted by decontamination methods such as organic material and water treatments [176]. Besides, an increase in filtration efficiency usually compromises breathability due to the pore-size-dependant filtration mechanism of masks.

Despite the efficiency of masks against pandemics/epidemics, the conventional masks

have limitations mainly due to high stability of pathogens, single-use, microplastics/fibers from mask wastes. For pathogen stability, the effect of environmental factors (i.e., temperature, humidity salinity, protein, mucus, and pH) and substrate properties (i.e., material type, roughness, porosity, fiber diameter, and surface charge) on the transmission and stability of the virus has been extensively investigated. It is generally believed that the influenza virus exhibits higher stability and transmissibility in cold and dry conditions than in normal conditions.[177] Similarly, SARS-CoV-2 survived longer at 5 °C/75% relative humidity (RH) (up to 21 days) than at 25 °C/70% RH (up to two days) in an experiment [178]. Inert and nonporous substrates such as glasses tend to result in higher pathogen stability. This propensity was clearly illustrated by SARS-CoV-2 that displayed a longer life-time on smooth solid substrates (i.e., stainless steel (< 7 days), glass substrate (< 4 days), and plastics (< 7 days)) compared to cloth (< 2 days) and paper (< 3 hrs) at 22 °C/65% RH [179]. Given that people touch their self-face 50.07 times per an hour, the survival time of pathogens are long enough to be transmitted to hands or other surfaces [180]. Besides, it has been reported that virus positivity increases over time from 2% to 14.1% by wearing a medical mask for > 6 hours in health care settings [181, 182].

The environmental impact of using masks is also significant. WHO modeling estimated that approximately 89 million masks are needed per month in the US to combat pandemics as of March 2020, and Japan secured more than 600 million face masks per month as of April 2020. Additionally, mask production in China increased to 110 million per day in 2020 to meet such demands [170]. Masks can degrade into microplastics/fibers (< 5 mm) due to environmental conditions such as exposure to ultraviolet rays and the cold and anoxic conditions of the marine environment. This can lead to leaching into groundwater and contamination in oceans, rivers, lakes, and ponds [183]. The microplastics, due to their small size, can be ingested by marine organisms, causing physical harm and potentially toxic effects. These particles can accumulate

in the human body when consumed through the food chain, posing risks such as inflammation, reduced fertility, and mortality in wildlife, with the potential for similar impacts in humans [184].

Despite the effectiveness of masks in controlling pandemics, conventional masks limitations, including pathogen stability on various substrates, single-use implications, and environmental concerns related to microplastic pollution from discarded masks. Research into antimicrobial technologies is crucial to resolve the aforementioned issues. Moreover, the environmental impact of increased mask usage, particularly the generation of microplastics and their entry into ecosystems, underscores the need for sustainable mask solutions to mitigate harm to wildlife and humans.

#### **1.3.4 Mask decontamination methods and technical challenges**

A variety of decontamination methods utilizing heat, gas, liquid chemical, or radiation treatment have been investigated to evaluate the reusability of respiratory devices (Table 1.1). However, there have been major concerns in decontaminating masks, including potential contamination during handling, degradation of filter quality, and the production of undesired byproducts due to sanitization procedures. For example, high humidity conditions may degrade the surface charge of PP filters, and water-based treatments (e.g., steam and chlorine-based solution treatments) may fail to penetrate deeply into the fabrics since masks/respirators are hydrophobic [185]. Also, gas sterilization methods consume significant amounts of time as they require multiple steps and involve the use of reactive agents with high toxicities such as chlorine dioxide, hydrogen peroxide, and formaldehyde [186, 187]. Organic solvents have been shown to lower the filtration efficiency of PP masks due to increased electron mobility [188]. Moreover, filtering facepiece (FFP) filters have been found subject to degradation by high doses ( $> 1,000$

J/cm<sup>2</sup>) of ultraviolet germicidal irradiation (UVGI) and/or high heat (> 92 °C); meanwhile, UV penetration does not reach deep enough to deactivate small viral particles within fabrics [185, 189]. Occupational Safety and Health Administration (OSHA) did not recommend the use of an autoclave, dry heat, isopropyl alcohol, soap, dry microwave irradiation, chlorine bleach, disinfectant wipes, and ethylene oxide to decontaminate masks due to their well-explored negative side effects [190].

In order to achieve the safe reuse of masks/respirators, decontamination method should inactivate pathogens while also meeting the desired quality of filter performance and mask fitting. At the same time, the decontamination practice requires i) careful protocols to prevent transmission/infection of virus and ii) other resources such as materials, equipment, and specialists for implementation. It should be noted that the reuse of respirators has been strictly limited even during the COVID-19 pandemic. Therefore, much attention has been focused on antimicrobial technology as an alternative strategy for the safe and extended use of respiratory devices.

**Table 1.1.** Decontamination methods tested for face masks/medical masks/respirators under investigation. Abbreviations: surgical mask (SM), N95 respirator (N95), cloth mask (CM), filtering facepiece (FFP)

Type	Method	Procedure	Drawbacks	Filter performance
Heat	Dry heat	<ul style="list-style-type: none"> <li>Preserve at 75 °C for 30 min (N95) [185]</li> </ul>	<ul style="list-style-type: none"> <li>Degradation of filter</li> </ul>	Pressure drop decreases by 30% (after 1 cycle of treatment)
		<ul style="list-style-type: none"> <li>Preserve at 70 °C for 30, 60, and 90 min</li> <li><i>S.aureus</i> is used for filtration efficiency (SM) [191, 192]</li> </ul>	<ul style="list-style-type: none"> <li>Slow disinfection rate (1.8 log<sub>10</sub> reduction in 30 min</li> <li>3.5 log<sub>10</sub> reduction in 60 min</li> <li>4.5 log<sub>10</sub> reduction in 90 min)</li> <li>May not reduce malodour for reuse</li> </ul>	No significant decrease in filtration efficiency of N95 respirators (after 3 cycle of treatment)
	Steam	<ul style="list-style-type: none"> <li>Steam on boiling water for 10 min (N95) [185]</li> </ul>	<ul style="list-style-type: none"> <li>Degradation of filter</li> </ul>	Filtration efficiency decreases by 12% (after 5 cycles of treatment)
		<ul style="list-style-type: none"> <li>Steam on boiling water for 30 min (SM) [193]</li> </ul>	<ul style="list-style-type: none"> <li>Degradation of filter</li> </ul>	Fractional efficiency decreases by < 20% (after 5 cycles of treatment)

	Autoclave	<ul style="list-style-type: none"> <li>• 121 °C with 1.06 kg/cm<sup>2</sup> for 15 min (N95) [194]</li> </ul>	<ul style="list-style-type: none"> <li>• Degradation of filter</li> </ul>	Filtration efficiency decreases by 20% (after 1 cycle of treatment)
		<ul style="list-style-type: none"> <li>• 132 °C for 30 min (SM) [188]</li> </ul>	<ul style="list-style-type: none"> <li>• Degradation of filter</li> </ul>	Fractional efficiency decreases by < 20% (after 4 cycles of treatment)
<b>Gas</b>	Ethylene oxide	<ul style="list-style-type: none"> <li>• Concentration: 100% ethylene oxide</li> <li>• Operation of sterilizer for 1-3 hr at 54 °C (N95, SM) [195, 196]</li> </ul>	<ul style="list-style-type: none"> <li>• Production of 2-hydroxyethyl acetate (hazardous byproduct)</li> <li>• Oxidization of metal parts</li> </ul>	No significant decrease in filtration efficiency of N95 respirators (after 1 cycle of treatment)
	Formaldehyde vapor	<ul style="list-style-type: none"> <li>• Concentration: 2% of formaldehyde</li> <li>• Operation of sterilizer for 153min at 78 °C (N95, FFP2) [197]</li> </ul>	<ul style="list-style-type: none"> <li>• Changes in appearances; irregular fit factors after treatment</li> <li>• Toxicity of formaldehyde</li> </ul>	No significant decrease in filtration efficiency (after 2 cycle of treatment)
	Chlorine dioxide	- (N95, SM) [198]	<ul style="list-style-type: none"> <li>• Degradation of filter</li> </ul>	Filtration efficiency decreases by 18% of surgical mask (after 1 cycle of treatment)
	Peracetic acid	<ul style="list-style-type: none"> <li>• Concentration: 0.18% of peracetic acid</li> <li>• Aerosol development, dwell, scrub and vent phases for 44 min (N95) [199]</li> </ul>	-	No significant decrease in filtration efficiency
	Hydrogen peroxide gas plasma	<ul style="list-style-type: none"> <li>• Concentration: 59% of hydrogen peroxide</li> <li>• Operation of Sterilizer for ~55min at 45-50 °C (N95) [196]</li> </ul>	<ul style="list-style-type: none"> <li>• Degradation of filter</li> </ul>	Filtration efficiency decreases by 5-9% (after 1 cycle of treatment)
		- (SM) [198]	<ul style="list-style-type: none"> <li>• Degradation of filter</li> </ul>	Pressure drop decreases by < 50% (after 1 cycle of treatment)
<b>Liquid chemical</b>	Chlorine-based solution	<ul style="list-style-type: none"> <li>• Concentration: 2% of chlorine</li> <li>• Spray for 5 min (N95) [200]</li> </ul>	<ul style="list-style-type: none"> <li>• Degradation of filter</li> </ul>	Filtration efficiency decreases by 24% (after 1 cycle of treatment)
		<ul style="list-style-type: none"> <li>• Concentration: 0.5% sodium hypochlorite</li> <li>• Submersion for 10 min (N95) [194]</li> </ul>	<ul style="list-style-type: none"> <li>• Odor due to residual treated materials</li> </ul>	Filtration efficiency decreases by 20% (after 1 cycle of treatment)
		<ul style="list-style-type: none"> <li>• Chlorine dioxide solution (SM) [198]</li> </ul>	<ul style="list-style-type: none"> <li>• Degradation of filter</li> </ul>	Filtration efficiency decreases by 17% (after 1 cycle of treatment)
	Dimethyldioxirane (DMDO)	<ul style="list-style-type: none"> <li>• Concentration: 10% Oxone, 10% acetone,</li> <li>• 5% sodium bicarbonate</li> <li>• Submersion for 30 min (N95, SM) [195]</li> </ul>	<ul style="list-style-type: none"> <li>• Oxidization of metal parts</li> </ul>	-
	Isopropanol	<ul style="list-style-type: none"> <li>• Concentration: 100% isopropanol</li> <li>• Submersion for 10 min (N95) [194]</li> </ul>	<ul style="list-style-type: none"> <li>• Degradation of filter</li> </ul>	Filtration efficiency decreases by 30% (after 1 cycle of treatment)
		<ul style="list-style-type: none"> <li>• Concentration: 70%</li> <li>• Submersion for 1 sec and 1 min (N95) [164]</li> </ul>	<ul style="list-style-type: none"> <li>• Degradation of filter</li> </ul>	Filtration efficiency decreases by 18% and 22% for 1 sec and 1 min submersion, respectively (after 1 cycle of treatment)
		<ul style="list-style-type: none"> <li>• Concentration: 75%</li> <li>• Submersion for 10 min/ spray with small garden sprayer (SM) [188]</li> </ul>	<ul style="list-style-type: none"> <li>• Degradation of filter</li> </ul>	Fractional efficiency decreases by < 65% for both soaking and spraying (after 1 cycles of treatment)
Ethanol	<ul style="list-style-type: none"> <li>• Concentration: 70% ethanol</li> <li>• Submersion for 10 min</li> </ul>	<ul style="list-style-type: none"> <li>• Degradation of filter</li> </ul>	Filtration efficiency decreases by 30%	

		(N95) [194]		(after 1 cycle of treatment)
		<ul style="list-style-type: none"> <li>Concentration: 70% ethanol</li> <li>Submersion for 2 hour (SM) [201]</li> </ul>	<ul style="list-style-type: none"> <li>Degradation of filter</li> </ul>	Filtration efficiency decreases by < 25% (after 1 cycle of treatment)
	hydrogen peroxide	<ul style="list-style-type: none"> <li>Concentration: 30% hydrogen peroxide vapor (N95) [196, 202]</li> </ul>	<ul style="list-style-type: none"> <li>Oxidization of metal parts</li> </ul>	No significant decrease in filtration efficiency
		<ul style="list-style-type: none"> <li>Concentration: 6% Liquid hydrogen peroxide</li> <li>Submersion for 6 min (N95) [196]</li> </ul>	<ul style="list-style-type: none"> <li>Oxidization of metal parts</li> </ul>	No significant decrease in filtration efficiency
		<ul style="list-style-type: none"> <li>Concentration: 59% hydrogen peroxide vapor (FFP2) [203]</li> </ul>	<ul style="list-style-type: none"> <li>May toxic to users; aeration is required</li> </ul>	-
	Soap and water	<ul style="list-style-type: none"> <li>Submersion for 2 and 20 min (N95) [164]</li> </ul>	<ul style="list-style-type: none"> <li>Degradation of filter</li> </ul>	Filtration efficiency decreases by 38% and 35% for 2 and 20 min submersion, respectively (after 1 cycle of treatment)
		<ul style="list-style-type: none"> <li>Rubbing for 10 sec (CM) [204]</li> </ul>	<ul style="list-style-type: none"> <li>Manual rubbing may impact filters</li> </ul>	No significant decrease in particle emission
<b>Radiation</b>	Cobalt 60 gamma rays or electron accelerators	<ul style="list-style-type: none"> <li>0-50 kGy of gamma radiation (N95) [205]</li> </ul>	<ul style="list-style-type: none"> <li>Degradation of polymers</li> </ul>	Filtration efficiency decreases by 20% (after 1 cycle of treatment)
		<ul style="list-style-type: none"> <li>15 and 25 kGy of gamma radiation (SM) [206]</li> </ul>	<ul style="list-style-type: none"> <li>Degradation of filter</li> </ul>	Filtration efficiency decreases by 27% for both 15 and 25 kGy (after 1 cycle of treatment)
		<ul style="list-style-type: none"> <li>15 and 25 kGy of gamma radiation (CM) [206, 207]</li> </ul>	<ul style="list-style-type: none"> <li>Low filtration efficiency of intact CM (56 % and 21 % at 20 LPM with 1.0, <math>\geq</math> 0.3 <math>\mu</math>m polystyrene latex, respectively)</li> <li>Effectiveness varies with fabrics used</li> <li>Degradation of filter</li> </ul>	Filtration efficiency decreases by 10% for 25 kGy (after 1 cycle of treatment)
	Microwave	<ul style="list-style-type: none"> <li>Microwave (dry condition) with 1100 W for 2 min (N95) [208]</li> </ul>	<ul style="list-style-type: none"> <li>Melted filters around metallic nosebands by over 100 °C heat</li> </ul>	No significant decrease in filtration efficiency
		<ul style="list-style-type: none"> <li>Microwave-generated steam with 50-200 ml of tap water at 1100-1800 W (N95) [209, 210]</li> </ul>	<ul style="list-style-type: none"> <li>Reduced water repellent properties of SM</li> </ul>	No significant decrease in filtration efficiency of N95
		<ul style="list-style-type: none"> <li>Microwave-generated steam with 100 and 200 ml of water at 900 and 1800 W (SM) [191]</li> </ul>	<ul style="list-style-type: none"> <li>Loss of adhesion of metal nose clip</li> </ul>	No significant decrease in filtration efficiency of N95 respirators (after 3 cycle of treatment)
	UVGI	<ul style="list-style-type: none"> <li>Preservation in sterilization cabinet for 15-30 min with UVGI (254 nm) (N95) [200, 211]</li> </ul>	<ul style="list-style-type: none"> <li>May not penetrate deeply into filters</li> </ul>	Pressure drop decreases by 20% (after 1 cycle of treatment)
		<ul style="list-style-type: none"> <li>UV-C light (100-280 nm) for 5 min (SM) [188]</li> </ul>	<ul style="list-style-type: none"> <li>May not penetrate deeply into filters</li> </ul>	No significant decrease in filtration efficiency of N95 respirators (after 5 cycle of treatment)

### **1.3.5 Conventional antimicrobial substance and the limitations in the application to surgical masks**

Diverse antimicrobial substances have been developed to counteract the spread of pathogens, including metals and metal oxides, halogen-based disinfectants, antimicrobial peptides, natural polymers, and advanced materials. For nanoparticles, metals and their oxide counterparts are reported to exhibit antimicrobial properties (e.g., silver, copper, and zinc oxide) [212, 213]. These metal and metal oxides can disrupt microbial cell membranes through electrostatic activity, generate reactive oxygen species (ROS) that damage cellular components, and interfere with microbial metabolism and DNA replication [213]. As an example, silver nanoparticles (AgNPs) have been widely studied. It has been reported that nanoparticles sized 15-50 nm exhibit the highest inactivation efficiency compared to those sized 30-200 nm when tested against *P. aeruginosa* and *E. coli*. This is believed to be due to the high surface-to-volume ratio of the nanoparticles and the electrostatic attraction between the positively charged Ag ions and the negatively charged bacterial cells [214]. In the case of copper oxide (CuO) nanoparticles, they also exhibited significant inactivation efficiency when the size of the nanoparticles was small, with a zone of inhibition of 20-25 mm for 20 nm CuO nanoparticles and 10-15 mm for 27 nm CuO nanoparticles, when tested against *E. coli*, *P. aeruginosa*, *B. subtilis*, and *S. aureus*. Similarly, size-dependent inactivation efficiency was also observed in zinc oxide (ZnO) nanoparticles, with 9 nm particles having an 18 mm zone of inhibition and 33 nm particles having a 14 mm zone [215]. Despite the significant inactivation efficiency of nanoparticles, their application in masks is limited mainly due to toxicity. Due to their small size, nanoparticles can penetrate and deposit into the lungs once inhaled, which can induce inflammation, genotoxicity, and cytotoxicity [216].

Halogen-based disinfectants are widely used for their potent antimicrobial properties, capable of effectively killing or inactivating a wide range of microorganisms, including bacteria, viruses, fungi, and protozoans. Their inactivation mechanism is related to strong oxidation, leading to pathogen denaturation and membrane disruption [217]. The most commonly used halogens in disinfectants are chlorine and iodine, each available in various formulations and applications. Sodium hypochlorite, a widely used chlorine-based disinfectant, has been shown to achieve more than 90% bacterial growth prevention with a concentration of less than 1% in 10 min [218]. Calcium hypochlorite is used as an alternative to liquid bleach, favored for its longer shelf life and ease of handling. It is commonly used for water treatment in swimming pools and as a disinfectant for surfaces in food processing and healthcare settings. In tests, concentrations of 1 and 300 ppm of calcium hypochlorite inactivated 6.3 logs of vegetative cells and 7.7 logs of spore forms of *Bacillus anthracis*, respectively, within 10 min [219]. Povidone-iodine (PVP-I), an iodine-based disinfectant, has also demonstrated significant inactivation efficiency against diverse pathogens, including enteroviruses, showing a 4-5 log reduction in 30 seconds following treatment with 1% PVP-I [220]. However, the application of halogen materials on mask filters shows inconsistency in efficiency, depending on the storage conditions of the masks, which vary in time, temperature, and humidity [221].

Antimicrobial peptides (AMPs) are a diverse group of molecules found in a wide range of organisms, from bacteria to humans, playing a crucial role in the innate immune system by providing a rapid and effective defense against a broad spectrum of pathogens. AMPs vary significantly in size, structure, and mode of action but generally act by disrupting microbial membranes through electrostatic attraction. Positively charged AMPs interact with negatively charged pathogen membranes, resulting in membrane adsorption and conformational change [222]. AMPs can be sourced from mammals (e.g., human, sheep, and cattle), insects (e.g., guppy

silkworm, bees, and *Drosophila*), and microorganisms (e.g., *Lactococcus lactis*, *Bacillus subtilis*, and *Bacillus brevis*) [223]. Depending on the target pathogens, AMPs can be divided into antibacterial peptides, antifungal peptides, and antiviral peptides. Currently, more than 800 sequences of antibacterial peptides and proteins have been developed with various structures, such as linear peptides and  $\alpha$ -helices [224]. These peptides have demonstrated their efficiency against diverse pathogens, including *Staphylococcus aureus*, *Listeria monocytogenes*, *Escherichia coli*, *Vibrio parahaemolyticus*, and *Acinetobacter baumannii* [223]. Antifungal peptides are also gaining attention due to the development of antibiotic-resistant pathogens and the increasing number of diseases related to immunity deficiencies. The main inactivation mechanisms of antifungal peptides include the inhibition of 1,3- $\beta$ -glucan synthesis and/or chitin biosynthesis to destroy the cell wall, and the destabilization of glucosylceramide in the membrane to disrupt the Na<sup>+</sup>/K<sup>+</sup> pump [225]. Antiviral peptides have also exhibited significant inactivation efficiency, offering a novel therapeutic approach by targeting diverse viral molecules (e.g., protease, polymerase, and viral structural proteins) [226]. However, there are limitations to applying antimicrobial peptides on mask filters, due to the stability of functionalized peptides on masks under different environmental conditions and their pathogen-specific inactivation mechanisms.

Natural polymers are materials derived from plants, animals, or microorganisms, which include chitosan, lignin, and allicin. Chitosan can inactivate pathogens through electrostatic attraction, as it is positively charged. Specifically, the NH<sub>3</sub><sup>+</sup> sites in chitosan interact with the negatively charged phospholipids and lipopolysaccharides in the lipid membranes of pathogens [227]. Lignin, on the other hand, inactivates pathogens by using its phenolic hydroxyl groups to interact with amino and thiol groups from the membrane proteins of pathogens. Additionally, it can interact with lipid membranes of pathogens through hydrophobic interactions [228]. Allicin,

obtained from garlic, contains reactive sulfur species that are electrophilic and readily interact with nucleophilic sites, such as thiol groups in glutathione and proteins commonly found in pathogens [229]. However, there are limitations to applying these on mask surfaces due to the high concentrations of materials needed to rapidly inactivate pathogens and/or stability issues related to degradation at room temperature [230-232].

Advanced materials such as graphene oxide, carbon nanotubes, and dendrimers have been developed. Graphene oxide (GO) is reported to inactivate pathogens through various means, including physical and chemical interactions. The sharp edges of GO can physically damage pathogens, leading to the leakage of cellular contents. Additionally, GO can induce the production of reactive oxygen species (ROS) in pathogens, which may cause DNA damage and mitochondrial dysfunction [233]. Similarly, carbon nanotubes (CNTs) inactivate pathogens by disrupting cell membranes through physical attacks using their needle-like structures and by initiating oxidative stress in pathogens [234]. Dendrimers, highly branched synthetic macromolecules characterized by a tree-like structure, are applied in diverse fields such as drug delivery and gene therapy. In antimicrobial material development, dendrimers are formulated to have positive charges to interact with the lipid membranes of pathogens. Furthermore, they interfere with normal cellular processes by binding to cellular components such as proteins or DNA, inhibiting their function [235]. Despite their significant inactivation efficiency, the potential detachment of these antimicrobial materials and their cytotoxicity should be considered when designing antimicrobial masks using these materials [236-238].

To be effective on mask filters, the functionalized antimicrobial materials should achieve rapid pathogen inactivation, strain-nonspecific inactivation, and exhibit no toxicity upon inhalation. Given these criteria, the aforementioned antimicrobial materials are not suitable for use with masks.

### 1.3.6 Requirements for antimicrobial masks and respirators

Universal masking can substantially reduce the chance of viral infection and mortality in both healthcare facilities and the general public. Healthcare workers at high risk of infection are advised to wear only medical masks (surgical masks, procedure masks) or respirators that are subject to regulatory standards. Initially, respiratory devices have been recommended for single uses. However, despite underlying concerns about the safety, performance, and degradation issues, respiratory protection devices have been worn for extended time periods and reused due to the limited supply and high cost. To this end, the antimicrobial face mask technology received global attention to resolve the numerous technical challenges of current respiratory protection devices (Figure 1.4).

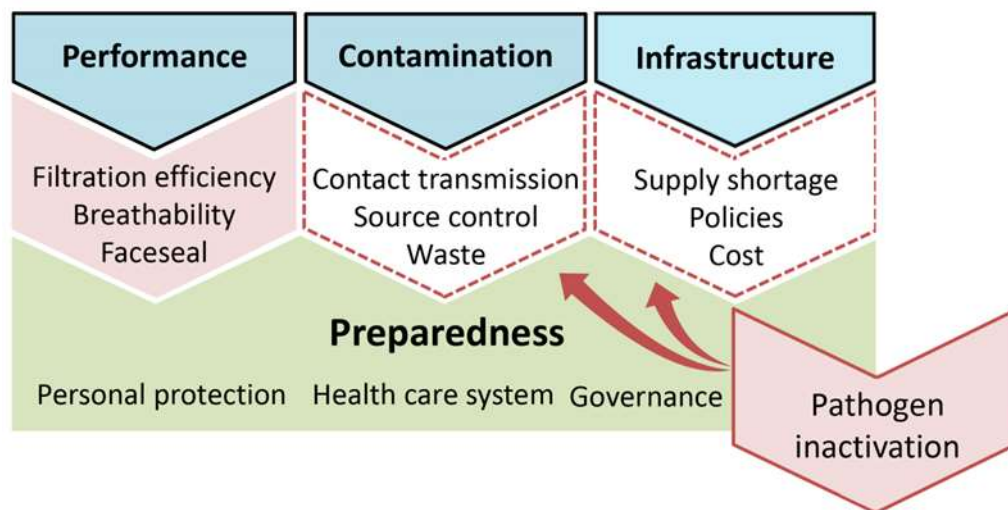


**Figure 1.4.** Implications of respiratory protection for pandemic/epidemic preparedness. The development of pathogen inactivating respiratory devices can contribute to narrowing the gap between contamination/infrastructure and pandemic readiness with regards to personal protection, health care system, and governance. Reproduced (Adapted) with permission from 20. Copyright 2020 University of Alberta.

The underlying principles behind antimicrobial technologies target bacteria and viruses by disrupting cell membranes, denaturing proteins, inhibiting synthesis of cellular components (i.e., cell wall/DNA/protein), and disturbing metabolic pathways [239, 240]. However, the application of the antimicrobial substances to respiratory devices must satisfy diverse stringent

requirements defined as (1) use of safe materials, (2) rapid pathogen inactivation, (3) type/strain non-specific inactivation, (4) manufacturability, (5) compatibility with existing device production process, (6) low material/production cost, and (7) easy scale-up (see Antimicrobial Substances in Biotechnology in the Supporting Information).

### **1.3.7 Application methods of antimicrobial coatings on mask fabrics**

Antimicrobial substances can be applied on masks/respirators with numerous methods (Figure 1.5). The encapsulation method embeds an antimicrobial substance into polymer fibers during the fiber fabrication process (i.e., electrospinning and solution/melt/force spinning). Among the available methods, electrospinning has been widely used because of its applicability to diverse materials such as polymers and ceramics [241]. Despite the advances made in the fiber fabrication methods, the encapsulation approach has several drawbacks. Since electrospinning is performed with polymers and antimicrobials dissolved in solvents, diverse factors should be taken into consideration (i.e., solution flow rate, solution viscosity, polymer concentration, and needle diameter) [242]. In particular, the encapsulation method may lead to a loss of the antimicrobial agents embedded within the fiber, as only those exposed to the surface can contribute to the inactivation of pathogens. The surface adsorption method employs the physical coating of antimicrobial substances by dip- or spray-coating processes followed by drying. This method can be used to easily form coatings on fibers and is compatible with manufacturing scale-up. On the other hand, the fabrication procedure has limitations due to difficulty in coating thickness modulation and the low penetration efficiency of spray coatings [243]. Importantly, antimicrobial substances do not have strong adhesion to their substrates, giving rise to safety issues regarding the inhalation of the materials and degradation of the antimicrobial performance of the filters [244]. Alternatively, antimicrobial substances/moieties can be covalently grafted to the substrate fiber (chemical functionalization). However, this method can only be applied to

specific types of substrate polymers that allow for grafting reactions [245]. The majority of polymers used in masks/respirators rely on chemically inert PP fabrics, which limits the general application of the approach.

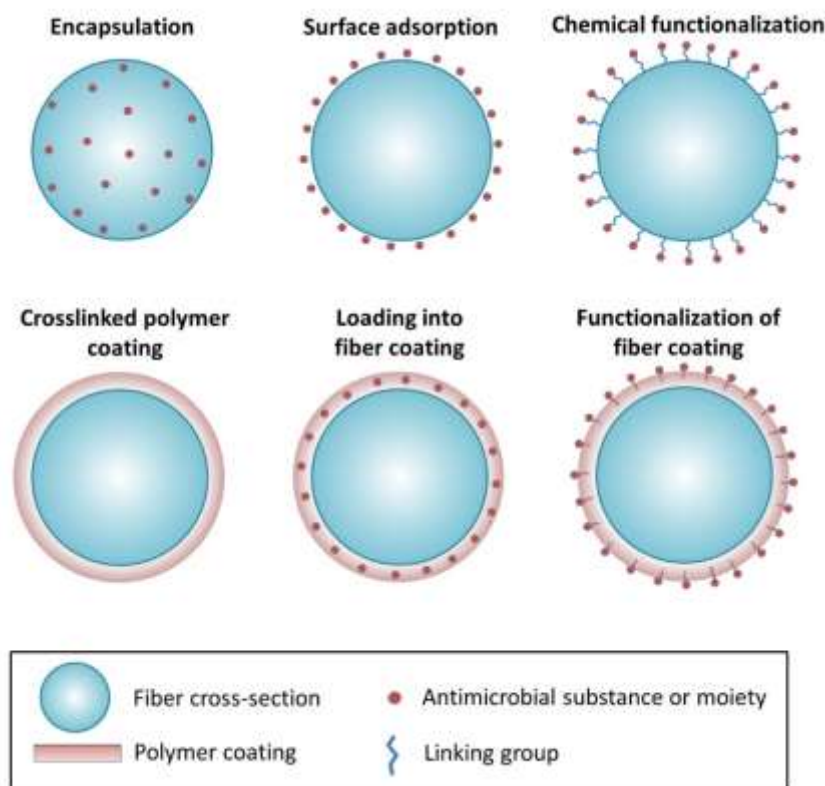


**Figure 1.5.** Antimicrobial functionalization strategies for mask fibers.

The application of the three methods explored above requires the direct interaction between antimicrobial substances and polymer fibers. Each approach has major limitations for its practical application in masks/respirators. To address these problems, the formation of a continuous coating on the surface of fibers has been investigated. The polymer coating can be cross-linked to form a core-shell structure [246]. Alternately, antimicrobial substances can be incorporated into the coating or functionalized to the polymer. The cross-linking of shell-forming polymers can bestow competent mechanical strength for the coating and flexibility in

the selection of polymers, which in turn provides a wide variety of conjugation strategies for antimicrobial substances/moieties and polymer coating. Using this method can save effort on achieving the chemical modification of PP fibers.

### **1.3.8 Standards for filtration efficiency and breathability tests**

Currently, masks can be broadly categorized into three categories: respirators (e.g., NIOSH N95, KN95, KF94, and, FFP2), surgical/medical masks, and non-medical masks (e.g., homemade and commercially available cloth masks) [247]. Respirators are primarily categorized based on their filtration efficiency (Table 1.2). For instance, the NIOSH 42CFR84 standard refers to the classification of particulate respirators certified by the National Institute for Occupational Safety and Health (NIOSH) [248]. This classification is based on the respirator's ability to filter out particles and its resistance to oil. The three series (N, R, and P) and the filtration efficiency levels (95, 99, and 100, corresponding to 95%, 99%, and  $\geq 99.97\%$  of filtration efficiency, respectively) provide information about these characteristics [248]. N-Series are not oil resistant, meaning they should not be used in environments where oil aerosols are present as the presence of oil can reduce the filtration efficiency [248]. R-Series are somewhat resistant to oil and thus are used in environments where oil aerosols are present, but only for a limited time. The time limit is determined based on several factors, including the manufacturer's recommendations, the concentration of oil in the air, the breathing rate of the user, and the specific conditions of the workplace. P-Series are oil-proof, enabling their use in environments with oil aerosols without any time limitation [248]. Similarly, GB 2626-2006, a Chinese regulation for respiratory protective equipment, categorizes respirators based on oil resistance (KN and KP) and filtration efficiency (90, 95, and 100, corresponding to 90%, 95%, and  $\geq 99.97\%$  of filtration efficiency, respectively) [249]. The KP series indicates the mask's filtration efficiency against both non-oily and oily particles, while the KN series is only for non-oily

particles [249]. On the other hand, EN149, a European Standard for respiratory protective devices, does not categorize respirators based on oil resistance. However, the standard categorizes respirators based on filtration efficiency into filtering face pieces (FFP) 1, FFP2, and FFP3 having filtration efficiencies of 80%, 94%, and 99%, respectively [250]. Similarly, MFDS 2020-6 standard divides respirators into Korean Filter (KF) 80, KF94, and KF99, which correspond to filtration efficiencies of 80%, 94%, and  $\geq 99\%$ , respectively [251].

**Table 1.2.** Standards for particulate filtration efficiency (PFE) of respirators and surgical/medical masks

Country	Agency	Standard	Particles	Size	Flow rate	Filtration efficiency	Sample type
USA	National Institute for Occupational Safety and Health (NIOSH) [248]	NIOSH 42CFR84	NaCl	0.3 $\mu\text{m}$ polydisperse	85 L/min	95/99/99.97%	Respirators
			Diocetyl phthalate	0.3 $\mu\text{m}$ polydisperse	85 L/min	95/99/99.97%	Respirators
	American Society for Testing and Materials (ASTM) [252]	ASTM F2100-19e1	Polystyrene latex (PSL) microspheres	0.1 $\mu\text{m}$ monodisperse	28.3 L/min	95/98/98%	Surgical masks
EU	European Committee for Standardization (CEN) [250]	EN 149	NaCl	0.6 $\mu\text{m}$ polydisperse	95 L/min	80/94/99%	Respirators
			Paraffin oil	0.6 $\mu\text{m}$ polydisperse	95 L/min	80/94/99%	Respirators
China	Standardization Administration of the People's Republic of China (SAC) [249]	GB 2626-2006	NaCl	0.3 $\mu\text{m}$ polydisperse	85 L/min	90/95/99.97%	Respirators
			Paraffin oil, dioctyl phthalate	0.3 $\mu\text{m}$ polydisperse	85 L/min	90/95/99.97%	Respirators
Korea	Ministry of Food and Drug Safety (MFDS) [251]	Notice of MFDS 2020-6	NaCl	0.6 $\mu\text{m}$ polydisperse	95 L/min	80/94/99%	Respirators
			Paraffin oil	0.4 $\mu\text{m}$ polydisperse	95 L/min	80/94/99%	Respirators

Compared to respirators, which are subject to various standards regarding Particle Filtration Efficiency (PFE), surgical/medical masks are governed by fewer standards. However, surgical masks are more frequently evaluated for Bacterial Filtration Efficiency (BFE); notably, N95 respirators do not have BFE standards (Table 1.3) [252-254]. This difference is presumed to be due to their distinct purposes: respirators are designed to filter a wide range of particle sizes,

from aerosols to splashes, whereas surgical/medical masks are intended to capture relatively larger particles such as droplets and splashes [255]. Similar to PFE, BFE is also used to categorize surgical/medical masks. For example, ASTM F2100, a test method developed by ASTM International, classifies surgical/medical masks into Level I, Level II, and Level III. Level I requires a minimum of 95% PFE and BFE, while both Level II and III require  $\geq 98\%$  [252]. Additionally, other factors such as fluid resistance, breathability, and flammability must also meet specified levels. Similarly, EN14683, a European Standard specifying requirements and test methods for medical face masks, is divided into Type I, Type II, and Type IIR. Type I is required to satisfy 95% BFE, whereas Type II and Type IIR must achieve at least 98% BFE [253]. The EN14683 standards do not mention PFE; however, they require a fluid resistance of  $>120$  mmHg for a mask to be categorized as Type IIR [253]. Unlike ASTM F2100 and EN14683, the Chinese Standard YY 0469-2011 for surgical/medical masks does not classify masks based on BFE [254].

**Table 1.3.** Standards for bacterial filtration efficiency (BFE) of respirators and surgical/medical masks

Country	Standard	Bacteria	Particle size	Particle concentration	Aerosol detector	Flow rate	Test	Filtration efficiency
USA	ASTM F2101 and ASTM F2100 [252, 256]	<i>Staphylococcus aureus</i>	$3.0 \pm 0.3$ $\mu\text{m}$ MPS	$2200 \pm 500$ viable particles per test	Six-stage viable particle cascade impactor	28.3 L/min	2 min aerosol exposure per test	95/98/98%
EU	EN14683 [253]	<i>Staphylococcus aureus</i>	$3.0 \pm 0.3$ $\mu\text{m}$ MPS	1700-3000 CFU per test	Six-stage viable particle cascade impactor	28.3 L/min	2 min aerosol exposure per test	95/98/98%
China	YY 0469-2011 [254]	<i>Staphylococcus aureus</i>	$3.0 \pm 0.3$ $\mu\text{m}$ MPS	$2200 \pm 500$ viable particles per test	Six-stage aerosol sampler	28.3 L/min	2 min aerosol exposure per test	$\geq 95\%$

Breathability is also a crucial factor in the design of respirators and surgical/medical masks, impacting their comfort and functionality. The design and testing protocols for these

protective devices vary according to their intended use. For instance, respirators are subjected to both inhalation and exhalation tests to ensure they provide adequate airflow. In contrast, surgical masks are tested primarily for inhalation resistance, reflecting their primary role in preventing the transmission of respiratory droplets. Besides, respirators are generally tested as a whole unit, whereas surgical masks are tested in smaller sections (4.9 cm<sup>2</sup>). This difference in testing reflects their distinct purposes [252, 253]. There are various breathability standards that are used to classify the protective devices based on differential pressure ( $\Delta$  Pa). For instance, EN 149 divides respirators into FFP1 (60 Pa at 30 L/min and 210 Pa at 95 L/min), FFP2 (70 Pa at 30 L/min and 240 Pa at 95 L/min), and FFP3 (100 Pa at 30 L/min and 300 Pa at 95 L/min) [250]. For surgical/medical masks, ASTM 2100 categories them into level I (< 50 Pa/cm<sup>2</sup>), level II (< 60 Pa/cm<sup>2</sup>), and level III (< 60 Pa/cm<sup>2</sup>) [252]. EN 14683 also divides surgical/medical masks into type I (< 40 Pa/cm<sup>2</sup>), type II (< 40 Pa/cm<sup>2</sup>), and type IIR (< 60 Pa/cm<sup>2</sup>) [253].

**Table 1.4.** Standards for breath resistance of respirators and surgical/medical masks

Country	Agency	Standard	N95, FFP2, KN95, KF94 (Inhalation/exhalation)		Surgical/medical masks (breath resistance/surface area)	
USA	National Institute for Occupational Safety and Health (NIOSH) [248]	NIOSH 42CFR84	311 Pa (85 L/min)	249 Pa (85 L/min)	-	-
	American Society for Testing and Materials (ASTM) [252]	ASTM F2100-19e1	-	-	245/294/294 Pa (8 L/min)	4.9 cm <sup>2</sup>
EU	European Committee for Standardization (CEN)	EN 149 [250]	210/240/300 Pa (90 L/min) and 60/70/100 Pa (30 L/min)	300 Pa (160 L/min)	-	-
		EN 14683 [253]	-	-	196/196/294 Pa (8 L/min)	4.9 cm <sup>2</sup>
China	Standardization Administration of the People's Republic of China (SAC) [249]	GB 2626-2006	350 Pa (85 L/min)	250 Pa (85 L/min)	-	-
	China Food and Drug Administration (CFDA) [254]	YY 0469-2011	-	-	240 Pa (8 L/min)	-
Korea	Ministry of Food and Drug Safety (MFDS) [251]	Notice of MFDS 2020-6	70 Pa (30 L/min)	-	-	-

## 2 Novel approach in airborne disease control

### 2.1 Goal and hypothesis

Developing an effective way to combat airborne respiratory disease is a key challenge in public health. As previously discussed, the development of vaccines and the inherent stability of pathogens present obstacles in controlling the spread of these diseases. Besides, there are several drawbacks in decontamination procedure (e.g., filter degradation, low pathogen inactivation efficiency, residual odor, toxicity, time-consuming/resource-constrained processes, etc.) and conventional antimicrobial substances (i.e., toxicity, stability, inactivation efficiency, environmental stability, pathogen specificity, scalability, etc.). To overcome these challenges, our team has introduced an innovative approach: the use of salt-coated filters as a potential alternative for pathogen inactivation. The design of these antimicrobial masks is guided by several key criteria: rapid neutralization of pathogens, effectiveness against various types of pathogens, adaptability to different fabric types, scalability for mass production, and affordability. We achieved this by applying a saline solution to polypropylene spunbond mask fabric. The primary aim of our project is to significantly improve pathogen control, contributing to enhanced global health measures.

**Hypothesis:** Salt-coated filters were hypothesized to (1) induce pathogen inactivation against universal pathogen, including environmentally stable pathogens, (2) inactivate pathogens through physical damage caused by salt recrystallization occurring upon contact with pathogen-embedded aerosols, and (3) reduce contact-based transmission to hands or other surfaces.

Overall, this work was divided into multiple research goals:

1. Investigation of the main mechanisms of pathogen inactivation on salt-coated filters, including salt recrystallization, osmotic pressure, and ionic effects.
2. Assessment of the pathogen inactivation effectiveness of salt-coated filters through experiments focusing on the two main transmission modes: droplets and aerosols.
3. Evaluation of the efficiency of pathogen inactivation by salt-coated filters when exposed to pathogens in different media, specifically artificial saliva and deionized (DI) water.
4. Testing the efficacy of salt-coated filters against resilient pathogens such as spore-forming bacteria and non-enveloped viruses.
5. Measurement of the filtration efficiency and breathability of salt-coated filters to ensure practical application.
6. Determination of the optimal arrangement of salt-coated fabrics to maximize overall performance of salt-coated polypropylene fabrics.
7. Analysis of contact-based pathogen transmission through both contaminated bare and salt-coated filters.

## 2.2 Formulation of salt coating

A wide range of physicochemical properties of natural salts, i.e. critical relative humidity (CRH), phase transformation kinetics, and crystal shape/structure, provide a powerful set of tools for application-specific antimicrobial coatings (Table 2.1). First, salts used in coating formation should be safe for respiratory application without causing harmful effects to the human body. Unlike conventional antimicrobial materials, there are choices for safe alternatives in natural salts for application to respiratory devices, ensuring no or low toxicity. Second, CRH represents a threshold relative humidity above which the salt begins to absorb water from the environment, and it essentially determines environmental stability of salt coatings [257]. Depending on the geographical location and indoor/outdoor environmental conditions, a salt with the maximum performance can be selected. A unique advantage of using salts is that the physical properties of the coating, such as environmental stability or crystal morphology, can be modified by using a mixture of multiple salt types. Third, the solubility of a salt in water is related to the amount of the resulting salt crystal coating on the mask fabrics. As the amount of salt coating affects its antimicrobial performance, salts with high water solubility would be used to improve mask performance by simply adjusting the concentration or volume of the coating formulation. Fourth, the complex nature of salt crystallization is dependent on a number of factors such as salt type, additives in the coating formulation, pathogen carrying media (i.e., saliva, water, saline solution, and culture medium), environmental conditions, etc. Given the significance of the crystallization topic in Materials Science and Engineering, the concept of fundamental materials is central to our pathogen inactivation strategy; the three major components (structure, properties, and processing) affect the antimicrobial performance of the salt-coated filters by altering the microstructural morphology and kinetics during the dynamic recrystallization process.

**Table 2.1.** Properties of salts (CRH at 20 °C from [258])

		MgCl <sub>2</sub>	K <sub>2</sub> CO <sub>3</sub>	NaCl	KBr	KCl	KNO <sub>3</sub>	K <sub>2</sub> SO <sub>4</sub>
<b>CRH (%)</b>		33	44	75	84	86	94	97
<b>Toxicity (GHS)</b>	<b>Inhalation (LC50 in mg/L)</b>	Irritant, corrosive	Irritant	Irritant	Irritant	Not classified	Irritant, oxidizer	Corrosive
		-	Rat (> 0.5)	Rat (> 42)	-	-	-	-
	<b>Dermal (LD50 in mg/kg)</b>	-	-	Rabbit (>10000)	-	-	-	-
	<b>Oral (LD50 in mg/kg)</b>	Mouse (4700)	Mouse (2570)	Mouse (4000)	Mouse (3120)	Mouse (1500)	Rabbit (1901)	Mouse (6600)
		Rat (2800)	Rat (1870)	Rat (3000)	Rat (3070)	Rat (2600)	Rat (3010)	Rat (6600)
-		Wild bird (100)	-	-	-	-	Guinea pig (6600)	
<b>Crystal system</b>		Hexagonal	Monoclinic	Cubic	Cubic	Cubic	Orthorhombic	Orthorhombic
<b>Solubility in water at room temperature (mg/ml)</b>		489	138	357	650	347	320	111

### 2.3 Salt coating process

Salt coating is accomplished primarily through three procedures. The first method is to dry pre-wet fabrics to form a salt coating on the surface of fibers (Figure 2.1A). The amount of the coated salt is limited by the volume and concentration of the salt coating solution absorbed into the fabrics. Secondly, pre-wet fabrics can be dried in a reservoir containing the coating solution or the coating solution can be directly sprayed onto the pre-wet fabrics during drying to increase the amount of the salt coating (Figure 2.1B). It was experimentally determined that the amount of the coated salt increases linearly with the volume of the coating solution provided during drying. It is noted that the drying of fabrics in the coating solution would not only increase the thickness of the fibers as a consequence of the salt film formation, but also exhibit crystal aggregation (Figure 2.1B). The formation of large salt crystals is dominantly observed when pre-wet meltblown and spunbond fabrics are incubated in more than 300  $\mu$ L and 600  $\mu$ L of concentrated saline solutions (NaCl: ~29.0 w/v%, KCl: ~26.3 w/v%), respectively: no overgrown crystals were observed from K<sub>2</sub>SO<sub>4</sub> under the same testing conditions due to its

lower solubility limit. From a perspective of filter performance, the formation of the crystal aggregates may increase the pressure drop. It may, however, be favorable for fabrics to have large salt crystals in a form similar to a salt-fiber composite: they may serve as a source of salt supply to the salt film on fibers where salt supply is needed as a result of salt dissolution and redistribution after exposure to humidity. Lastly, pre-wet fabrics can be vacuumed to produce fabrics coated with uniform salt crystals (Figure 2.1C). The application of vacuum minimizes the heterogeneous distribution of the coating solution on the fabrics during the drying process, thus inhibiting the formation of large salt crystals. Through experiments, a trend has been found to suggest that the breathability of melt-blown PP filters with smaller pores would be more easily affected by the amount of the salt coating and the presence of large salt crystals compared to spunbond PP fabrics with larger pores. Therefore, in the case of melt-blown PP filters, the sacrifice of breathability caused by large crystals can be offset by the improvement of the antimicrobial effects.

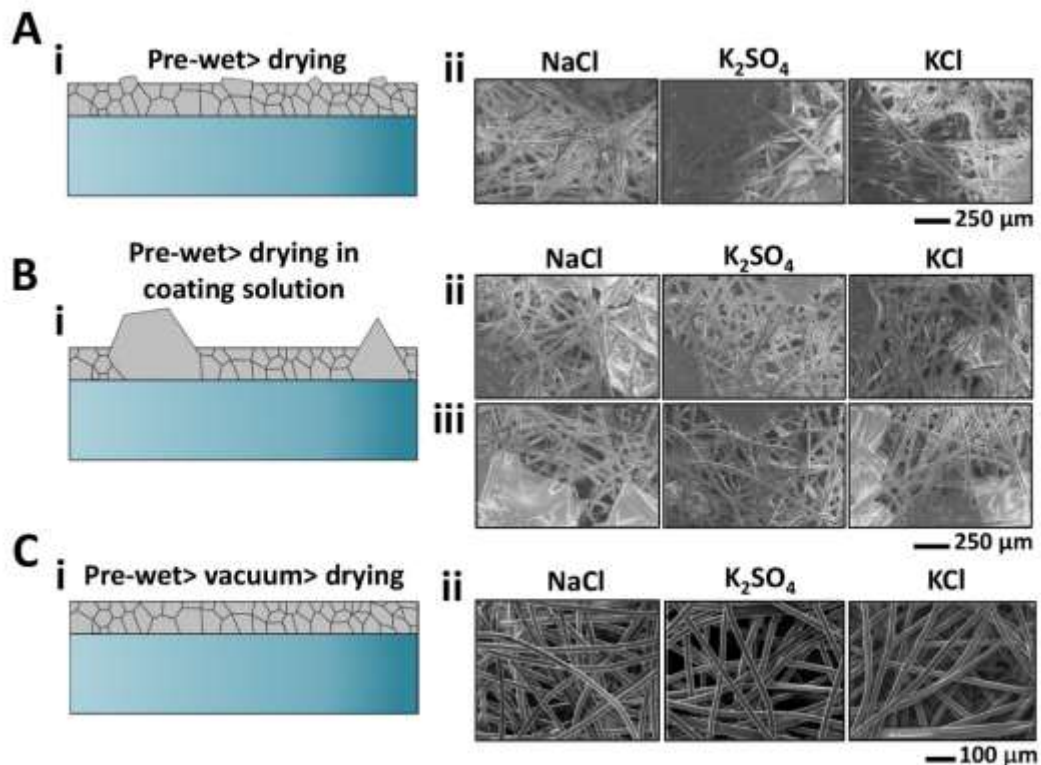


**Figure 2.1.** Production of salt-coated filters. Fabrication of salt-coated filters by drying pre-wet (via dip- or spray-coating) filters (A; i: schematic, ii: scanning electron microscope (SEM) images of spunbond PP fabrics[259]), drying pre-wet spunbond PP fabrics in a coating formulation (B; i: schematic, ii: pre-wet+600  $\mu$ L[259], iii: pre-wet+1200  $\mu$ L[259]), and application of vacuum to pre-wet PP fabrics followed by drying (C; i: schematic, ii: SEM images[259]). (A-ii, B-ii,iii, and C-ii) Reproduced (Adapted) with permission from reference [259]. Copyright 2021 ACS.

## 2.4 Methodology

### 2.4.1 RNA extraction, cDNA synthesis, and qPCR

To quantify the viral genome of RNA viruses (e.g., influenza viruses and coronaviruses), RNA extraction, cDNA synthesis, and qPCR are performed. We used the methods to evaluate the inactivation efficiency of salt-coated filters against RNA viruses by quantifying the intact RNA genome after and before exposure of salt-coated filters. RNA viruses do not contain DNA but RNA, which is synthesized into DNA in the host using the host's enzymes for replication [260].

The RNA extraction is performed by treating with a cell lysis buffer containing detergents such as SDS or Triton X-100 to solubilize membrane lipids and proteins. This is followed by a purification step involving protease treatment to digest proteins. Then, the impurities are removed by centrifugation and RNA precipitation is performed by adding ethanol as RNA is insoluble in ethanol. The RNA is then captured by a column containing silica through charge interaction, followed by elution with DI water [261, 262]

The complementary DNA (cDNA) synthesis is performed using the extracted RNA molecules. The RNA is mixed with reverse transcriptase (an enzyme that synthesizes cDNA from an RNA template), primers (short DNA sequences that initiate cDNA synthesis), and deoxynucleotide triphosphates (dNTPs) (A, T, G, and C nucleotides used to build cDNA). Then, the mixture is subjected to heat treatment, which is determined by the optimal activity temperature of the reverse transcriptase enzyme [262, 263].

The quantitative polymerase chain reaction (qPCR) is used to quantify DNA molecules.

To this end, the synthesized cDNA is mixed with primers designed to replicate a certain region of DNA and agents that emit a fluorescent signal, such as fluorescently labeled probes or SYBR Green. Fluorescently labeled probes are designed to hybridize specifically to a target sequence within the PCR product, whereas SYBR Green is a fluorescent dye that binds nonspecifically to double-stranded DNA (dsDNA), with its fluorescence increasing significantly upon binding to dsDNA [264, 265].

#### **2.4.2 CFU and PFU**

The colony-forming unit (CFU) and plaque-forming unit (PFU) are used for the quantification of bacteria and viruses, respectively. In our research, we also performed these assays to measure the number of live, infective pathogens before and after exposure to salt-coated filters. CFU involves several steps: serial 10-fold dilution of bacterial samples, plating the bacterial samples on nutritious agar plates, incubation, counting the number of colonies, and calculating the CFU/ml [266]. PFU proceeds with the dilution of viral samples, infection of host cells, overlay to facilitate the virus's spread to nearby host cells, incubation, counting the number of plaques, and calculating the PFU/ml [267].

#### **2.4.3 BCA assay**

The bicinchoninic acid (BCA) assay is used to determine the total concentration of protein in a solution. We performed this assay to measure the protein concentration of bacteria samples, which is used to normalize the CFU/ml calculated from the CFU assay. Protein measurement is carried out using a colorimetric readout that is proportional to the protein concentration in the sample. The color develops due to the reduction of  $\text{Cu}^{2+}$  to  $\text{Cu}^{1+}$  by proteins in an alkaline solution (provided by the BCA reagent), followed by the chelation of  $\text{Cu}^{1+}$  with bicinchoninic acid to form

a purple-colored product. The intensity of this purple color correlates with the protein concentration [268].

#### **2.4.4 TCID<sub>50</sub> assay**

The 50% tissue culture infectious dose (TCID<sub>50</sub>) assay is used to estimate the infectious titer of viruses, specifically the concentration at which 50% of the culture wells or units show cytopathic effect (CPE) from viral infection[269]. In our research, the TCID<sub>50</sub> assay was performed to assess the infectivity of viruses after and before exposure to salt-coated filters. The assay involves several steps: serial 10-fold dilution of viral samples, infection of host cells, incubation, and calculation of TCID<sub>50</sub>/ml. For calculating TCID<sub>50</sub>//ml, the Reed-Muench method and the Spearman-Karber methods are widely used. Both methods involve statistical calculations to estimate the dilution at which 50% of the wells would be expected to exhibit CPE [267, 269].

#### **2.4.5 HA assay**

The Hemagglutination (HA) assay is used to measure the concentration of viruses, especially influenza viruses, that have the ability to agglutinate red blood cells (RBCs). The HA titer represents the highest dilution of the virus that causes visible agglutination of RBCs [270]. Using the HA assay, we analyzed the inactivation efficiency of salt-coated filters against influenza viruses. This assay is based on the principle that certain viruses can bind to receptors on the surface of RBCs, causing them to clump together or agglutinate. The HA titer is an indirect measure of the amount of virus present in a sample. The procedure follows: dilution of viral samples, mixing viral samples with RBCs, incubation, and titer calculations [270].

# **3 Investigation on the Impact of Salt Coating on Mask Performance**

The impact of respiratory diseases is vast and multifaceted, affecting individuals, healthcare systems, and global economies. In response to the spread of respiratory pathogens, masks and respirators have become pivotal, demonstrating their capability to mitigate transmission. However, conventional masks have limitations (e.g., single-use, environmental contamination, and the potential for contact-based transmission). These challenges have accelerated the development of antimicrobial masks. Designing effective antimicrobial masks requires a deep understanding of the properties of each layer and the identification of an optimal configuration to enhance their protective efficiency. In this study, we thoroughly examined both the main and limited filtration mechanisms of diverse mask fabrics and identified an optimal configuration for salt-coated fabric masks. Moreover, we explored the impact of wetness on the performance of both bare and salt-coated fabrics; while bare fabrics showed a decrease in filtration efficiency with increased wetness, salt-coated fabrics exhibited enhanced filtration efficiency. This study not only highlights the significance of salt-coated fabric masks but also points towards potential improvements in respiratory disease prevention strategies.

### 3.1 Background

Pandemics/epidemics pose significant threats to public health, prompting the development of various respiratory protection devices and strategies. The influenza pandemic of 1918, commonly known as the Spanish Flu, marked one of the first instances where cloth masks were utilized on a mass scale for public health protection [271]. Since that time, the innovation and adoption of disposable masks and respirators have become integral in combating subsequent pandemics and epidemics. The efficacy of wearing masks in reducing pathogen transmission is noteworthy, with studies demonstrating a 70–79% reduction in infection rates [272-274], leading to an escalated demand for masks. The SARS-CoV-2 pandemic brought about the challenges associated with a sudden increase in mask usage, shortages in mask supplies, and the consequent environmental contamination from discarded masks [170]. One of the fundamental causes of numerous issues is linked to the disposable nature of masks. It is recommended that surgical masks be replaced immediately if they become wet and at least every 4 hours to ensure filter efficiency and mitigate the risk of pathogen spread due to surface contamination [275]. The environmental impact of mask waste is concerning, as discarded masks can degrade into microplastic fibers smaller than 5 mm, entering waterways and potentially disturbing ecosystems [170]. This cycle of demand, usage, and environmental impact underscores the need for reusable antimicrobial masks to protect public health while minimizing ecological damage.

The antimicrobial masks should be designed to fulfill multiple criteria, including non-toxicity, rapid antimicrobial activity, a pathogen non-specific antimicrobial effect, ease of scale-up, and compatibility with existing manufacturing processes [276]. Moreover, the masks should conform to guidelines such as filtration efficiency (surgical masks:  $\geq 95\%$  at 28.3 L/min and respirators:  $\geq 80-95\%$  at 85 L/min) and breathability (surgical masks:  $\leq 294$  Pa at 8 L/min and respirators:  $\leq 240-350$  Pa at 85–90 L/min for inhalation and  $\leq 250-300$  Pa at 85–160 L/min for

exhalation) (see Supporting Information Table S1,2 for international standards) [252, 277-281]. To satisfy all the requirements, selecting appropriate antimicrobial material functionalization strategy is crucial (e.g., encapsulation in fiber, fiber surface adsorption, chemical functionalization on fiber, crosslinked antimicrobial coating, loading into fiber coating, and functionalization on fiber coating) [282]. Surgical masks and respirators typically consist of 3 or 4 layers, including the outermost, middle, and inner layers. The outermost layer acts as a physical barrier to prevent contamination of the middle layer, which serves as the main filter capturing most particles. The inner layer that directly contacts with face supports the middle layer [283]. The selection of the mask's target layer for antibacterial treatment must take into account the type and size of the primary medium carrying the pathogen, along with the functionalization strategy, while meeting the various performance-related requirements outlined above.

Particle-dependent filtration efficiency can be used for testing the performance of the designed masks. The main filtration mechanism depends on particle size; for instance, sedimentation and inertial impaction are mainly observed for large particles (1–10  $\mu\text{m}$ ), while interception and diffusion are significant for particles ranging from 0.1–1  $\mu\text{m}$ , and electrostatic attraction is crucial for particles smaller than 300 nm [284]. Understanding size-dependent filtration efficiency enables the identification of primary mechanisms for capturing infectious aerosols/droplets carrying viruses and bacteria, as well as the quantitative assessment of each layer's role in pathogen capture. The predominant size of aerosols or droplets generated varies depending on the nature of human activities; talking (35–150  $\mu\text{m}$ ), coughing (45–200  $\mu\text{m}$ ), resting (< 0.57–0.71  $\mu\text{m}$ ), and manual rubbing of mask fabric (0.3–2  $\mu\text{m}$ )[285-288]. Consequently, specific filtration mechanisms are needed for different activities to effectively capture particles. For instance, in healthcare settings or during active conversation, numerous

large particles may be generated, necessitating the use of masks with high filtration efficiency against large-sized particles. Consequently, this yields crucial insights into which layers of masks/respirators should be targeted for antimicrobial functionalization.

Examining the impact of environmental conditions and surface treatments on mask performance is another crucial aspect that must be considered when characterizing filter effectiveness. In real-world scenarios, masks frequently encounter humid conditions, especially when worn for extended periods or in colder climates. This humidity, primarily originating from the breath of wearers, can substantially affect the filtration efficiency of masks. Exhaled breath humidity typically ranges from 41.9–91% at temperature of 31.4–35.4 °C [289]. Furthermore, studies suggest that humidity levels may further increase as temperatures decrease. For instance, at room temperature (22 °C), humidity levels are observed to be 55–60% RH for N95 masks and less than 38% RH for surgical masks, when the tests performed at 27% RH condition [290]. Moreover, many mask/respirator meltblown (MB) filters depend on electrostatically charged fibers for enhanced particle capture. However, previous reports have demonstrated that exposure to humidity can significantly reduce this electrostatic charge, thereby impairing the filtration efficiency of masks. For instance, polypropylene (PP) filters have been shown to lose 56.9% to 61.2% of their electric potential after being subjected to 90% RH for 48 hrs [291]. Considering that electrostatic charge accounts for about 69% of the filtration efficiency of masks, the degradation of this charge due to humidity is of considerable importance [292]. Therefore, integrating the considerations of wetness and humidity into the evaluation of filtration efficiency is important for accurate assessment of mask performance. Furthermore, ignoring these factors could result in an overestimation of the effectiveness of masks, especially under diverse environmental conditions.

To effectively prevent infection and contact transmission through biocontaminated mask surface, various antimicrobial masks have been developed and have proven their antimicrobial efficiency. Recently, we have developed salt-coated fabrics that inactivate pathogens through salt recrystallization, which occurs when pathogen-laden aerosols/droplets come into contact with the salt-coated fabrics. In a previous paper, we demonstrated the efficiency of salt-coated fabrics against diverse pathogens, including bacteria (e.g., *E. coli*, *K. pneumonia*, *S. pyogenes*, *P. aeruginosa*, and MRSA) and viruses (e.g., influenza viruses and coronaviruses), and their antimicrobial activities were demonstrated [259, 293, 294]. However, their filter performance was not fully characterized. Hence, the primary objective of this paper is to examine the mask performance of salt-coated fabrics with different salt quantity (5, 9, and 13 mg/cm<sup>2</sup>) and type (NaCl, KCl, and K<sub>2</sub>SO<sub>4</sub>) using different sized aerosols. The results will be compared with those of bare filters to identify the effects of salt coating on mask performance and the functionalization strategy. Therefore, this study can contribute to reveal 1) particle-size dependent filtration mechanism, 2) effects of salt coating on mask performance and main particle capturing mechanism, and 3) the effects of wetness on filtration efficiency and breathability.

## **3.2 Methods**

### **3.2.1 Preparation of salt-coated fabrics**

The preparation of salt-coated spunbond (SB) polypropylene (PP) fabric samples was executed following method detailed in previous studies [294]. The process began with the collection of inner SB layers from surgical masks (Fisherbrand Facemasks; Fisher Scientific, Pittsburgh, PA). For the salt coating, saline solutions were prepared with deionized (DI) water, filtered through a 0.22 μm pore-size filter (Corning, Tewksbury, MA), to achieve saturated

concentrations specific to each salt: 29.03 w/v % for NaCl, 26.31 w/v % for KCl, and 9.72 w/v % for K<sub>2</sub>SO<sub>4</sub>. Following this, the inner SB fabric layers were immersed in these saline solutions. The fabrics were gently scrubbed to ensure the elimination of any trapped air bubbles, facilitating an even coating. The volume of saline solution absorbed by the fabrics was adjusted by applying vacuum pressure. Fabrics coated with 5 mg/cm<sup>2</sup> of K<sub>2</sub>SO<sub>4</sub>, 9 mg/cm<sup>2</sup> of KCl, and 13 mg/cm<sup>2</sup> of NaCl were produced by applying a vacuum (5 inHg). Similarly, a vacuum of 8 inHg was applied to achieve 9 mg/cm<sup>2</sup> of NaCl coating, and 15 inHg was used to obtain 5 mg/cm<sup>2</sup> of KCl and NaCl. The fabrics were then dried overnight in an incubator (Thermolyne 42000; Dubuque, IA), and the coated fabrics were screened by measuring their weights before and after the coating process. For comparison purpose, PP SB fabrics coated only with Tween 20 (T20) were also prepared by soaking the inner fabrics in DI water containing 1 v/v % T20. The SB fabric was gently scrubbed to release any trapped bubbles and vacuumed at 5 inHg, followed by overnight drying.

The obtained fabrics were labeled as Fabric<sub>Coating×#Amount</sub>. In the notation, Fabric specifies the type of PP fabric (Inner SB layer (I), middle meltblown (MB) layer (M), or outer SB layer (O)); "Coating" indicates the type of coating material (T20, NaCl, KCl, or K<sub>2</sub>SO<sub>4</sub>); "#" represents the number of stacked SB PP fabrics (1, 2, 3, 4, or 5); and "Amount" denotes the quantity of salt coating (5, 9, or 13 mg/cm<sup>2</sup>). Bare fabrics are labeled as "Fabric×#", where "#" is the number of stacked fabrics. The symbol "/" is used to show the arrangement of filter layers, with "A/B" meaning layer A is placed above layer B.

### 3.2.2 Wetness test

To analyze the effect of wetness on filter performance, I×3 and I<sub>salt</sub>×3 was sprayed with DI water using a sprayer (Uline, Milton, ON). The amount of sprayed water on the fabric was regulated by weighing the masks before and after spraying with an Explorer Pro balance (Ohaus;

Parsippany, NJ). This was followed by calculating the water content per surface area (1, 6, and 12 mg/cm<sup>2</sup>). The wet filters were then immediately tested for filtration efficiency according to the NIOSH 42CFR84 standard and for breathability following the ASTM F2100-19e1 standards, using the PMFT 1000 (PALAS; Karlsruhe, Germany).

To visually observe the wetness-dependent morphological changes in fabrics, a solution of 1 mM sulforhodamine B (SRB; Sigma-Aldrich) in DI water was sprayed onto salt-coated fabrics. The amount of SRB applied was varied, similar to the above tests, by modulating the volume of the solution sprayed, which was determined by weighing the fabrics before and after spraying. Following this application, the fabrics were characterized through imaging with an optical microscope (Omax G223A-CA; Kent, WA).

### **3.2.3 Filtration efficiency and breathability tests**

Filtration efficiency and breathability tests of N95 respirators (3M; Saint Paul, MN) and surgical masks (Fisherbrand Facemasks; Fisher Scientific, Pittsburgh, PA) were performed using the PMFT 1000 (PALAS; Karlsruhe, Germany). The NIOSH 42CFR84 standard, certified by the National Institute for Occupational Safety and Health (NIOSH), was employed for measuring the filtration efficiency of all mask conditions and the breathability of N95 respirators. The NIOSH 42CFR84 filtration efficiency standard necessitates the use of 0.3  $\mu\text{m}$  polydisperse aerosols of 5% NaCl and dioctyl phthalate (DOP) at an airflow rate of 85 L/min[277]. Masks tested must achieve a minimum efficiency of 95%, 99%, and 99.97% for N95, N99, and N100 respirators, respectively. The NIOSH 42CFR84 breathability standard specifies a maximum resistance of  $\leq 311$  Pa at 85 L/min for inhalation airflow and  $\leq 249$  Pa at 85 L/min for exhalation airflow[277]. Filtration efficiency was calculated by comparing the particle size distribution before and after penetration through the filter, recorded by the Promo LED 2300 (PALAS;

Karlsruhe, Germany).

The ASTM F2100-19e1 standards, developed by ASTM International, were utilized for measuring the breathability of surgical masks[252]. This test method classifies surgical/medical masks into Level I, Level II, and Level III, where the maximum differential pressure allowed for Level I masks must be  $< 50 \text{ Pa/cm}^2$ , and that for both Level II and III masks  $\leq 60 \text{ Pa/cm}^2$ . The standard specifies the use of an 8 L/min airflow through 4.9 cm<sup>2</sup> filters, which corresponds to testing a full mask at 163 L/min[252]. The measured differential pressure (Pa) was normalized to the standard surface area to calculate the pressure (Pa/cm<sup>2</sup>).

### **3.2.4 Statistical analysis.**

Statistical tests, including the *t*-test, one-way ANOVA, and General Linear Model, were conducted using SPSS version 29 (IBM, Armonk, NY, USA). A P value below 0.05 was deemed significant for significance assessments.

## **3.3 Results and discussion**

### **3.3.1 Filter performance of bare fabrics**

Filtration efficiency and breathability are two essential factors used in categorizing the performance levels of surgical masks and respirators (see Table 1.2–1.4 for detailed guidelines). Filtration efficiency was tested using two different types of aerosols: 5% NaCl (hydrophilic, dissociate into charged ions) and dioctyl phthalate (DOP; hydrophobic, uncharged), in accordance with NIOSH 42CFR84 standards. Primary goal was to evaluate the performance of individual layers within a 3-ply mask, as well as the performance of masks across various architectural configurations. To this end, the following conditions were tested: single layers (outer: O, middle: M, and inner: I); stacked inner layers (2, 3, 4, and 5 stacked inner layers; a

stack of  $n$  inner layers is abbreviated as  $I \times n$ ); 3-ply masks ( $O \times 1/M \times 1/I \times 1$ ), including both intact ones and those that were separated and then reassembled (referred to as recombined 3-ply masks, i.e. 3-ply mask<sub>c</sub>); and architectures employing a single or stacked inner layer(s) as a mask cover ( $I \times 1/3$ -ply mask and  $I \times 3/3$ -ply mask) and an outer layer of a mask (denoted as  $I \times 1/M \times 1/I \times 1$  and  $I \times 3/M \times 1/I \times 1$ ).

It is noted that the middle layer exhibits the highest filtration efficiency when tested with both 5% NaCl and DOP aerosols, exhibiting an average filtration efficiency of  $88 \pm 4\%$  for 5% NaCl aerosols and  $83 \pm 4\%$  for DOP aerosols (Figure 3.1a(i,ii)). Thus, no significant difference in filtration efficiency was observed from the 3-ply mask with a cover and inner layer(s) as an outer layer of a 3-ply mask, compared to a middle layer only or 3-ply mask due to its dominant role in particle capturing efficiency ( $t$ -test,  $P = 0.0095$  for Figure 3.1a(i) and  $P = 0.1344$  for Figure 3.1a(ii)). We also note that the filtration efficiency increases with the number of stacked inner layers in both NaCl and DOP aerosols. In the case of NaCl aerosols (Figure 3.1a(i)), the increasing trend is more pronounced:  $I \times 1$  ( $9 \pm 4\%$ ),  $I \times 2$  ( $15 \pm 3\%$ ),  $I \times 3$  ( $21 \pm 4\%$ ),  $I \times 4$  ( $30 \pm 9\%$ ), and  $I \times 5$  ( $40 \pm 5\%$ ) ( $t$ -test,  $P < 0.0001$ ). However, the increase in the DOP tests (Figure 3.1a(ii)) was much less significant:  $I \times 1$  ( $4 \pm 3\%$ ),  $I \times 2$  ( $6 \pm 4\%$ ),  $I \times 3$  ( $7 \pm 5\%$ ),  $I \times 4$  ( $8 \pm 4\%$ ), and  $I \times 5$  ( $12 \pm 3\%$ ) ( $t$ -test,  $P = 0.2015$ ).

To further investigate the differences in filtration efficiency between NaCl and DOP aerosols, particle size-dependent filtration efficiency was monitored for both NaCl and DOP aerosol conditions. Interestingly, filtration efficiency against NaCl aerosols exhibited a biphasic behavior: a rapid decrease of filtration efficiency up to  $0.3\text{--}0.75 \mu\text{m}$  (first phase), followed by a gradual increase of the filtration efficiency with particle size (second phase) (Figure 3.1b(i,ii)). It is also clear that the increase in the number of stacked inner layers resulted in higher filtration efficiency as observed in Figure 3.1a(i). Considering the size of most viruses ( $< 0.4 \mu\text{m}$ ) and

bacteria ( $< 5 \mu\text{m}$ ), this data implies that stacking of inner spunbond PP fabrics can be effectively used to improve the protection of the mask against respiratory diseases[295]. Unlike NaCl aerosols, size-dependent biphasic behavior was not noticeable in filtration efficiency against DOP aerosols (compare Figure 3.1b with 3.1c). On the other hand, it is noted that filtration efficiency increased with particle size  $> 1 \mu\text{m}$  (Figure 3.1c). As a result, the filtration efficiency of three stacked inner layers ( $I \times 3$ ) was measured to be  $23 \pm 15\%$  and  $85 \pm 31\%$  at 2 and 3  $\mu\text{m}$  DOP aerosols, respectively.

The primary filtration mechanisms are strongly associated with the particle size: 1–10  $\mu\text{m}$  (sedimentation and inertial impaction), 0.1–1  $\mu\text{m}$  (interception and diffusion), and  $< 300 \text{ nm}$  (electrostatic attraction) [284]. The initial high filtration efficiency in the first phase in Figure 3.1b can be explained by electrostatic attraction between NaCl aerosols and the spunbond fibers. The decrease in filtration efficiency in the first phase as particle size increases is likely due to the increase in aerodynamic drag, which diminishes the effectiveness of electrostatic attraction [296]. However, at the second phase, physical mechanisms (interception, diffusion, sedimentation, and inertial impaction) play a dominating role in filtration efficiency, leading to a significant increase in filtration efficiency. This observation elucidates the particle capturing behavior demonstrated by the stacked inner layers. Specifically, these layers exhibit an increase in filtration efficiency in the first phase, attributed to electrostatic interaction, and a subsequent enhancement in efficiency during the second phase, driven by the influence of physical mechanisms. Thus, it is reasonable to assume that the non-charged hydrophobic nature of DOP does not exhibit electrostatic attraction with fibers, leading to the disappearance of biphasic filtration efficiency behavior (Figure 3.1c). The higher filtration efficiency observed in tests with increasing DOP aerosol sizes, compared to NaCl aerosols, is likely related to the hydrophobic properties of masks that repel water particles and attract oil particles[297]. Similar patterns were

also observed in the particle size-dependent filtration efficiency of the meltblown PP middle layer (Figure 3.2a) (GLM analysis,  $P < 0.0001$ ). The filtration efficiency against 5% NaCl aerosols was maintained at  $> 86\%$ , while efficiency decreased to 59% with DOP aerosols, presumably due to the lack of charge in DOP. As observed in inner layers, the single spunbond outer layer showed higher filtration efficiency when tested with DOP than with NaCl aerosols, indicating hydrophobic interaction between hydrophobic fabrics and DOP (Figure 3.2b) (GLM analysis,  $P < 0.0001$ ).

Breathability of various architectures was tested by measuring pressure drop under the same test conditions (Figure 3.3). The overall trend aligns with filtration efficiency, with the middle layer exhibiting the highest pressure drop ( $38 \text{ Pa/cm}^2$ ), compared to other single layers (O:  $2 \text{ Pa/cm}^2$  and I:  $1 \text{ Pa/cm}^2$ ). Besides, the pressure drop increases with the addition of more inner layers: I $\times$ 2 ( $3.9 \text{ Pa/cm}^2$ ), I $\times$ 3 ( $6.0 \text{ Pa/cm}^2$ ), I $\times$ 4 ( $7.9 \text{ Pa/cm}^2$ ), and I $\times$ 5 ( $10.5 \text{ Pa/cm}^2$ ). Importantly, the use of stacked inner layers as a cover on top of a 3-ply mask or outer layer of a 3-ply mask does not exceed the pressure drop  $50 \text{ Pa/cm}^2$ . This indicates that stacked inner layers can be flexibly used in the fabrication of respiratory devices by meeting differential pressure guidelines (see Table 1.4).

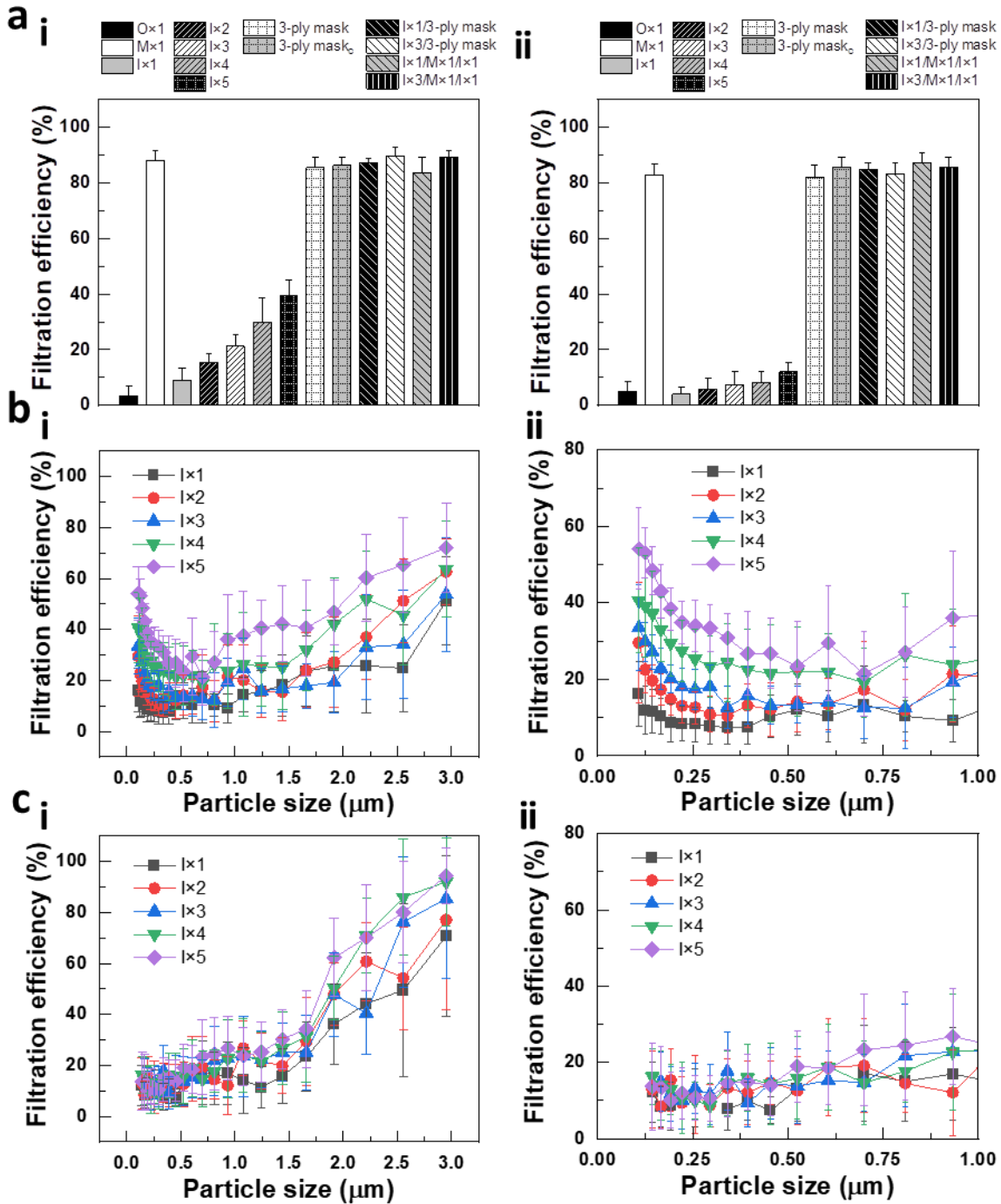


**Figure 3.1.** Filter performance of bare fabrics. Filtration efficiency was performed according to NIOSH 42CFR84 standard. (a) Overall filtration efficiency of bare fabrics tested with 5% NaCl aerosol (i) and DOP aerosol (ii). (b,c) Particle size–dependent filtration efficiency tested with 5% NaCl aerosols (b) and DOP aerosols (c) (i: filtration efficiency of bare fabrics and ii: zoomed–in filtration efficiency of the bare fabrics). (n = 7–21 for b and 9–24 for c, mean  $\pm$  SD).

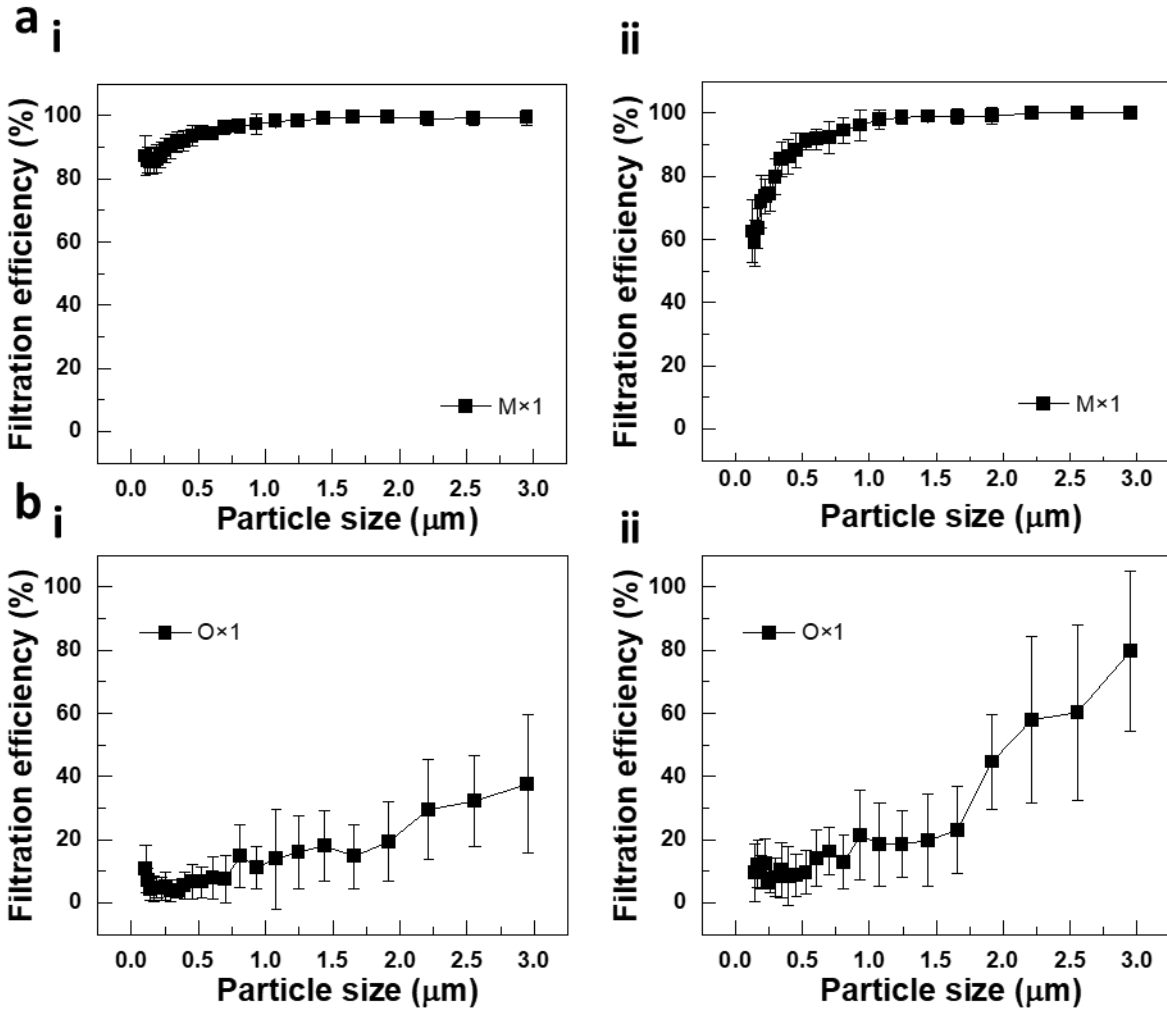


**Figure 3.2.** Particle size–dependent filtration efficiency of single bare fabrics. (a–b) 5% NaCl aerosol (i) and DOP aerosol (ii) used to measure the filtration efficiency of fabrics: (a) M×1 and (b) O×1. (n = 7–15 for a and n = 9–19 for b, mean ± SD)).

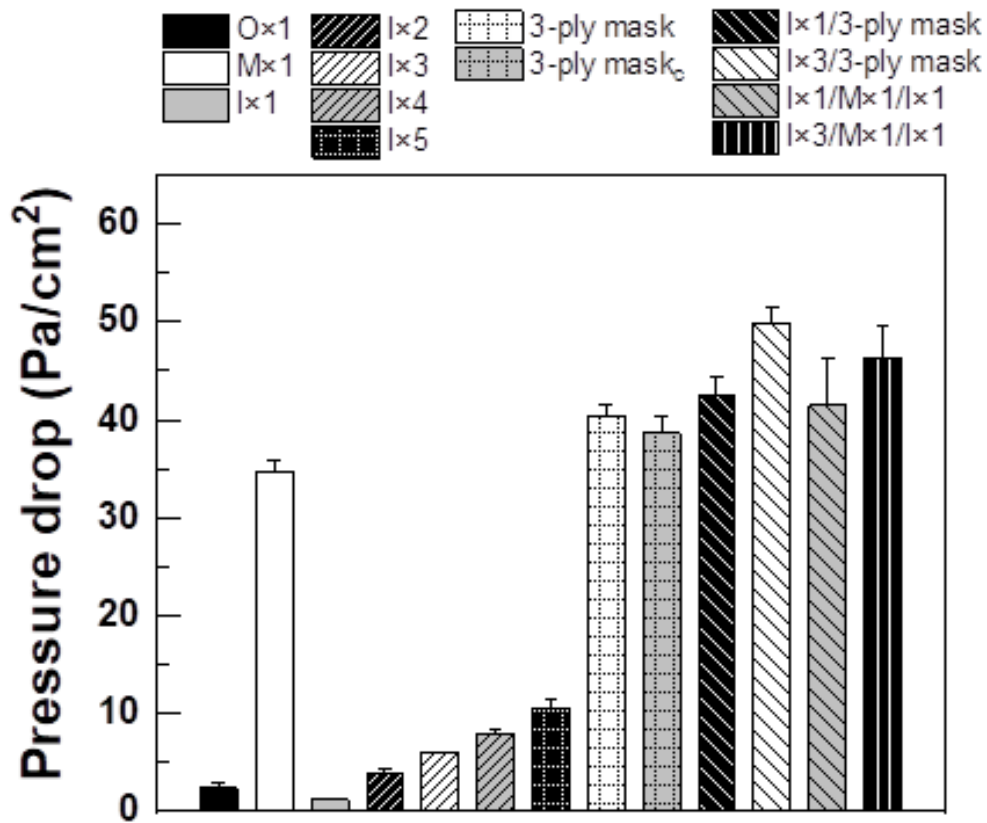


**Figure 3.3.** Breathability of bare fabrics with different staking sequences. Breathability was performed according to ASTM F2100–19e1 standard. (n = 9–12, mean ± SD).

### 3.3.2 Performance of salt-coated stacked spunbond (SB) fabrics

To evaluate the filter performance of salt-coated SB PP fabrics, filtration efficiency and breathability were characterized at the same testing conditions as in section 3.3.1. For this purpose, three different types of salts (NaCl, KCl, K<sub>2</sub>SO<sub>4</sub>) with different amounts of salts (NaCl: 5, 9, and 13 mg/cm<sup>2</sup>; KCl: 5 and 9 mg/cm<sup>2</sup>; K<sub>2</sub>SO<sub>4</sub>: 5 mg/cm<sup>2</sup>) were coated onto the three stacked SB inner membranes. To evaluate the effect of surfactant added into the salt coating formulation, SB inner layers treated with Tween 20 (T20) were also tested. This resulted in the similar fiber diameter and pore size of I<sub>NaCl</sub>×3<sub>9</sub> fabrics (20.9 μm and 5-67 μm) compared to bare fabrics (20.4 μm and 7-58 μm). As shown in Figure 3.4a(i), salt-coated SB fabrics exhibited 3–5% of overall filtration efficiency against NaCl aerosols, lower than that of three stacked SB inner layers (I×3: 21 ± 4%) (*t*-test, *P* = 0.1021). However, the difference in the DOP test was not as pronounced as in NaCl (Figure 3.4a(ii)) (*t*-test, *P* = 0.3858). The underlying reason for these differences was explored by examining the particle size-dependent filtration efficiency. As shown in Figure 3.4b(i), I<sub>NaCl</sub>×3 showed lower filtration efficiency against small particles (≤ 0.3 μm) compared to I×3 (GLM, *P* < 0.0001). Given that the primary mechanism of filtration efficiency at ≤ 0.3 μm is electrostatic attraction and that both bare and salt-coated SB fabrics have similar pore sizes, the decrease in filtration efficiency against NaCl aerosols can be attributed to the lack of charge in the salt-coated stacked SB fabrics (see Figure 3.4b(i) for NaCl and Figure 3.5 for KCl and K<sub>2</sub>SO<sub>4</sub>). However, when testing with non-charged DOP aerosols, both I×3 and I<sub>NaCl</sub>×3 displayed similar particle-size dependent filtration efficiency trends, with no significant capturing efficiency for particles ≤ 0.3 μm, regardless of type of salts (see Figure 3.4b(ii) for NaCl and Figure 3.6 for KCl and K<sub>2</sub>SO<sub>4</sub>). Notably, the low filtration efficiency against ≤ 0.3 μm sized NaCl particles, was also evident in Tween 20 (T20)-treated filters (I<sub>T20</sub>×3), demonstrating that the surfactant itself also degrades the electrets on the SB inner

layers, thereby eliminating electrostatic attraction between the fibers and aerosols (Figure 3.5). Considering that salt coating formulation contains surfactant, previously observed filtration efficiency of the salt-coated inner layers might be attributed to the presence of T20 added into the formulation to enhance salt coating. As indicated in Figure 3.7, the pressure drop showed no significant difference between  $I \times 3$  and  $I_{\text{salt}} \times 3$ , with values ranging from 5–8 Pa/cm<sup>2</sup> across all conditions. This is in consideration of the maximum differential pressure (50/60/60 Pa/cm<sup>2</sup>) mentioned in ASTM F2100-19e1 standard. The trend was not affected by the type of salt (NaCl, KCl, and K<sub>2</sub>SO<sub>4</sub>) and the quantity of salt used (5 mg/cm<sup>2</sup>, 9 mg/cm<sup>2</sup>, and 13 mg/cm<sup>2</sup>). This means that a stack of salt-coated SB fabrics does not cause noticeable breathability decrease that can be a common concern arising from filter functionalization.

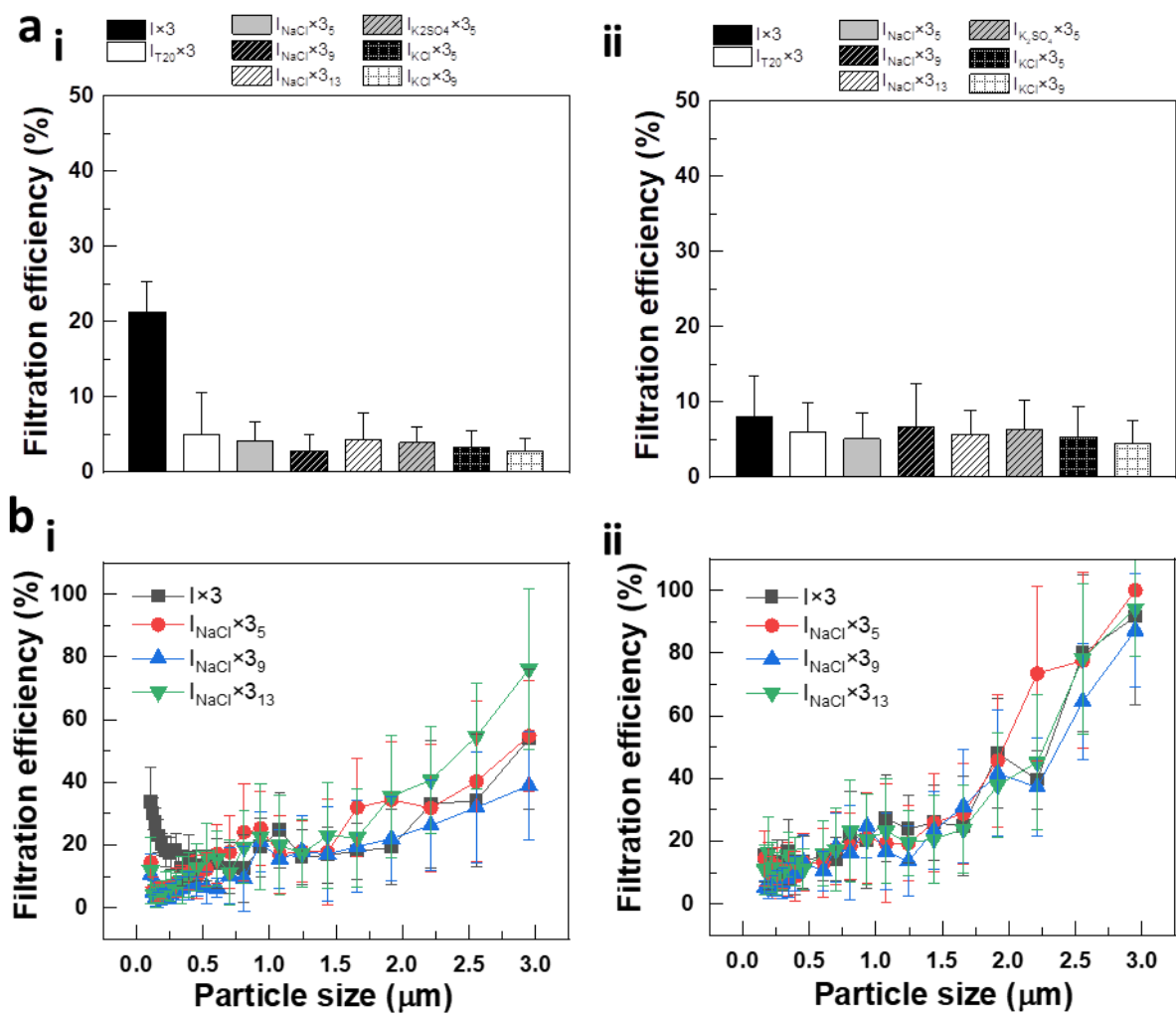


**Figure 3.4.** Filter performance of salt-coated fabrics. Filtration efficiency was performed according to NIOSH 42CFR84. (a,b) Overall filtration efficiency (a) and particle size-dependent filtration efficiency (b) of salt-coated fabrics tested with 5% NaCl aerosol (i) and DOP aerosol (ii). (n = 13–23 for a(i), n = 12–22 for a(ii), n = 9–21 for b(i), and n = 8–24 for b(ii) mean ± SD).

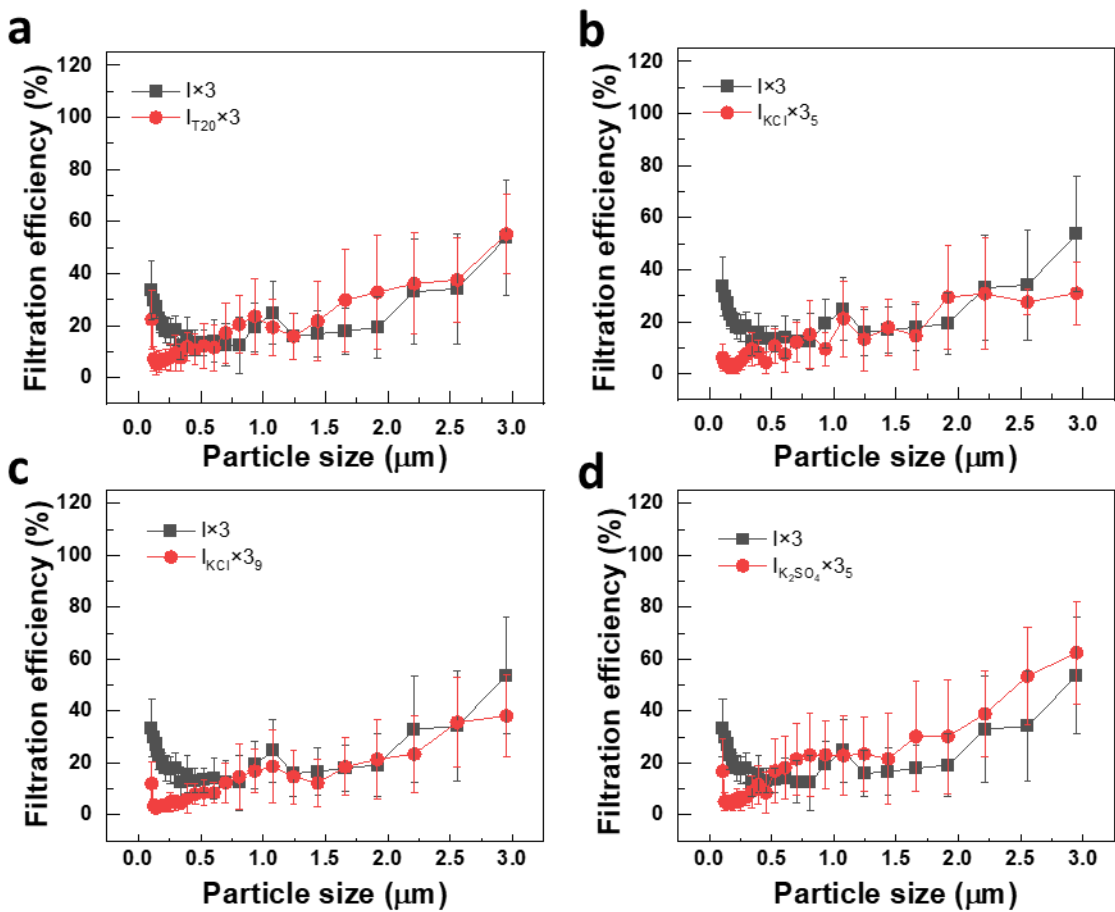


**Figure 3.5.** Particle size–dependent filtration efficiency of salt–coated fabric only conditions tested. (a–d) 5% NaCl aerosol used to measure the filtration efficiency of different salt coating conditions: (a)  $I_{T20} \times 3$  ( $n = 6–24$ , mean  $\pm$  SD), (b)  $I_{KCl} \times 3_5$  ( $n = 7–24$ , mean  $\pm$  SD), (c)  $I_{KCl} \times 3_9$  ( $n = 7–24$ , mean  $\pm$  SD), and (d)  $I_{K_2SO_4} \times 3_5$  ( $n = 7–24$ , mean  $\pm$  SD).

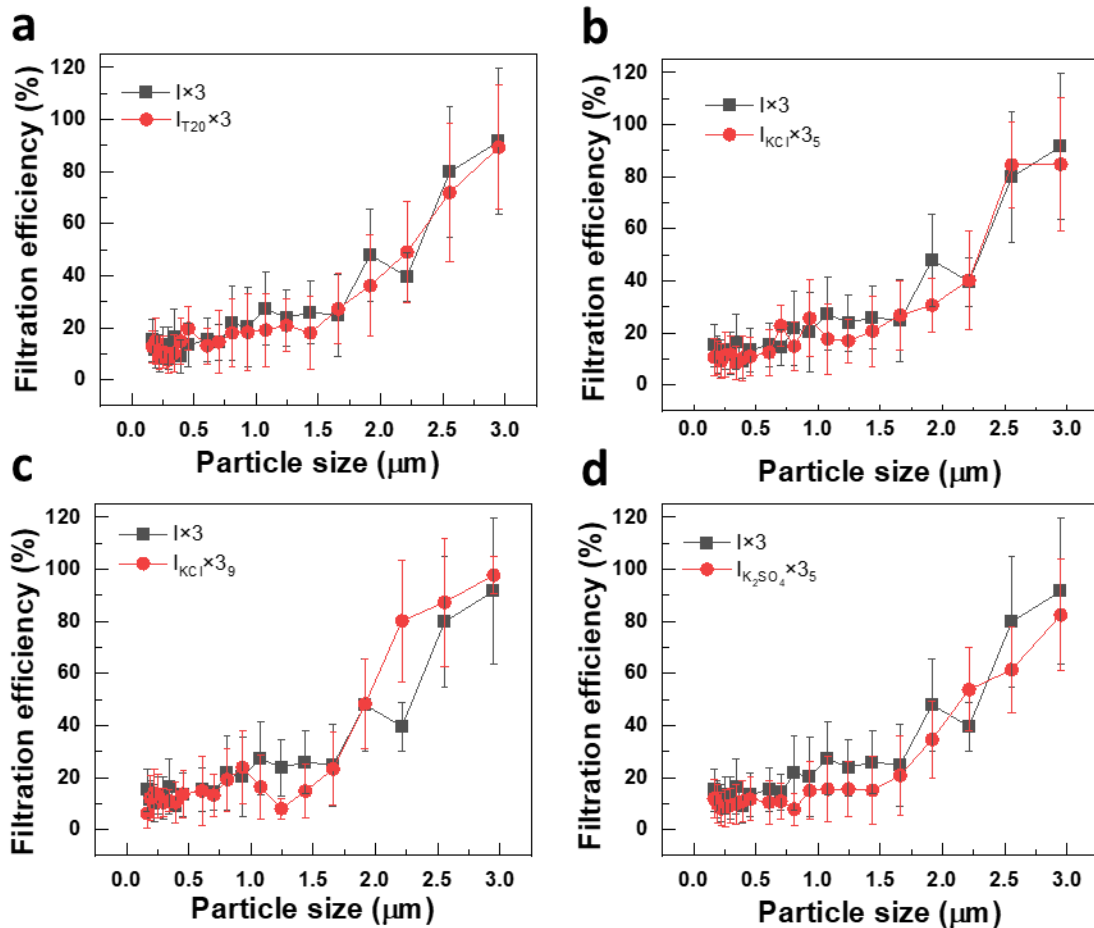


**Figure 3.6.** Particle size–dependent filtration efficiency of salt–coated fabric only conditions tested. (a–d) DOP aerosol used to measure the filtration efficiency of different salt coating conditions: (a)  $I_{T_{20}} \times 3$  ( $n = 6–24$ , mean  $\pm$  SD), (b)  $I_{KCl} \times 3_5$  ( $n = 7–24$ , mean  $\pm$  SD), (c)  $I_{KCl} \times 3_9$  ( $n = 7–24$ , mean  $\pm$  SD), and (d)  $I_{K_2SO_4} \times 3_5$  ( $n = 7–24$ , mean  $\pm$  SD).

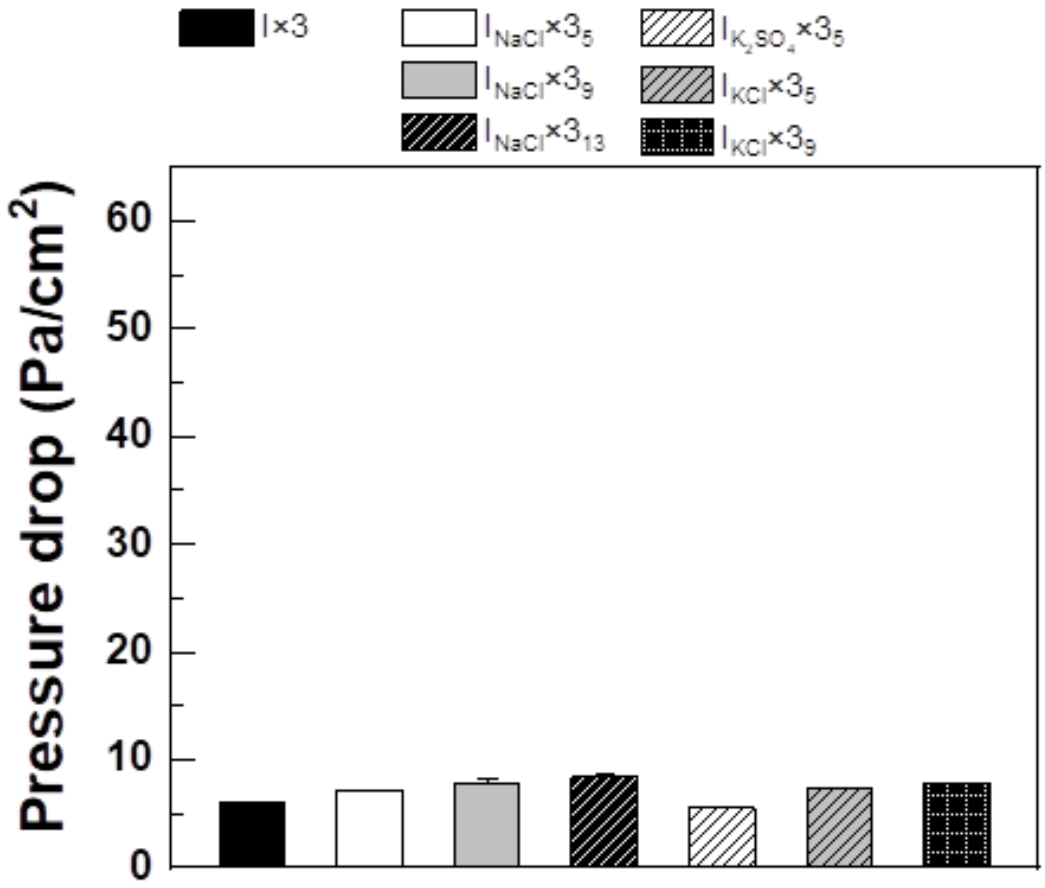


**Figure 3.7.** Breathability of salt-coated fabrics with different staking sequences. Breathability was performed according to ASTM F2100–19e1 standard. (n = 10–15, mean ± SD).

### 3.3.3 Application of stacked salt-coated SB fabrics to a mask cover and outer layer of a mask for antimicrobial face masks

Taking advantages of pathogen inactivation due to salt coating and insignificant increase in breathing resistance due to salt coating, salt-coated SB fabrics can be importantly used to prevent the spread of disease due to contact with biocontaminated mask surface. By using salt-coated stacked SB fabrics as an outermost layer of a mask, i.e. a cover on top of a 3-ply mask or outer layer of a 3-ply mask, contact transmission can be eliminated through the inactivation of pathogens on the surface of the mask that can be touched by hands. Hence, it is anticipated that this mask structure (for example,  $I_{\text{salt}} \times 3/3$ -ply mask or  $I_{\text{salt}} \times 3/M \times 1/I \times 1$ ) would combine the benefits of conventional masks (e.g., high filtration efficiency across all particle sizes due to the presence of MB middle layer) with those of salt-coated fabrics (e.g., rapid pathogen inactivation, reusability, and no concerns over contact transmission).

Mask performance has been tested by employing NaCl-coated SB fabrics and bare SB fabrics either as a cover over a conventional 3-ply mask (stacking sequence:  $I_{\text{NaCl}} \times 3$  (cover)/ $O \times 1/M \times 1/I \times 1$ , Figure 3.8) or as an outer layer of a 3-ply mask (stacking sequence:  $I_{\text{NaCl}} \times 3$  (outer layer)/ $M \times 1/I \times 1$ , Figure 3.9). As shown in Figure 3.8a, the filtration efficiency of a salt-coated mask cover over a 3-ply exhibited 2–5% higher than a conventional 3-ply mask comprising  $O \times 1/M \times 1/I \times 1$ , regardless of the aerosol type used in testing (i: NaCl, ii: DOP). However, no significant difference in filtration efficiency was observed between  $I \times 3/3$ -ply masks (i.e., a stack of three bare inner SB fabrics on top of a 3-ply mask) and  $I_{\text{NaCl}} \times 3/3$ -ply masks (*t*-test,  $P = 0.2119$  for Figure 3.8a(i) and  $P = 0.0715$  for Figure 3.8a(ii)). Upon replacing the outer layer with three stacked SB fabric ( $I_{\text{NaCl}} \times 3/M \times 1/I \times 1$ ), a similar filtration behavior was observed as in mask cover (i.e.,  $I \times 3/O \times 1/M \times 1/I \times 1$  and  $I_{\text{NaCl}} \times 3/O \times 1/M \times 1/I \times 1$ ; Figure 3.8). Also,

particle-size dependent filtration efficiency measurements indicate that the previously observed filtration efficiency decrease at  $\leq 0.3 \mu\text{m}$  for 5% NaCl particles was no longer evident regardless of salt quantity and stacking sequence (Figures 3.8b and 3.9b). This is presumed to be due to the high filtration efficiency of the MB middle layer (Figure 3.2a), rendering the effects of other layers on filtration efficiency less critical.

The application of the  $I_{\text{NaCl} \times 3}$  as a cover on top of a 3-ply mask and replacement of the outer layer of a 3-ply mask with  $I_{\text{NaCl} \times 3}$  (Figure 3.10) appear to increase the pressure drop up by 9–10 and 7–9  $\text{Pa}/\text{cm}^2$ , respectively, compared to the conventional 3-ply mask. Importantly, both architectures irrespective of the amount of coated salt align with the ASTM F2100-19e1 guidelines, which define a differential pressure below 50  $\text{Pa}/\text{cm}^2$  for Level I masks and  $\leq 60 \text{ Pa}/\text{cm}^2$  for Level II and III masks (Figure 3.10). Taken together, these findings indicate that when salt-coated SB fabrics are used as a mask cover and an outer layer of a mask, they achieve high filtration efficiency, effectively addressing the limitations observed with salt-coated fabrics alone against small aerosols, and breathability by maintaining pathogen inactivation functionality.

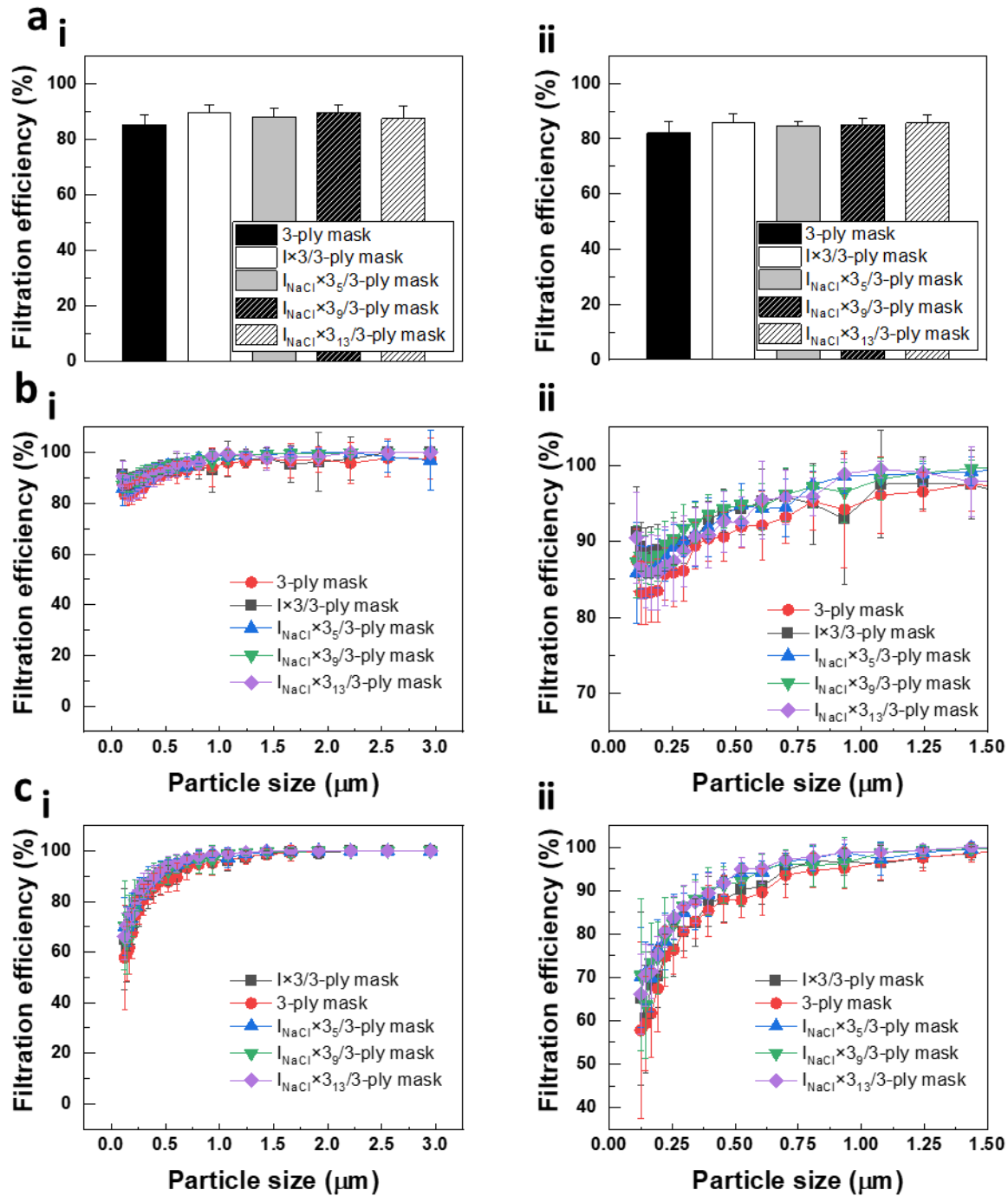


**Figure 3.8.** Filter performance of bare and salt-coated fabrics with different stacking sequences. Filtration efficiency and breathability were performed according to NIOSH 42CFR84 and ASTM F2100–19e1 standards, respectively. (a) Overall filtration efficiency of I×3 and I<sub>NaCl</sub>×3 as a cover of the 3-ply mask (i: 5% NaCl aerosol and ii: DOP aerosol). (n = 10–20 for a(i) and n = 10–15 for a(ii), mean ± SD) (b,c) Particle size-dependent filtration efficiency of I×3 and I<sub>NaCl</sub>×3 as cover of the 3-ply mask, tested with 5% NaCl aerosol (b) and DOP aerosol (c) (i: filtration efficiency of stacked fabrics and ii: zoomed-in filtration efficiency of the stacked fabrics). (n = 10–20 for b and n = 10–15 for c, mean ± SD).

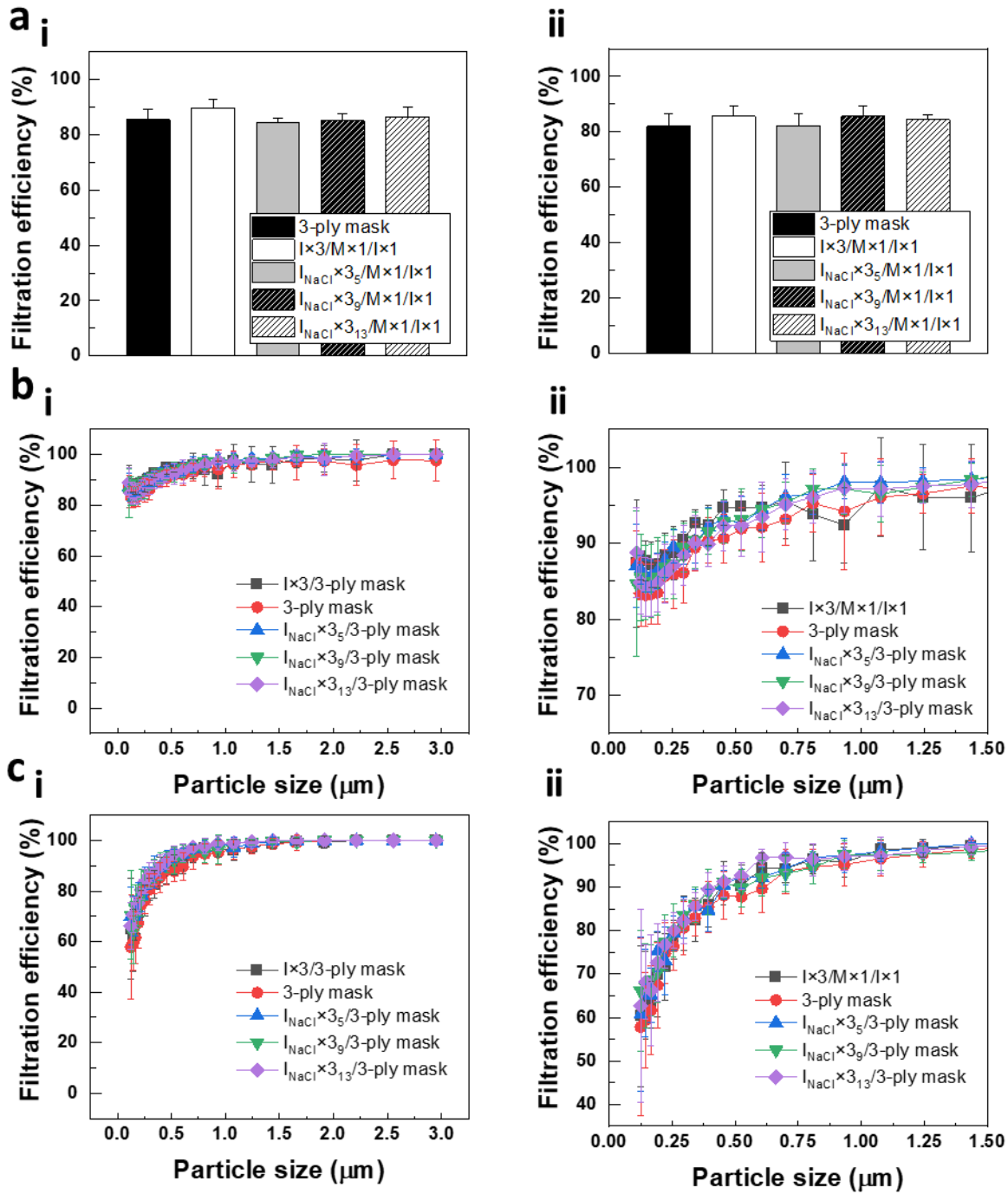


**Figure 3.9.** Filter performance of bare and salt-coated fabrics with different stacking sequences. Filtration efficiency and breathability were performed according to NIOSH 42CFR84 and ASTM F2100–19e1 standards, respectively. (a) Overall filtration efficiency of  $I \times 3$  and  $I_{NaCl} \times 3$  as an outer of the 3-ply mask (i: 5% NaCl aerosol and ii: DOP aerosol). ( $n = 12–19$  for a(i) and  $n = 11–16$  for a(ii), mean  $\pm$  SD) (b,c) Particle size-dependent filtration efficiency of  $I \times 3$  and  $I_{NaCl} \times 3$  as an outer of the 3-ply mask, tested with 5% NaCl aerosol (b) and DOP aerosol (c) (i: filtration efficiency of stacked fabrics and ii: zoomed-in filtration efficiency of the stacked fabrics). ( $n = 12–19$  for b and  $n = 7–16$  for c, mean  $\pm$  SD). (c) Breathability of  $I \times 3$  and  $I_{NaCl} \times 3$  used as an outer. ( $n = 9–12$ , mean  $\pm$  SD).

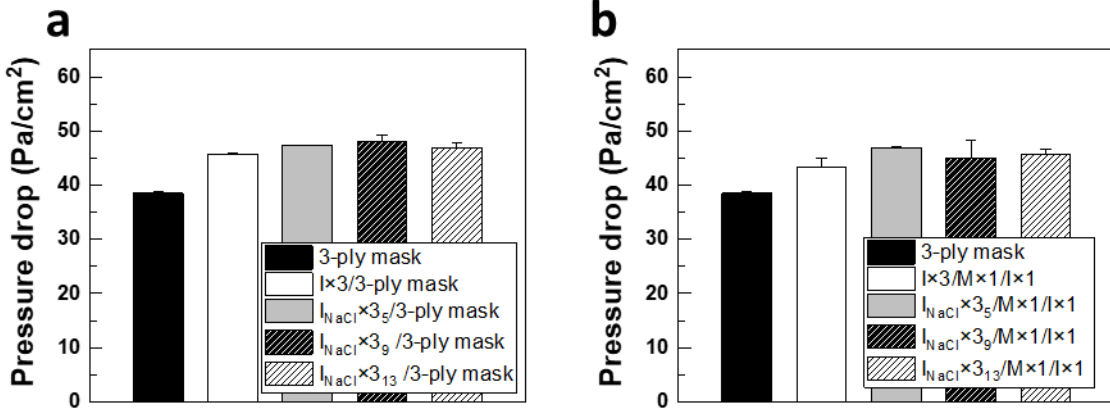


**Figure 3.10.** Breathability of I×3 and I<sub>NaCl</sub>×3 used as an outer (a) and cover (b). Breathability was performed according to ASTM F2100–19e1 standard. (n = 9–12, mean ± SD).

### 3.3.4 Filter performance of three stacked salt-coated SB fabrics in wet conditions

To examine the effect of wetness on filter performance, both I×3 and I<sub>NaCl</sub>×3<sub>9</sub> were subjected to different amounts of water spray (1, 6, and 12 mg H<sub>2</sub>O/cm<sup>2</sup>). The level of wetness was modulated by measuring the weight of the filter before and after water spray (see Figure 3.11 for optical microscope images after spraying sulforhodamine B solution onto I<sub>NaCl</sub>×3<sub>9</sub> fabrics). As shown in Figure 3.12, the overall filtration efficiency of I×3 fabrics decreased with increasing amount of water sprayed (one-way ANOVA,  $P < 0.0001$ ). In the case of salt-coated fabrics (I<sub>NaCl</sub>×3<sub>9</sub>), the mean filtration efficiency seemed to increase as the degree of wetting increased (one-way ANOVA,  $P = 0.0023$ ). When tested with DOP aerosols, wetting did not affect filtration efficiency for both bare and salt-coated fabrics (Figure 3.12a(ii)) (one-way ANOVA,  $P = 0.3829$  for bare and  $P = 0.0073$  for salt-coated fabrics).

Particle-size dependent filtration efficiency analysis revealed different behaviors. For I×3 fabrics, the filtration efficiency against 5% NaCl aerosols exhibited a biphasic behavior, i.e. initial decrease is followed by the gradual increase (Figure 3.12b), and no significant effect of the wetness was observed (GLM analysis,  $P = 0.0678$ ). On the other hand, as the degree of wetting increases, a relatively rapid increase in the filtration efficiency of I<sub>NaCl</sub>×3<sub>9</sub> was observed with NaCl aerosol size (at size  $> 0.3 \mu\text{m}$ ; GLM analysis,  $P > 0.0001$ ) (Figure 3.12c). This effect might be attributed to the hydrophilicity of salts that enable formation of water film around fibers. Compared to NaCl aerosol testing conditions, when testing with DOP aerosols, no change was observed in I×3 fabrics regardless of wetness, while a slight higher filtration efficiency was detected for I<sub>NaCl</sub>×3<sub>9</sub> with 12 mg H<sub>2</sub>O/cm<sup>2</sup> of water spray (Figure 3.13).

The wet test was also performed using I×3 and I<sub>NaCl</sub>×3<sub>9</sub> as both a cover and an outer layer of a 3-ply mask. To this end, I×3 and I<sub>NaCl</sub>×3<sub>9</sub> were placed on the top of either a 3-ply mask or M×1/I×1, followed by the application of varying amounts of water spray (1, 6, and 12 mg

H<sub>2</sub>O/cm<sup>2</sup>). As anticipated, all conditions maintained high filtration efficiency, regardless of the positioning of I×3 and I<sub>NaCl</sub>×3<sub>9</sub>. Moreover, as shown in Figure 3.14, the differences among the conditions were not significant compared to the overall high filtration efficiency (see Figures 3.15 for particle size-dependent filtration efficiency) (one-way ANOVA; P = 0.0044 for Figure 3.14a I×3, P = 0.0018 for Figure 3.14a I<sub>NaCl</sub>×3<sub>9</sub>, P = 0.3711 for Figure 3.14b I×3, and P = 0.0073 for Figure 3.14b I<sub>NaCl</sub>×3<sub>9</sub>). Notably, in contrast to I×3 conditions, pressure drop was observed to increase with water in I<sub>NaCl</sub>×3<sub>9</sub>, which is presumed to be due to the formation of water film around fibers (Figure 3.16; one-way ANOVA, P > 0.0001).

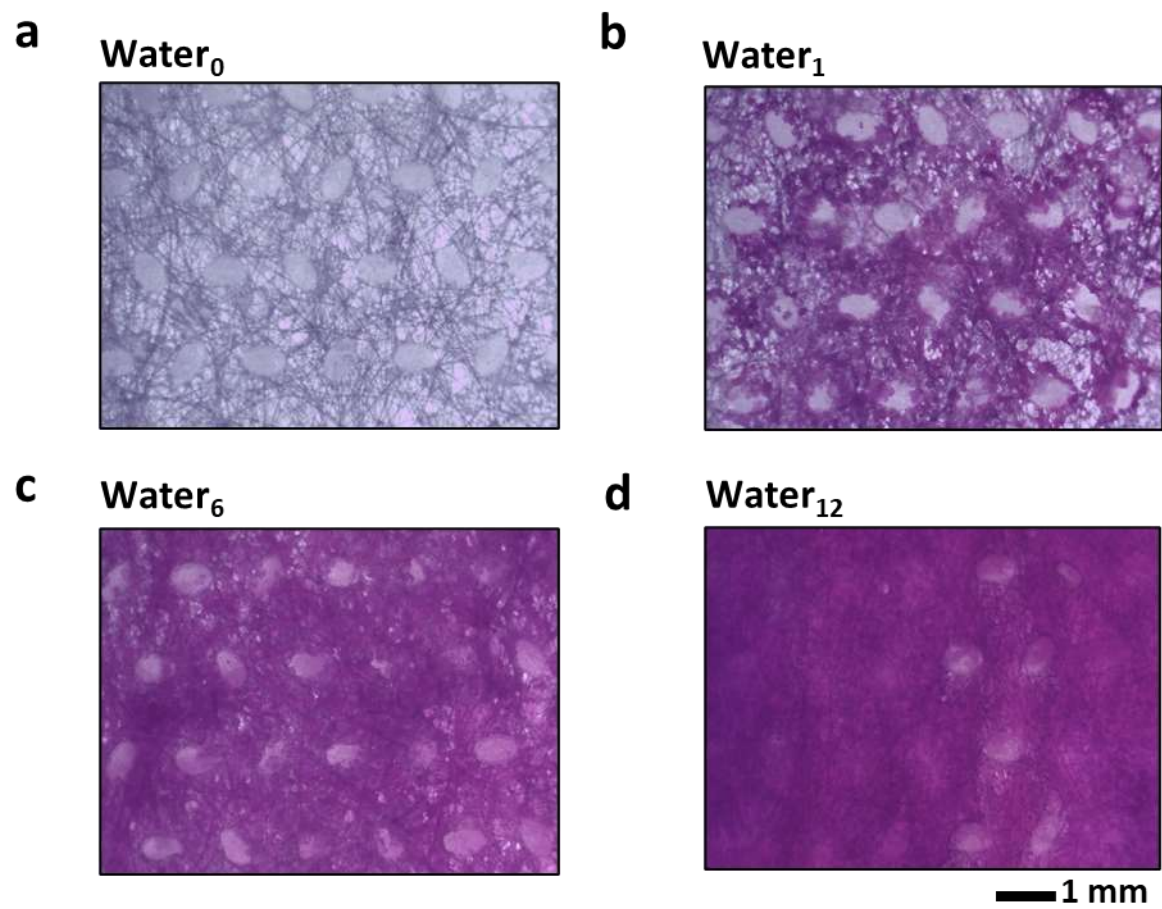


**Figure 3.11.** Characterization of  $I_{NaCl} \times 3_9$  fabrics after spraying DI water for the measurement of effects of wetness on filtration efficiency. Sulforhodamine B (SRB) was used to visualize the wetness of fabrics in the images; however, for filtration efficiency tests and breathability tests, DI water was used. (a–d) different amount of SRB was sprayed: (a)  $0 \text{ mg/cm}^2$ , (b)  $1 \text{ mg/cm}^2$ , (c)  $6 \text{ mg/cm}^2$ , and (d)  $12 \text{ mg/cm}^2$ .

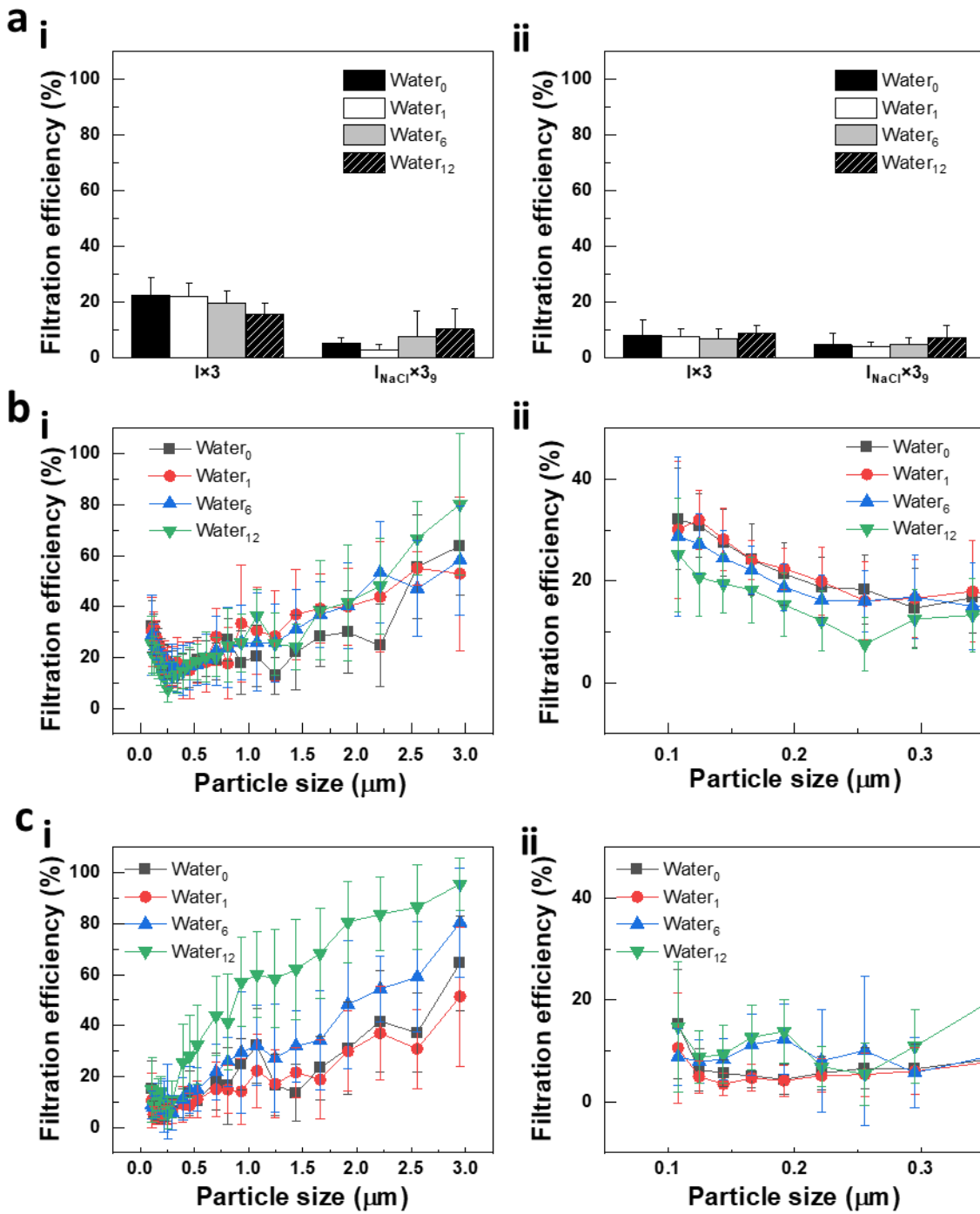


**Figure 3.12.** Filter performance of bare and salt-coated fabrics with different wetness. See Figure 3.9 for the optical microscope images of wet fabrics. The wetness of the samples was measured by weighting the samples before and after water spray, followed by dividing the values by mask surface area. Filtration efficiency was performed according to NIOSH 42CFR84 standard. (a) Overall filtration efficiency tested with 5% NaCl (i) and DOP aerosols (ii). ( $n = 13-30$ , mean  $\pm$  SD). (b,c) particle size-dependent filtration efficiency of wet  $I \times 3$  and wet  $I_{NaCl} \times 3_9$ , tested with 5% NaCl (b) and DOP (c) aerosols (i: filtration efficiency of fabrics and ii: zoomed-in filtration efficiency of the fabrics). ( $n = 7-29$  for b and 6-29 for c, mean  $\pm$  SD).

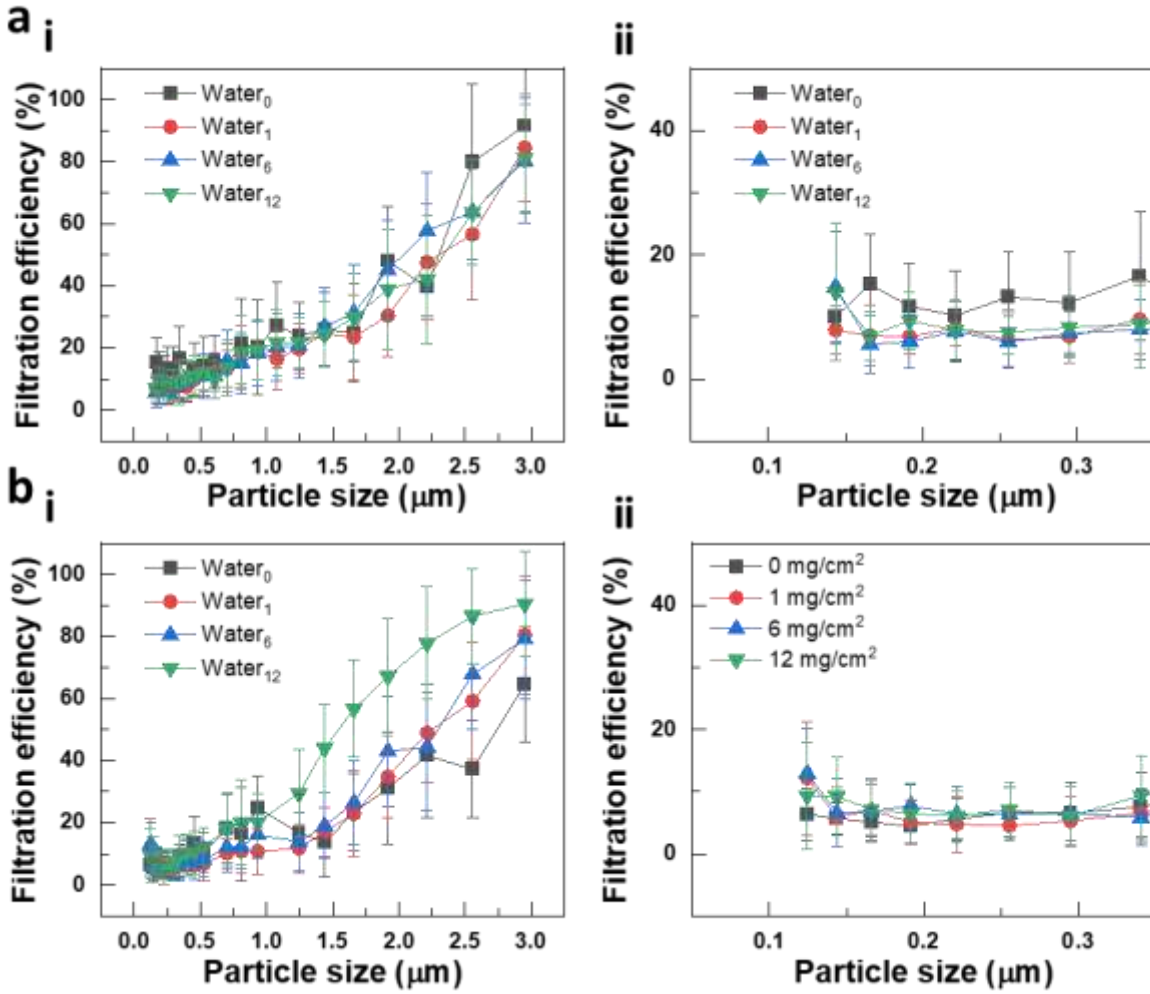
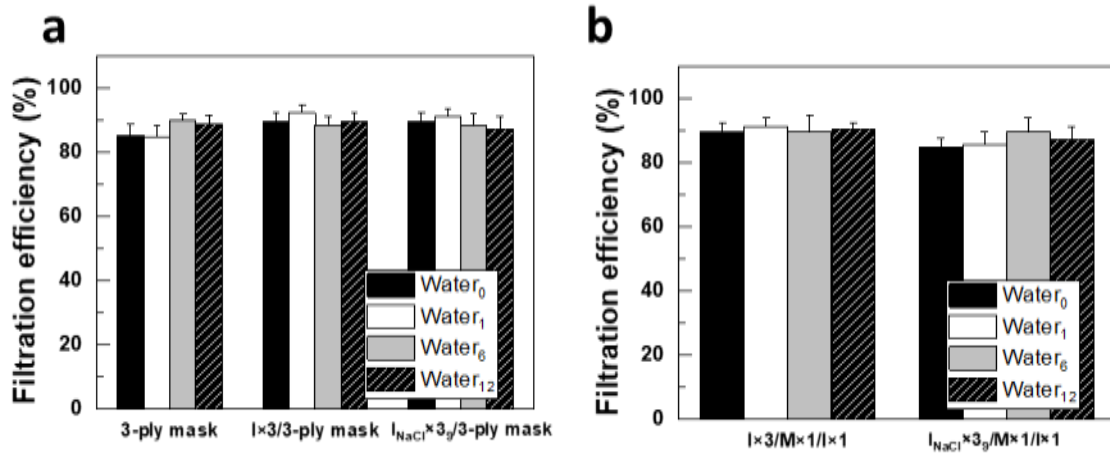
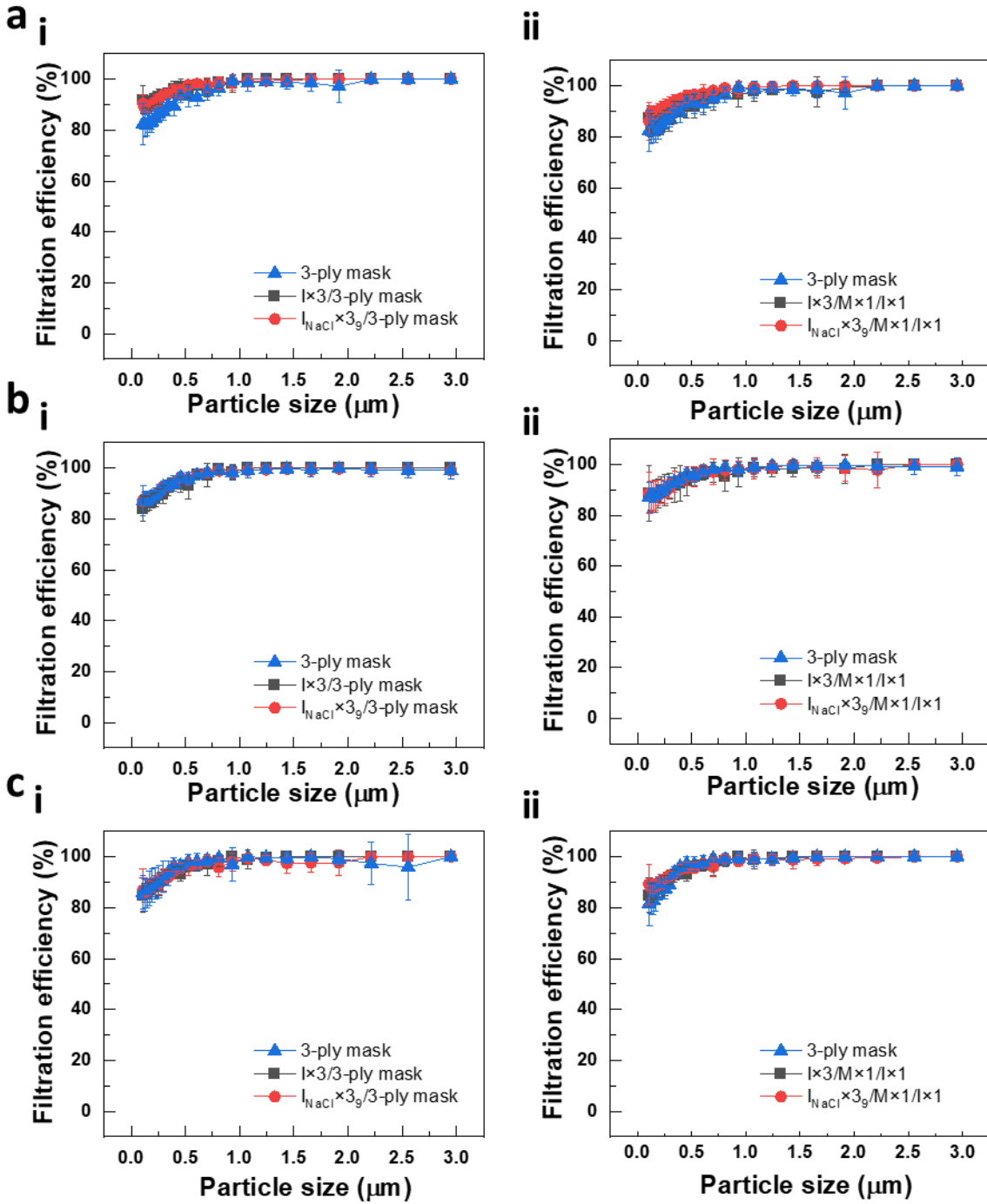


Figure 3.13. Particle size–dependent filtration efficiency of I×3 (a) and I<sub>NaCl</sub>×3<sub>9</sub> (b) tested with DOP aerosols (i: filtration efficiency of fabrics and ii: zoomed–in filtration efficiency of the fabrics). (n = 12–29, mean ± SD).



**Figure 3.14.** Filtration efficiency of wet I×3 and I<sub>NaCl</sub>×3 as a cover and an outer of the 3-ply mask, tested with 5% NaCl aerosol according to NIOSH 42CFR84. (a,b) Overall filtration efficiency of I×3 and I<sub>NaCl</sub>×3<sub>g</sub> fabrics used as a cover (a) and an outer layer (b). (n = 9–20, mean ± SD).



**Figure 3.15.** Filtration efficiency of wet  $I \times 3$  and  $I_{\text{NaCl}} \times 3$  as a cover and an outer of the 3-ply mask, tested with 5% NaCl aerosol according to NIOSH 42CFR84. (a–c)  $I \times 3$  and  $I_{\text{NaCl}} \times 3_g$  fabrics used as a cover (i) and an outer layer (ii): (a) 1 mg/cm<sup>2</sup> of water (n = 10–13, mean  $\pm$  SD), (b) 6 mg/cm<sup>2</sup> of water (n = 9–13, mean  $\pm$  SD), and (c) 12 mg/cm<sup>2</sup> of water (n = 10–11, mean  $\pm$  SD)

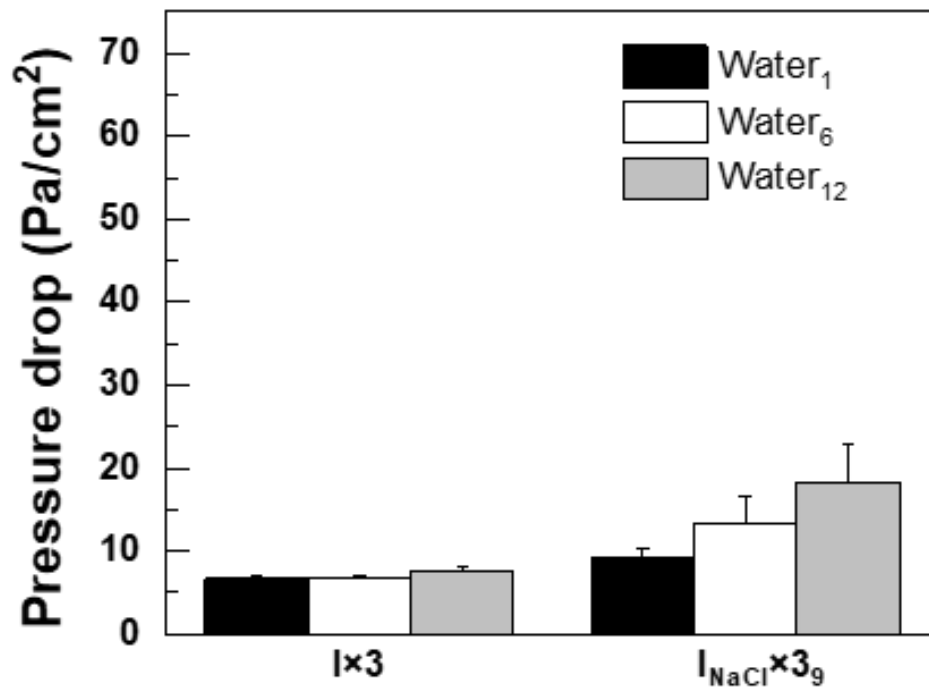


**Figure 3.16.** Breathability of bare and salt-coated fabrics with different wetness. Breathability was performed according to ASTM F2100-19e1 standard. (n = 9-14, mean ± SD).

### **3.3.5 Filter performance of N95 respirators only and when combined with I×3 and I<sub>NaCl</sub>×3<sub>9</sub> as a cover**

The salt-coated filters demonstrated high filtration efficiency when used as a cover and an outer layer for the 3-ply mask. To assess the compatibility of salt-coated filters with other types of respiratory protection systems, N95 respirators were tested alongside the salt-coated filters. As shown in Figure 3.17, a slight increase in pressure drop was observed when I<sub>NaCl</sub>×3<sub>9</sub> was used as a cover, for instance, during inhalation (N95 (102 ± 5 Pa), I×3/N95 (124 ± 6 Pa), and I<sub>NaCl</sub>×3<sub>9</sub>/N95 (138 ± 5 Pa)) and exhalation (N95 (114 ± 4 Pa), I×3/N95 (123 ± 6 Pa), and I<sub>NaCl</sub>×3<sub>9</sub>/N95 (139 ± 4 Pa)). However, considering the NIOSH 42CFR84 standard, which stipulates that the differential pressure should remain below 311 Pa for inhalation airflow and below 249 Pa for exhalation airflow, the observed increase in mean values is not significant. In terms of filtration efficiency, all conditions achieved significantly high filtration efficiency, exceeding 98%. The high filtration efficiency was also further supported by particle size-dependent filtration efficiency tests, with all efficiencies exceeding 98%. In DOP tests, although a slight decrease in filtration efficiency was observed for 5% NaCl particles ≤ 0.3 μm in size, a filtration efficiency of > 97% was still achieved. These findings demonstrate that while salt-coated fabrics themselves may not be suitable for capturing small particles (≤ 0.3 μm), their limitations can be overcome when used as a cover or an outer layer for 3-ply masks or N95 respirators.

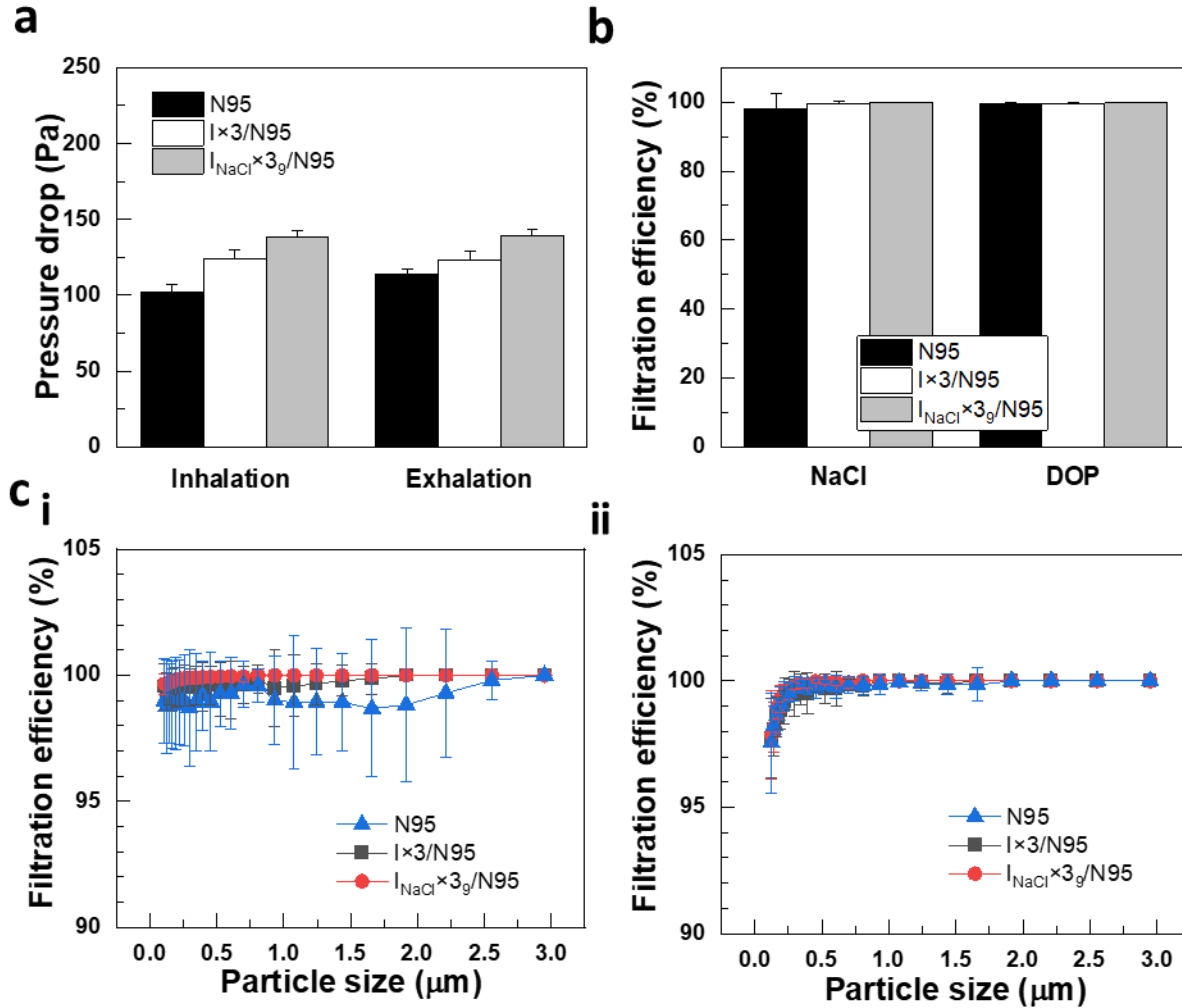


**Figure 3.17.** Filter performance of N95 respirators. Filtration efficiency and breathability were performed according to NIOSH 42CFR84. (a,b) N95 respirators alone, and with I×3 and I<sub>NaCl</sub>×3<sub>g</sub> as a cover of N95. (a: breathability and b: overall filtration efficiency) (n = 10–15 for a and n = 11–18 for b, mean ± SD). (c) Particle size–dependent filtration efficiency tested with 5% NaCl aerosols (i) and DOP aerosols (n = 15–19 for i and n = 10–18 for ii, mean ± SD) (ii).

### 3.3 Conclusion

In this comprehensive study, we explored the strategic functionalization of protective masks, focusing on the implementation and efficacy of salt-coated fabrics on mask performance. Key findings include the effect of salt coating on filtration efficiency, depending on the type and quantity (5, 9, and 13 mg/cm<sup>2</sup>) of salt used (NaCl, KCl, and K<sub>2</sub>SO<sub>4</sub>), and the significant role of water exposure on mask performance. Furthermore, our results underscore the compatibility of salt-coated filters with surgical masks and N95 respirators, demonstrating their potential to maintain high filtration efficiency without compromising breathability. Notably, when salt-coated fabrics were used as covers and outer layers of surgical masks and respirators, they exhibited high filtration efficiency, overcoming the limited filtration efficiency found at particles smaller than 0.3 μm in size for 5% NaCl aerosols, when only salt-coated fabrics were tested. Additionally, water exposure enhanced the filtration efficiency of salt-coated fabrics due to the hydrophilicity of the salt-coated fabrics, which enables the formation of a water film around fibers. Our investigation into particle size-dependent filtration efficiency revealed the main and limited filtration mechanisms involved in the overall filtration efficiency of salt-coated fabrics, enhancing our understanding of filtration efficiency and paving the way to improve the limited aspects. Overall, this study not only revealed the effects of salt coating and environmental conditions on mask performance but also offers crucial insights for the development of other antimicrobial face masks.

# 4 Mechanistic study of pathogen inactivation on salt-coated filters

To counteract the spread of pathogens, our team developed antimicrobial filters by applying salt coatings to membrane fibers. This study scrutinized the mechanism behind the inactivation of pathogens upon exposure to salt-coated filters. We investigated the recrystallization process of various salts (i.e., sodium chloride (NaCl), potassium sulfate (K<sub>2</sub>SO<sub>4</sub>), and potassium chloride (KCl)), when exposed to aerosol particles. The time-dependent recrystallization processes of each salt were compared with their time-dependent antimicrobial efficiency. Our findings indicate that the process of recrystallization aligns with the inactivation of pathogens, H1N1 influenza virus and *Klebsiella pneumoniae*. Furthermore, other factors, such as osmotic pressure and ionic effects, did not show significant antimicrobial efficiency, indicating that salt recrystallization is the main factor in pathogen inactivation. The salt-coated filters effectively reduce the viability of pathogens, irrespective of whether transmission occurs via aerosols or droplets, in both DI water and artificial saliva. These findings advance our understanding of salt-recrystallization technology and open up possibilities for creating versatile antimicrobial filters.

This paper is based on the significant inactivation efficiency of salt-coated fabrics against diverse pathogens including viruses and bacteria, which was published by I. Rubino et al. and Quan, F.-S. et al [293, 294]. For this paper, I contributed as co-first author and was responsible for performing experiments (investigation of pathogen inactivation efficiency and the effect of vacuum application on salt-coated fabrics), data analysis, and manuscript writing. I. Rubino as a co-first author performed experiments (investigation of pathogen inactivation efficiency and salt recrystallization pattern), data analysis, and manuscript writing.

## 4.1 Background

Pandemic and epidemic respiratory diseases can cause high morbidity and mortality, as exemplified by coronavirus disease 2019 (COVID-19). Pathogens, including bacteria and viruses, have different transmission strategies. For instance, *Bordetella pertussis*, *Chlamydia pneumoniae*, *Haemophilus influenzae*, mumps virus, *Mycoplasma pneumoniae*, *Neisseria meningitidis* and *Streptococcus pneumoniae* mainly transmit through droplets; influenza virus, severe acute respiratory syndrome (SARS)-associated coronavirus and varicella-zoster virus transmit through droplets and aerosols; and *Mycobacterium tuberculosis* mainly transmits through aerosols [298]. There have been diverse efforts to prevent their spread, with face masks playing a crucial role as first means of protection against infection. Among respirators, the N95 respirator has been most widely used for healthcare and the public. The N95 respirator can protect the respiratory system from splashes, droplets as well as aerosols. However, the large thickness and small pore size of the N95 respirator decrease breathability and comfort. Thus, surgical masks are often used as a preferable type of respiratory protection device due to reasonable prices and considerably higher breathability than respirators, although they are not designed to filter out aerosols [299-301].

In spite of their primary role in preventing infection, no significant improvement in the performance of available face masks has been made and gaps remain in mask technology [302]. Live pathogens captured on the surface of the mask can be a source of environmental contamination and pose a risk of contact transmission. Additionally, since the supply of face masks is limited, disposable masks tend to be reused, which can cause cross-infection. Various methods to decontaminate face masks have been tested, such as applying ethylene oxide, formalin, UV and bleach treatments. However, each method has undesired effects, including generation of hazardous byproducts, residual odor and degradation of the face masks [303, 304].

Furthermore, these methods are not easy to perform individually as they require specialized settings, and contact transmission is unavoidable since the filters do not have an incorporated antimicrobial effect. Thus, a novel approach for the development of antimicrobial mask filters is needed to address these issues.

We previously reported the first-of-its-kind salt-coated antimicrobial filter that employs the natural salt recrystallization process to inactivate viruses and bacteria [305, 306]. Our investigations on salt-coated face masks have successfully demonstrated the proof-of-concept antimicrobial filters, which enable the reuse of the face mask by physically destroying pathogens. Upon exposure to pathogen-carrying aerosols, the salt coating dissolves and evaporation-induced salt recrystallization damages and destroys the pathogens.

Here, we report mechanistic studies to investigate the recrystallization-based pathogen inactivation and the effectiveness of the salt-coated filters in terms of pathogen transmission mode. To this end, the effect of salt type and morphology on pathogen inactivation kinetics was studied by observing the salt recrystallization behavior in salt powders and comparing it with that in the salt coatings on filters. A new method of producing the salt-coated filters was characterized in terms of salt coating morphology and pathogen inactivation. Additionally, the performance of the salt-coated filters was evaluated against pathogenic aerosols (diameter = 2.5–4  $\mu\text{m}$ ) and droplets (5  $\mu\text{L}$ ) generated from DI water and artificial saliva to evaluate their biocidal effect, depending on the size and composition of the pathogen-carrying medium.

## 4.2 Methods

### 4.2.1 Filters preparation

Spunbond polypropylene membranes ( $\sim 25 \text{ g/m}^2$ , pore size =  $\sim 60 \text{ }\mu\text{m}$ ) obtained from the innermost layer of three-ply surgical masks (Fisherbrand Facemasks; Fisher Scientific, Pittsburgh, PA, USA) were used for preparation of NaCl,  $\text{K}_2\text{SO}_4$  and KCl salt filters, as reported previously 8. Briefly, the membranes were cut into circular samples with 3-cm radius (bare membranes, labelled as Bare). The salt coating solutions were prepared in filtered ( $0.22 \text{ }\mu\text{m}$  pore size; Corning, Tewksbury, MA, USA) DI water by dissolving the salts at 400 rpm and  $90 \text{ }^\circ\text{C}$  in the case of NaCl (final concentration: 29.03 w/v%) and 400 rpm and room temperature (RT) in the case of  $\text{K}_2\text{SO}_4$  (9.72 w/v%) and KCl (26.31 w/v%), with the addition of Tween 20 surfactant (Fisher Scientific) at 1 v/v% as wetting agent. Membrane samples were completely pre-wet in the respective coating solution by submersion in the coating solution (final volume of solution present in the membranes after pre-wetting was completed:  $\sim 350 \text{ }\mu\text{L}$ ). The pre-wet membranes were placed in  $60 \times 15 \text{ mm}$  petri dishes containing different volumes of coating solution (0, 300, 600, 900 or  $1200 \text{ }\mu\text{L}$ ). Three layers of pre-wet membranes were overlapped for each filter, which was shown to offer effective filtration efficiency and pressure drop performances 8. Finally, the samples were dried overnight at  $45 \text{ }^\circ\text{C}$  (Thermolyne 42000 incubator; Dubuque, IA, USA). The obtained salt filters contained varying amounts of coated salt and were labelled as Saltvol, where Salt is the salt type (NaCl,  $\text{K}_2\text{SO}_4$  or KCl) and vol is the volume of coating solution in which the filters were dried (0, 300, 600, 900 or  $1200 \text{ }\mu\text{L}$ ).

Filters coated with salt through a vacuum process were prepared as follows. The circular membrane samples (radius = 1.7 cm) were submerged in the NaCl,  $\text{K}_2\text{SO}_4$  or KCl coating solution for pre-wetting (final volume of solution present in the membranes after pre-wetting was completed:  $\sim 110 \text{ }\mu\text{L}$ ). Three layers of pre-wet membranes were overlapped in a petri dish.

Then, the 3-layered sample was exposed to different vacuum levels (5, 10 or 15 inHg) applied for 1 sec on each side of the sample using a vacuum pump (Laboport UN 840 FTP; KNF Neuberger, Trenton, NJ, USA). This process was repeated twice, before transferring the sample to a new 60 × 15 mm petri dish for drying overnight at 37 °C. The obtained filters were labelled as Saltvacuum, where Salt is the salt type (NaCl, K<sub>2</sub>SO<sub>4</sub> or KCl) and vacuum is the applied vacuum level (5, 10 or 15 inHg).

#### **4.2.2 Bacteria and influenza virus preparation**

Following streaking on tryptone soya agar (TSA; Oxoid, Nepean, Ontario, Canada) plates and incubation at 37 °C for 24 h, *Klebsiella pneumoniae* (ATCC BAA-1705) single colonies were added in tryptic soy broth (TSB; BD, Franklin Lakes, NJ, USA) and incubated at 37 °C and 200 rpm for 24 h. The suspension was then transferred into fresh TSB at 37 °C and 200 rpm (1:500). After the *K. pneumoniae* suspension entered the exponential growth phase, it was frozen in 20% glycerol (Fisher Scientific) at -80 °C for storage. For experiments, frozen aliquots were grown with Mueller Hinton (MH) broth (BD; 1:500, 37 °C, 200 rpm) until the OD<sub>600</sub> was 0.8, and then washed 3 times in phosphate buffered saline (PBS).

Influenza virus A/Puerto Rico/8/34 (PR/34, H1N1) was grown in 11-day old embryonated chicken eggs and purified from allantoic fluids by passing through the cell strainer (70 µm; Fisherbrand), low-speed centrifugation (2,800 rpm, 4 °C, 15 min) and high-speed centrifugation (30,000 rpm, 4 °C, 1 h). Madin-Darby Canine Kidney (MDCK) cells were grown and maintained in Dulbecco's modified Eagle's medium (DMEM; Corning) at 37 °C and 5% CO<sub>2</sub>.

#### **4.2.3 Test of pathogen stability change on salt powders**

The NaCl, K<sub>2</sub>SO<sub>4</sub> and KCl powders (300 mg) were each uniformly deposited in a well of a 12-well plate. For bacteria stability tests, *K. pneumoniae* was cultured and washed as described above, and resuspended in DI water (OD<sub>600</sub> of 10-fold dilution = 1.25). For viral stability tests, the PR/34 influenza virus stock was resuspended in DI water. The nebulizer unit (Aeroneb Lab Nebulizer System; Aerogen, Galway, Ireland), was placed in the well with a tight seal and 20 µL of bacteria or virus suspension were aerosolized (diameter = 2.5–4 µm) for 30 sec. The pathogenic aerosols were incubated on top of the powders at ambient condition for a specific time point (3, 5, 15, 30 or 60 min). Then, the bacteria/virus were reconstituted by adding 2 mL (NaCl and KCl powders) or 4 mL (K<sub>2</sub>SO<sub>4</sub> powder) of PBS and mixing with pipette to completely dissolve the salt powder. The recovered bacteria/virus were centrifuged (14,000 rpm, 15 min, 4 °C) to discard the dissolved salt, and then resuspended in fresh PBS. The pathogens at 0 min incubation were collected by aerosolizing the pathogens into 15-mL tubes, followed by resuspension in PBS; this was similarly conducted for all pathogen stability tests in this work. For *K. pneumoniae*, viability change was determined by colony forming unit (CFU) measurements onto MH II agar plates (5 µL of 10-fold dilutions, incubation at 37 °C overnight). The CFU were divided by the amount of bacteria used for assays, determined as protein concentration measured by bicinchoninic acid assay (Micro BCA protein assay kit; Thermo Fischer Scientific, Waltham, IL, USA) with bovine serum albumin (BSA) standard. For PR/34, stability change of the virus was determined by measuring hemagglutinin activity (HA) with chicken red blood cells (0.7% suspension; Lampire Biological Laboratories, Pipersville, PA). The CFU and HA titer measurements were then expressed as relative to the measurements at 0 min incubation on the powders.

To test the effect of osmotic pressure during the experimental procedure, 300 mg of each powder were dissolved in 1.5 mL (NaCl and KCl powders) or 3.5 mL (K<sub>2</sub>SO<sub>4</sub> powder) of PBS in

a 15-mL tube. The *K. pneumoniae* suspension (20  $\mu$ L) was aerosolized into the tube for 30 sec, followed by 1-min aerosolization of DI water and vortex (final volume: 2 mL for NaCl and KCl, 4 mL for K<sub>2</sub>SO<sub>4</sub>). The bacteria were incubated in the dissolved salt powder for a specific time point (15, 30 or 60 min), and then centrifuged (14,000 rpm, 15 min, 4 °C) to interrupt the incubation and resuspend in 100  $\mu$ L of fresh PBS. CFU measurements were conducted as described above.

#### 4.2.4 Test of pathogen stability change due to osmotic pressure

To test the effect of hyperosmotic pressure due to increases in salt concentration during aerosol drying, 20  $\mu$ L of *K. pneumoniae* or PR/34 suspension were added into a 15-mL tube containing 2 mL of salt solution for 30 sec, followed by vortex. The bacteria or virus was incubated in the salt solution for a specific time point (bacteria: 15, 30 and 60 min; virus: 5 and 30 min), and then centrifuged (14,000 rpm, 15 min, 4 °C) to interrupt the incubation and resuspend in 100  $\mu$ L of fresh PBS. CFU and HA titer tests were conducted as described above. As salt solutions can include both osmotic pressure and ionic effect on the HA titer detection, the test of PR/34 stability was similarly run in sucrose solution, where no ionic effect is present. After incubation, the sucrose solution with virus was diluted with PBS to form a pellet by centrifugation. The aqueous salt and sucrose solution conditions tested are summarized in Table 4.1.

**Table 4.1.** Salt and sucrose solution conditions used for tests of the osmotic pressure effect on bacteria and virus during aerosol drying. \*Saturated condition.

NaCl Concentration (w/v%)	K <sub>2</sub> SO <sub>4</sub> Concentration (w/v%)	KCl Concentration (w/v%)	Sucrose Concentration (w/v%)
29*	10*	26*	200*
26	7	18	
18	4	10	
10			

#### 4.2.5 Test of pathogen stability change on filters

To analyze the time-dependent inactivation, bacteria and virus aerosols were exposed to the bare membranes (Bare) and salt-functionalized filters ( $\text{NaCl}_{600}$ ,  $\text{K}_2\text{SO}_4_{600}$ ,  $\text{KCl}_{600}$ ). For bacteria, *K. pneumoniae* was cultured and washed as described above, and resuspended in DI water ( $\text{OD}_{600}$  of 10-fold dilution = 1.25). For viral stability tests, the PR/34 influenza virus stock was resuspended in DI water. 20  $\mu\text{L}$  of bacteria or virus suspension (identified during preliminary tests as an adequate volume to detect the bacteria/virus after reconstitution) were aerosolized on top of 1.2-cm radius samples for 30 sec and incubated at ambient condition for 3, 5, 15, 30 or 60 min. To reconstitute the bacteria/virus, the samples were soaked in PBS and vortexed, and any remaining bacteria/virus trapped in the filters was collected by centrifuging the samples (6,000 rpm, room temperature, 1 min) in a new tube. To remove salt/surfactant dissolved from the samples, the recovered bacteria/virus was centrifuged at 14,800 rpm and 4 °C for 15 min and resuspended in fresh PBS. Structural stability of bacteria and virus was analyzed by transmission electron microscopy (TEM); remaining activity of virus was characterized by measuring hemagglutinin activity (HA) with chicken red blood cells and virus titers on confluent MDCK monolayers. The plaque forming units (PFU) were divided by the amount of virus used to infect the cells (determined as protein concentration measured by BCA assay with BSA standard). The HA titer and PFU measurements were expressed as relative to the measurements at 0 min incubation on the filters.

To analyze the time-dependent inactivation on the salt-coated filters prepared with vacuum process, bacteria were exposed to the bare membranes and  $\text{NaCl}_{15\text{inHg}}$ . To study the effect of particle size and composition, aerosols and droplets were generated from both DI water and artificial saliva (0.6 g/L  $\text{Na}_2\text{HPO}_4$ , 0.6 g/L anhydrous  $\text{CaCl}_2$ , 0.4 g/L  $\text{KCl}$ , 0.4 g/L  $\text{NaCl}$ , 4 g/L mucin and 4 g/L urea in deionized water, pH 7.2) bacteria suspensions. *K. pneumoniae* was

cultured and washed as described above, and resuspended in DI water or artificial saliva to 550  $\mu\text{g}/\text{mL}$  (protein concentration measured by BCA assay;  $\text{OD}_{600}$  of 10-fold dilution = 1.25). For aerosol tests, 20  $\mu\text{L}$  of bacteria DI water or artificial saliva suspension were aerosolized on top of 1.7-cm radius samples for 30 sec. For droplet tests, 5- $\mu\text{L}$  droplets of bacteria DI water or artificial saliva suspension were added on top of four different locations of each 0.5-cm radius sample (total volume = 20  $\mu\text{L}$ ). The bacteria aerosols/droplets were incubated on the samples at ambient condition for 5, 10 and 30 min. The bacteria were reconstituted from the samples as described above. Stability of bacteria was analyzed by CFU measurements, conducted as described above.

To test the effect of osmotic pressure during the experimental procedure, the filters ( $\text{NaCl}_{600}$ ,  $\text{K}_2\text{SO}_4_{600}$ ,  $\text{KCl}_{600}$ ) and bare membranes as a control were dissolved in PBS in a 15-mL tube. Each time, the virus suspension (20  $\mu\text{L}$ ) was aerosolized into the tube for 30 sec, followed by 1-min aerosolization of DI water and vortex. The virus was incubated in the dissolved filter solutions for 60 min, and then centrifuged (14,800 rpm, 15 min, 4  $^{\circ}\text{C}$ ) to stop the incubation and resuspend in fresh PBS. HA and virus titers were conducted as described above.

Dynamic viscosity of artificial saliva and DI water used for pathogen suspensions were determined using a rotational rheometer (Discovery HR-3; TA Instruments, New Castle, DE, USA). Rheology experiments were performed in a parallel plate (diameter = 40 mm, gap = 56  $\mu\text{m}$ ), where artificial saliva or DI water was filled at 22  $^{\circ}\text{C}$ . Shear rate of 0–400  $\text{s}^{-1}$  and measurement time of 300 s were used to test the apparent viscosity of the sample as a function of shear rate. To consider the condition of human saliva, the viscosity was determined at shear rates between 10 and 200  $\text{s}^{-1}$ , which is generally considered as the condition due to the chewing and speaking action of the mouth.

#### 4.2.6 X-ray diffraction (XRD) analysis

To monitor the formation of crystalline NaCl, K<sub>2</sub>SO<sub>4</sub> and KCl over time during aerosol drying, filters (NaCl<sub>600</sub>, K<sub>2</sub>SO<sub>4</sub><sub>600</sub>, KCl<sub>600</sub>; sample size = 2.5 × 2.5 cm) and powders were mounted on glass slides for XRD analysis (Bruker D8 Discover; Billerica, MA, USA); bare membranes were analyzed as controls. XRD spectra were obtained in  $\theta$ -2 $\theta$  mode using a CuK $\alpha$  radiation before and right after DI water aerosol exposure (20  $\mu$ L), and at 5, 15 and 30 min. The aerosol exposure process was set-up to render the time to load the samples and start the XRD measurements negligible; the XRD scan time was 3 min. Miller indices corresponding to NaCl, K<sub>2</sub>SO<sub>4</sub> and KCl crystals, respectively, were identified based on the standard spectra in JCPDS cards and a reference [307].

#### 4.2.7 Microscopy analysis

To characterize the morphological changes due to salt recrystallization, NaCl, K<sub>2</sub>SO<sub>4</sub> and KCl powders were monitored over time during aerosol drying under an optical microscope (Omax G223A-CA; Kent, WA, USA). The powders (300 mg) were each uniformly deposited in a well of a 12-well plate. Images (Moticam; Motic, Hong Kong) were obtained before DI water aerosol exposure (20  $\mu$ L), and at 3, 5, 15, 30 and 60 min after exposure. The morphological changes of the salts were further analyzed by scanning electron microscopy (SEM; Hitachi S-3000N; Hitachi, Toronto, Canada) in a secondary electron mode at 20 kV before and after aerosol exposure. The size of the salt powders was obtained from SEM images with ImageJ. To observe the morphology of the crystalline NaCl, K<sub>2</sub>SO<sub>4</sub> and KCl coatings on the filters, the samples were analyzed by SEM and energy dispersive X-ray (EDX; Oxford Instruments detector; Concord, MA, USA). The powder and filter samples were coated with a 10-nm layer of gold; after aerosol exposure, the powder samples were completely dried before applying the gold

coating.

Transmission electron microscopy (TEM) analysis of bacteria/virus reconstituted during the stability tests was carried out at 200 kV (JEOL JEM 2100; JEOL, Peabody, MA, USA) on bacteria/virus samples deposited on copper grids (Electron Microscopy Sciences, Hatfield, PA, USA). Negative staining of the samples with tungsten was applied with a solution of 1.5 w/v% phosphotungstic acid hydrate with pH 7.0 (Sigma Aldrich).

#### **4.2.8 Statistical analysis**

The statistical analysis was performed by Regression Analysis, student's t-test, one-way ANOVA and General Linear Model with Minitab (Minitab, State College, PA). The significance was considered by P value; P value of less than 0.05 was considered significant.

### **4.3 Results and discussion**

#### **4.3.1 Characterization of the salt powder recrystallization**

To study the effect of the interaction with salt crystals as a sole factor on the pathogen inactivation mechanism, the salt-based pathogen inactivation was investigated by directly exposing aerosols to NaCl, K<sub>2</sub>SO<sub>4</sub> and KCl salt powders (see Figure 4.1 for particle-size distributions). To this end, XRD was used to study the recrystallization of NaCl, K<sub>2</sub>SO<sub>4</sub> and KCl powders over time, by obtaining XRD spectra at different time points following exposure to DI water aerosol (see Figure 4.2 for XRD spectra; i: 2θ range of 20–60°, ii: zoomed-in XRD peaks). For the NaCl powder (Figure 4.2a), it was noted that the (220) peak intensity decreased right after exposure to aerosols. On the other hand, the intensity of the (200) peak showed a rapid increase right after aerosol exposure; within 5 min, the (200) peak intensity further increases.

This indicates the aerosols preferentially dissolved (220) planes, followed by the evaporation-induced recrystallization of the NaCl crystals with a change of their preferred orientation plane to (200). It should be noted that 3 minutes were needed to obtain a full XRD spectrum. As such, the XRD spectrum right after aerosol exposure (0 min in the graph) represents the microstructural change of the sample that occurred during incubation for 3 min including the scan time. This clearly indicates that salt recrystallization starts to occur in the first 3 min following aerosol exposure at ambient conditions (scan time of the 0-min spectrum), and is complete within 5 min. In the case of the K<sub>2</sub>SO<sub>4</sub> powder, the (200), (130), (031) and (312) peaks exhibited a significant decrease in their intensities or disappeared from the XRD patterns right after aerosol exposure (see Figure 4.2b). At 5 min, the (211), (002) and (331) peak intensities started to increase and a new (330) peak was observed. The variation of XRD peaks upon exposure to aerosols as opposed to before aerosol exposure can be explained by the microstructural changes of the K<sub>2</sub>SO<sub>4</sub> powders due to salt recrystallization. Figure 4.2c shows the XRD spectra for the KCl powder before and after aerosol exposure. As can be seen from the time-dependent intensity variation, the intensity of the (200) peak decreased and the (400) peak disappeared right after exposure to aerosols, in contrast to the intensity increase of the (220) peak. Similar to NaCl, this indicates the recrystallization for the KCl powder proceeded within 5 min (i.e., in about 3 min considering the scan time). Thus, time-dependent peak change of characteristic XRD peaks of NaCl, K<sub>2</sub>SO<sub>4</sub> and KCl clearly demonstrates the recrystallization of the salts after exposure to aerosols. It is also evident that the recrystallization of the NaCl and KCl powders initiated before 5 min, and the K<sub>2</sub>SO<sub>4</sub> powder started to recrystallize after 5 min under our experimental conditions.

While the structural change of salts at nano- and macro-scale can be detected by XRD analysis, the gross and microscopic surface morphology of the salts was monitored by using

optical and scanning electron microscopy, respectively (see Figure 4.3 for optical microscope images and Figure 4.4 for SEM images). At 3 min, the surface of the salt powders remained wet due to aerosol-induced dissolution. However, the roughness of the salt powder surface was observed to be higher at 3 min compared to the salts before aerosol exposure in the case of NaCl and KCl, indicating early-stage salt recrystallization. At 5 min, NaCl and KCl salts exhibited active crystallization as supported by the observation of a significant increase in surface roughness, formation of aggregates of salt crystals, and sharp edges. On the other hand, formation of regular, geometric crystals and aggregates for  $K_2SO_4$  was observed at 15 min.

The effect of DI water aerosol exposure followed by recrystallization on morphological characteristics of the salts was further verified by SEM. As shown in Figure 4.4, the SEM images show the formation of sharp edges and agglomeration on the NaCl and KCl powders after aerosol exposure (compare L and R in Figure 4.4a and 4.4c); the  $K_2SO_4$  powder exhibited a transformation from randomly shaped crystals (before aerosol exposure, see Figure 4.4b-L) to regular, geometric crystals (after aerosol exposure, see Figure 4.4b-R). The morphological changes of the salt powders were associated with salt recrystallization over time, as evidenced by the formation of small crystals on the surface of salt powders (Figure 4.4a (i,ii)-R), and bridging and agglomeration of salt powders (Figure 4.4a and 4.4c (i,ii)-R).

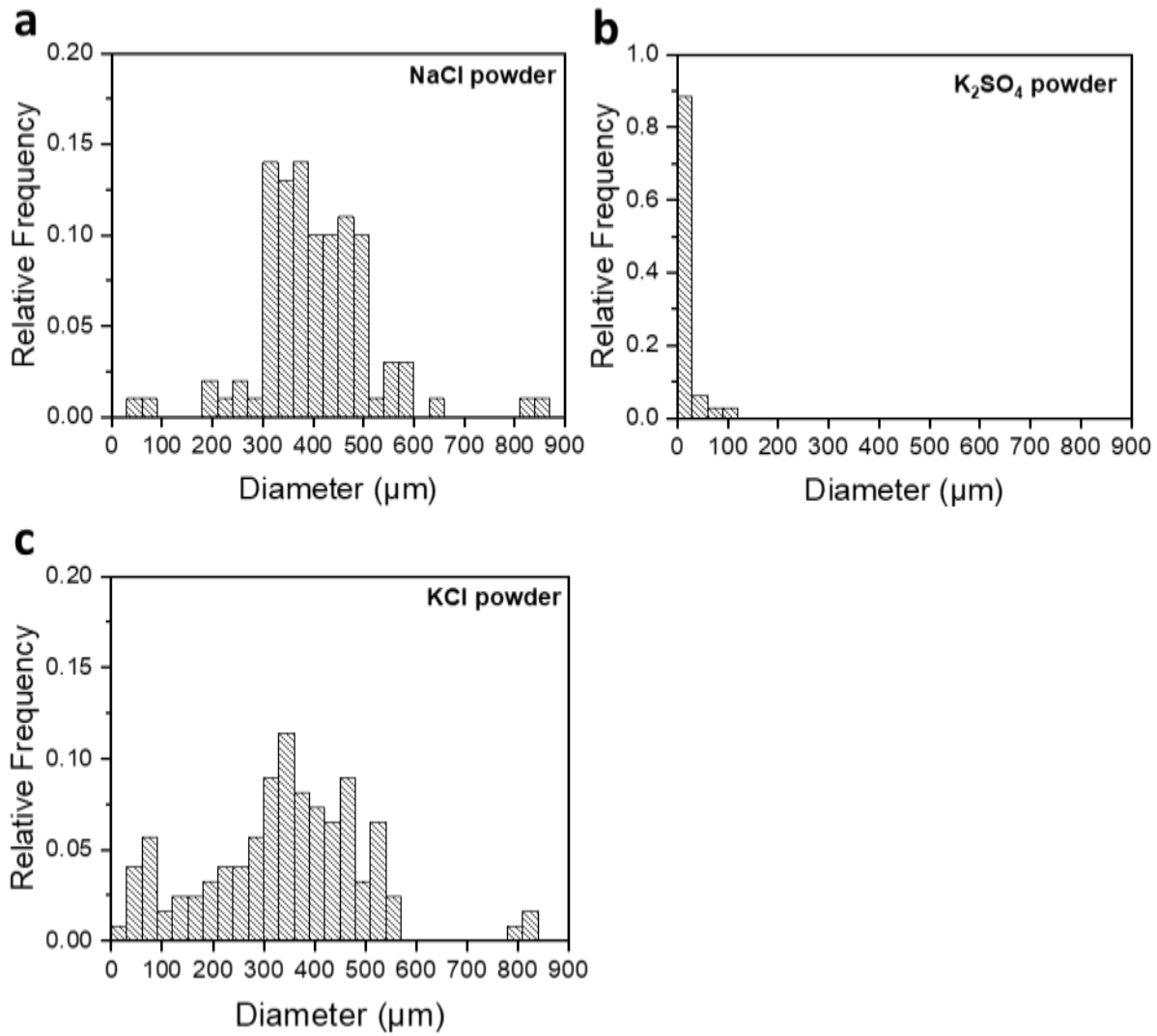


**Figure 4.1.** Salt powder size. Histogram of NaCl (a), K<sub>2</sub>SO<sub>4</sub> (b), and KCl (c) powder size ( $n = 100$  for (a),  $n = 181$  for (b),  $n = 123$  for (c)).

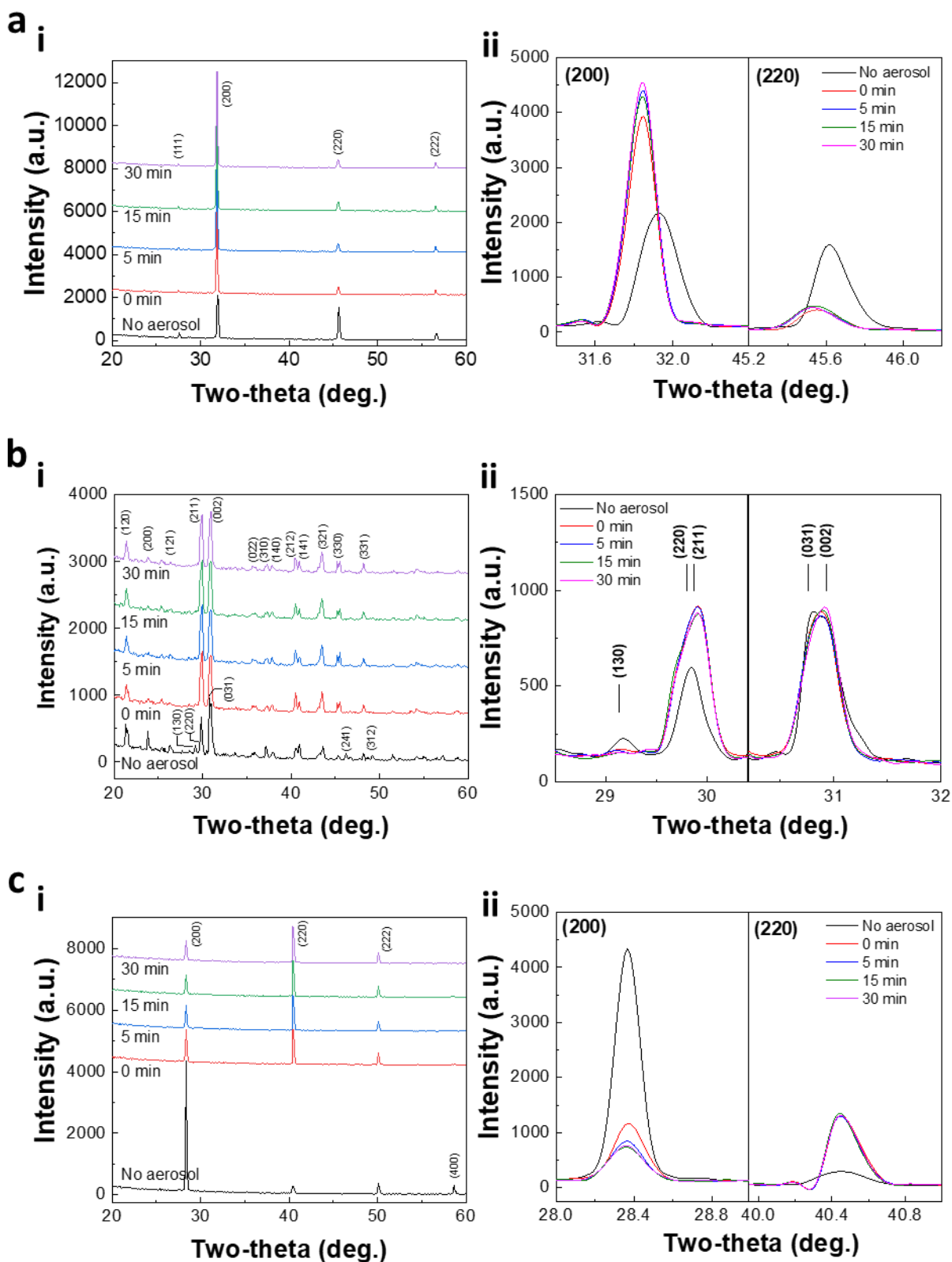


**Figure 4.2.** Characterization of the salt powder recrystallization. (a–c) Relevant XRD peaks of NaCl (a),  $K_2SO_4$  (b), and KCl (c) powders before aerosol exposure (No aerosol), right after aerosol exposure (0 min), and at 5, 15 and 30 min. Miller indices of relevant peaks corresponding to NaCl,  $K_2SO_4$  and KCl crystals, respectively, are shown in each XRD spectrum for phase/plane identification (i: scanning range 20–60°, ii: zoomed-in XRD patterns after curve fitting). Inserted numbers are Miller indices. Scan time was set to 3 min per XRD spectrum acquisition at each

incubation time.

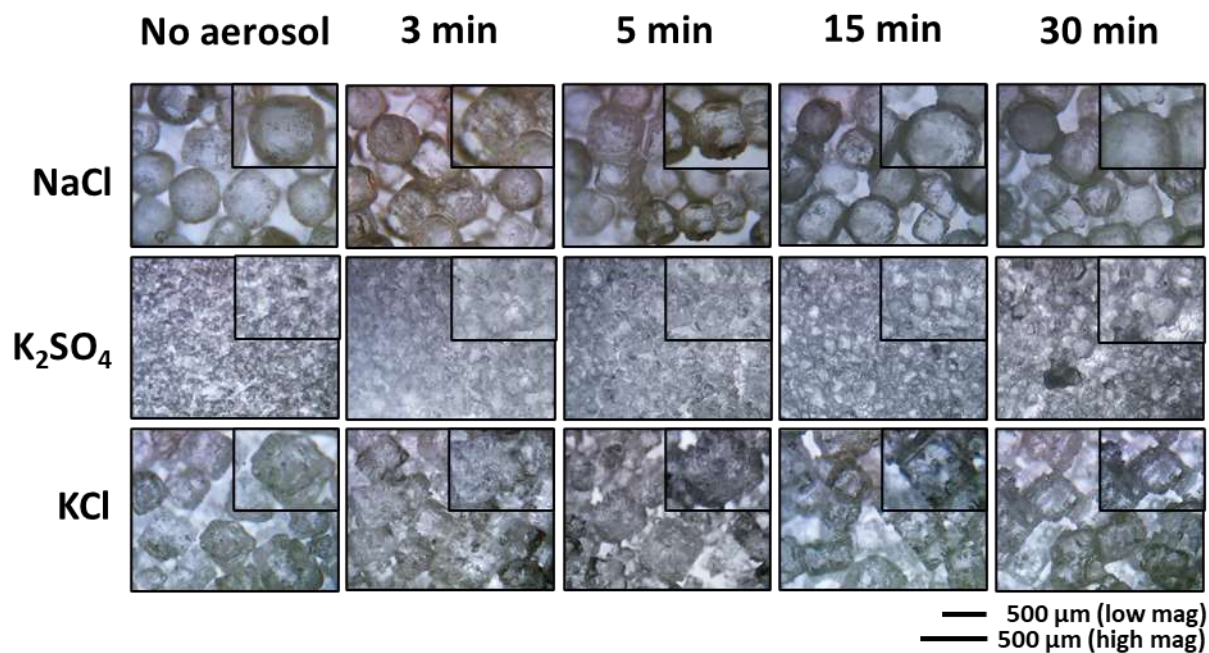


**Figure 4.3.** Morphological changes due to salt powder recrystallization. Optical microscope images of NaCl (top), K<sub>2</sub>SO<sub>4</sub> (middle) and KCl (bottom) before aerosol exposure (i.e., No aerosol), and at 3, 5, 15 and 30 min after exposure, showing the morphological changes during the evaporation-induced salt recrystallization.

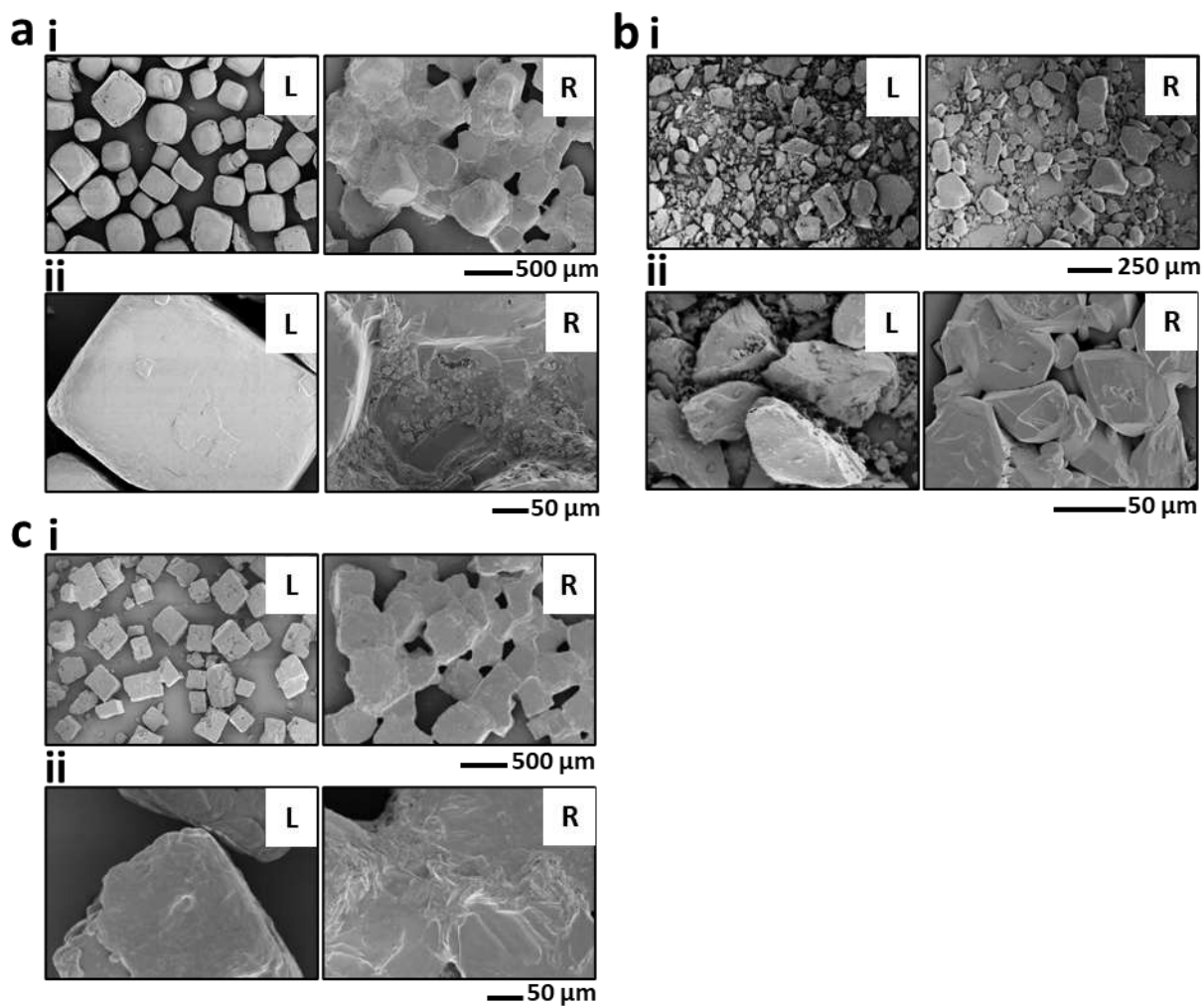


**Figure 4.4.** Morphological changes due salt powder recrystallization. (a-c) SEM images of NaCl (a), K<sub>2</sub>SO<sub>4</sub> (b), and KCl (c) before (L: left) and after (R: right; >60-min incubation) aerosol exposure ((i): low magnification, (ii): high magnification), showing the morphological changes due to the evaporation-induced salt recrystallization.

### 4.3.2 Pathogen inactivation on the salt powders

To investigate the pathogen inactivation mechanisms, *K. pneumoniae* and influenza virus A/Puerto Rico/8/34 (PR/34) were aerosolized and incubated on the salt powders. As shown in Figure 4.5a, all salt powders caused time-dependent inactivation of bacteria (General Linear Model,  $P < 0.001$ ). NaCl and KCl caused rapid CFU reduction within 5 min, and  $K_2SO_4$  caused drastic 4-log CFU reduction within 15 min (one-way ANOVA,  $P < 0.001$ ). From the TEM analysis, the bacteria incubated on the salt powders showed severe physical disruption, including structural damages, deformation and rupture (Figure 4.5b). The osmotic pressure due to the experimental procedure (i.e., dissolving the salts in PBS to recover the pathogens after incubation) appeared to have no effect on the bacteria viability (Figure 4.6). In parallel, the effect of different levels of osmotic pressure for each salt type was tested. As shown in Figure 4.7a, only the higher osmotic pressure levels of NaCl and KCl solutions (~ saturated conditions) exhibited a minor effect on bacteria viability, only up to 1-log CFU reduction (General Linear Model,  $P < 0.001$  for NaCl 26, 29 w/v% and KCl 26 w/v%,  $P > 0.05$  for all other conditions). This was also confirmed by the TEM analysis, which showed no significant effect on the structural stability of the bacteria following incubation in the salt solutions at ~ saturated condition (Figure 4.7b).

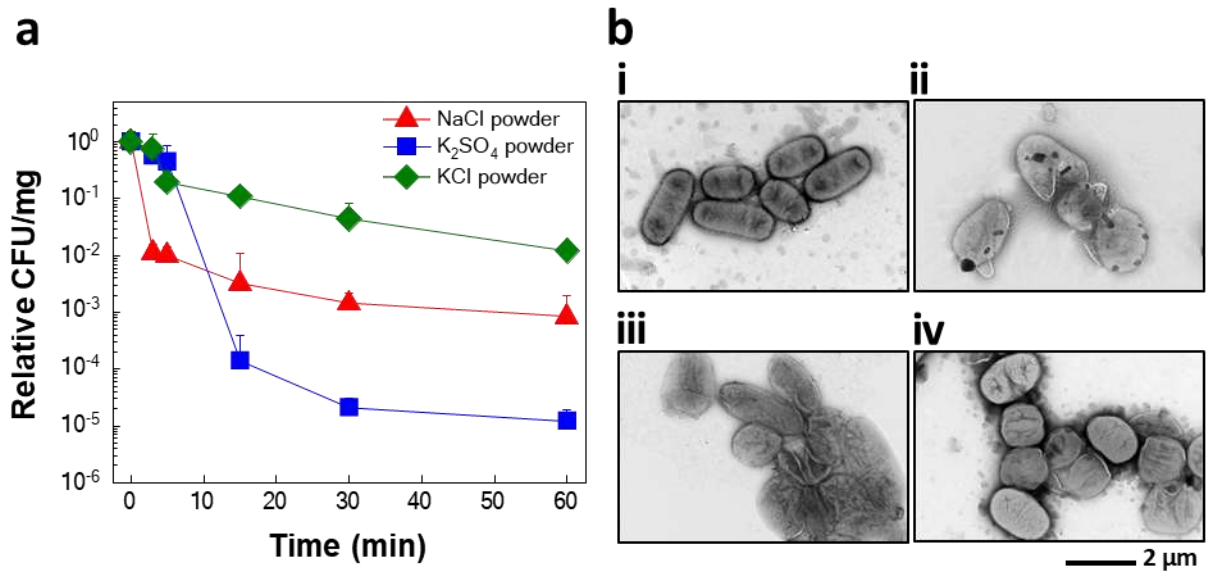


**Figure 4.5.** Pathogen inactivation on salt powders. (a) CFU change showing the effect of incubation time on *K. pneumoniae* exposed to NaCl, K<sub>2</sub>SO<sub>4</sub> and KCl powders (n = 4–20, mean ± SD). (b) TEM images of *K. pneumoniae* aerosolized control (i), and following incubation on NaCl (ii), K<sub>2</sub>SO<sub>4</sub> (iii) and KCl (iv) powders for 30 min.

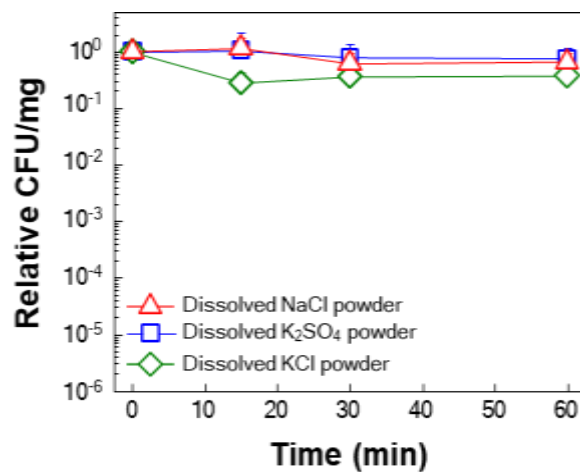


**Figure 4.6.** Bacteria incubation in dissolved salt powders. CFU change showing the effect of incubation time on *K. pneumoniae* exposed to dissolved salt powders during the experiments (n = 4–20, mean ± SD).

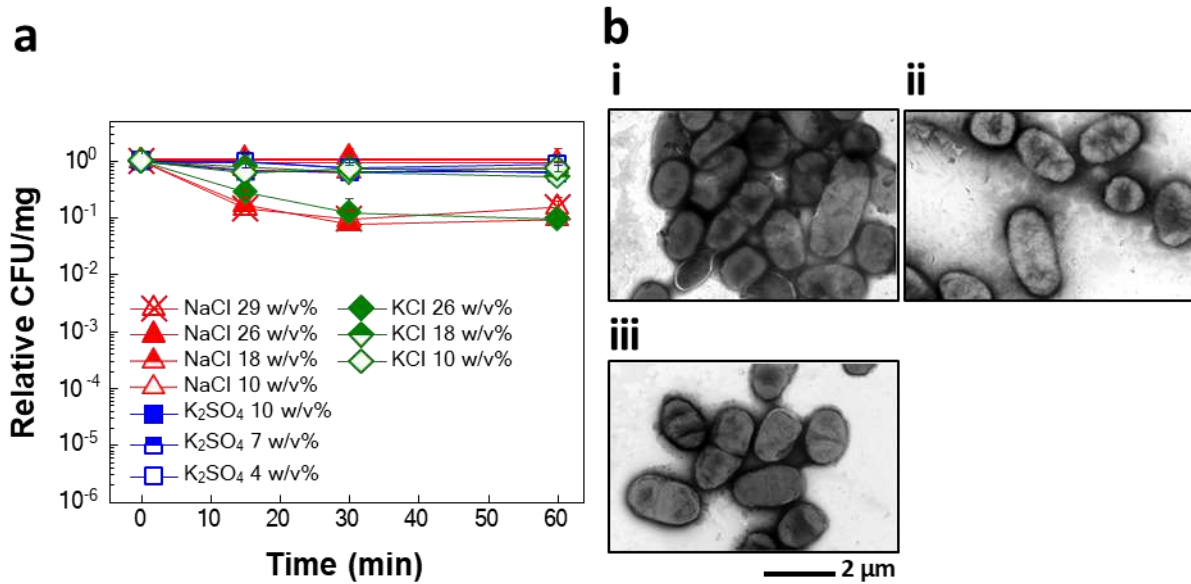


**Figure 4.7.** Effect of osmotic pressure on pathogens. (a) CFU change showing the effect of incubation time on *K. pneumoniae* exposed to NaCl, K<sub>2</sub>SO<sub>4</sub>, and KCl solutions at varying osmotic pressure levels (n = 3–30, mean ± SD) (b) TEM images of *K. pneumoniae* following incubation in NaCl 29 w/v % (i), K<sub>2</sub>SO<sub>4</sub> 10 w/v % (ii), and KCl 26 w/v % (iii) solutions for 30 min.

Similarly, PR/34 influenza virus showed a time-dependent, dramatic HA activity loss on all salt powders (one-way ANOVA,  $P < 0.001$ ) (Figure 4.8a). NaCl and KCl caused more rapid HA activity reduction than  $K_2SO_4$  within 5 min (one-way ANOVA,  $P < 0.001$ ). From the TEM analysis, the virus incubated on the salt powders showed complete destruction within 30 min (Figure 4.8b). As influenza is an enveloped virus, osmotic pressure might have a destabilizing effect on the proteins/virus [308-310]. Following virus exposure to the salt solutions close to saturation concentration, NaCl and KCl solutions displayed an HA activity decrease to  $72.5 \pm 18.5\%$  and  $80.8 \pm 65.8\%$ , respectively, after 5-min incubation (NaCl: one-way ANOVA,  $P < 0.001$ , KCl: one-way ANOVA,  $P < 0.05$ ) (Figure 4.8c). Compared to NaCl and KCl solutions, no significant level of HA activity decrease was observed from  $K_2SO_4$  within 5 min (remaining HA activity:  $95.4 \pm 8.8\%$ ; one-way ANOVA,  $P > 0.05$ ). Even after 30 min at high osmotic pressure conditions, which is a longer incubation time than what the pathogens experience at this condition during aerosol evaporation, the remaining HA activity was  $70.1 \pm 24.9\%$ ,  $86.2 \pm 12.6\%$  and  $65.8 \pm 15.0\%$  in NaCl,  $K_2SO_4$  and KCl solutions, respectively. This indicates that the exposure of the virus to highly concentrated saline solution has limited destabilizing effects on the PR/34 influenza virus.

Incubation in 29 w/v% NaCl solution showed to cause aggregation of PR/34 virus, as seen in the TEM images (Figure 4.9a). Aggregation and/or fusion are presumed to be induced by ions, leading to a change of viral surface charges [311]. Although the ions seem to affect the morphology of the virus and could partially cause a decrease in HA activity titers, the virus particles were not significantly affected or damaged by osmotic pressure. This is further confirmed by no change in HA activity after 30 min for PR/34 in sucrose solution close to saturation concentration (Figure 4.9b), which has a purely osmotic pressure effect with no ionic effect. While osmotic pressure-induced HA activity reduction was not observed in this work, it

should be emphasized that only 10-20% HA activity loss has been reported for PR/34 under hyperosmotic condition [309]. As such, it is reasonable to presume that hyperosmotic pressure does not play a significant role in destabilization of pathogens during recrystallization process. The observed stability of *K. pneumoniae* and influenza virus against hyperosmotic stress might be explained by the presence of a rigid cell wall and a shell of matrix protein supporting the lipid bilayer, respectively. Therefore, it was concluded that the salt recrystallization process is mainly responsible for pathogen inactivation, although high salt concentration during aerosol drying caused minor cell viability loss and virus destabilization.

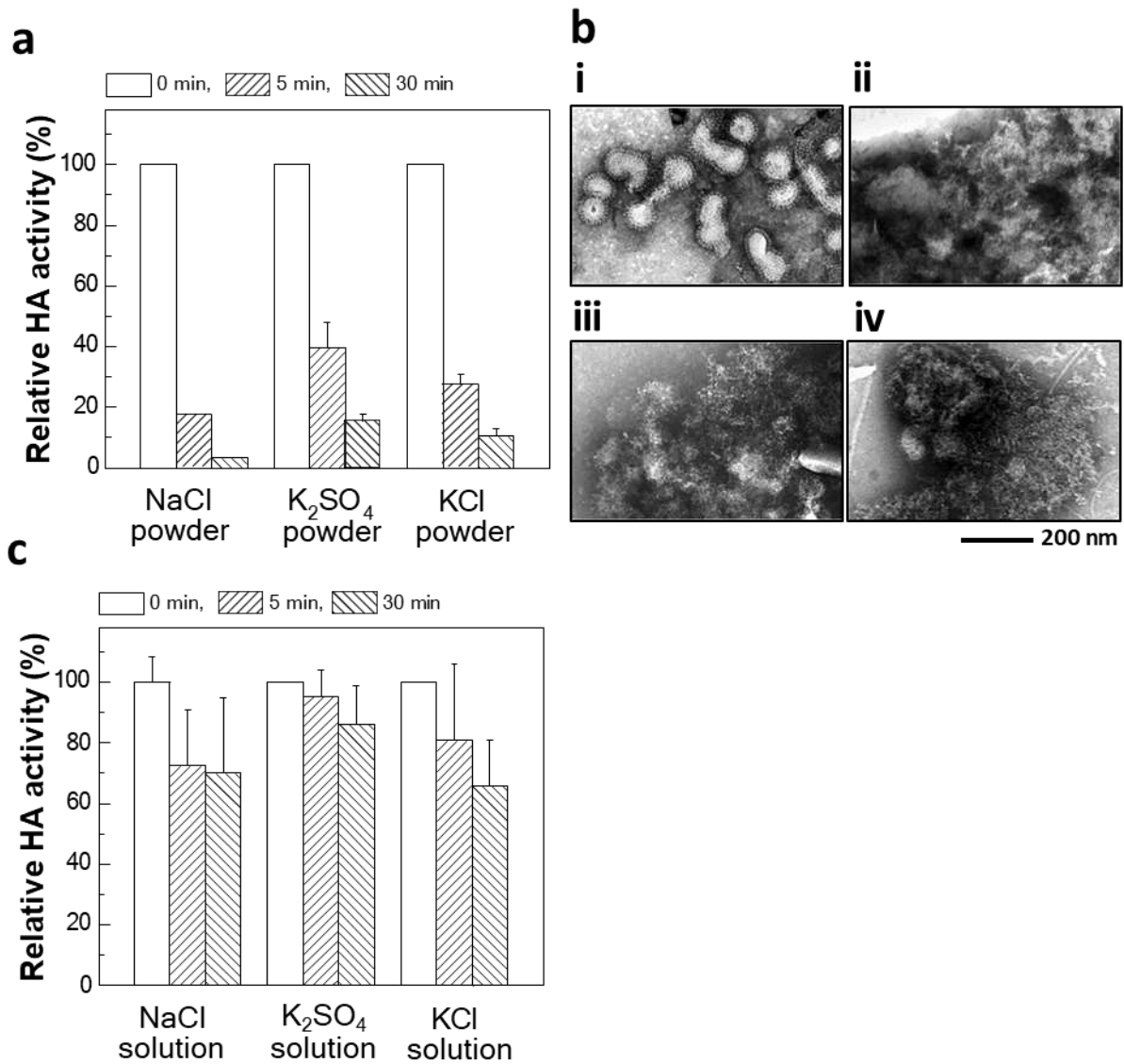


**Figure 4.8.** Effect of osmotic pressure on pathogens. (a) HA titer showing the effect of incubation time on the PR/34 virus exposed to NaCl, K<sub>2</sub>SO<sub>4</sub>, and KCl powders (n = 8, mean ± SD). (b) TEM images of the PR/34 virus control (i) and following incubation on NaCl (ii), K<sub>2</sub>SO<sub>4</sub> (iii), and KCl (iv) powders for 30 min. (c) HA titer showing the effect of incubation time on the PR/34 virus exposed to NaCl 29 w/v %, K<sub>2</sub>SO<sub>4</sub> 10 w/v %, and KCl 26 w/v % solutions (n = 12–13, mean ± SD)

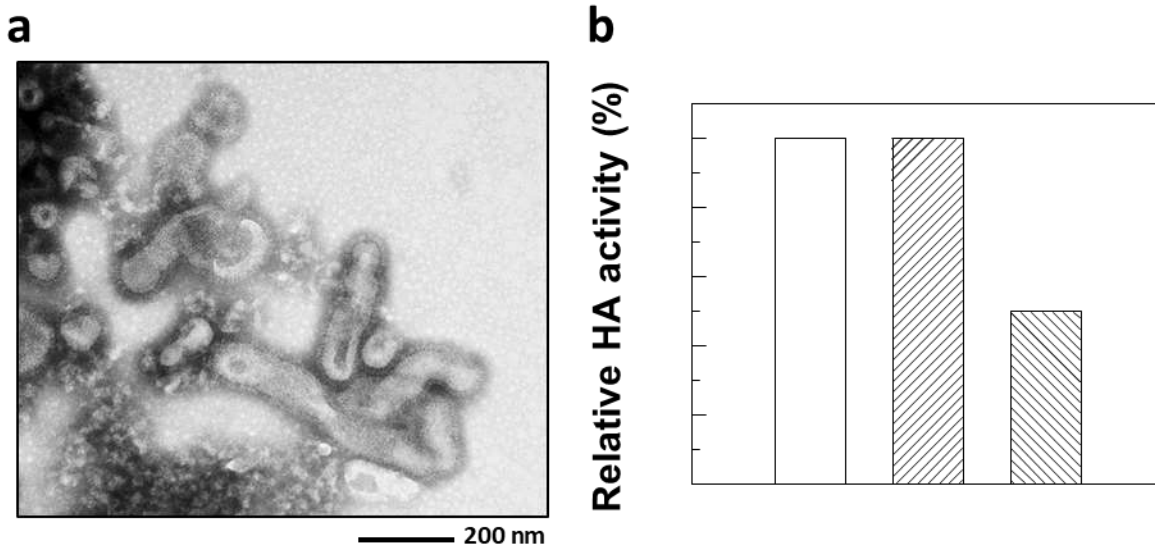


**Figure 4.9.** Effect of osmotic pressure on pathogens. (a) TEM images of PR/34 virus following incubation in NaCl 29 w/v% solution for 30 min. (b) HA titer showing the effect of incubation time on PR/34 virus exposed to sucrose 200 w/v% solution (n = 8, mean  $\pm$  SD).

The different pathogen inactivation kinetics on each salt type are in good agreement with the differences in recrystallization behaviors over time (where NaCl and KCl powders exhibit more rapid recrystallization as compared to K<sub>2</sub>SO<sub>4</sub>). This is explained by the crystallization kinetics of the salts. NaCl, K<sub>2</sub>SO<sub>4</sub> and KCl have similar constant crystal growth rates  $R_g$ , in the order of  $10^{-8}$ – $10^{-7}$  m/s [312-320]. Since nucleation time can be significant for drying salt aerosols (in the order of a few minutes) [321], differing nucleation kinetics are hypothesized to explain the different pathogen inactivation behaviors. Substances with higher molecular weight show a lower nucleation order  $n$  [322]. The molecular weights of NaCl, K<sub>2</sub>SO<sub>4</sub> and KCl are 58, 174 and 75 g/mol, respectively. Therefore:

$$n_{NaCl} > n_{KCl} \gg n_{K_2SO_4}$$

which matches the pathogen inactivation behavior well. In summary, NaCl and KCl exhibit quicker nucleation than K<sub>2</sub>SO<sub>4</sub>, leading to quicker overall crystallization and the earlier onset of pathogen inactivation with higher activity loss within 3–5 min. Within 5-15 min, K<sub>2</sub>SO<sub>4</sub> overall crystallization effectively causes pathogen inactivation at similar or higher levels than NaCl and KCl. Although the effects of the initial particle size and crystal shape on pathogen inactivation were not considered in this study, these analyses prove that salt recrystallization plays a critical role in rapid inactivation of bacteria and virus.

### **4.3.3 Characterization of the salt filter recrystallization**

After identification of the salt recrystallization as the major pathogen inactivation factor, we performed pathogen inactivation tests using salt-coated filters to verify our finding in the filter system. The surface of the polypropylene microfibers of three layers of large-pore membranes were coated with NaCl, K<sub>2</sub>SO<sub>4</sub> or KCl salts, which we previously reported to yield filters with high filtration and breathability performance [305].

The scanning electron microscopy (SEM) and energy dispersive X-ray (EDX) mapping showed the resulting homogeneous NaCl, K<sub>2</sub>SO<sub>4</sub> and KCl salt coatings on the surface of the fibers and throughout the cross section of the filters (see Figure 4.10 for EDX images and Figure 4.11 for SEM images). As shown in Figures 4.12 and 4.13, the recrystallization of bare membranes (control), and NaCl, K<sub>2</sub>SO<sub>4</sub> and KCl coated-filters after DI water aerosols exposure was monitored over time by XRD. For the NaCl coating (Figure 4.12a), the intensity of the (200) peak decreased right after aerosol exposure, as the aerosols dissolved the NaCl salt; within 5 min, the (200) peak intensity increased with time. The (220) peak intensity was similarly increasing at 5 min. For the K<sub>2</sub>SO<sub>4</sub> coating (Figure 4.12b), the intensity of the (022) peak decreased and the (141), (321), (213) and (060) peaks disappeared upon exposure to aerosols. On other hand, the (211) and (002) peaks grew in intensity after 5–15 min during the recrystallization process. For the KCl coating (Figure 4.12c), the intensity of the (200) peak decreased right after aerosol exposure, meanwhile within 5 min the intensity was increasing with time. The (220) peak increased in intensity right after aerosol exposure, and decreased within 5 min. Overall, similarly to the observations obtained for the salt powders, the XRD spectra indicate that the NaCl and KCl coatings start to recrystallize before 5 min, and the onset of the K<sub>2</sub>SO<sub>4</sub> coating recrystallization is within 15 min.

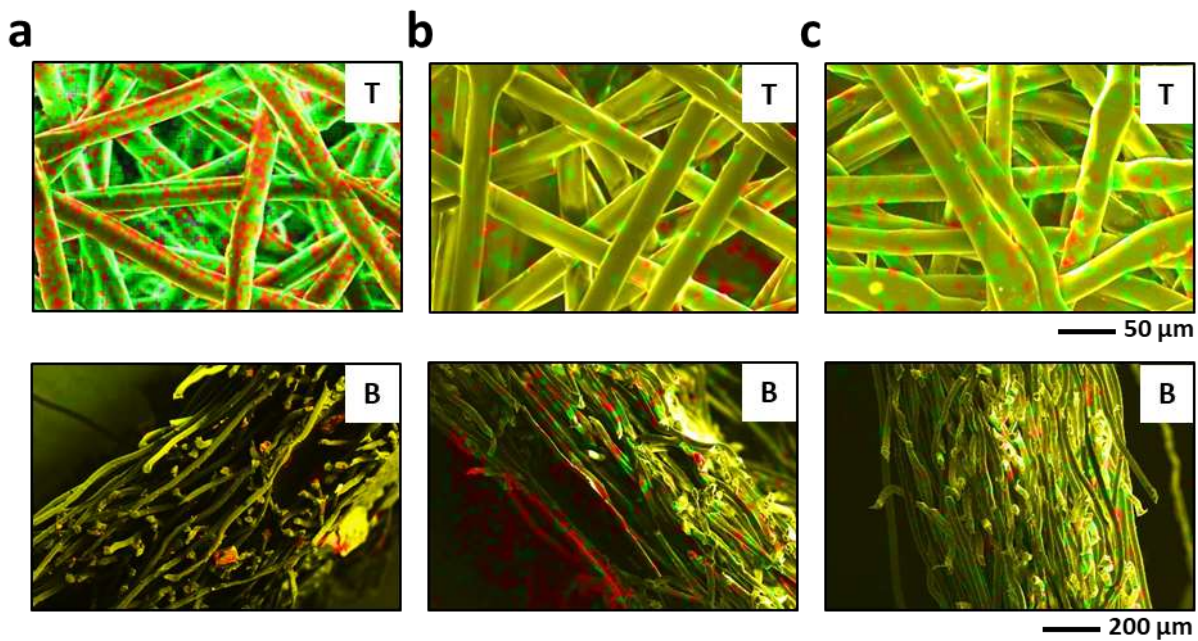


**Figure 4.10.** Characterization of salt-coated filters. Plan-view (T: top) and cross-sectional (B: bottom) EDX mapping images of salt-functionalized filters, showing the salt coating on the surface of the filter fibers. (a) NaCl filter (combination of Na (red) and Cl (green) mapping images), (b) K<sub>2</sub>SO<sub>4</sub> filter (combination of K (red) and S (green)), (c) KCl filter (combination of K (red) and Cl (green)).

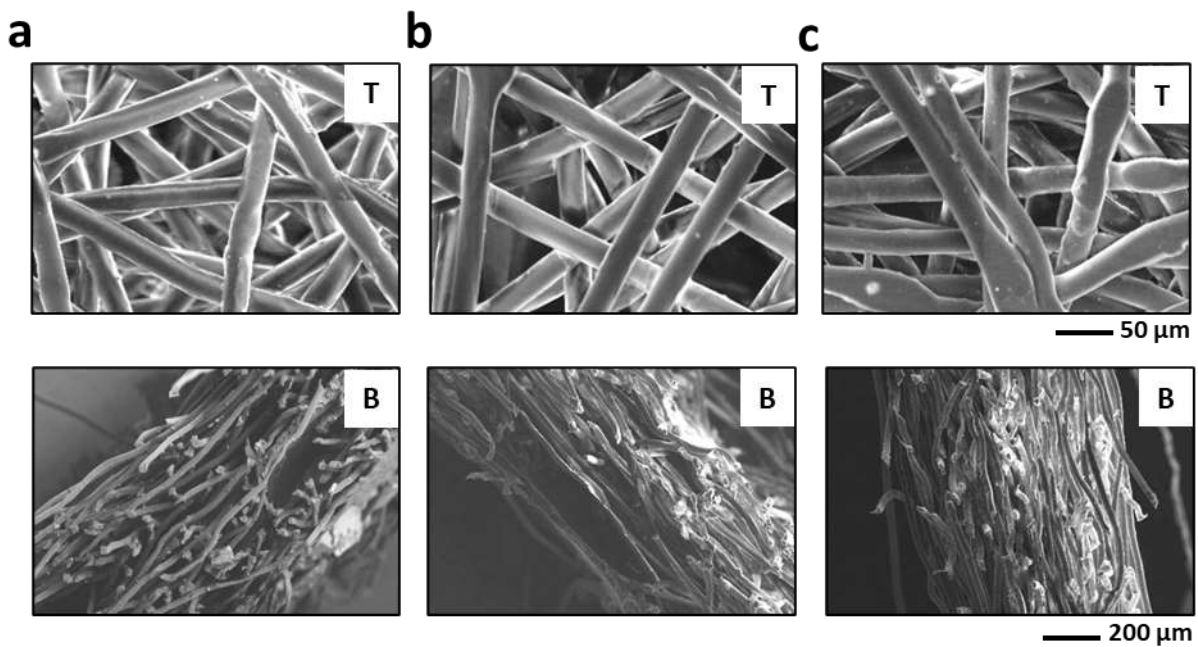


**Figure 4.11.** Plan-view (T: top) and cross-sectional (B: bottom) SEM images NaCl (a), K<sub>2</sub>SO<sub>4</sub> (b) and KCl (c) filters.

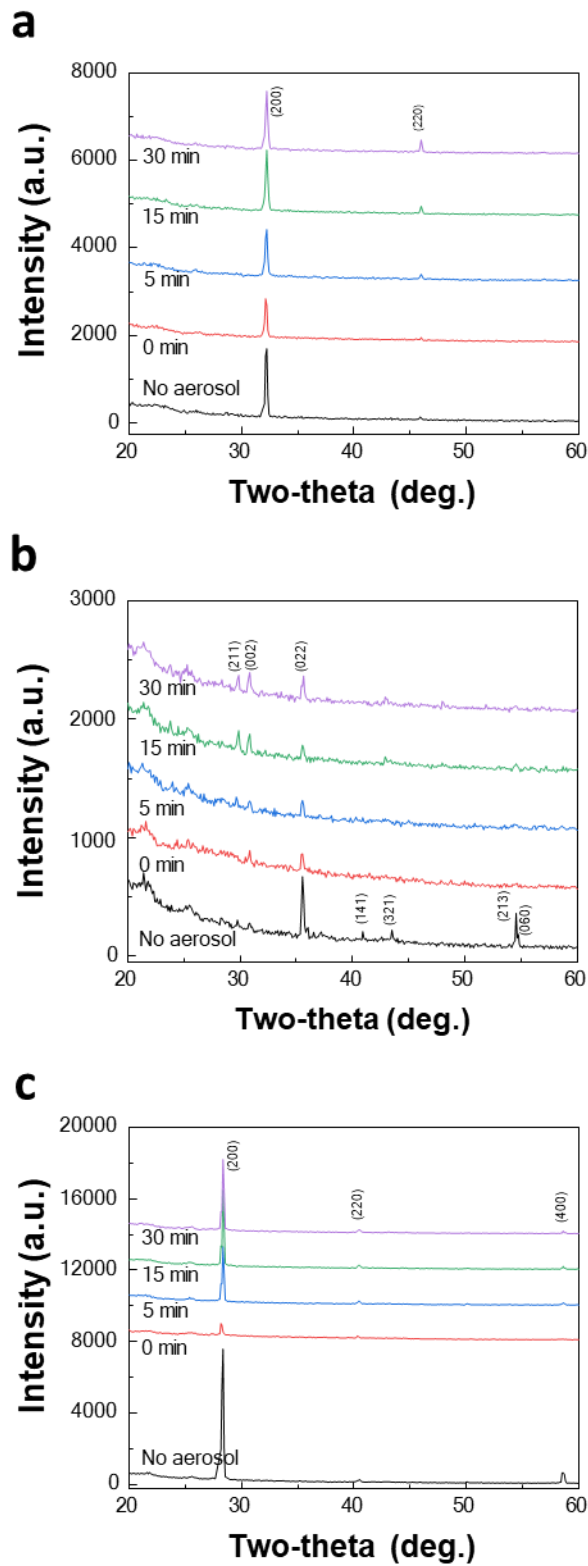


**Figure 4.12.** Characterization of the salt recrystallization on the salt-coated filters. (a-c) Relevant XRD peaks of NaCl600 (a), K<sub>2</sub>SO<sub>4</sub> 600 (b), and KCl600 (c) before aerosol exposure (No aerosol), right after aerosol exposure (0 min), and at 5, 15 and 30 min. Miller indices of relevant peaks corresponding to NaCl, K<sub>2</sub>SO<sub>4</sub> and KCl crystals, respectively, are shown in each XRD spectra for phase/plane identification. Scan time was set to 3 min per XRD spectrum acquisition at each incubation time.

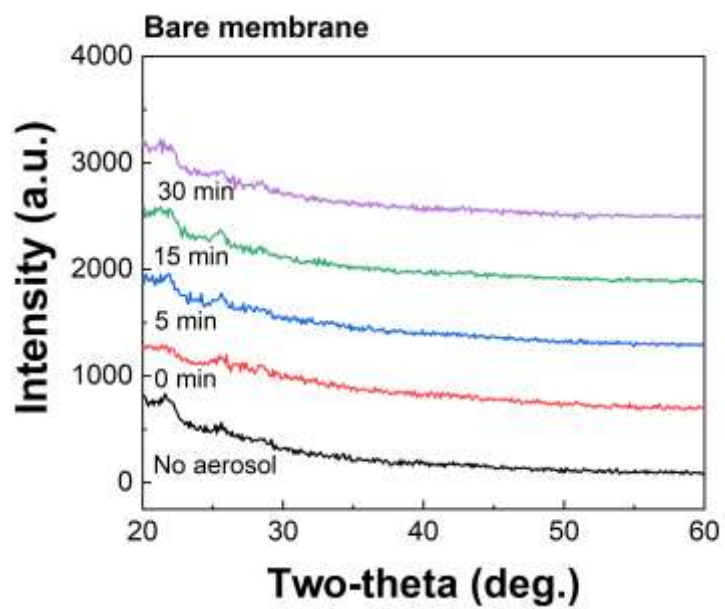


**Figure 4.13.** XRD spectra of bare membrane before aerosol exposure (No aerosol), right after aerosol exposure (0 min), and at 5, 15 and 30 min.

#### 4.3.4 Pathogen inactivation on the salt filters

We have previously reported that bacteria aerosolized on salt-coated filters quickly lost viability [305]. The TEM analysis showed that the bacteria recovered from the salt-coated filters were severely damaged, as opposed to the control exhibiting the intact structure of the bacteria (Figure 4.14a). Virus inactivation on NaCl, K<sub>2</sub>SO<sub>4</sub> and KCl coated filters was evaluated by exposure to aerosolized PR/34. Similar to bacteria, all salt filters exhibited inactivation capability. In particular, bare membranes showed no HA activity loss within 5 min, in contrast to >50% loss on NaCl and KCl filters; K<sub>2</sub>SO<sub>4</sub> filters caused a substantial HA activity loss of >70% within 15 min (Figure 4.14b). It is evident that the remaining HA activity of the virus recovered from the salt-coated filters exhibited a significant decrease with increases in incubation time (General Linear Model,  $P < 0.001$ ). Furthermore, the virus titer levels on all salt-coated filters were significantly lower compared to those of the bare membranes, and negligible within 30–60 min (one-way ANOVA,  $P < 0.001$ ) (Figure 4.14c). The TEM analysis confirmed the virus inactivation on the salt-coated filters, showing complete destruction of the virus following incubation on the filters (Figure 4.14d).

It was confirmed that the osmotic pressure due to the experimental procedure and the materials from the surface of the filters, including salt and surfactant (derived from immersing the filters in PBS to recover the pathogens after incubation), had almost no effect on the virus (Figure 4.15). After 60-min incubation, no change in the HA titer was detected (Figure 4.15a) and the virus titer level decreased by ~ 1 log (Figure 4.15b) (one-way ANOVA,  $P < 0.001$ ). Therefore, these results indicated that dramatic virus destabilization and infectivity loss on all salt-coated filters are mainly associated with salt recrystallization.

Notably, pathogen inactivation on the salt-coated filters was generally consistent with the pathogen inactivation patterns observed on the salt powders. Additionally, the XRD results

obtained from the salt-coated filters following aerosol exposure matched the time-dependent pathogen inactivation patterns, where NaCl and KCl coated filters caused pathogen inactivation initiation earlier than K<sub>2</sub>SO<sub>4</sub> filters. As such, it was concluded that salt recrystallization constitutes the main mechanism of virus inactivation observed on the filters, although high osmotic pressure generated during aerosol drying caused a minor decrease in pathogen activity.

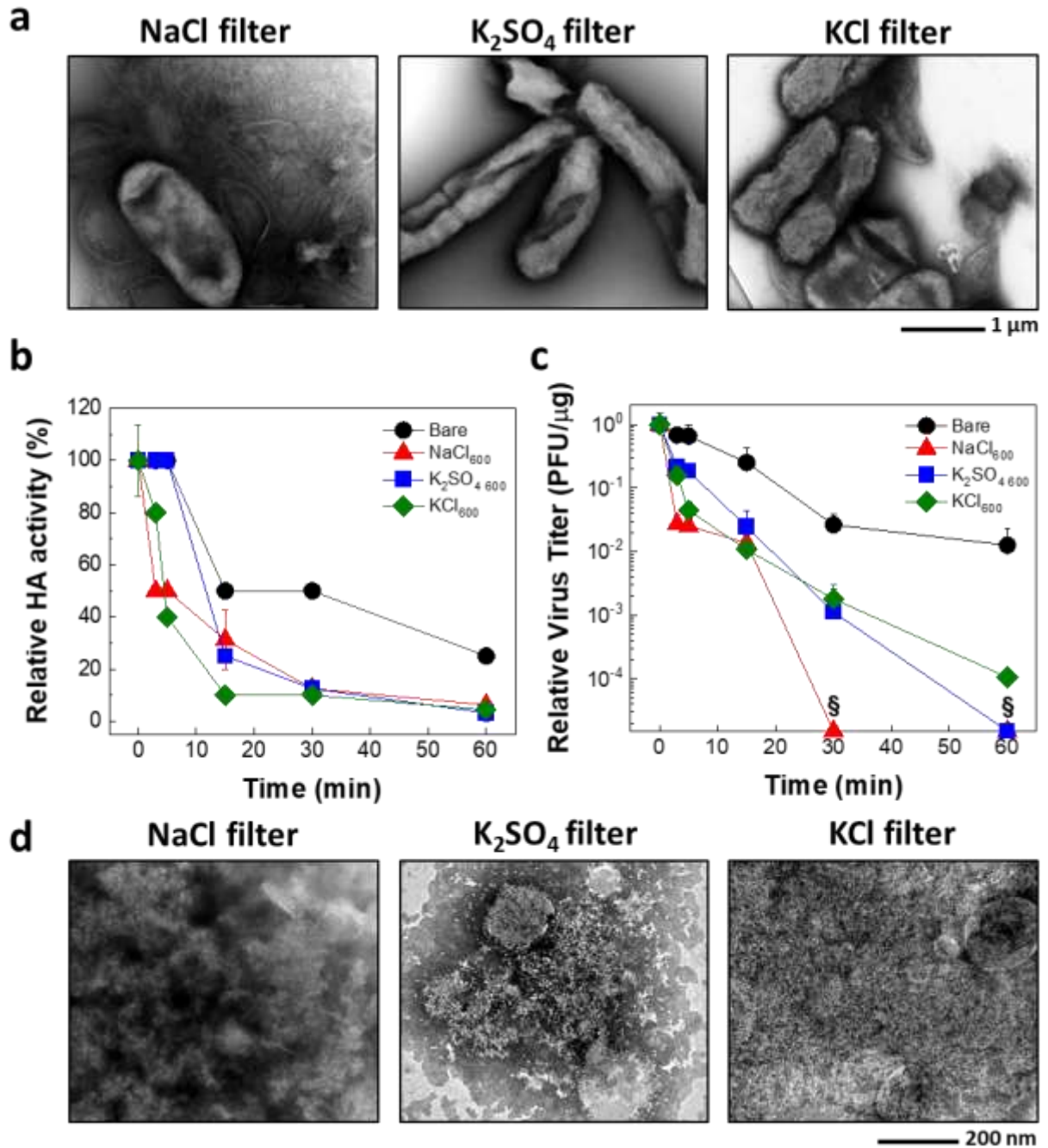


**Figure 4.14.** Pathogen inactivation on salt-coated filters. (a) TEM images of *K. pneumoniae* following 30-min incubation on NaCl, K<sub>2</sub>SO<sub>4</sub> and KCl filters. (b,c) Relative HA activity (b) and virus titer (c) showing the effect of incubation time on PR/34 virus exposed to Bare, NaCl<sub>600</sub>, K<sub>2</sub>SO<sub>4 600</sub> and KCl<sub>600</sub> (n = 8–53 for (a), n = 4–33 for (b), mean  $\pm$  SD). Relative: with respect to 0 min. §: below detection limit. (d) TEM images of PR/34 virus following 30-min incubation on NaCl<sub>600</sub>, K<sub>2</sub>SO<sub>4 600</sub> and KCl<sub>600</sub>.

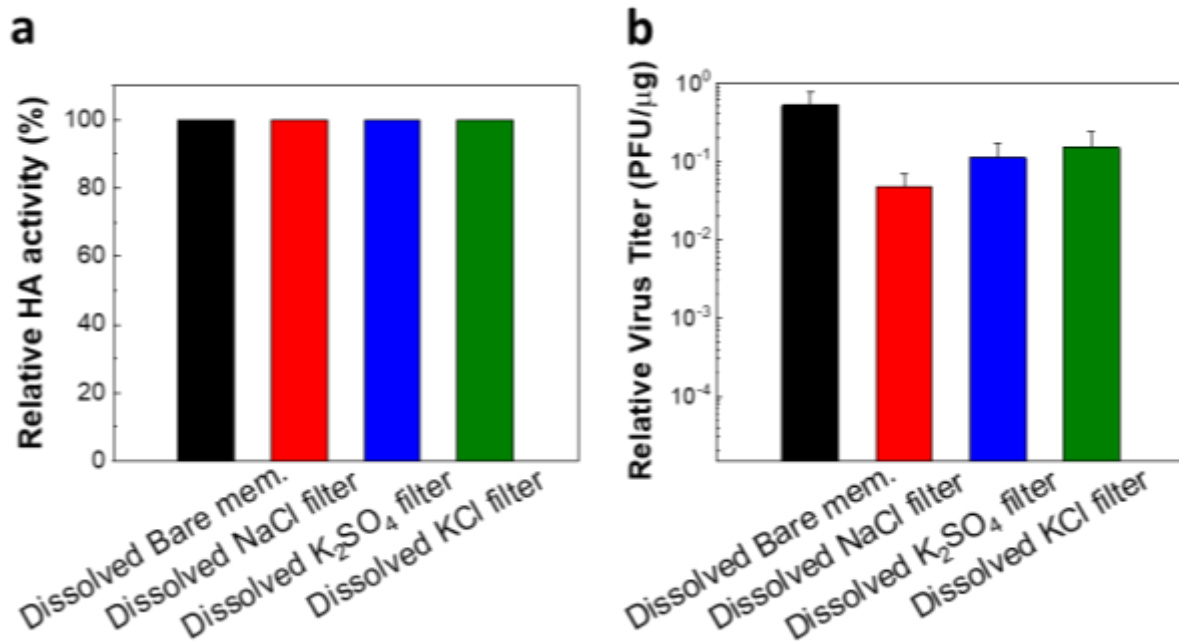


**Figure 4.15.** Virus incubation in dissolved salt-functionalized filters. HA titer (a) and virus titer (b) showing the effect of osmotic pressure on PR/34 virus exposed to dissolved Bare, NaCl600, K<sub>2</sub>SO<sub>4</sub> 600 and KCl600 for 60 min (n = 8–53 for (c), n = 5–33 for (d), mean ± SD). Relative: with respect to 0 min. Mem: membrane.

### 4.3.5 Effect of salt amount and coating process on the salt coating morphology

By varying the volume of coating solution in which the membranes are dried, the amount of salt coated on the filters per unit area can be controlled. The SEM images in Figures 4.16, 4.17 and 3.18 show the morphology of the salt coatings at different amounts of coated salt. At higher levels of salt amount, formation of large salt crystals was observed along the surface of the salt filters (Figures 4.16a and 4.17a); for filters prepared with  $>600 \mu\text{L}$  of coating solution, larger salt crystals were detected at the interfaces between stacked layers of pre-wet membranes (Figures 4.16b, 4.17b and 4.18). However, large salt crystals can provide a source of salt that can diffuse on the surface of the fibers when the salt partially dissolves upon exposure to humidity, due to the presence of surfactant.

To prevent the formation of large salt crystals, an alternative preparation process was investigated, where the membranes were pre-wet with the NaCl,  $\text{K}_2\text{SO}_4$  or KCl salt coating solution and exposed to varying levels of vacuum ( $V$ ) before drying. The obtained filters were coated with different amounts of salt ( $W_{\text{salt}}$ ); the linear relationship between  $W_{\text{salt}}$  and  $V$  is indicated in Figures 4.19 (Regression Analysis,  $P < 0.001$ ). From the SEM and EDX analysis, the fibers showed uniform coating with the salts (Figures 4.20 and 4.21). As can be seen from the SEM images, the salt aggregates decreased on the surface of the fibers and throughout the cross section with the increase in vacuum level. These results indicate that the use of a vacuum process during fabrication of the salt filters yields increased uniformity in the coating procedure with high quality control.

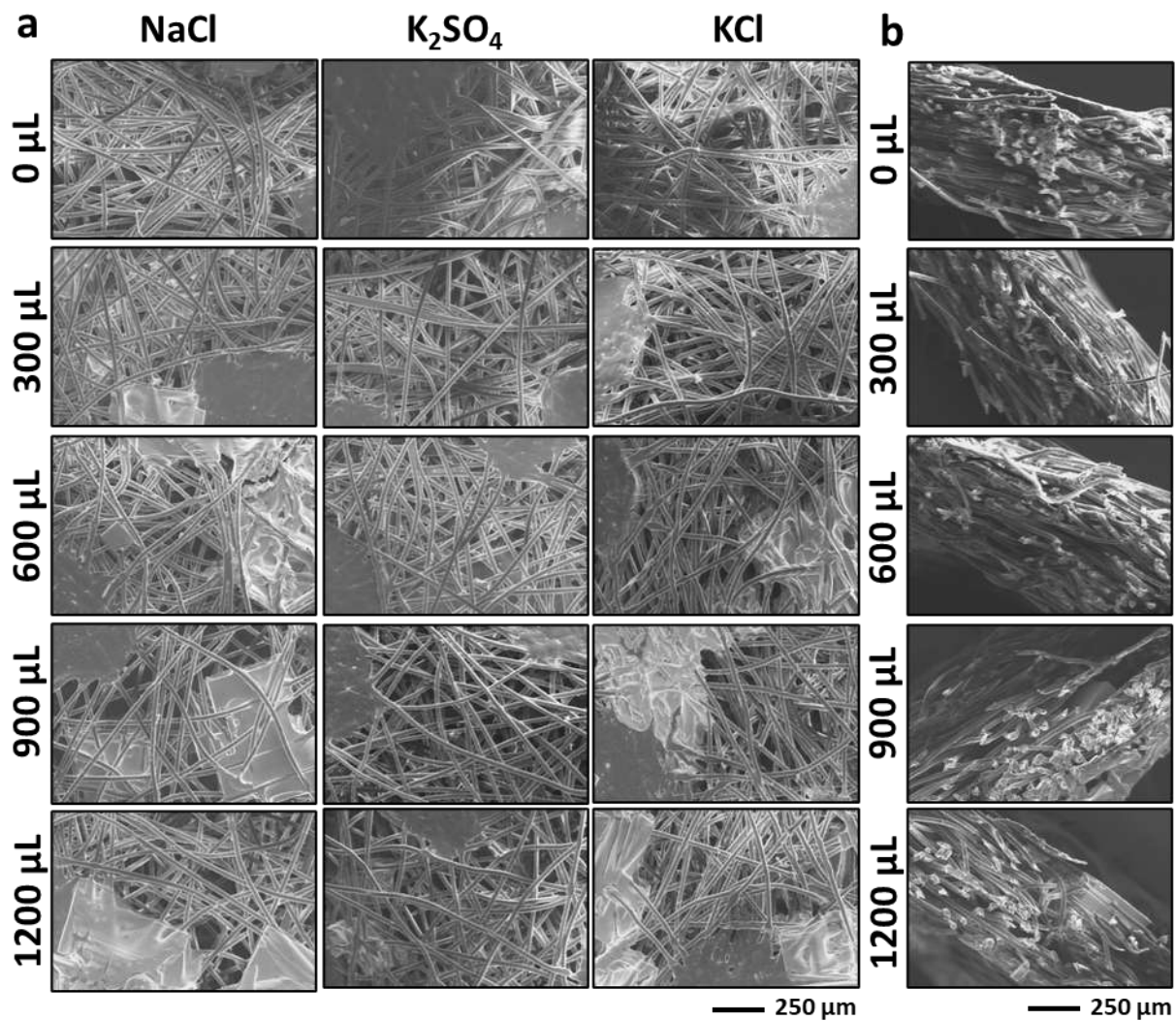


**Figure 4.16.** Characterization of filters prepared with different amounts of coated salt. (a) Plan-view SEM images of NaCl, K<sub>2</sub>SO<sub>4</sub> and KCl filters, showing the morphology of the salt coatings at different amounts of coated salt. (b) Cross-sectional SEM images of NaCl<sub>0</sub>, NaCl<sub>300</sub>, NaCl<sub>600</sub>, NaCl<sub>900</sub> and NaCl<sub>1200</sub>, showing the morphology of the salt coatings at different amounts of coated salt.

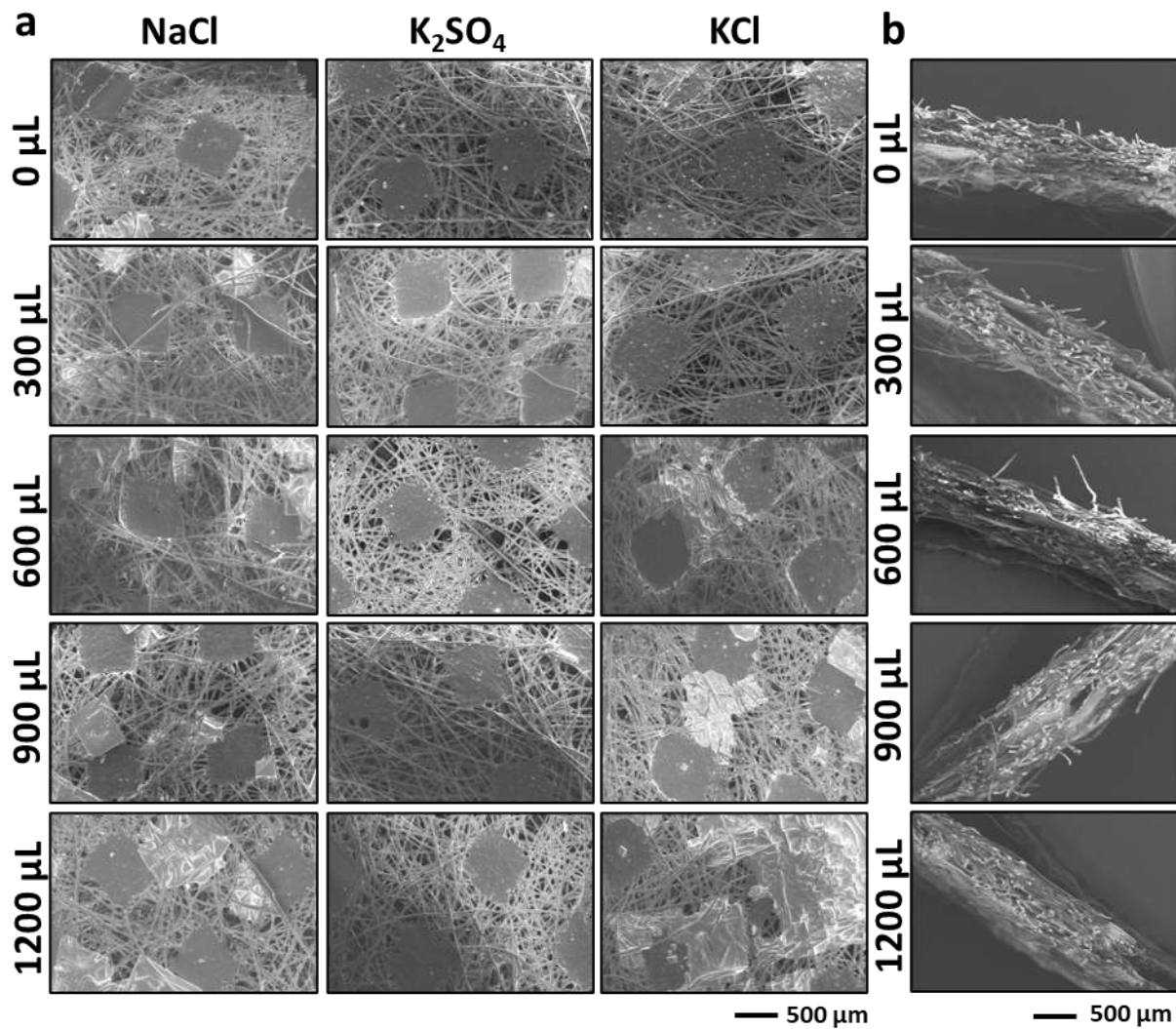


**Figure 4.17.** (a) Low-magnification SEM images of filters functionalized with NaCl (left),  $K_2SO_4$  (center) and KCl (right), showing the morphology of the salt coatings at different amounts of coated salt. (b) Low-magnification, cross-sectional SEM images of NaCl-functionalized filters, showing the morphology of the salt coatings at different amounts of coated salt.

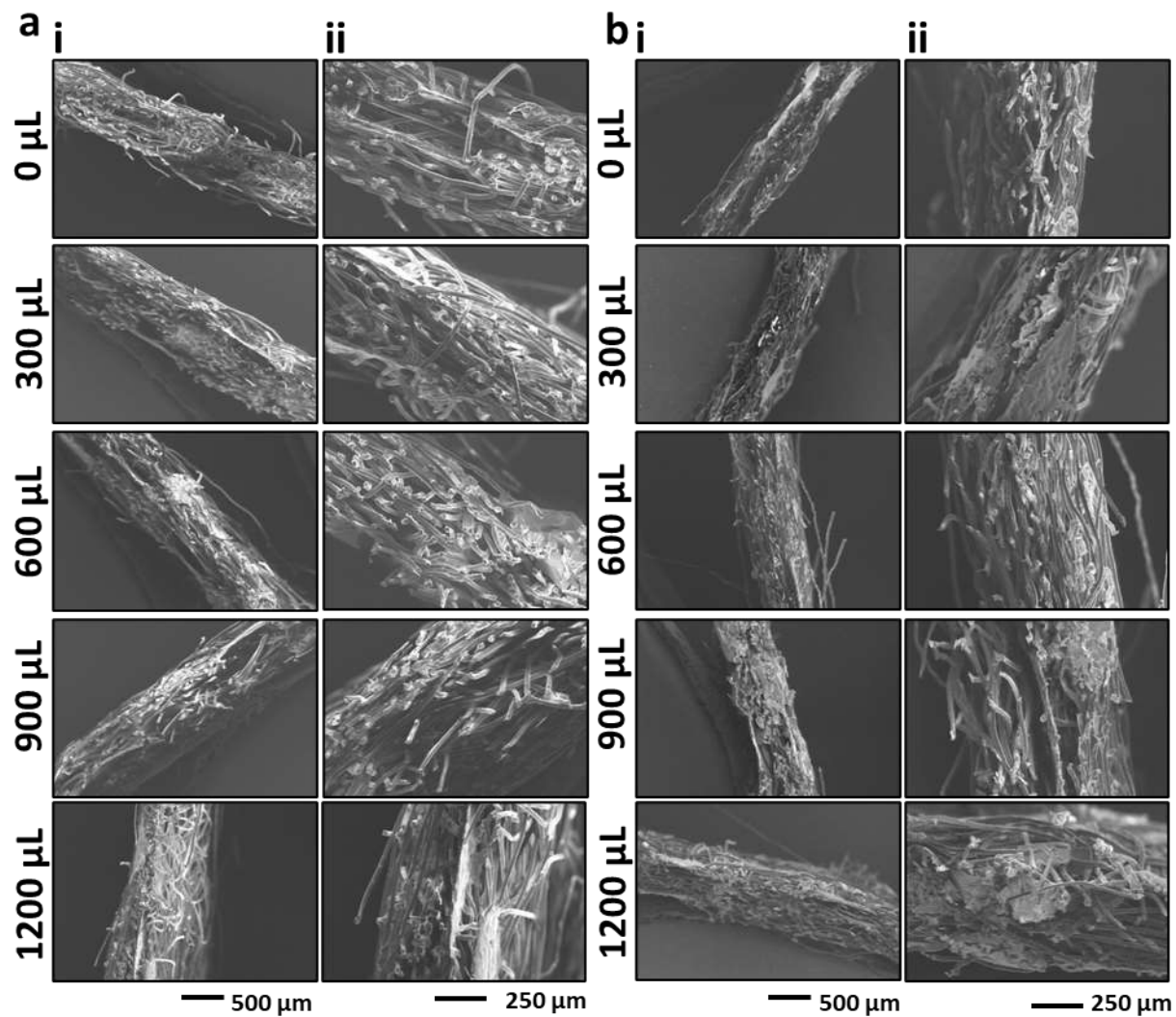


**Figure 4.18.** (a,b) Cross-sectional SEM images of  $K_2SO_4$  (a) and  $KCl$  (b) functionalized filters, showing the distribution of the salt coatings at different amounts of coated salt (i: low magnification, ii: high magnification).

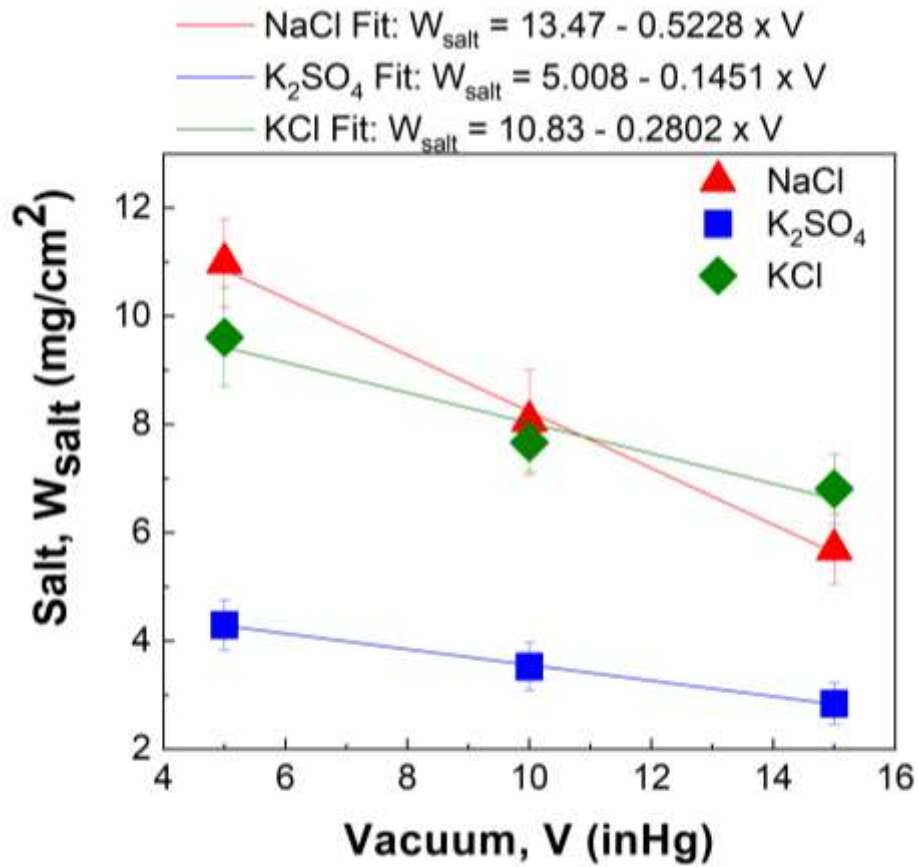


**Figure 4.19.** Production of salt-coated filters with vacuum application. Relationship between level of vacuum applied during salt coating (V) and amount of salt coated on the filters ( $W_{\text{salt}}$ ) (n = 6–15, mean  $\pm$  SD). Linear fit equations are shown ( $P < 0.001$ )

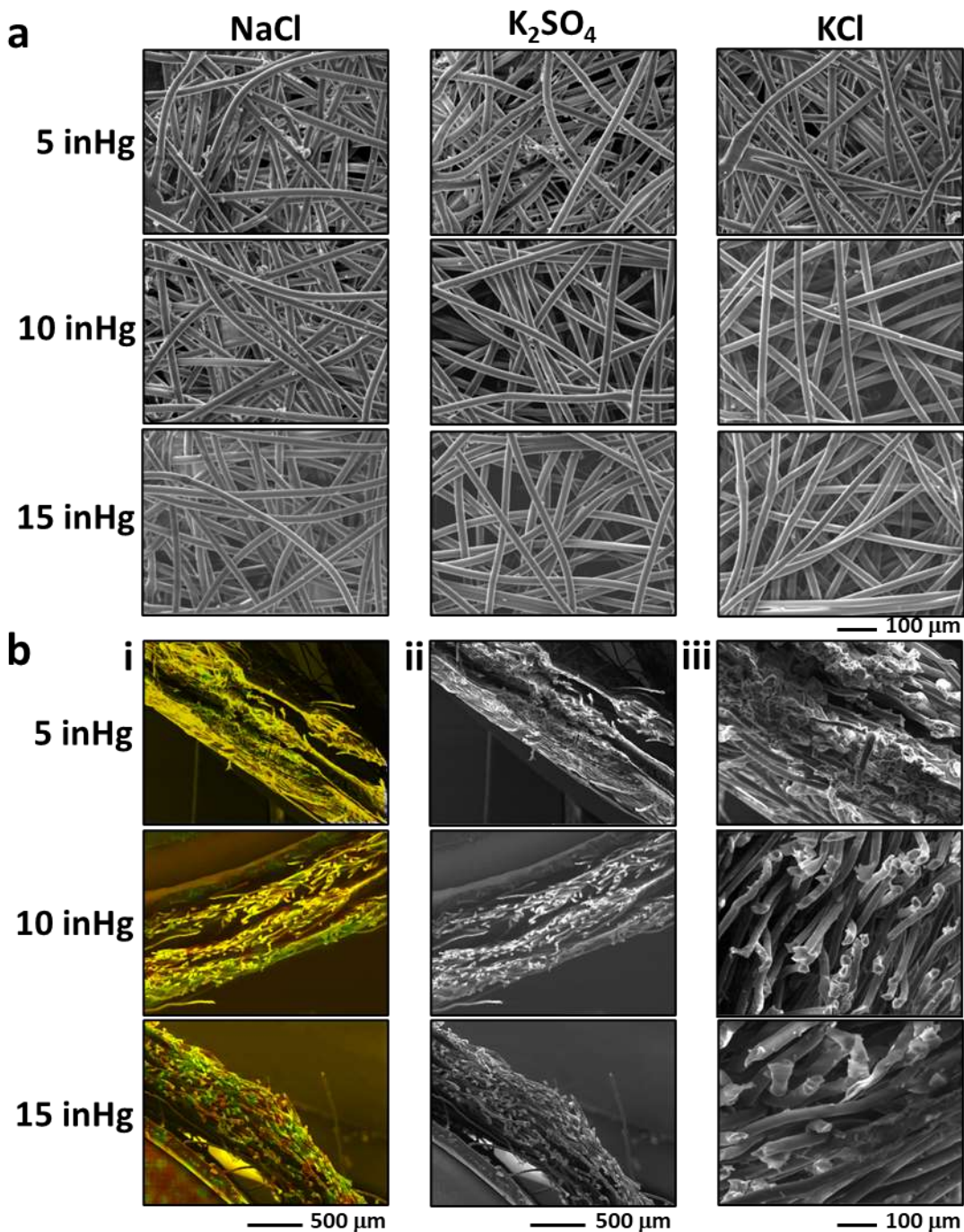


**Figure 4.20.** Characterization and pathogen inactivation on salt-coated filters prepared with vacuum process. (a) SEM images of filters functionalized with NaCl (left), K<sub>2</sub>SO<sub>4</sub> (center) and KCl (right), showing the morphology of the salt coatings at different levels of vacuum applied during coating. (b) Cross-sectional EDX mapping (combination of Na (red) and Cl (green) mapping images) (i), and SEM (ii, iii) images of NaCl-functionalized filters, showing the distribution of the salt coatings at different levels of vacuum applied during coating.

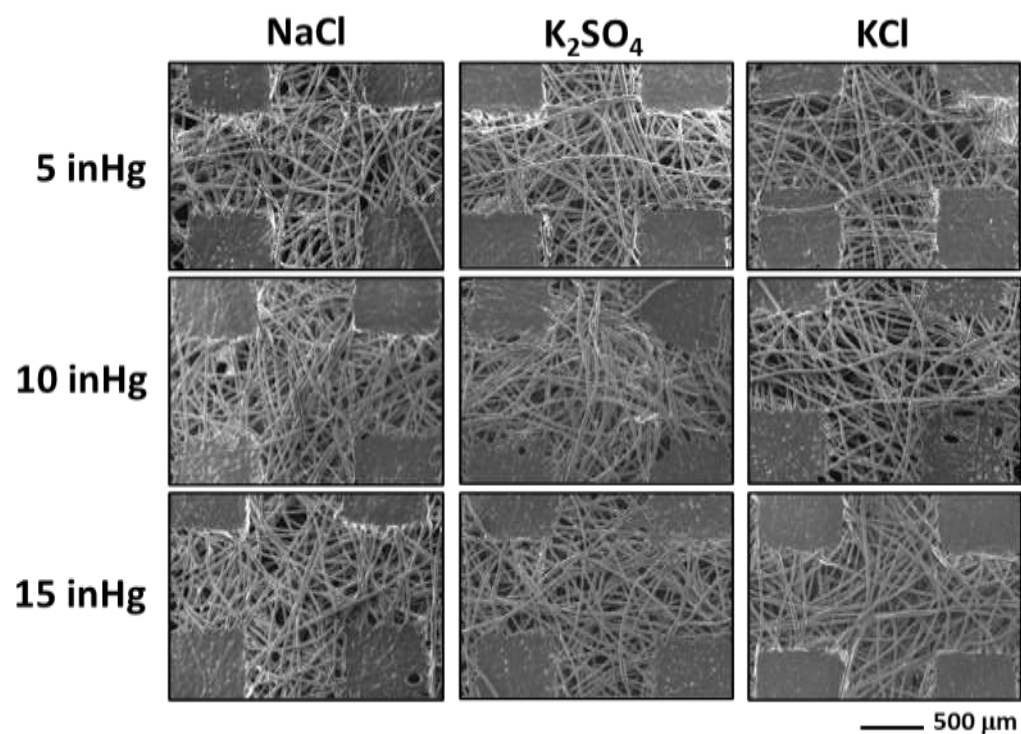


**Figure 4.21.** Production of salt-coated filters with vacuum application. Low-magnification SEM images of filters functionalized with NaCl (left),  $K_2SO_4$  (center) and KCl (right), showing the morphology of the salt coatings at different levels of vacuum applied during coating.

### 4.3.6 Effect of droplet size and composition on pathogen inactivation

To investigate the pathogen inactivation on the salt filters prepared with a vacuum process, *K. pneumoniae* was aerosolized and incubated on NaCl<sub>15inHg</sub>. As shown in Figure 4.22a, NaCl<sub>15inHg</sub> caused time-dependent inactivation of bacterial DI water aerosols (one-way ANOVA,  $P < 0.001$ ). As opposed to the bare membranes that did not cause any significant change in CFU (one-way ANOVA,  $P > 0.05$ ), NaCl<sub>15inHg</sub> caused rapid  $>2$ -log CFU reduction within 5 min (one-way ANOVA,  $P < 0.001$ ). Additionally, to study the effect of droplet/aerosol composition, the bacteria were aerosolized in artificial saliva. The bacteria in artificial saliva aerosols exhibited time-dependent inactivation on NaCl<sub>15inHg</sub> (one-way ANOVA,  $P < 0.001$ ), with no significant difference compared to the bacteria in DI water aerosols over time (General Linear Model,  $P > 0.05$ ).

To investigate the effectiveness against different pathogen transmission modes, *K. pneumoniae* 5- $\mu$ L droplets were incubated on NaCl<sub>15inHg</sub>. As shown in Figure 4.22b, NaCl<sub>15inHg</sub> caused time-dependent inactivation of bacterial droplets, in the case of both DI water and artificial saliva (one-way ANOVA,  $P < 0.001$ ), although DI water droplets exhibited greater CFU reduction than artificial saliva in the first 5 min (one-way ANOVA,  $P < 0.01$ ). The later onset of bacteria inactivation in artificial saliva droplets compared to DI water droplets is explained by the higher viscosity measured for artificial saliva ( $1.3 \pm 0.07$  mPa·s) compared to DI water ( $1.0 \pm 0.01$  mPa·s), which can delay the salt recrystallization process on the filters (Student's *t*-test,  $P < 0.001$ ) [308]. Additionally, the aerosolized bacteria incubated on the salt filters showed higher CFU reduction over time compared to the bacteria in droplets, in the case of both DI water and artificial saliva (General Linear Model,  $P < 0.001$ ). This is due to the faster evaporation of the aerosols compared to the droplets, which leads to faster salt recrystallization.

Overall, these results indicate that the salt filters prepared with a vacuum process quickly inactivate pathogens transmitted by both aerosols and droplets, although with different inactivation rates due to the different evaporation-induced salt recrystallization rates. Furthermore, the salt filters inactivate the pathogens even under mimicked real condition of pathogen transmission in saliva.

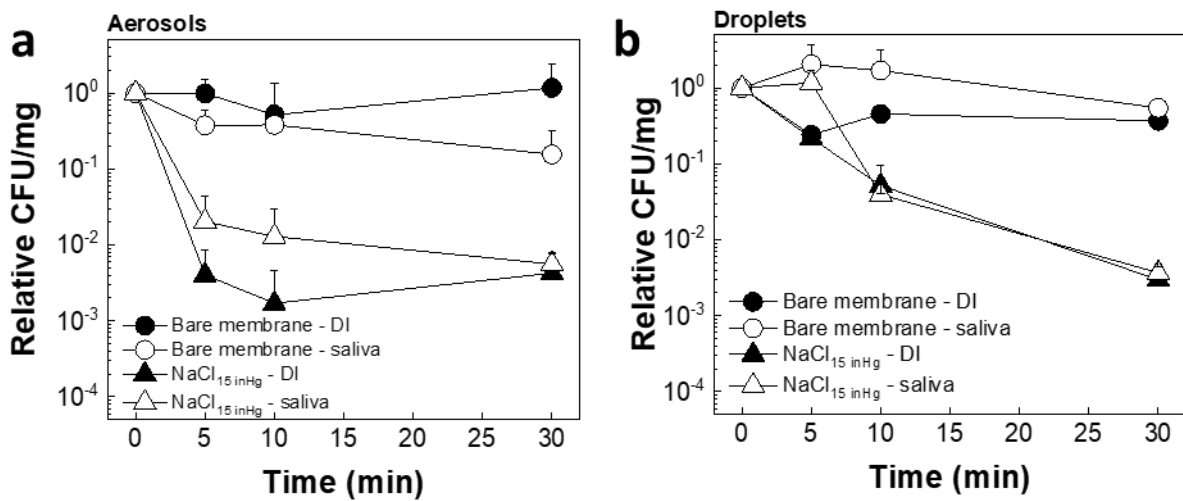


**Figure 4.22.** CFU change showing the effect of incubation time and dispersed medium (DI water and artificial saliva) on *K. pneumoniae* exposed to NaCl<sub>15</sub> inHg in the form of aerosols (a) and droplets (b) (n = 5 for (a), n = 3 for (b), mean ± SD).

## 4.4 Conclusion

In this work, we first showed that the salt type-dependent pathogen inactivation rates observed on the salt-functionalized filters are due to the different crystallization behaviors. In particular, by studying the pathogen inactivation directly on the salt powders, it was found that the recrystallization of the different salt coatings over time well matched the pathogen inactivation patterns on the functionalized filters. We found that (i) NaCl and KCl caused pathogen inactivation earlier than  $K_2SO_4$  (3–5 vs 5–15 min) and (ii) the differing recrystallization kinetics of the salt powders over time could explain this pathogen inactivation behavior. Importantly, it was determined that the salt recrystallization constitutes the main destabilizing mechanism, although the increasing osmotic pressure experienced by the pathogens during aerosol evaporation contributed in small part to the pathogen inactivation. It was also observed that the virus aggregated when exposed to extremely high concentration of salt solution, which could be due to an ionic effect on the viral surface charge; although this phenomenon was not found to damage the virus particles, future characterization of the ionic effect can be of interest. Second, the salt-coated filters prepared without a vacuum process had large salt aggregates when high amounts of salt were incorporated, which may function as sources of salt when the salt coating is partially dissolved upon exposure to humidity, increasing the lifetime of the coating. On the other hand, the filters coated with salt using a vacuum process exhibited a more uniform coating and higher quality control. Finally, the salt-coated filters were proven to inactivate pathogens irrespective of the transmission mode (aerosol/droplet), including under mimicked real-life conditions of pathogen suspension in saliva. As such, our research can contribute to the development of antimicrobial filters for face masks or other infection prevention strategies to contain the spread of viruses and bacteria and to provide improved protection against respiratory diseases.

# **5 Efficient Inactivation of Resilient Pathogens and Prevention of Contact Transmission using salt-coated filters**

Addressing respiratory diseases effectively requires the development of an effective respiratory protection system. Despite the efficiency of conventional masks in reducing pathogen spread, these masks can be a potential source of contact-based transmission. As such, we have designed antimicrobial face mask and mask covering using a stack of salt-coated spunbond (SB) fabric. This fabric acts as an outer layer for the face mask and as a covering over a conventional mask, respectively. We evaluated the universal antimicrobial performance of the salt-coated three-stacked SB fabric against enveloped/non-enveloped viruses and spore-forming/non-spore-forming bacteria. In addition, we tested other filter attributes, such as filtration efficiency and breathability, to determine the optimal layer for salt coating and its effects on performance. Our findings revealed that the outer layer of a conventional face mask plays a crucial role in contact transmission through contaminated face masks and respirators. Through contact transmission experiments, the salt-coated stacked SB fabric demonstrated a superior effect in preventing contact transmission compared to SB or meltblown (MB) polypropylene fabrics—an issue challenging to existing masks. Our results demonstrate that the use of salt-coated stacked SB fabric as i) the outer layer of a mask and ii) a mask cover over a mask enhances overall filter performance against infectious droplets, achieving high pathogen inactivation and low contact-based transmission while maintaining breathability.

## 5.1 Background

To combat the spread of respiratory diseases, mask-wearing has become a global norm, serving both as a protective measure against infectious diseases and as a precaution for symptomatic individuals [323]. However, the limitation of conventional masks (e.g., contact transmission via contaminated mask surface and concern over biohazardous waste) has underscored the need of antimicrobial face masks for personal and public infection control strategies [282]. In addition, current masks/respirators are not designed for disinfection and reuse; they are recommended for single use only [324]. Despite the increasing demand and ongoing efforts to integrate antimicrobial concepts, certain challenges remain. Addressing these challenges is essential for the successful implementation of antimicrobial face masks.

Primarily, antimicrobial masks have been investigated to target enveloped viruses (e.g., influenza viruses, human coronaviruses, human immunodeficiency viruses, etc) and non-spore-forming bacteria (e.g., *Pseudomonas aeruginosa*, *Klebsiella pneumoniae*, *Escherichia coli*, etc). Thus, limited research has been conducted on non-enveloped viruses and spore-forming bacteria, which exhibit greater resistance to environmental conditions and antimicrobial materials [325-327]. Spore-forming bacteria feature multiple layers, including the inner forespore membrane, cortex, outer forespore membrane, basement layer, inner coat, outer coat, and crust. These layers collectively act as a barrier against environmental stress [328]. The dormant form of bacteria, known as spores, can survive over decades or even centuries under harsh conditions such as nutrient deprivation, heat treatment, and antibiotic exposure [329]. When conditions are favorable, they can transform back into vegetative forms, capable of metabolism and growth [329]. In addition, non-enveloped viruses, lacking an external lipid envelope, exhibit greater stability compared to viruses with a lipid envelope, which are susceptible to environmental stresses like alcohol-based disinfectants, temperature, and humidity. The capsid-only structure of

non-enveloped viruses contributes to better maintaining their integrity [330, 331]. As such, non-enveloped viruses have been reported to maintain infectivity on surfaces for extended periods, surpassing the survivability of enveloped viruses. For instance, non-enveloped viruses, including rotaviruses and astroviruses, can remain infective for > 2 months on the same surfaces where enveloped viruses lose their infectivity within a few hours to several days [332]. Due to their inherent stability, spore-forming bacteria and non-enveloped viruses can more easily spread, potentially leading to the development of serious diseases in humans through inhalation or contact transmission of these pathogens [330, 333].

Second, development of antimicrobial masks should include thorough analysis of each layer of the mask and its function in combination. Analyzing the properties of each layer enables the determination of the most suitable layer for antimicrobial coating. Besides, it allows for the identification of the optimal stacking sequence of layers, which can maximize the filter performance of masks. It has been reported that each layer of masks has its own role: the inner layer (support layer for the middle layer), the middle layer (main filter media), and the outer layer (protective layer for the middle layer) (see Figure 5.1) [283]. To fulfill different roles, each layer is produced in a different way with the outer and inner layers manufactured through a spunbonding process, while the middle filter is created through a meltblowing process [334-336]. This results in varying properties of surgical masks such as fiber diameter (spunbond fabric, hereafter abbreviated as SB: 20  $\mu\text{m}$  and meltblown fabric, hereafter abbreviated as MB: 3  $\mu\text{m}$ ), thickness (SB fabric: 170  $\mu\text{m}$  and MB fabric: 240  $\mu\text{m}$ ), and fiber volume fraction (SB fabric: 11% and MB fabric: 42%) [337]. Due to the high volume fraction of meltblown fabric, its pressure drop ( $\sim 148.7$  Pa, 8 LPM) is much higher than SB fabrics ( $\sim 4.4$  Pa, 8 LPM) [337]. To enhance filtration efficiency, meltblown fibers are often electrically charged with a corona charging treatment (surface charge density of the MB fabric in N95 respirators: 17.3-27.3

$\mu\text{C}/\text{m}^2$ ) [338]. However, relying on surface charge to enhance filtration performance has limitations, as this effectiveness may decline due to surface charge degradation from overuse, decontamination procedures, and exposure to humidity [338]. Hence, owing to the distinct characteristics of each layer, the development of antimicrobial masks should be designed with a comprehensive understanding of the impact of functionalization on mask performance.

According to a previous study, the filtration efficiency of SB and MB fabric in surgical masks is noted as 6-10% and 19-33%, respectively, when tested with particles smaller than  $0.8 \mu\text{m}$  at 32 LPM [339]. Therefore, further research is required to comprehend the size-dependent performances of individual layer of the mask, considering the diverse sizes of pathogens (around 100 nm for viruses and a few micrometers for bacteria) and the infectious medium (aerosols, droplets) carrying these pathogens. The findings from such research would then be used to select the appropriate layer for functionalization and choosing a suitable strategy (e.g., encapsulation, surface adsorption, chemical functionalization, crosslinked polymer coating, loading into fiber coating, and functionalization of fiber coating) to develop application-specific antimicrobial face masks [282]. For instance, the coating or functionalization of the MB filter should be carefully designed not to significantly increase the thickness or eliminate surface charges, considering that they are major factors for high breath resistance and filtration efficiency, respectively.

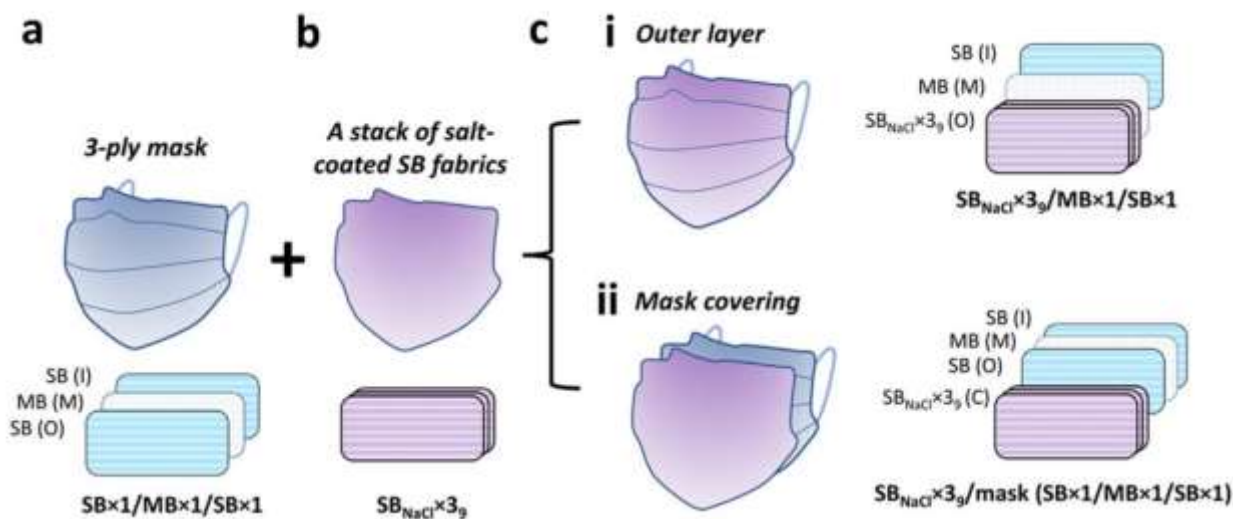


**Figure 5.1.** Schematic presentation of antimicrobial face mask and mask covering based on salt coated stacked spunbond polypropylene (PP) fabric. (a) Schematic representation of a 3-ply face mask (top) and mask structure (bottom; SB: spunbond fabric, MB: meltblown fabric; I: inner layer, M: middle layer, O: outer layer). (b) Schematic representation of salt-coated stacked SB fabric (top) and salt-coated three-stacked SB fabric (bottom). (c) The proposed design and architecture of antimicrobial face mask (i) and mask covering (ii). The fabrics were labeled FabricSalt×#Amount, where Fabric is the PP fabric type (SB or MB), Salt the type of salt (NaCl, KCl, or K<sub>2</sub>SO<sub>4</sub>), # the number of stacked fabrics (1 or 3), and Amount the quantity of salt coating (5, 9, or 13 mg/cm<sup>2</sup>). Bare fabrics are labelled Fabric×#. For the fabrication of stacked SB fabrics in (b), SB PP fabric used as the inner layer of a conventional 3-ply mask (i.e., SB(I) in (a)) have been utilized.

Lastly, despite extensive research on contact transmission from solid surfaces to hands (e.g., toys, bed rail, and bedside table) [340-342], it is noteworthy that some investigations into transmission through mask surfaces carry significant implications. For example, research involving healthcare workers found that after their shifts, approximately 15.9% of masks were contaminated with MRSA, 14.3% with *K. pneumoniae*, 13.0% with *Enterobacter* spp., and 4.2% with *E.coli* [343]. This research underscores the potential threat posed to healthcare workers who come into contact with contaminated mask surfaces, potentially affecting patients susceptible to pathogenic contamination. Furthermore, it has been reported that after 4 hrs of mask usage in non-hospital, indoor settings,  $1 \times 10^4$  CFU/mask of bacteria were detected, and more than 80% of these bacteria originated from sources other than the wearer's own microbiome, i.e. *Bacillus* (40.4%) and *Staphylococcus* (42.6%). This occurs due to accumulation of pathobionts from

human saliva and exhaled breath [344]. The research highlights that face masks can be easily contaminated not only in healthcare settings but also in daily life. Therefore, gaining a more profound understanding of face mask-hand contact transmission rates becomes a crucial step in developing antimicrobial face masks for effectively mitigating this risk.

In our previous studies, we proposed the idea of using salt-recrystallization process as a major pathogen inactivation mechanism and demonstrated significant antimicrobial effects using salt-coated polypropylene (PP) fabrics against enveloped viruses and non-spore-forming bacteria in droplets or aerosols [259, 282]. It was proven that salt-coated PP fabrics induce rapid and universal inactivation of the pathogens due to physical damage associated with the process of salt recrystallization during the drying process of the dissolved salt coating. The practical issue of salt-coated MB filters lies in the clogging of pores by salt crystals during the drying process, attributable to the small pore size. This easily leads to an increase in pressure drop. A potential solution involves applying vacuum to enhance the uniformity of the salt coating or forming a thin salt coating only on the single side of the MB filter. However, it should be noted that these processes have limitations in terms of achieving a significant amount of salt and that the effectiveness of pathogen inactivation diminishes as the quantity of coated salt decreases [293]. Furthermore, the salt coating formed on the electret fiber's surface negates the filtration efficiency advantage conferred by the charge on the surface of the MB PP fiber. Thus, these factors must be carefully considered when devising the salt coating strategy for MB filters. On the other hand, the salt coating process on SB PP fabrics is less restrictive compared to MB PP filters, offering greater flexibility. This is associated with the large pore size, which reduces the impact of the amount of salt coating on breathability. Besides, the salt coating on the SB PP fabric can lead to a reduction in contact-based transmission. The SB fabric, used as outermost layer, is susceptible to contamination. Considering the antimicrobial effect of salt coating, it is

reasonable to assume that salt-coated SB fabric can reduce contact transmission. Therefore, this study was proposed based on the hypothesis that applying the salt coating concept to SB fabric can achieve two primary objectives: effectively eliminating viruses/bacteria and preventing contact transmission.

This research aims to investigate 1) antimicrobial effects of salt-coated polypropylene (PP) fabrics on the spore-forming bacteria, i.e. *Clostridium difficile* (*C. difficile*), and non-enveloped viruses, i.e. human rhinovirus (HRV) 16, compared with non-spore-forming bacteria, *Klebsiella pneumoniae* (*K. pneumoniae*), and enveloped virus, A/California/04/2009 (CA/09, H1N1), 2) filtration efficiency and breathability of salt-coated stacked SB fabrics as both an outer layer of a mask and mask cover w/ and w/o air flow conditions,, and 3) contact transmission behavior of salt-coated fabrics against simulated dye contaminants and bacterial (*K. pneumoniae*)/viral (A/Puerto Rico/8/34 (PR/34, H1N1)) contaminants. Ultimately, this paper presents an approach demonstrating how salt-coated PP fabric can offer a solution to the two fundamental issues of masks: killing pathogens and eliminating the problem of contact transmission. This work is anticipated to contribute to determining the optimal design of a salt-coated mask and mask cover for superior performance in inhibiting disease transmission and infection.

## **5.2 Methods**

### **5.2.1 Preparation of salt-coated fabrics**

Inner spunbond polypropylene (SB PP) layers of three-ply surgical masks (Fisherbrand Facemasks; Fisher Scientific, Pittsburgh, PA) were collected for salt coating with NaCl, KCl, and K<sub>2</sub>SO<sub>4</sub>, as previously reported [294]. Each salt was dissolved in filtered (0.22 μm pore size; Corning, Tewksbury, MA) DI water to make a final concentration of 29.03 w/v % for NaCl,

26.31 w/v % for KCl, and 9.72 w/v % for K<sub>2</sub>SO<sub>4</sub>. The prepared saline solutions were mixed with 1 v/v% of Tween-20 (Fisher Scientific) to facilitate salt coating on the spunbond PP fabrics. Then, fabrics were submerged in each saline solution and gently rubbed to remove any trapped bubbles. The pre-wet fabrics were either stacked (three salt-coated stacked fabrics) or used individually (single-layer salt-coated fabric). This is followed by either adding more saline solution or removing excess solution using a vacuum to achieve a salt amount of 5, 9, and 13 mg/cm<sup>2</sup>. Finally, the salt-coated fabrics were dried overnight at 45 °C in an incubator (Thermolyne 42000 incubator; Dubuque, IA). The obtained fabrics were labeled as Fabric<sub>Salt</sub>×#<sub>Amount</sub>. In the notation, Fabric specifies the type of PP fabric, either spunbond (SB) or meltblown (MB), Salt the type of salt used (NaCl, KCl, or K<sub>2</sub>SO<sub>4</sub>), # the number of stacked SB PP fabrics (1 or 3), and Amount the quantity of salt coating (5, 9, or 13 mg/cm<sup>2</sup>). Bare fabrics are labelled Fabric×#, where # is the number of stacked fabrics.

### 5.2.2 Bacteria preparation

Antibacterial activity of non-spore-forming and spore-forming bacteria was compared against *Klebsiella pneumoniae* (*K. pneumoniae*, ATCC BAA-1705) and *Clostridium difficile* (*C. difficile*, ATCC 43598), respectively. The culture of *K. pneumoniae* followed the methods reported in a previous report[294]. First, *K. pneumoniae* was streaked on tryptone soy agar (TSA; Oxoid, Nepean, Ontario, Canada) plates and incubated overnight at 37 °C. Then, a single colony was inoculated in tryptone soy broth (TSB; BD, Franklin Lakes, NJ, USA), followed by incubation overnight at 37 °C. The cultured *K. pneumoniae* was transferred to fresh TSB at a 1:500 ratio and further incubated at 37 °C and 200 rpm for 4 hrs (OD<sub>600</sub> 1). The cells were harvested at OD<sub>600</sub> 0.6 and centrifuge-washed three times at 11,000 rpm for 10 min each. The final cell pellet was resuspended in DI water for inactivation tests (10<sup>6</sup> cells/mL). Separately, *K.*

*pneumoniae* stocks were prepared by mixing the cells and 30% glycerol in a 1:1 ratio, followed by storage at -80 °C.

Similarly, the culture of *C. difficile* followed the methods reported in a previous report[345]. *C. difficile* was streaked on a germination plate composed of brain heart infusion broth (3.7 w/v %), yeast extract (0.5 w/v %), agar (1.5 w/v %), taurocholic acid (10 w/v %), and L-cysteine (10 w/v %). The plate was incubated with a gas pack (BD) in an anaerobic jar (anaerobic condition) at 37 °C for 1-2 days. A colony was streaked on a sporulation plate composed of Bacto peptone (6.3 w/v %), proteose-peptone (0.35 w/v %), ammonium sulfate (0.07 w/v %), Tris base (0.106 w/v %), BHI broth (1.11 w/v %), yeast extract (0.15 w/v %), agar (1.5 w/v %), and L-cysteine (10 w/v %). This was followed by incubation with a gas pack (BD) in an anaerobic jar for 4-5 days at 37 °C. The cells were harvested and suspended in DI water, followed by incubation overnight for 16 hrs at 4 °C for the spores to be released from mother cells. To separate the spores from mother cells, the cell/spore mixture was centrifuged 20 min at 4,000 rpm and 4 °C in a sucrose gradient 50 w/v % (Sigma-Aldrich, Burlington, MA). The relatively heavy spores will sink, while the lighter mother cells will float on the sucrose. The pellet resuspended in DI water was used for inactivation test, and the supernatant containing mother cell debris was discarded.

### **5.2.3 Virus preparation**

Antiviral activities of enveloped and non-enveloped viruses were investigated by using the influenza virus A/California/04/2009 (CA/09, H1N1) and HRV 16 (ATCC VR-283), respectively. Along with CA/09, the influenza virus A/Puerto Rico/8/34 (PR/34, H1N1) was also prepared for contact transmission tests. CA/09 and PR/34 viruses were prepared by using embryonated chicken eggs, following the procedure reported [259]. Briefly, this involved the

injection of viruses into 11-day-old embryonated chicken eggs, incubation for 2 days, extraction of allantoic fluid, and virus purification using 70 µm filters (Fisher brand). This was followed by low-speed centrifugation (2,800 rpm, 4 °C, 15 min) and high-speed centrifugation (30,000 rpm, 4 °C, 1 hr).

On the other hand, cell-based culture was performed to cultivate HRV 16[346]. For this purpose, HeLa (ATCC CRL-1958) cells were cultured in Dulbecco's Modified Eagle Medium (DMEM; Corning, Corning, NY) supplemented with 10% fetal bovine serum (FBS; Thermo Fisher Scientific, Waltham, MA), 100 U/mL penicillin G, and 100 µg/mL streptomycin (Thermo Fisher Scientific). At 80% cell confluency, the medium was replaced to DMEM supplemented with 2% FBS, 100 U/mL penicillin G and 100 µg/mL streptomycin sulfate. Then, virus inoculation was performed at a multiplicity of infection (MOI) of 0.1 and incubated at 33 °C and 5% CO<sub>2</sub> for 5 days. For virus collection in the medium, purification was performed using low speed centrifugation (2,800 rpm, 4 °C, 15 min), filtration (0.2 µm; Fisher Scientific), and high-speed centrifugation (30,000 rpm, 4 °C, 1 hr). Cells were treated with trypsin (Thermo Fisher Scientific) and freeze-thawed three times to lyse the cell membranes to obtain virus. This was followed by purification steps, including low speed centrifugation (2,800 rpm, 4 °C, 15 min), filtration (0.2 µm; Fisher Scientific), and high-speed centrifugation (30,000 rpm, 4 °C, 1 hr).

To control the initial concentration of PR/34 viruses, a 50% tissue culture infectious dose (TCID<sub>50</sub>) assay was conducted, following procedures outlined in a previous report with slight procedural modifications[347]. Briefly,  $3 \times 10^4$  of MDCK cells were seeded in each well of a 96-well plate with 1 µg/mL of tosyl phenylalanyl chloromethyl ketone (TPCK; Sigma-Aldrich) and DMEM supplemented with 10% FBS, 100 U/mL penicillin G, and 100 µg/mL streptomycin. This was followed by overnight incubation at 37 °C and 5% CO<sub>2</sub>. The wells were rinsed with PBS and inoculated with the viruses in 10-fold serial dilution, followed by the addition of 1

µg/mL TPCK. After 2 hours of incubation at 37 °C and 5% CO<sub>2</sub>, inoculum was replaced with 1 µg/mL of TPCK and DMEM supplemented with 2% FBS, 100 U/mL penicillin G, and 100 µg/mL streptomycin. The cells were further incubated at 37 °C and 5% CO<sub>2</sub> for 3 days, then washed three times with washing solution (PBS with 0.2% Tween-20), followed by straining with 0.5% crystal violet in ethanol.

#### **5.2.4 Antimicrobial activity test on salt-coated fabrics**

The antimicrobial performance was tested as reported in our previous work[276]. In brief, 20 drops (size: 5 µl) of each bacterial/viral stocks, including *K. pneumoniae* (10<sup>6</sup> cells/mL), *C. difficile* (10<sup>6</sup> cells/mL), influenza viruses (CA/09, PR/34; 230 mg/mL), and HRV 16 (10<sup>3</sup> PFU/mL), were applied onto salt-coated spunbond PP fabrics using a pipette. After incubation for 5, 10, and 30 min, salt-coated fabrics were soaked in PBS and vortexed, followed by centrifugation 1 min (6,000 rpm, room temperature (RT); mini-centrifuge (Fisher Scientific)) with one end of the fabric being fixed to the cap of the 1.5 mL Eppendorf tube, to separate the solution containing bacteria/viruses from the SB fabrics. After removing the SB fabrics, the solution was subjected to additional centrifugation (14,800 rpm, 4 °C, 15 min; Eppendorf 5804R, Hamburg, Germany) to produce bacterial/viral pellets.

For the analysis of *C. difficile* viability, spore-forming units (SFUs) were compared relative to the measurement of initial stock. In the case of *K. pneumoniae*, the colony forming units (CFUs) were divided by the amount of bacteria used in the assays (CFU/mg), which was determined based on protein concentrations measured via the bicinchoninic acid assay (Micro BCA protein assay kit; Thermo Fischer Scientific). To characterize the stability of CA/09 influenza viruses, viral RNA was extracted using viral RNA/DNA mini kit (Invitrogen; Carlsbad, CA, USA)[348]. The RNA was synthesized to cDNA using a reverse transcription kit

(Applied Biosystems), followed by preparation of mixtures containing the cDNA product, SYBR green PCR Master Mix (Applied Biosystems, Waltham, MA, USA) and nucleoprotein (NP) targeting primers (forward primer: 5'-CACGGTCTGCACTCATATT-3', reverse primer: 5'-C TCCTCCACTTCTGGTCCTTAT-3'). The mixtures were used for real-time amplification of cDNA products using the ABI 7500 Fast Real-Time PCR System (Applied Biosystem).

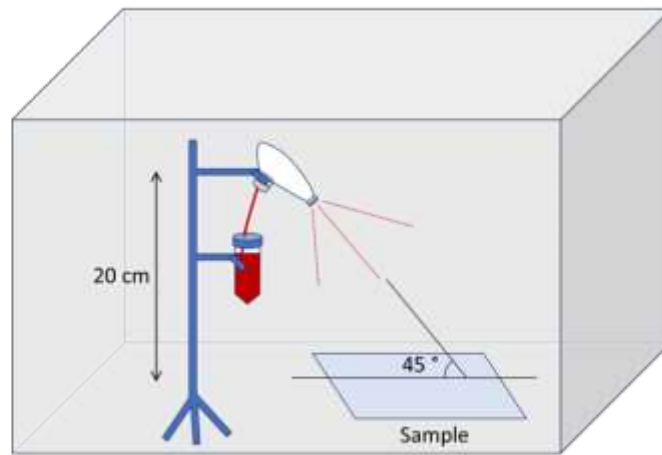
The plaque forming unit (PFU) assay was performed for HRV 16 inactivation tests. To this end, HeLa cells were plated onto 6-well plates (Corning) at a density of  $10^6$  cells per well and incubated overnight at 37 °C. Then, ten-fold serially diluted HRV 16 samples were inoculated onto the cells and incubated for an additional 1.5 hrs while continuously rocking. Subsequently, agarose overlays containing 0.25 w/v % of agarose (VWR life science, Radnor, PA) and 30 mM of  $MgCl_2$  (Sigma-Aldrich) were added and incubated for 2 days.

### **5.2.5 Filtration efficiency and breathability tests**

To investigate the particle capturing efficiency of each layer of mask against aerosol and droplets, a 1 mM of sulforhodamine B (SRB; Sigma-Aldrich) suspension in DI water was used. A whole mask comprising an outer/middle/inner layer was exposed to aerosols (2.5-4  $\mu m$  in diameter based on manufacturer's information; 0.3 mg/cm<sup>2</sup>) and droplets (352 ± 207  $\mu m$  in diameter, refer to Figure 5.2 for information on size distribution and measuring conditions; 1.5 mg/cm<sup>2</sup>) using a nebulizer (Aeroneb Lab Nebulizer System; Aerogen, Galway, Ireland) and a sprayer (Uline, Milton, ON), respectively. The nebulizer unit was positioned atop the fabric samples, loaded with a suspension for aerosolization. The amount of applied dye was controlled by measuring the weight of filters before and after applying aerosols/droplets. Following that, each layer of the entire mask was separated and immersed in DI water, followed by vortexing and centrifugation (6,000 rpm, RT, 1 min) to recover all dye from the filters. The collected

solution was subjected to fluorescence intensity measurement at 565/586 nm (excitation/emission) using the Citation 5 Imaging Reader (BioTek). The fluorescence intensity of individual layer relative to the whole mask was used to calculate the filtration efficiency of the layer in the mask.

**a**



**b**

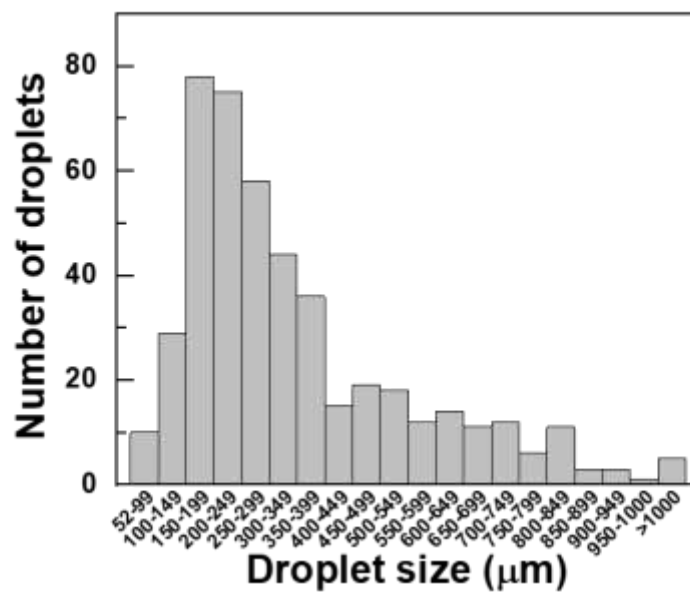


**Figure 5.2.** Spray test setup and spray droplet size distribution. (a) Spry system setup and (b) size distribution of the sprayed droplets. n=460. To measure the droplet size, droplets were sprayed onto a non-porous polypropylene sheet, and measurements of individual droplets were performed using MOTIC 2.0 software under an optical microscope.

To take airflow into consideration, filtration efficiency was also measured using PALAS PMFT 1000 (PALAS; Karlsruhe, Germany) [349]. The filtration efficiency was performed following 42 CFR 84 standard; 0.3  $\mu\text{m}$  sized polydisperse 5% NaCl particles were applied onto mask filters at a flow rate of 85 LPM [350]. Particle size and count were measured by Promo LED 2300 (PALAS; Karlsruhe, Germany). The difference in particle size distribution of upstream (particles before penetration through a filter) and downstream (particles after penetration through a filter) was used to calculate filtration efficiency, as described below:

$$\text{Filtration efficiency (\%)} = 100 \times (1 - A_d/A_u)$$

where  $A_d$  (number of particles/cm<sup>3</sup>) and  $A_u$  (number of particles/cm<sup>3</sup>) represent the number of aerosol particles in the downstream and upstream, respectively. Also, the breathability of the filters was characterized in accordance with the ASTM (F2100-19e1; F2101-01; MIL-M-36954C) standard. According to the protocol, testing of surgical/medical masks must be conducted under an airflow condition of 8 LPM with 4.9 cm<sup>2</sup> filters, equivalent to testing a whole mask at 163 LPM. After the measurement of differential pressure (Pa), the values were divided by the standard surface area for normalization [351]. Based on the calculated differential pressure (Pa/cm<sup>2</sup>), masks can be categorized into three levels: 50 Pa/cm<sup>2</sup> (level 1) and 60 Pa/cm<sup>2</sup> (level 2 and 3) [352-354].

### 5.2.6 Contact transmission test

The contact transmission test was conducted in two ways: through a simulation experiment using fluorescent dye and an experiment involving actual viruses and bacteria. Sulforhodamine

B (SRB, 1 mM; Sigma-Aldrich) and calcofluor white (CW, 1 mM; Sigma-Aldrich) were used to simulate biological contaminants on masks. To control the amount of the fluorescent dye sprayed on filters ( $\sim 1.5 \text{ mg/cm}^2$ ), their weight changes were monitored before and after spraying using an ExplorerPro balance (Ohaus; Parsippany, NJ). The sprayed filters were labeled as Contaminant-Fabric<sub>Salt</sub> $\times$ #<sub>Amount</sub>. Here, Contaminant refers to the type of contaminants used in the experiments (SRB or CW), while Fabric<sub>Salt</sub> $\times$ #<sub>Amount</sub> adheres to the definition outlined in section 4.1. The symbol “/” represents the stacking arrangement of the filters (i.e., A/B indicates that a layer A is positioned on top of a layer B). Different contamination scenarios were prepared: outermost layer contamination (SRB-SB $\times$ 1, SRB-SB $\times$ 3, and SRB-SB<sub>NaCl</sub> $\times$ 3<sub>9</sub>), middle layer only contamination (CW-MB $\times$ 1 and SB $\times$ 1/CW-MB $\times$ 1), and both outermost and middle layer contamination (SRB-SB $\times$ 1/CW-MB $\times$ 1). After spraying, the filters were incubated for 1, 5, 10, 15, 20, and 30 min, which was followed by gentle and strong pressing against the fabrics with the gloved (Ansell; Cowansville, QC) thumb and index finger. The pressure corresponding to the gentle and strong press of thumb was measured to be  $6.4 \pm 1.4 \text{ kPa}$  and  $11.3 \pm 3.6 \text{ kPa}$ , respectively. Similarly, the strong and gentle presses of index finger correspond to  $10.9 \pm 1.3 \text{ kPa}$  and  $5.8 \pm 2.1 \text{ kPa}$ , respectively. The glove was then cut, soaked in DI water for 1 min (500  $\mu\text{L}$ , RT), and subjected to vortexing and centrifugation (6,000 rpm, RT, 1 min) to resuspend the dye from the glove surface. Fluorescent intensity was measured using Citation 5 Imaging Reader (BioTek) at excitation/emission wavelengths of 565/586 nm (SRB) or 350/432 nm (CW), with a detection limit of 0.0002-0.00625 mM for SRB and 0.00005-0.025 mM for CW. Dye translocation (%) was calculated based on the fluorescent intensity of each sample and dye sprayed onto the finger-sized fabric.

In parallel with fluorescent dye experiments, contact transmission tests were performed using *K. pneumoniae* ( $10^8$  cells/mL) and PR/34 influenza viruses (Reed-Muench

method:  $1.2 \times 10^5$  TCID<sub>50</sub>/mL, Spearman Karber method:  $1.19 \times 10^5$  TCID<sub>50</sub>/mL). Similar to the fluorescent dye-based contact transmission test, 1.5 mg/cm<sup>2</sup> of bacteria/virus was sprayed onto filters. A gloved thumb was applied to the fabric after 1, 5, 10, 15, 20, and 30 min of incubation. Subsequently, the gloves were immersed in PBS, followed by vortexing and centrifugation (6,000 rpm, RT, 1 min) using a mini-centrifuge (Fisher Scientific) to detach bacteria/viruses from the gloves. This was succeeded by a second centrifugation step (14,800 rpm, 4 °C, 15 min; Eppendorf) and resuspension in PBS. CFU measurements were carried out to evaluate the viability of *K. pneumoniae* in each sample, and quantitative PCR (qPCR) for PR/34 influenza viruses as in CA/09 influenza viruses (see section 4.4). In the case of PR/34 influenza viruses, hemagglutinin (HA) gene was targeted with forward primer (5'-GGAAAGAAGTCCTCGTGCTATG-3') and reverse primer (5'-CAATCGTGGACTGGTGTATCTG-3')[348].

### **5.2.7 Finger pressing measurement**

The method used for measuring finger pressure involved the use of the Discovery HR 2 series rheometer (TA Instruments, New Castle, DE, USA) operated at 22°C. The axial force exerted by the finger's touch was assessed using a mechanized z-axis stage and a force gauge integrated into the rheometer system. An index finger applied pressure onto a 25 mm standard stainless-steel plate to replicate the impression force similar in size to the pressured area. The force measurements were acquired through force-displacement analysis. Initially, measurements were taken without any finger touch to establish a baseline, followed by measurements taken during both soft and hard fingertip presses. The force exerted was measured in Newton by comparing the initial state (no finger touch) to the soft and hard fingertip pressure touch states.

### **5.2.8 Microscopy analysis**

An optical microscope (Omax G223A-CA; Kent, WA) analysis was performed to observe time-dependent morphological changes of droplets/aerosols containing fluorescent dyes on filters and their transfer behavior to gloves after finger press. For glove samples, fluorescent microscopes (TCS SP2; Leica Microsystems, Wetzlar; excitation/emission wavelengths at 565/586 nm for SB and 350/432 nm for CW) were employed in addition to the optical microscopy observation. Apart from this, the optical microscope was also used to measure the particle size of sprayed fluorescent dye ( $352 \pm 207 \mu\text{m}$  in average) on hydrophobic polypropylene plastic surface with MOTIC 2.0 software.

Morphological changes on bacteria and viruses were observed using transmission electron microscopy (TEM) at 20 kV (JEOL JEM 2100; JEOL, Peabody, MA). Negatively stained TEM samples were prepared by with 1.5 w/v % phosphotungstic acid hydrate at pH 7.0 (Sigma-Aldrich).

### **5.2.9 Statistical analysis**

Statistical analysis was carried out using *t*-test, one-way analysis of variance (ANOVA), and the General Linear Model (SPSS version 29; IBM, Armonk, NY, USA). For assessing significance in multiple comparisons, a *P* value of less than 0.05 was considered significant.

## **5.3 Results and discussion**

### **5.3.1 Antimicrobial activity of salt-coated stacked spunbond (SB) fabrics against resilient pathogens**

To assess antimicrobial efficacy of salt-coated SB fabrics against resilient pathogens such as spore-forming bacteria and non-enveloped viruses, time-dependent viability of spore-

forming *C. difficile* was monitored in comparison with non-spore-forming bacteria, *K. pneumoniae*. As illustrated in Figure 5.3a, exposure to a stack of three spunbond (SB) polypropylene (PP) fabrics coated with various salts (i: SB<sub>Salt</sub>×3<sub>5</sub>, ii: SB<sub>Salt</sub>×3<sub>9</sub>, and iii: SB<sub>Salt</sub>×3<sub>13</sub>) resulted in a rapid decrease in viability for *K. pneumoniae*. The inactivation behavior was consistently observed across all three types of salts (i.e., NaCl, KCl, and K<sub>2</sub>SO<sub>4</sub>), as well as the various amounts of salt coating used in this work (i.e., 5 mg/cm<sup>2</sup>, 9 mg/cm<sup>2</sup>, and 13 mg/cm<sup>2</sup>). The enhancement in pathogen inactivation, commensurate with the quantity of the salt coating, is in line with a prior study [293]. As a result, 5 mg/cm<sup>2</sup> and 9 mg/cm<sup>2</sup> of NaCl exhibited 1.5-log reduction in 5 min and > 3.8-log reduction within 30 min. At 13 mg/cm<sup>2</sup>, a 2.5-log reduction was detected within 5 min, and subsequently, no viable bacteria thereafter. On the other hand, *C. difficile* displayed < 1-log reduction on SB<sub>Salt</sub>×3<sub>9</sub> and 2.8-log reduction SB<sub>NaCl</sub>×3<sub>13</sub> within 30 min incubation. That is, the inactivation of spore-forming bacteria is significantly dependent on the amount of salt (GLM analysis, *P*= 0.0007), similar to non-spore-forming bacteria (GLM analysis, *P*= 0.0051). The observed similarity can be attributed to the shared major inactivation mechanism of salt recrystallization [259]. Additionally, the result demonstrates that effective inactivation of non-spore-forming bacteria occurred across all three salt amounts utilized in this experiment. However, spore-forming *C. difficile* proved more resilient to inactivation than non-spore-forming *K. pneumoniae*, necessitating the application of a higher salt concentration. This indicates the imperative nature of employing a higher salt quantity for the inactivation of spore-forming bacteria.

The morphological change of the bacteria was evaluated by using TEM analysis. As depicted in Figure 5.3c, structural integrity of both *K. pneumoniae* and *C. difficile* was affected when exposed to salt-coated stacked SB fabric, as evident in the comparison with stock. *K. pneumoniae* exhibited more severe damage than *C. difficile* under identical amount of salt, 9

mg/cm<sup>2</sup> (compare Figure 5.3c(i) and (ii)). This observation is consistent with CFU data, as demonstrated in Figure 5.3a with 5.3b. Another noteworthy observation is associated with Figure 5.3b. In contrast to the slight decrease in SFU observed, a notable increase in bacterial destruction was evident in TEM. This corresponds with trends identified in the literature that underscore disparities between bacterial viability test assay results and TEM analysis [348].

The higher susceptibility of *K. pneumoniae* to a stack of salt-coated SB fabrics can be attributed to the structural difference between spore-forming bacteria and non-spore-forming bacteria. That is, the presence of a thick, protective coat on spores confers heightened resistance to adverse conditions [355], elucidating the need for a higher salt amount for the inactivation of *C. difficile* compared to *K. pneumoniae* (compare Figure 5.3a with 5.3b). It is well-known that spore-forming bacteria present considerable challenges in sterilization owing to their resistant structures [355, 356]. Therefore, the observation of the lethal impact of salt-treated SB PP fabric on *K. pneumoniae* and *C. difficile* suggests that the disease-killing mechanism, occurring during the salt recrystallization process following the dissolution and evaporation of the salt coating, can be highly applicable to the inactivation of both non-spore-forming and spore-forming bacteria.

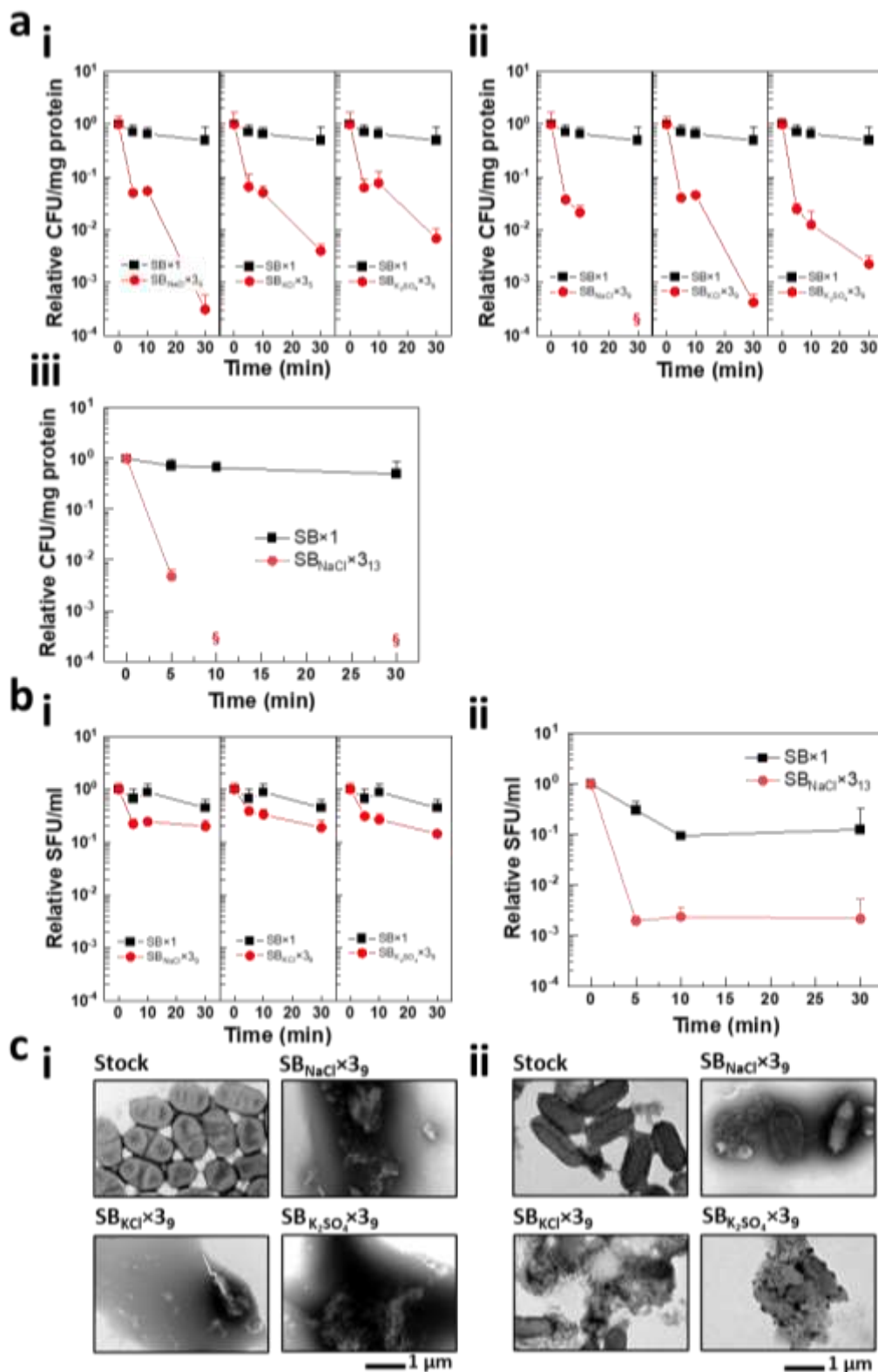


**Figure 5.3.** Time-dependent pathogen inactivation efficiency of salt-coated spunbond (SB) PP fabrics. Bacterial viability change showing the effect of incubation time on *K. pneumoniae* (a) and *C. difficile* (b) exposed to NaCl, KCl, and  $K_2SO_4$ -coated SB fabrics (in a, i: 5 mg/cm<sup>2</sup>, ii: 9 mg/cm<sup>2</sup>, and iii: 13 mg/cm<sup>2</sup>; in b, i: 9 mg/cm<sup>2</sup> and ii: 13 mg/cm<sup>2</sup>) for 30 min. (n=3, mean ± SD). Relative: with respect to 0 min. §: below detection limit. (c) TEM images of *K. pneumoniae* (i) and *C. difficile* (ii) after 30 min incubation on SB<sub>sal</sub>×3<sub>9</sub>, a stack of three SB fabrics w/ 9 mg/cm<sup>2</sup>

of salt coating.

The biocidal effects of salt-coated stacked spunbond (SB) PP fabrics on non-enveloped viruses were evaluated against human rhinovirus (HRV) 16 and their inactivation behavior was compared with CA/09 (i.e., enveloped virus). Figure 5.4 illustrate the time-dependent change in viability of CA/09 under varying salt type and salt amount, like the conditions used in bacteria. Viability was observed to decrease with the increase of salt amount across all types of salts, namely: NaCl (Figure 5.4a; GLM analysis,  $P < 0.0001$ ), KCl (Figure 5.4b; GLM analysis,  $P = 0.0003$ ), and  $K_2SO_4$  (Figure 5.4c; GLM analysis,  $P < 0.0001$ ). A rapid initial decrease in viability was followed by a gradual further decline. Within 30 min of incubation, there was a  $> 3.5$ -log viability reduction on  $SB_{NaCl \times 3_9}$  and  $SB_{KCl \times 3_9}$ , along with a 1.7-log decrease in viability on  $SB_{K_2SO_4 \times 3_9}$ . The greater susceptibility of CA/09 is associated with the presence of a lipid bilayer, rendering them more vulnerable to the effects of salt recrystallization.

Similar to CA/09, HRVs demonstrated a time-dependent decrease in viability down to a 2.5-log reduction on the  $SB_{NaCl \times 3_9}$  and  $SB_{KCl \times 3_9}$  fabrics ( $t$ -test,  $P < 0.0001$ ), and less than a one-log reduction on  $SB_{K_2SO_4 \times 3_9}$  fabrics ( $t$ -test,  $P = 0.0255$ ) within 30 min of incubation (see Figure 5.5a-ii for NaCl, 5.3b-ii for KCl, and 5.3c-ii for  $K_2SO_4$ ). As anticipated,  $SB_{NaCl \times 3_{13}}$  fabrics resulted in a higher viability loss, with 4-log reduction in 30 min of incubation ( $t$ -test,  $P < 0.0001$ ). These findings substantiate the effectiveness of the salt-coated stacked SB fabric in inactivating non-enveloped viruses. Considering that a 2-3 log reduction is required for a material to be classified as antimicrobial, SB fabrics coated with 9 and 13 mg/cm<sup>2</sup> of NaCl and KCl meet the threshold for antimicrobial applications [357]. Furthermore, we observe that  $> 5$  mg/cm<sup>2</sup> of salt is necessary for the effective inactivation of universal pathogens including spore-forming bacteria and non-enveloped viruses, i.e.,  $SB_{NaCl \times 3_9}$  and  $SB_{NaCl \times 3_{13}}$  in this work. The increased vulnerability in non-spore-forming bacteria and enveloped viruses than spore-forming bacteria and non-enveloped viruses attribute to their distinct structural features. While EPA-

registered antimicrobial products (e.g., sodium hypochlorite and hydrogen peroxide for *C.difficile*, and hypochlorous acid and citric acid for HRVs) have been used in inactivating resistant pathogens, it is important to acknowledge the limitations associated with applying them to face masks and respirators, primarily due to the toxicity [358, 359]. Despite the slightly reduced inactivation efficiency observed against resistant strains (specifically, *C. difficile* and HRVs in this study), the successful demonstration of antimicrobial efficacy with a stack of salt-coated SB fabrics suggests their potential for universal use in preventing the spread of both resistant and non-resistant diseases.

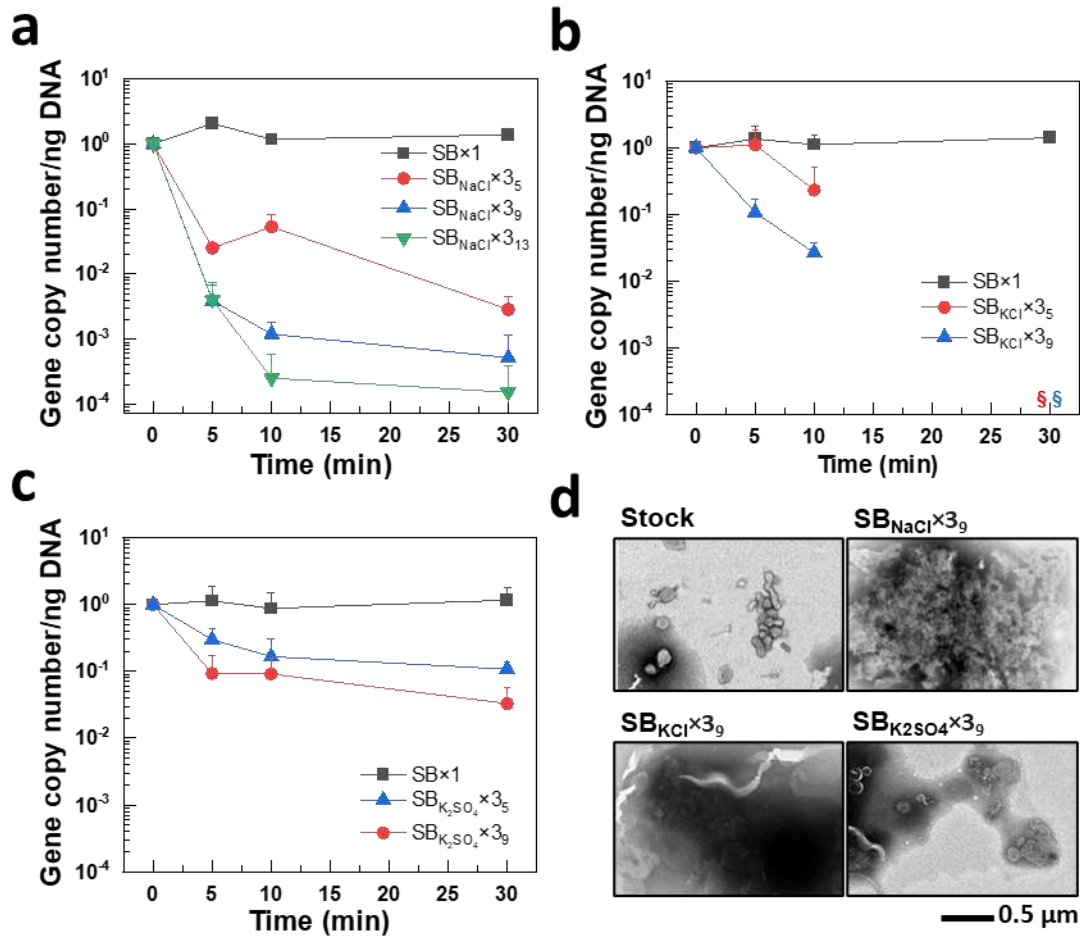


**Figure 5.4.** Viability reduction in CA/09 viruses using different salt-coated filters (a: NaCl-coated filters, b: KCl-coated filters, and c: K<sub>2</sub>SO<sub>4</sub>-coated filters). (d) TEM images of CA/09 after 30 min of exposure on NaCl-, KCl-, and K<sub>2</sub>SO<sub>4</sub>-coated filters (i.e., SB<sub>salt</sub>×3<sub>9</sub>: a stack of three SB fabrics w/ 9 mg/cm<sup>2</sup> of salt coating, SB×1: a bare SB fabric).

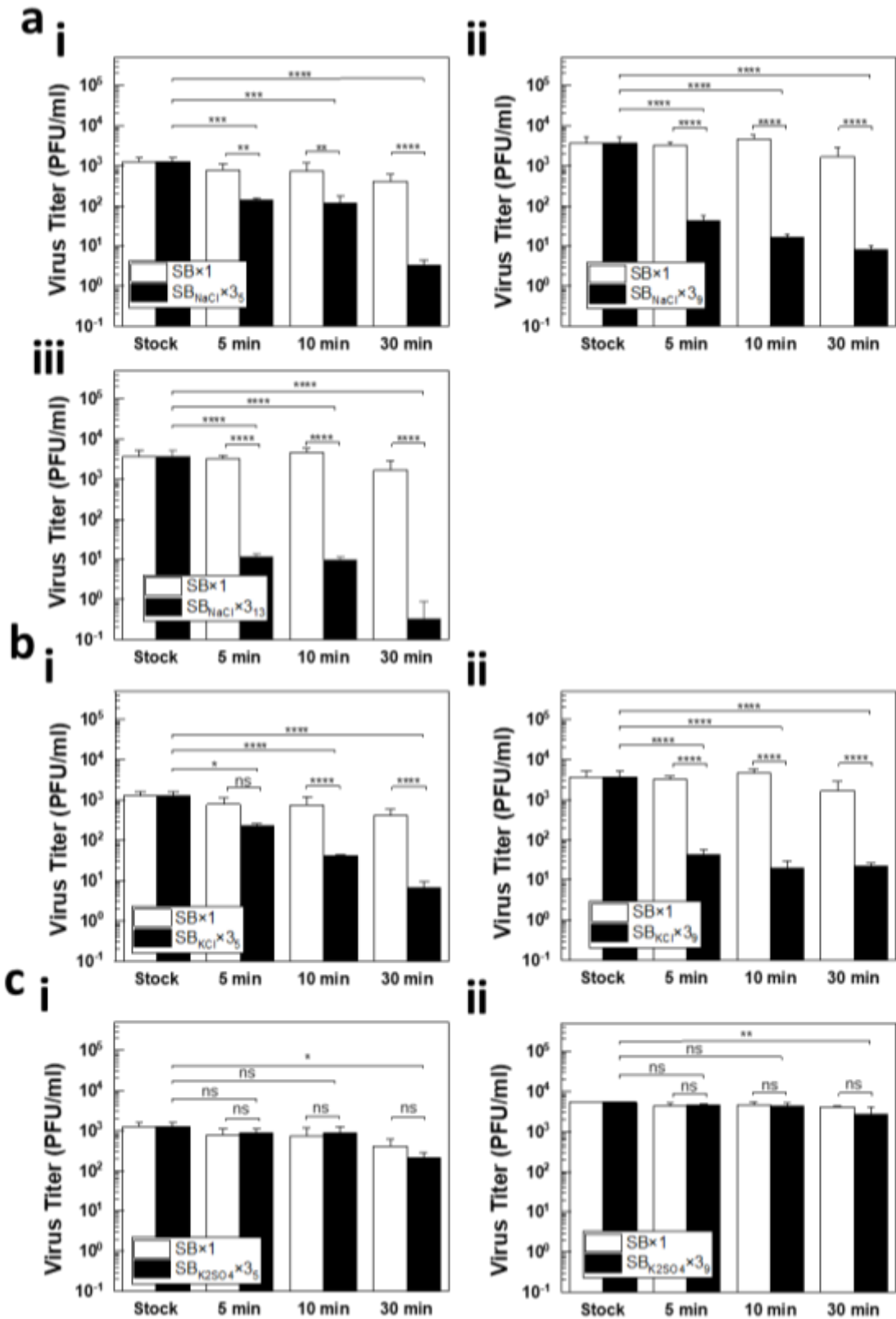


**Figure 5.5.** Virus titer showing the effect of incubation time on the viability of HRV 16 upon exposure to salt-coated filters (a: NaCl-coated filters, b: KCl-coated filters, and c: K<sub>2</sub>SO<sub>4</sub>-coated filters) with different salt amount (i: 5 mg/cm<sup>2</sup> and ii: 9 mg/cm<sup>2</sup>, and iii: 13 mg/cm<sup>2</sup>). (n = 3, mean ± SD). §: below detection limit. For all panels: ns: P > 0.05; \*P < 0.05; \*\*P < 0.01; \*\*\*P < 0.001; \*\*\*\*P < 0.0001, by one-way ANOVA.

### 5.3.2 Particle filtration efficiency and breathability: evaluating the effectiveness of salt-coated stacked SB fabrics as an outer layer and a cover for conventional mask

To characterize the performance of each mask layer and evaluate the effects of various layer sequences, we conducted breathability and filtration efficiency tests using both bare and salt-coated fabrics. This work was designed for two application purposes based on NaCl-coated SB fabrics: employing salt-coated SB fabrics and non-salt-coated fabrics either 1) as an outer layer of a 3-ply mask (stacking sequence: outer(O: SB×3)/middle(M: MB×1)/inner(I: SB×1) and outer(O: SB<sub>NaCl</sub>×3<sub>9</sub>)/middle(M: MB×1)/inner(I: SB×1) or 2) as a cover over a conventional 3-ply mask (stacking sequence: SB×3 and SB<sub>NaCl</sub>×3<sub>9</sub> on top of a 3-ply mask, i.e. cover(C: SB×3)/3-ply mask and cover(C: SB<sub>NaCl</sub>×3<sub>9</sub>)/3-ply mask).

As shown in the left of Figure 5.6, the pressure drop ( $\Delta P$ ) of SB and MB fabrics comprising outer(O)/inner(I) and middle(M) layers of a 3-ply mask was measure to be 1.2/2.1 and 34.2 Pa/cm<sup>2</sup>, respectively. Three stacked SB fabrics (SB×3) showed an increase of  $\Delta P$  to 6.1 Pa/cm<sup>2</sup> (one-way ANOVA,  $P < 0.0001$ ) compared to SB×1, and salt coating of 9 mg/cm<sup>2</sup> (SB<sub>NaCl</sub>×3<sub>9</sub>) appears to have the effect of further increasing  $\Delta P$  to 7.0 Pa/cm<sup>2</sup>, as determined through a comparison of mean values (one-way ANOVA,  $P < 0.0001$ ). It is noted that a conventional 3-ply mask (stacking sequence: SB×1/MB×1/SB×1), where a single SB fabric forms the outer layer, exhibits  $\Delta P$  of  $38.5 \pm 0.2$  Pa/cm<sup>2</sup> (right of Figure 5.6). When replacing the outermost layer with triple-stacked SB fabric (SB×3), the pressure drop ( $\Delta P$ ) increased by 4.8 Pa/cm<sup>2</sup> compared to the conventional mask with a single SB fabric in both the outer and inner layers ( $\Delta P = 43.3 \pm 1.7$  Pa/cm<sup>2</sup> for SB×3/MB×1/SB×1). In addition, a pressure drop of  $45.1 \pm 3.3$  Pa/cm<sup>2</sup> was observed in masks with salt-coated stacked SB fabric as the outer layer (i.e., SB<sub>NaCl</sub>×3<sub>9</sub>/MB×1/SB×1). In the case of using SB×3 and SB<sub>NaCl</sub>×3<sub>9</sub> as a mask cover,  $45.6 \pm 0.4$  Pa/cm<sup>2</sup> and  $48.1 \pm 1.2$  Pa/cm<sup>2</sup> were observed, respectively. This indicates that the use of three

stacked salt-coated SB PP fabrics ( $SB_{NaCl \times 3}$ ) as the outer layer and cover of a mask results in a 6.7 to 9.8 Pa/cm<sup>2</sup> of  $\Delta P$ , compared to a conventional 3-ply mask, showing a reduction in breathability. However, according to ASTM standards, the  $\Delta P$  of masks must be less than 50 Pa/cm<sup>2</sup> and 60 Pa/cm<sup>2</sup> for level 1 and level 2/3, respectively. Therefore, it is clear that using three stacked salt-coated SB fabrics as the outer layer of a 3-ply mask and cover on top of a conventional satisfy the pressure drop regulations set by ASTM, even though there is a slight decrease in breathability.

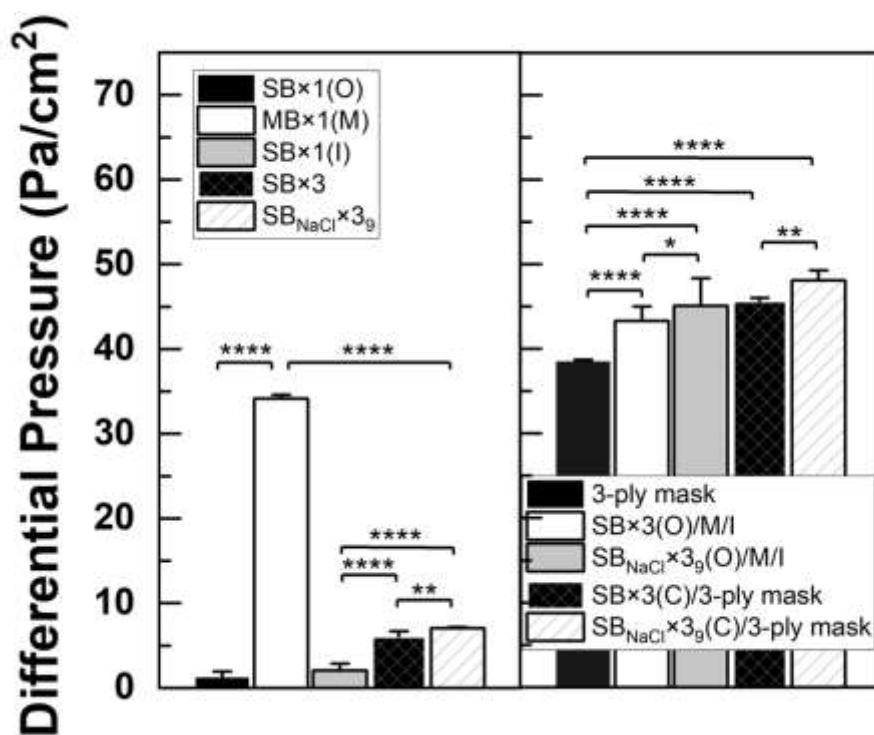


**Figure 5.6.** Breathability of salt-coated fabrics. Left: Differential pressure of each layer, i.e. spunbond fabrics (inner layer: SB×1, outer layer: SB×1), meltblown fabrics (middle layer: MB×1), a stack of 3 spunbond fabrics (3-inner PP fabric stack: SB×3), and a stack of salt-coated spunbond fabrics (3-inner PP fabric stack, coated with 9 mg/cm<sup>2</sup> NaCl: SB<sub>NaCl</sub>×3<sub>g</sub>). Right: Differential pressure of the bare or salt-coated spunbond fabrics when used as an outer layer of the 3-ply mask (SB<sub>NaCl</sub>×3<sub>g</sub>/middle/inner) or cover on top of a mask (SB<sub>NaCl</sub>×3<sub>g</sub>/whole mask). (n =10-11, mean ± SD).

Testing for particle capturing efficiency of a 3-ply mask was conducted using sulforhodamine B (SRB), a fluorescent dye, to simulate biocontamination. Particles are classified into three categories based on size: aerosol ( $< 5 \mu\text{m}$ ), droplets ( $< 100 \mu\text{m}$ ), and splash ( $> 100 \mu\text{m}$ )[64]. Various activities, such as breathing ( $1.19\text{-}1.58 \mu\text{m}$ ), talking ( $35\text{-}50 \mu\text{m}$ ), and coughing ( $35\text{-}100 \mu\text{m}$ ) have been reported to generate particles of different sizes, serving as a medium for infectious disease transmission [286, 360]. To encompass the range, we utilized two different-sized particles, specifically large droplets ( $352 \pm 207 \mu\text{m}$ ; see Figure 5.2 for size distribution and measuring conditions) and aerosols ( $2.5 - 4 \mu\text{m}$ ). When exposed to droplet spray, a 3-ply mask intercepted 92% with the outer layer (i.e., SB $\times$ 1), and the remaining 8% were captured by the middle layer (i.e., MB $\times$ 1) (Figure 5.7a-i). This is consistent with optical microscope observations, which showed that the majority of droplets were present on the outer layer (Figure 5.7a-ii). Similarly, 89% of aerosols were captured by the outer layer and 11% by the middle layer (Figure 5.7b-i), which was confirmed by optical microscope analysis (Figure 5.7b-ii). The filtration efficiency results indicate that the outer layer is primarily responsible for capturing most of large particles. However, it must be noted that this test has limitations in simulating real-case breathing scenarios due to the absence of airflow conditions, including inhalation rates during rest or rapid walking (10-40 LPM) and high labor intensity (85 LPM)[361].

In the case of aerosols, to predict the effects of inhalation airflow, the filtration efficiency of individual layer of 3-ply mask was characterized under an airflow of 85 LPM using 5% NaCl aerosol particles sized  $0.1\text{-}3 \mu\text{m}$  (Figure 5.8). Then, the obtained size-dependent filtration efficiency corresponding to  $3 \mu\text{m}$  particles (Figure 5.8) was used to predict the particle capturing efficiency of each layer of a 3-ply mask (Figure 5.9) and compared to the dye experiments involving a nebulizer (Figure 5.7b; particle size range:  $2.5\text{-}4 \mu\text{m}$ ). Since the filter tester

equipment is capable of measuring the filtration efficiency of particles as large as 3  $\mu\text{m}$  under specified airflow conditions, the filtration efficiency corresponding to 3  $\mu\text{m}$  particles was compared with that obtained from a dye experiment using aerosols to predict the effect of airflow on filtration efficiency. This comparison is based on the similarity of their sizes; that is, the average aerosol size is 3.25  $\mu\text{m}$ , close to 3  $\mu\text{m}$ , where sedimentation and inertial impaction are the main mechanisms influencing filtration efficiency [284]. As shown in Figure 5.9a, the capturing efficiency of individual layer of a 3-ply mask against 3  $\mu\text{m}$  particles was estimated to be  $49.2 \pm 24.9\%$  for SB $\times$ 1(O),  $48.2 \pm 8.1\%$  for MB $\times$ 1(M), and  $1.4 \pm 0.4\%$  for SB $\times$ 1(I), calculated based on the particle filtration efficiency at 3  $\mu\text{m}$  in Figure 5.8 (SB $\times$ 1(O):  $49.2 \pm 24.9\%$ , MB $\times$ 1(M):  $94.9 \pm 16.0\%$ , and SB $\times$ 1(I):  $53.7 \pm 15.9\%$ ). Upon comparing the individual layer performance of a 3-ply mask with and without inhalation airflow conditions (see Figure 5.7b and 5.9a), the capturing efficiency of particles for the outer layer (SB $\times$ 1) was noticeably lower when exposed to inhalation airflow compared to the condition without inhalation airflow (*t*-test,  $P = 0.059$  for outer layer). In contrast, the middle layer (MB $\times$ 1) exhibited the opposite trend (*t*-test,  $P = 0.0063$  for middle layer). Moreover, it is evident that the outermost layer (SB $\times$ 1) showed an increase in filtration efficiency with increasing droplet size and decreasing inhalation airflow (Figure 5.8 and 5.10). These results demonstrate that the SB layer of a 3-ply mask plays a crucial role in capturing larger infectious droplets carrying pathogens. The findings support the rationale for employing the salt-coated stacked SB layer, the focus of this study, either as the outermost layer of the mask or as a covering over it. In this work, considering the higher filtration efficiency of the inner SB fabric of a conventional 3-ply mask over the outer SB fabric (GLM,  $P = 0.0343$ ; Figure 5.8a and 5.8c), the stacked SB PP fabrics with and without salt coating (SB $\times$ # or SB<sub>Salt $\times$ #Amount</sub>), a key aspect of our investigation, have been fabricated for their application to the outer layer of a 3-ply mask or mask covering (see Figure 5.9b for particle

capturing efficiency of SB×1(I)/MB×1(M)/SB×1(I).

A stack of three SB fabrics showed a rapid increase in filtration efficiency with the increase of particle size under the standard filter testing conditions (85 LPM), as observed from the single SB fabric (see Figure 5.10a: SB×3 and 5.10b: SB<sub>NaCl</sub>×3<sub>9</sub>). Upon examining the particle size-filtration efficiency relationship, it is evident that the increase in filtration efficiency with particle sizes is more pronounced for particles larger than 1 μm in both stacked SB fabrics and salt-coated fabrics, when compared to the scenarios without stacking and salt coating (SB×1). This is confirmed through the comparison of the slope in the filtration efficiency vs particle size graph, ranging from 1 to 3 μm:  $20.6 \pm 2.8$  for SB×1 (Figure 5.8c-ii),  $23.8 \pm 4.8$  for SB×3 (Figure 5.10a), and  $27.7 \pm 3.3$  for SB<sub>NaCl</sub>×3<sub>9</sub> (Figure 5.10b).

Upon spraying large droplets ( $352 \pm 207$  μm; Figure 5.7a) and exposing aerosols (2.5 - 4 μm; Figure 5.7b), all droplets containing SRB dye were captured by three stacked SB PP fabrics both w/ and w/o salt coating (see Figure 5.11-i for SB×3 and Figure 5.11-ii for SB<sub>NaCl</sub>×3<sub>9</sub>). Therefore, a stack of salt-coated SB fabrics, when used as the outer layer of a 3-ply mask or a cover over a mask, demonstrates remarkable effectiveness in capturing micrometer-sized aerosols and large droplets while maintaining breathability—a crucial factor for user comfort. As such, salt-coated stacked SB fabric positioned at the top of masks can capture and destroy a greater number of infectious aerosols at the micron scale and large droplets, while MB fabrics provide high filtration efficiency against smaller aerosols at the submicron scale.

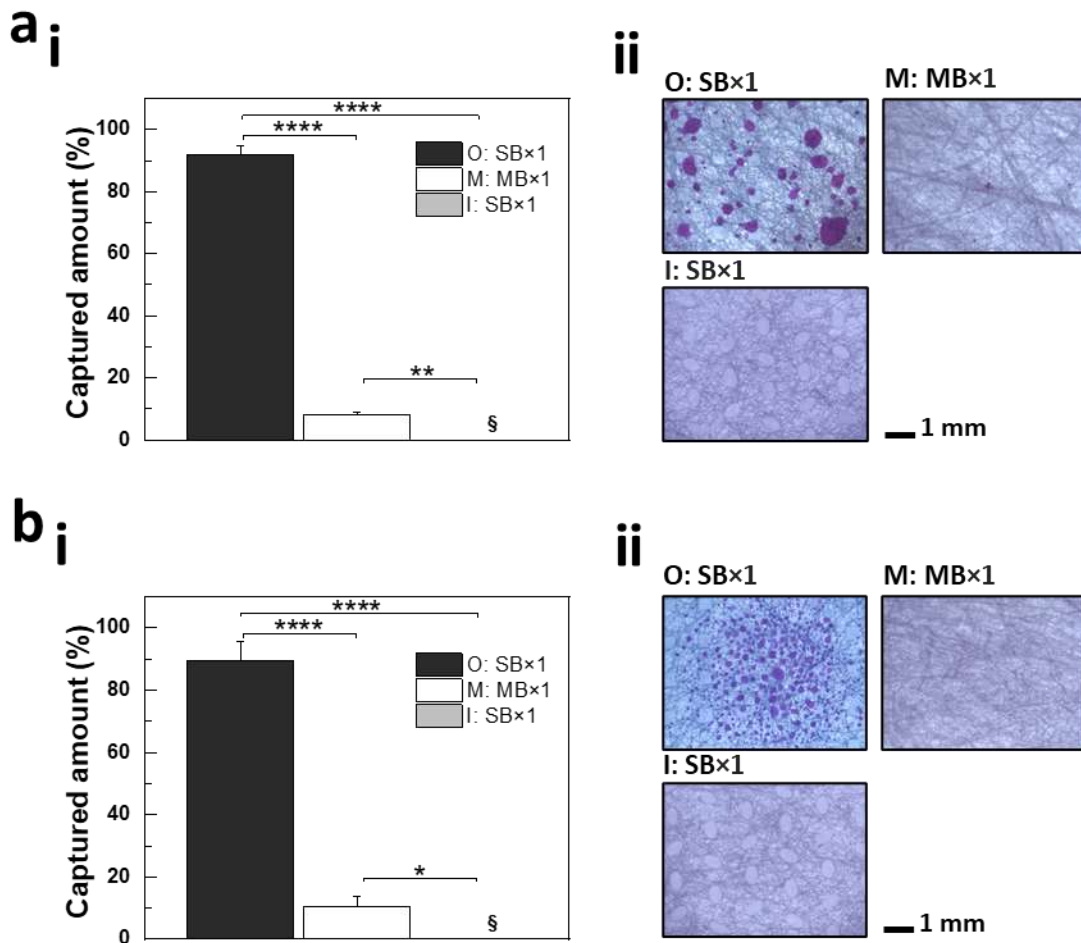


**Figure 5.7.** Particle capturing efficiency measurement of each layer of a surgical mask. (a, b) A 3-ply mask (stacking sequence: SB×1 (O)/MB×1 (M)/SB×1 (I)) underwent 1.5 mg/cm<sup>2</sup> of droplet spraying (a, 352 ± 207 μm in diameter) and 0.3 mg/cm<sup>2</sup> aerosol exposure (b, 2.5-4 μm in diameter) without airflow, followed by the separation of each layer and measurement of fluorescent intensity (i). (ii) Optical microscope images of SB×1 (O), MB×1 (M), and SB×1 (I) tested as aforementioned. (n = 3, mean ± SD). §: below detection limit. For all panels: ns: P > 0.05; \*P < 0.05; \*\*P < 0.01; \*\*\*P < 0.001; \*\*\*\*P < 0.0001, by one-way ANOVA.

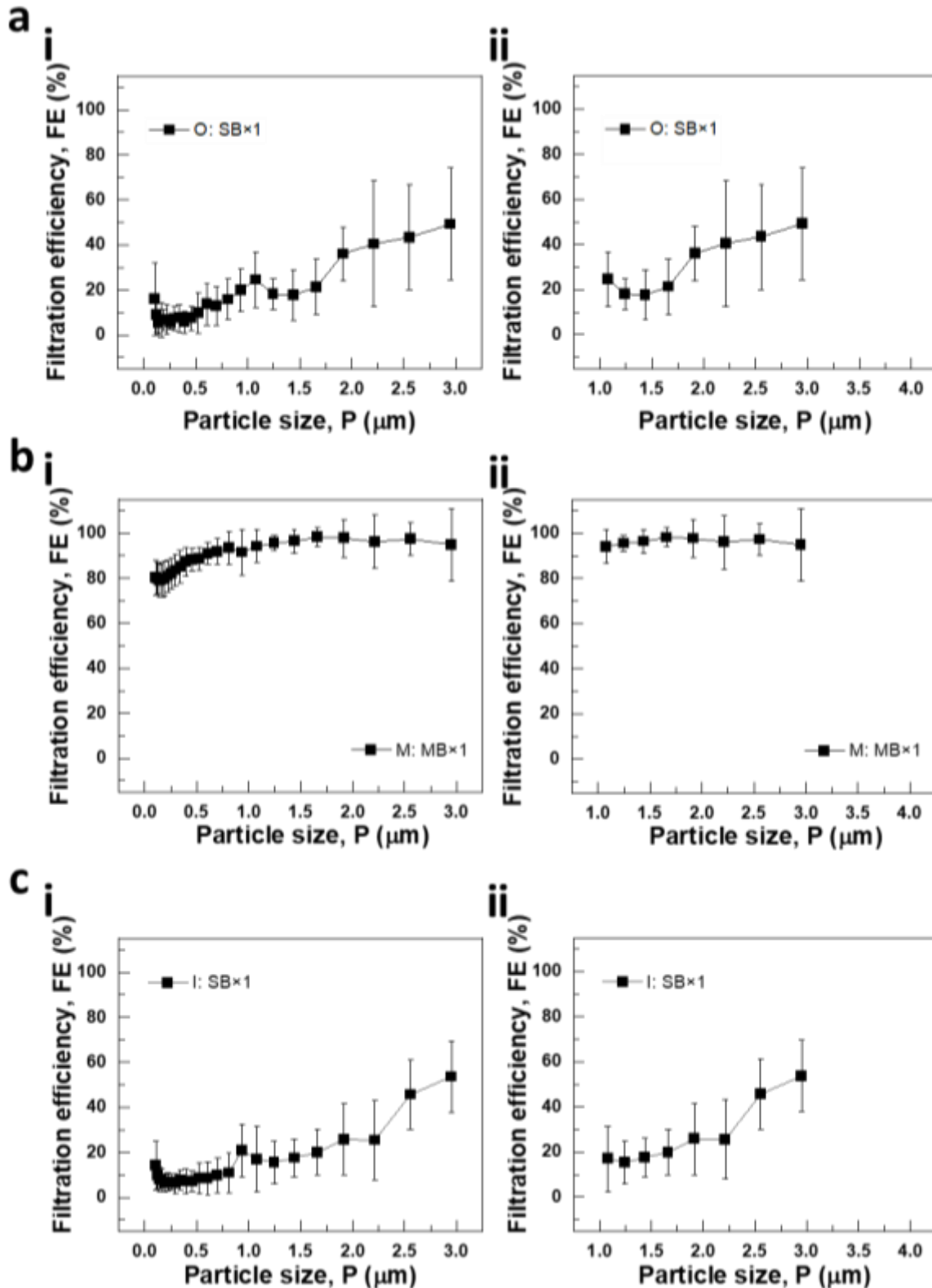


**Figure 5.8.** Particle size-dependent filtration efficiency of each layers of surgical masks. (i) Filtration efficiency of outer (a), middle (b), and inner (c) layers. (ii) Relationship between particle size ( $P$ ) and filtration efficiency (FE) examined within the particle size range of 1 to 4  $\mu\text{m}$  ( $n=9\text{-}24$ , mean  $\pm$  SD). Fitting equations are shown ( $R^2=0.75$  (a), 0.77 (b), and 0.9 (c)). The filtration efficiency values at 3.5 and 4  $\mu\text{m}$  particle size were calculated using the fitting equations. These values were then employed to estimate the average filtration efficiency of particles within the range of 2.5 to 4  $\mu\text{m}$  under specific airflow conditions. This estimation was compared to dye-based aerosol experiments conducted under conditions of no significant airflow.

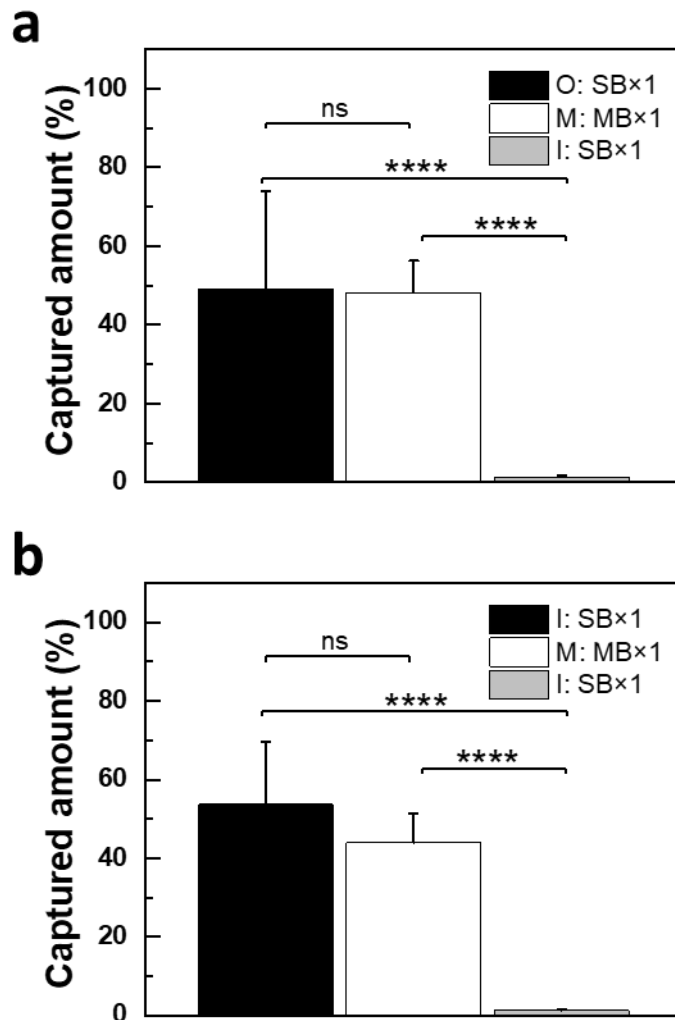


**Figure 5.9.** Particle capturing efficiency of individual layer of a surgical mask. (a) Conventional 3-ply mask (stacking sequence: SB×1(O)/MB×1(M)/SB×1(I)). (b) 3-ply mask (stacking sequence: SB×1(I)/MB×1(M)/SB×1(I)). (n = 12-14, mean ± SD). In this work, due to the higher filtration efficiency of the inner SB fabric of a conventional 3-ply mask compared to that of outer SB fabric, the stacked SB PP fabrics with and without salt coating (SB×# or SB<sub>Salt×#Amount</sub>), which are main focus of this study, have been fabricated for their application to the outer layer of a 3-ply mask or mask covering. This was achieved by utilizing the inner SB fabrics for their application to the outer layer of a conventional 3-ply mask and mask covering.

The particle capturing efficiency (PCE) of each layer in a 3-ply mask was calculated based on the average particle filtration efficiency (PFE) measurements at 3 μm particle size. Specifically, the capturing efficiency of the first layer ( $PCE_{1st-layer}$ ) is equal to the filtration efficiency of the first layer (i.e.,  $PFE_{1st-layer}$ ). The capturing efficiency of the second layer ( $PCE_{2nd-layer}$ ) is calculated as  $((100 - PCE_{1st-layer}) \times PFE_{2nd-layer} / 100)$ , and the capturing efficiency of the third layer ( $PCE_{3rd-layer}$ ) is calculated as  $((100 - PCE_{1st-layer} - PCE_{2nd-layer}) \times PFE_{3rd-layer} / 100)$ .

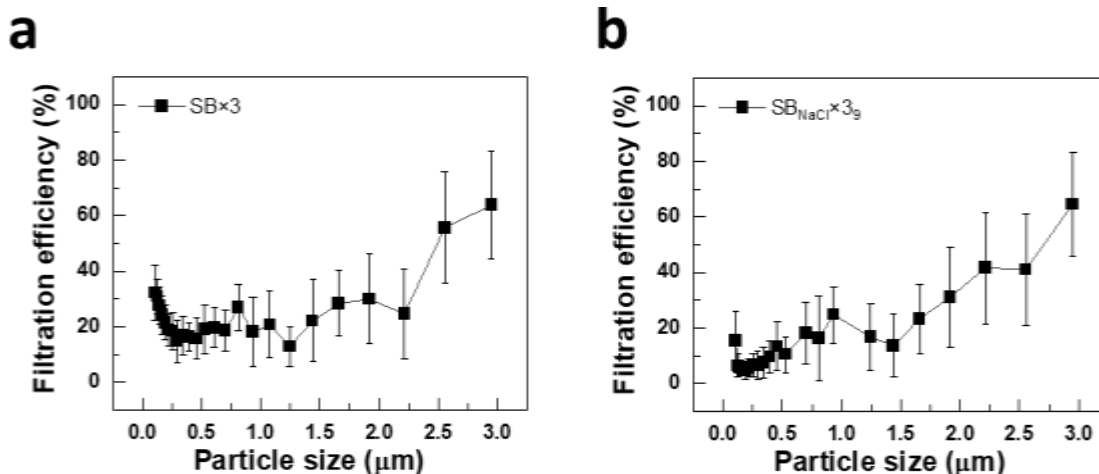


**Figure 5.10.** Particle size-dependent filtration efficiency of SB $\times$ 3 and SB<sub>NaCl</sub> $\times$ 3<sub>9</sub> fabrics. Each layer is subjected to a filtration efficiency test with airflow (85 LPM) using the PALAS PMFT 1000. (n = 7-13 for (i) and n = 8-19 for (ii), mean  $\pm$  SD).

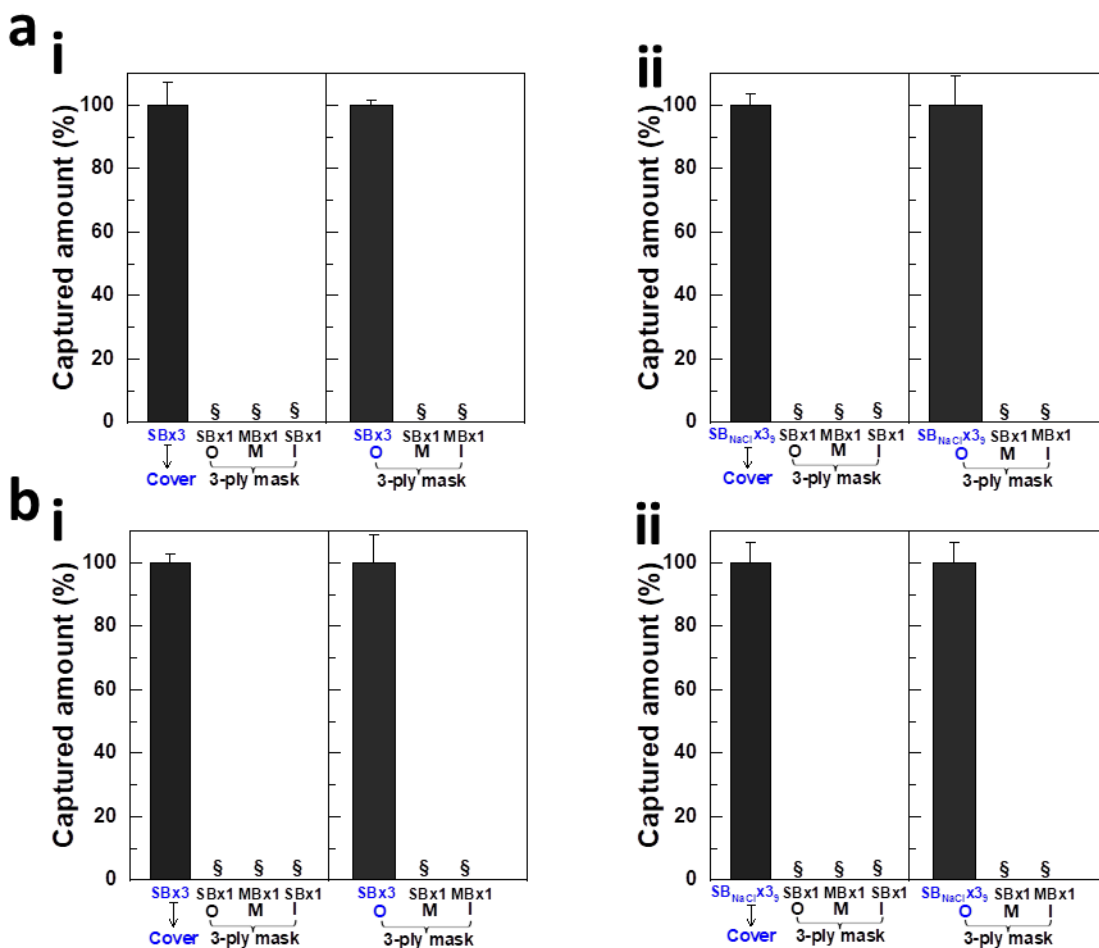


**Figure 5.11.** Filtration efficiency of SB $\times$ 3 (i) and SB<sub>NaCl</sub> $\times$ 3<sub>9</sub> (ii), measured using spray droplets (d) or aerosol (e), when they were used as a mask cover (stacking sequence: SB $\times$ 3 and SB<sub>NaCl</sub> $\times$ 3<sub>9</sub> on top of a 3-ply mask) and outer layer of a 3-ply mask (stacking sequence: SB $\times$ 3/middle/inner or SB<sub>NaCl</sub> $\times$ 3<sub>9</sub>/middle/inner). (n = 3 for c and d, mean  $\pm$  SD). §: below detection limit. For all panels: ns: P > 0.05; \*P < 0.05; \*\*P < 0.01; \*\*\*P < 0.001; \*\*\*\*P < 0.0001, by one-way ANOVA.

### 5.3.3 Contact transmission test through simulated biocontamination

To examine the pathogen translocation from contaminated masks to hands, fluorescent dyes (sulforhodamine b: SRB, calcofluor white: CW) were used to simulate contaminants on mask fabrics. For this purpose, three different types of architecture containing CW-contaminated MB (CW-MB) and/or SRB-contaminated SB (SRB-SB) fabrics were manufactured to compare and analyze the difference in transmission levels of contaminants based on the type of pressing pressure, fabric type, mask architecture, and salt coating: outermost layer contamination (SRB-SB×1, CW-MB×1, and SRB-SB×3, and SRB-SB<sub>NaCl</sub>×3<sub>9</sub>), middle layer only contamination (SB×1/CW-MB×1), and both outermost and middle layer contamination (SRB-SB×1/CW-MB×1). Figure 5.12 represents optical micrographs taken at 1, 5, 10, 15, 20, and 30 min of incubation after spraying 1.5 mg/cm<sup>2</sup> of large droplets containing dyes (red: SRB, blue: CW) on various mask fabrics. Simulated contaminant droplets are easily identified up to 10 min on both SRB-SB and CW-MB fabrics and rapidly shrink and fade over time due to water evaporation. On the other hand, contaminants sprayed on the salt-coated stacked SB fabric (SRB-SB<sub>NaCl</sub>×3<sub>9</sub>) were observed spreading widely over the fabric surface, in contrast to those on the non-salt-coated fabric, where they formed droplet shapes. This could be associated with the hydrophilic property of the salt-coated fabrics due to the presence of surfactant added to enhance salt coating on the fabrics.

To characterize contact transmission efficiency, the dye-contaminated fabrics, as shown in Figure 5.12, were pressed with a gloved thumb using both gentle ( $6.4 \pm 1.4$  kPa) and strong ( $11.3 \pm 3.6$  kPa) pressure. Microscope images in Figure 5.13 indicate that strong pressure shows clear droplet images up to 10 min of incubation, in contrast to 5 min by gentle pressure on non-salt-coated PP fabrics (see Figure 5.14 for micrographs corresponding to 15, 20, and 30 min

incubation). Interestingly, the image of the translocated dye was less clearly observed in the micrographs of the thumb touching the SRB-SB<sub>NaCl</sub>×3<sub>9</sub> fabric, unlike in the non-salt-coated fabric. Considering the use of the same amount of dye for contamination purposes, the seemingly reduced translocation behavior of SRB-SB<sub>NaCl</sub>×3<sub>9</sub> could be attributed to the accelerated evaporation of water resulting from spreading.

An additional intriguing observation is the significant role played by the outermost layer in the contact transmission of contaminants. As can be seen in Figure 5.13, in all architectures except for SB×1/CW-MB×1, featuring contaminated outermost layers, wet-state contaminants that persisted on fabrics touched directly by fingers were the primary contributors to the contamination of gloved fingers. This finding is further supported by the noticeable reduction in the translocation of contaminants when bare SB×1 is placed atop CW-MB×1. This observation emphasizes that the outermost layer of masks predominantly contributes to contact-based transmission. Consequently, prioritizing antimicrobial functionalization of this layer is essential to reduce the risk of contact-based disease transmission.

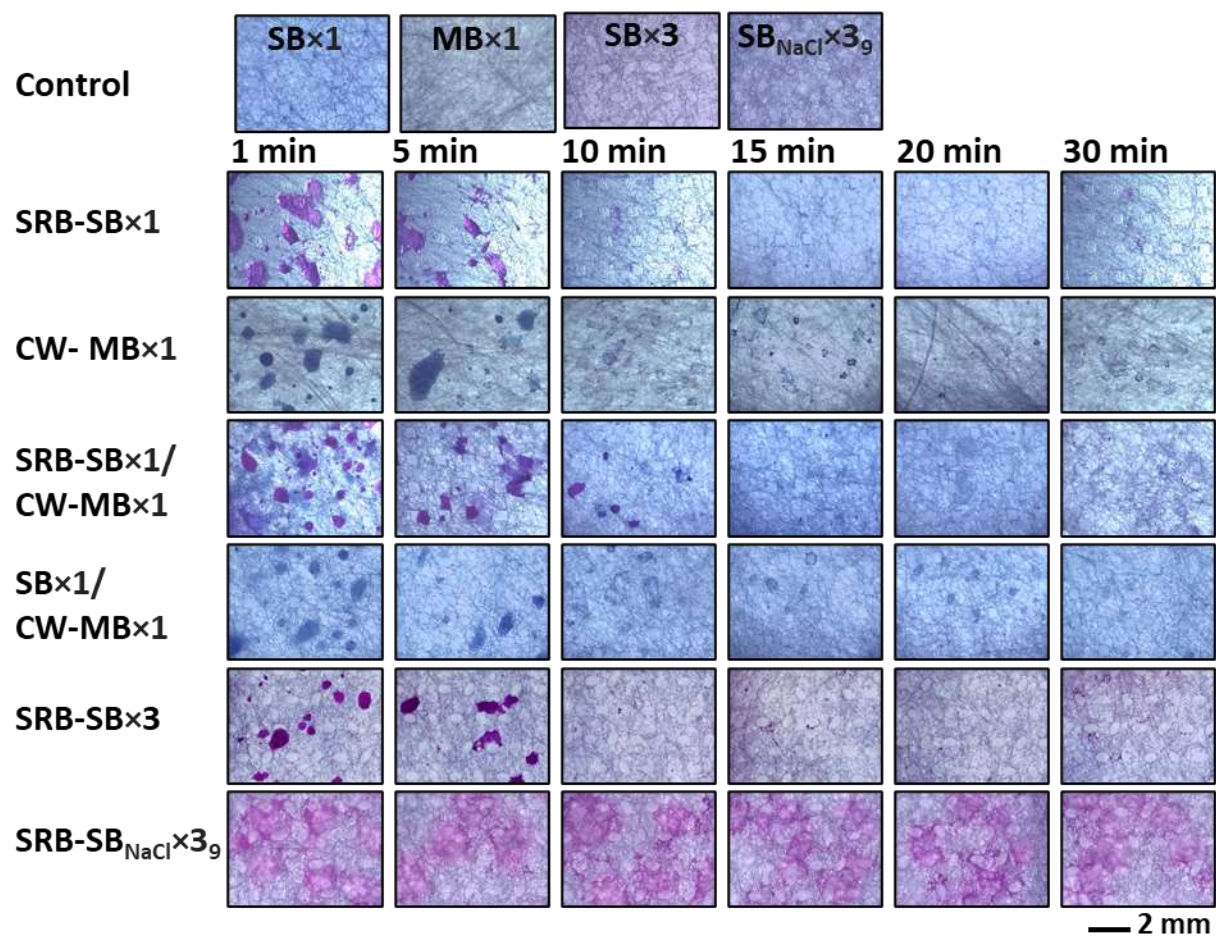


**Figure 5.12.** Bare and salt-coated filters before (control) and after spraying 1.5 mg/cm<sup>2</sup> of calcofluor white (CW) or sulforhodamine B (SRB) over the course of incubation time.

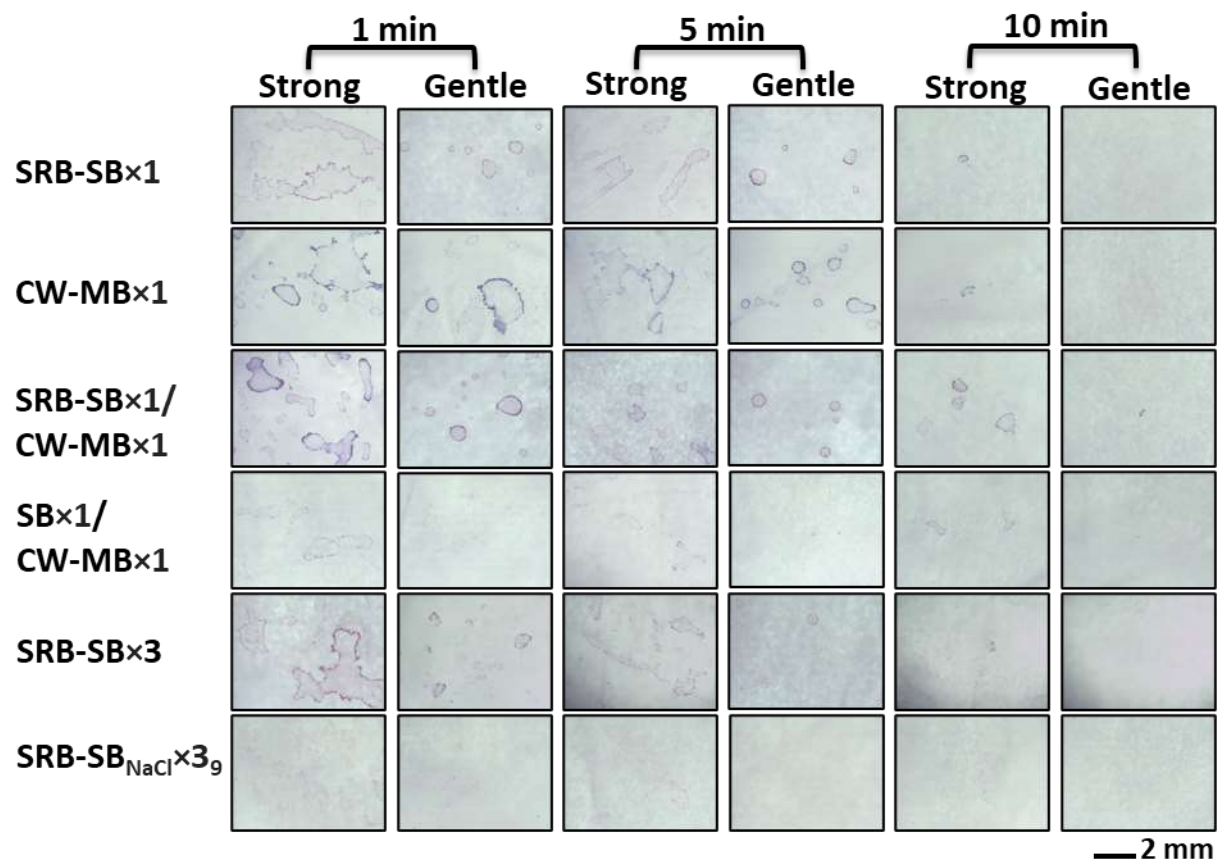


**Figure 5.13.** Characterization of gloves after strong/gentle pressing with a gloved thumb on various architecture containing calcofluor white (CW)-contaminated MB fabric and/or sulforhodamin B (SRB)-contaminated SB fabrics (w/ and w/o NaCl coating) after 1, 5, and 10 min of incubation at room temperature. Optical micrographs represent the transferred contaminants from mask fabrics to gloved thumbs.

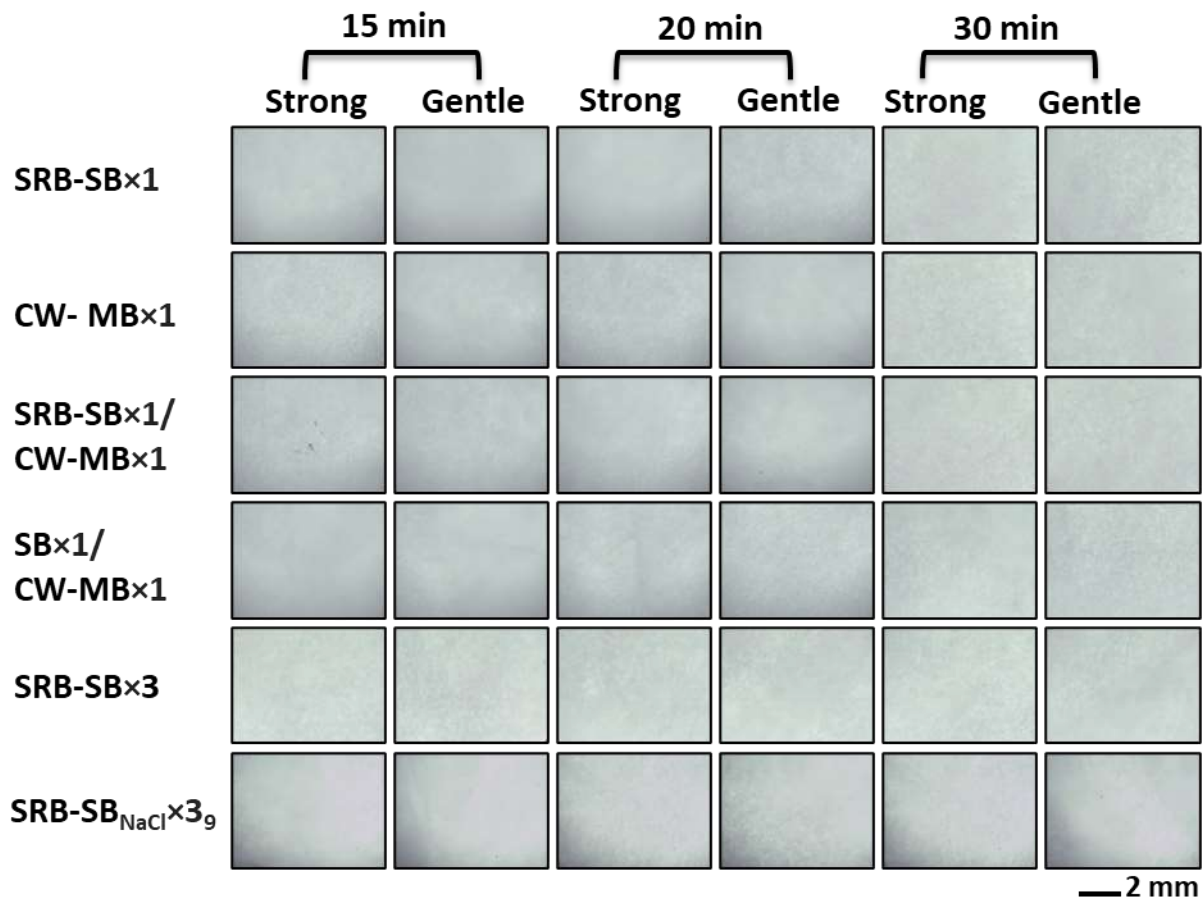


**Figure 5.14.** Optical microscopy analysis to investigate the role of individual mask layer of a 3-ply mask and the effects of mask architecture/salt coating on the contact transmission behavior using fluorescent dye-contaminated mask fabrics. Characterization of gloves after strong/gentle pressing with a gloved thumb on various architecture containing calcofluor white (CW)-contaminated MB fabric and/or sulforhodamin B (SRB)-contaminated SB fabrics (w/ and w/o NaCl coating) after 15, 20, and 30 min of incubation at room temperature. Optical micrographs represent the transferred contaminants from mask fabrics to gloved thumbs.

To determine the percentage of translocated CW, the fluorescence intensity—measured from the dye released from gloves—was utilized in relation to the amount of dye sprayed on the fabrics (Figure 5.15a: CW-MB×1 and 5b: SB×1/CW-MB×1), for the calculation of transmission efficiency. It is evident that a stronger press resulted in the transfer of more contaminants for both the thumb and index finger (GLM,  $P < 0.0001$ ; Figure 5.15a and b). Furthermore, the translocation percentage rapidly decreased over the increase in incubation time, with none detected after 10 or 15 min, as observed in Figure 5.14. Figure 5.15b highlights that, through a comparison of CW-MB×1 and SB×1/CW-MB×1, the outermost layer plays a key role in the transmission of contaminants. That is, the presence of a SB fabric on top of the CW-contaminated MB fabric (SB×1/CW-MB×1) exhibited a significantly lower level of contamination than CW-MB×1, as observed in the microscopy analysis in Figure 5.14 and supported by fluorescence microscopy analysis in Figure 5.15c.

A similar time and pressure-dependent transmission behavior was observed in the SRB-SB fabric system, as shown in Figures 5.16a and 5.16b. Moreover, as discussed in Figure 5.14 regarding the effects of salt coating on contamination behavior, SRB-SB<sub>NaCl×39</sub> fabrics exhibited a significantly lower level of contaminant translocation (GLM,  $P < 0.0001$ ; Figure 5.16c), further supported by fluorescence microscopy in Figure 5.17. Overall, it is evident that the initial 10 to 15 minutes are critical for the transmission from contaminated mask surfaces under our experimental conditions. The outermost layer emerged as the main source of contaminant transmission, emphasizing the importance of preventive strategies employing antimicrobial substances specifically targeting the outermost layer of a mask. Following the same logic, wearing a mask cover over a conventional mask can be an alternative approach. Therefore, a layer of salt-coated three stacked SB (SB<sub>NaCl×39</sub>) fabric can be importantly used to mitigate the

risk of contact transmission of conventional masks, either by replacing the SB×1 fabric of the outer layer of a mask (SB<sub>NaCl</sub>×3<sub>9</sub>/MB×1/SB×1) or by wearing it like a mask cover on top of a conventional face mask (SB<sub>NaCl</sub>×3<sub>9</sub>/3-ply mask).

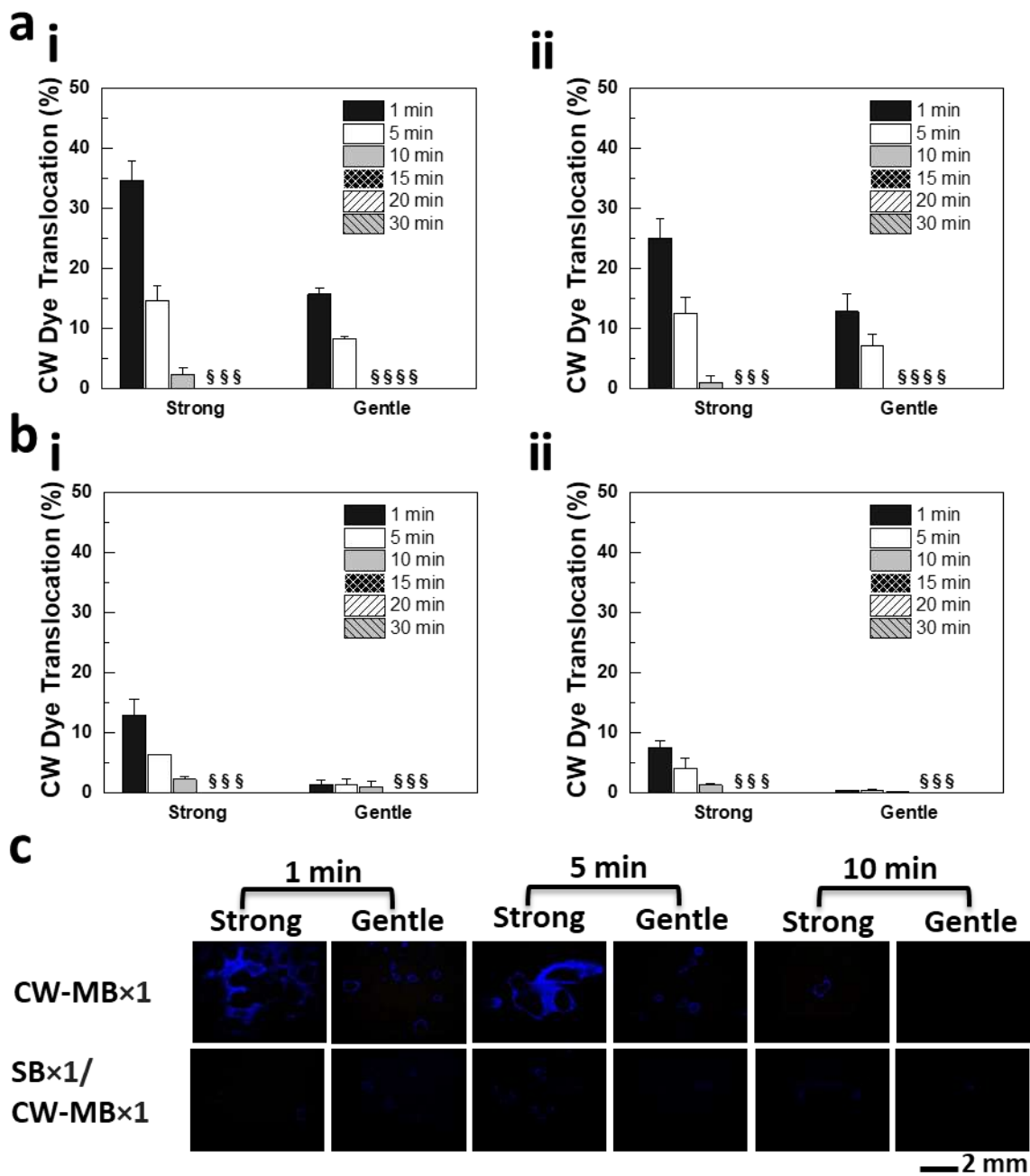


**Figure 5.15.** Contact transmission of calcofluor white (CW)-sprayed mask. Translocation of CW associated with a finger pressing from CW-contaminated meltblown (MB) middle layer (i.e., (a) CW-MB×1 and (b) SBx1/CW-MB×1) to thumb (i) and index finger (ii) pressing. The amount of the translocated CW was analyzed using fluorometer (excitation/emission: 350/432 nm). (n = 3, mean ± SD). §: below detection limit. (c) Fluorescent microscope images of thumb gloves subsequent to the contact with the CW-contaminated fabrics at 1, 5, and 10 min after CW spray.

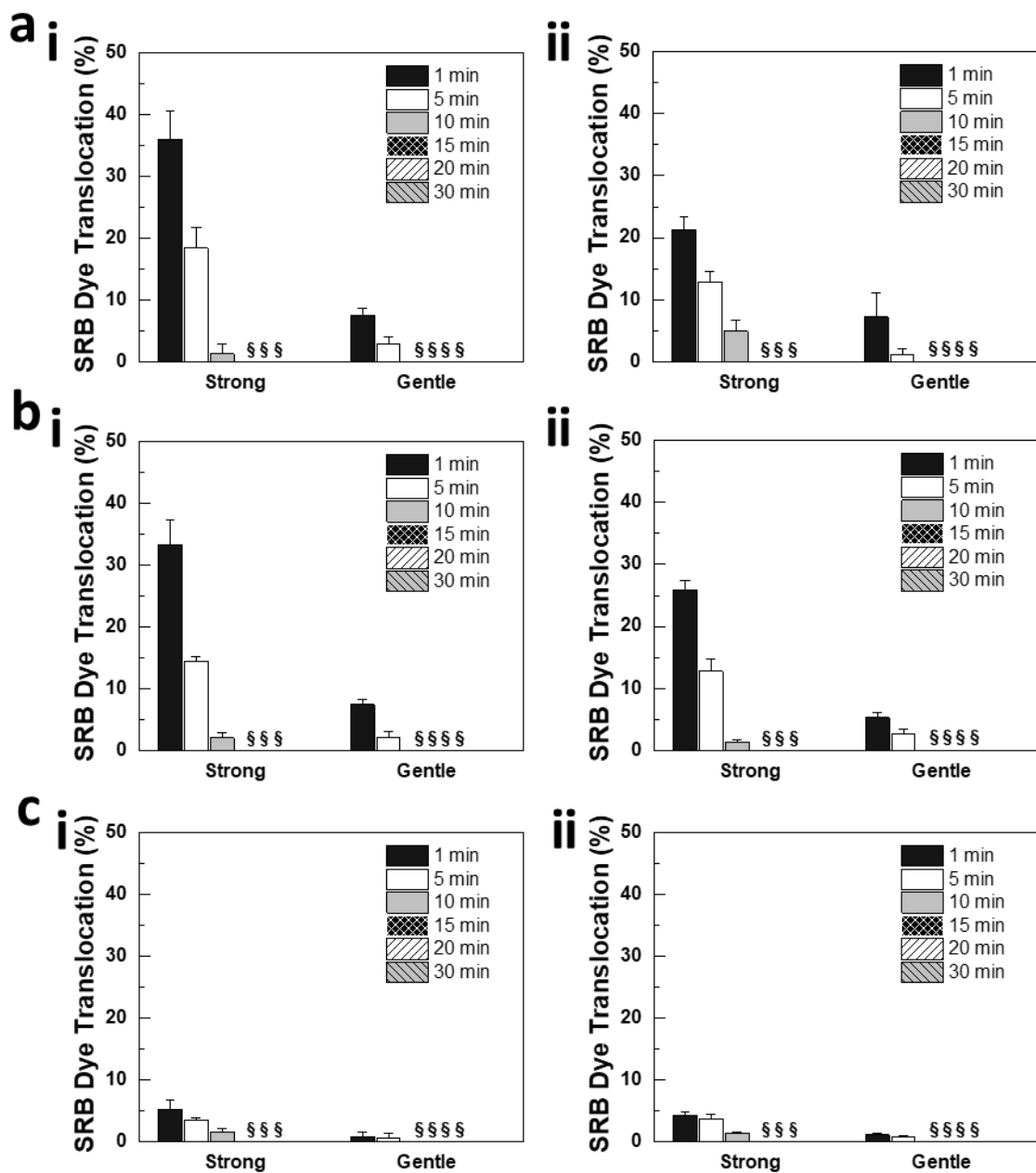


**Figure 5.16.** Contact transmission of sulforhodamine B (SRB)-sprayed mask. Translocation of SRB associated with a finger pressing from SRB-contaminated outermost layer (i.e., (a) SRB-SB $\times$ 1, (b) SRB-SB $\times$ 3 and (c) SRB-SB $\times$ 3<sub>NaCl</sub>) to thumb (i) and index finger (ii) pressing. The amount of the translocated SRB was analyzed using fluorometer (excitation/emission: 565/586 nm). (n = 3, mean  $\pm$  SD). §: below detection limit.

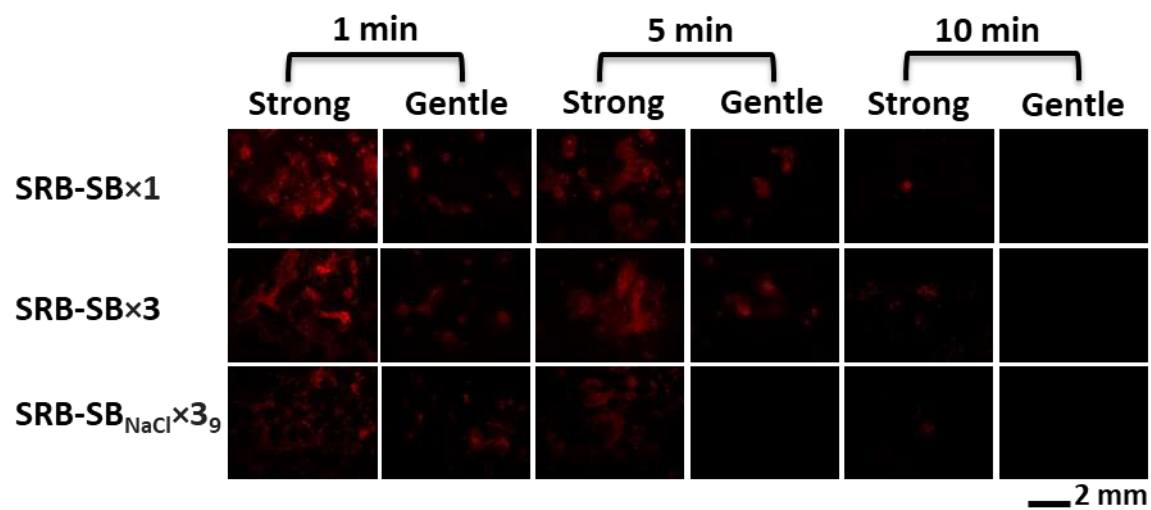


**Figure 5.17.** Fluorescent microscope images of gloves after the contact with the SRB-contaminated fabrics at 1, 5, and 10 min after SRB spray.

### 5.3.4 A stack of salt-coated SB fabrics: preventing contact transmission of bacterial droplets

After studying contact transmission through simulated contamination with fluorescent dyes, the effectiveness of salt-coated SB stacked fabric in mitigating contact transmission was assessed using *K. pneumoniae*. The tests were performed to reflect three different scenarios: contamination of the outermost layer of the mask ( $\text{SB}_{\text{NaCl}\times 3_9}(\mathbf{O})/\text{MB}\times 1(\text{M})/\text{SB}\times 1(\text{I})$ ), contamination of the middle layer ( $\text{SB}_{\text{NaCl}\times 3_9}(\text{O})/\mathbf{MB}\times 1(\mathbf{M})/\text{SB}\times 1(\text{I})$ ), and contamination of the mask cover ( $\text{SB}_{\text{NaCl}\times 3_9}(\mathbf{C})$ /a 3-ply mask). Herein, bold text indicates the contaminated layer. For this purpose,  $1.5 \text{ mg/cm}^2$  of *K. pneumoniae* stock was sprayed onto  $\text{SB}_{\text{NaCl}\times 3_9}$ , representing the contamination of i) the outer layer of a mask,  $\text{SB}_{\text{NaCl}\times 3_9}(\mathbf{O})/\text{MB}\times 1(\text{M})/\text{SB}\times 1(\text{I})$ , and ii) the mask cover,  $\text{SB}_{\text{NaCl}\times 3_9}(\mathbf{C})$ /a 3-ply mask (cover is abbreviated as C). Additionally,  $\text{MB}\times 1$  was contaminated by spraying *K. pneumoniae* droplets and stacked to create  $\text{SB}_{\text{NaCl}\times 3_9}/\text{MB}\times 1$ , representing the contamination of the middle filter layer of the 3-layered mask structure ( $\text{SB}_{\text{NaCl}\times 3_9}(\text{O})/\mathbf{MB}\times 1(\mathbf{M})/\text{SB}\times 1(\text{I})$ ). After contamination,  $\text{SB}_{\text{NaCl}\times 3_9}$  and  $\text{SB}_{\text{NaCl}\times 3_9}/\mathbf{MB}\times 1$  were pressed strongly/gently using a gloved thumb with an increase in incubation time, followed by the analysis of the number of bacteria transferred to the gloves.  $\mathbf{MB}\times 1$  and  $\text{SB}\times 1/\mathbf{MB}\times 1$  were compared to identify the effects of the outer layer in preventing contact transmission from contaminated middle layer.

As shown in Figure 5.18a, the level of bacterial translocation from contaminated  $\text{SB}\times 3$  decreased with increasing incubation time (GLM,  $P < 0.0001$ ). As expected, after 15 min, gentle pressing did not cause the translocation of bacterial contaminant from the fabric to gloves, compared to the translocation of 0.1% ( $\sim 3$ -log reduction) in 15 min and 0.02% ( $\sim 3.7$ -log reduction) in 30 min by the strong pressing (i: strong pressing, ii: gentle pressing). A rapid decrease in translocation efficiency around 10 to 15 min is consistent with our observation by using fluorescent dye experiments shown in Figure 5.16. A surprising finding was that bacteria

exposed to the  $SB_{NaCl \times 39}$  fabric exhibited a very rapid decrease in translocation compared to the non-salt coated fabric, irrespective of the pressing pressure level. Notably, a 4-log reduction occurred within the initial minute, followed by non-detection after 5 min under gentle pressing conditions. In addition, strong press exhibited a rapid decrease in translocation efficiency: a 2.5-log reduction within 1 min, followed by a subsequent 4.5-log reduction within 5 min, and non-detection from 15 min onwards. The remarkable efficacy of salt-coated stacked SB fabric in impeding bacterial disease transmission is presumed to stem from the combined effects of both pronounced pathogen inactivation due to salt recrystallization and a reduction in contact transmission due to its hydrophilic surface property.

Bacteria contaminated MB (i.e., **MB×1**) in Figure 5.18b showed a typical time-dependent decrease of translocation capacity, with a significant decrease in 10 to 15 min, as similarly observed in SB fabrics (Figure 5.18a) and tests with CW dye (Figure 5.15). As such, in 15 min of incubation, around 3 and 4 order decreased in translocation efficiency was observed from strong and gentle press conditions, respectively. It is also evident that the outermost SB fabric on top of the contaminated MB fabric (i.e., **SB×1/MB×1**) contributed to the reduction of bacterial translocation compared to **MB×1**, consistent with Figure 5.15b. However, unlike the contact transmission tests performed with fluorescent dye, where no transfer was observed after 15 min (Figure 5.15), *K. pneumoniae* transmission (with 4 orders of magnitude lower) continued up to 30 min for both **MB×1** and **SB×1/MB×1** under strong pressing (Figure 5.18b-i). Interestingly, as in Figure 5.18a, the use of the salt-coated stacked SB fabric layer over the contaminated MB fabric (i.e.,  $SB_{NaCl \times 39}/\mathbf{MB \times 1}$ ) showed an excellent translocation inhibition behavior (i: strong pressing, ii: gentle pressing). As a result, under our test conditions, the use of  $SB_{NaCl \times 39}$  as the outer layer of a mask was proven to prevent the contact transmission from contaminated MB filter: strong press (2.7-log reduction in 1 min and non-detection within 5

min) and gentle press (non-detection within 1 min). The results illustrate that incorporating a salt-coated multilayer SB nonwoven fabric as the outer layer of a mask or mask cover can significantly diminish bacterial infection through contact transmission, addressing a potential risk in current mask structures.

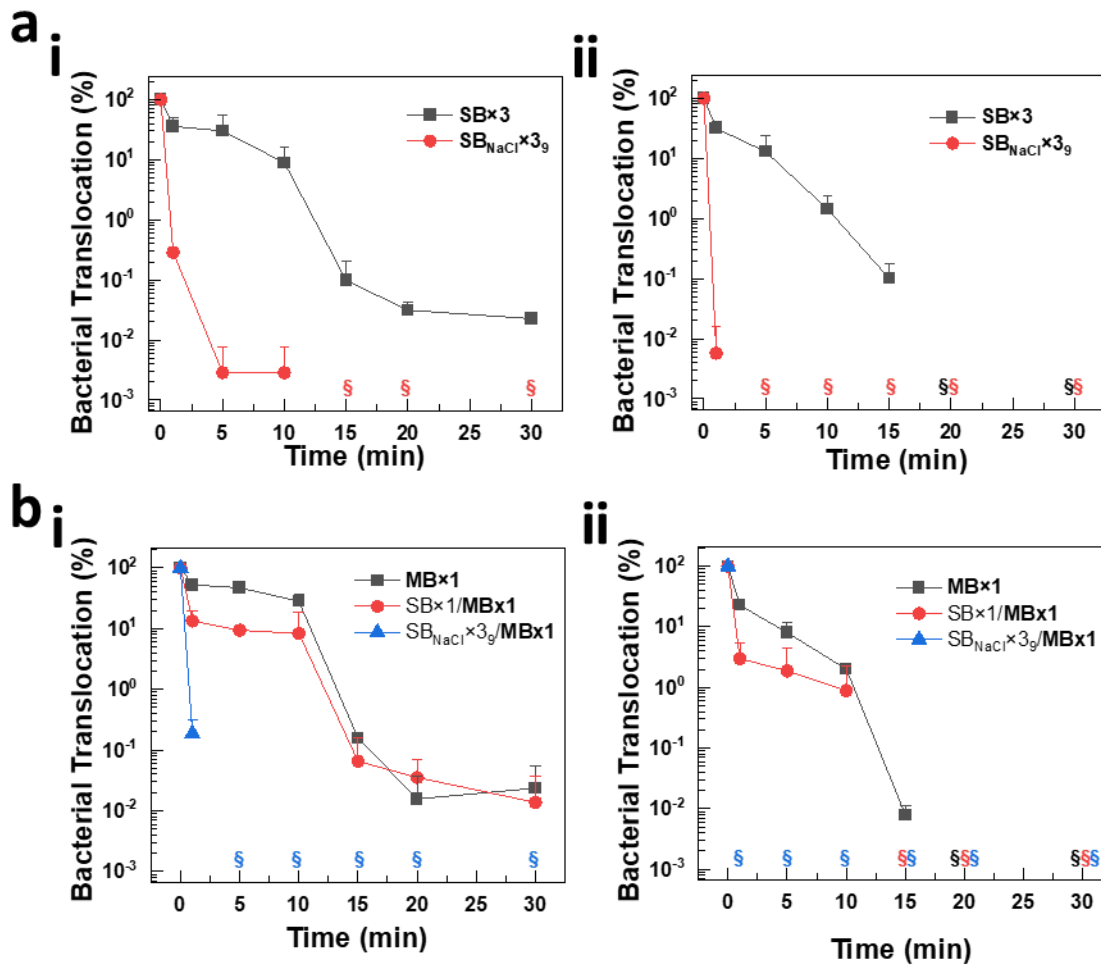


**Figure 5.18.** Bacterial translocation to fingers. Translocation of *K. pneumoniae* associated with a finger pressing from (a) contaminated outermost layer of a mask or mask cover (i.e., a stack of three SB fabrics w/ and w/o salt coating) and (b) contaminated MB layer (i.e., MB only, SB/MB, and salt-coated SB stack/MB) to a finger. (i) Strong and (ii) gentle pressing with the gloved thumb; the amount of the translocated bacteria was analyzed by comparing the number of sprayed *K. pneumoniae* on mask fabrics and translocated bacteria to gloves using CFU. ( $n=3$ , mean  $\pm$  SD). Relative: with respect to bacteria (CFU/mL) sprayed on thumb sized fabric. Bold text indicates the contaminated layer. §: below detection limit.

### 5.3.5 A stack of salt-coated SB fabrics: preventing contact transmission of viral droplets

After confirming the effectiveness in reducing contact transmission of bacteria, the study proceeded to investigate the efficiency of viral translocation using the PR/34 influenza virus. Viral translocation was characterized by measuring gene expression level of the hemagglutinin (HA) gene of the PR/34 virus. As observed in *K. pneumoniae*, viral translocation decreased over the course of incubation time (GLM,  $P < 0.0001$ ; Figure 5.19). Unlike the swift reduction in translocation observed in the bacterial system around 10-15 min, the deceleration was less pronounced in both SB and MB fabrics (i.e., **SB×3** and **MB×1**). However, the advantage of inhibiting translocation by employing SB fabric as an outer layer over the virus-contaminated MB fabric was more apparent even during the initial incubation period compared to the bacterial contaminant (i.e., compare **SB×1/MB×1** in Figure 5.19b with Figure 5.18b). Most importantly, the superior capability of preventing contact transmission was confirmed by utilizing three stacked salt-coated SB fabric and pressing a virus-contaminated mask cover (**SB<sub>NaCl</sub>×3<sub>9</sub>**, Figure 5.19a) and MB fabric (**SB<sub>NaCl</sub>×3<sub>9</sub>/MB×1**, Figure 5.19b). As depicted in Figure 5.19a,b-i, there was a 2 or 4 order of magnitude decrease in viral translocation during the initial incubation period for **SB<sub>NaCl</sub>×3<sub>9</sub>** and **SB<sub>NaCl</sub>×3<sub>9</sub>/MB×1**, respectively, followed by non-detection within 15 min. Additionally, gentle pressure did not reveal any evidence of virus translocation within 1 min of incubation for both architectures, as shown in Figure 5.19a,b-ii. These findings demonstrate that a layer of salt-coated stacked SB fabrics can significantly reduce the transfer efficiency of viruses, thereby minimizing contact-based transmission.

Under these experimental conditions, the virus contaminating the mask fabric surface corresponding to the area of the thumb ( $\sim 3.1 \text{ cm}^2$ ) equates to  $5.58 \times 10^2 \text{ TCID}_{50}$ . Assuming a particle size of  $3 \mu\text{m}$ , the filtration efficiency of **SB×3** and **SB<sub>NaCl</sub>×3<sub>9</sub>** exceeds 63% (Figure 5.10) under inhalation breathing conditions. Therefore, the anticipated amount of virus captured on the

stacked SB fabric is approximately  $3.52 \times 10^2$  TCID<sub>50</sub>. Based on the measurements of viral translocation over time as observed in Figure 5.19a-i, a strong press can induce translocation of  $1.34 \times 10^2$  TCID<sub>50</sub> (1 min), 18 TCID<sub>50</sub> (5 min), and  $> 14$  TCID<sub>50</sub> ( $\geq 30$  min) of virus to hands. On the other hand, **SB<sub>NaCl</sub>39** exhibited a 4-fold lower transmission rate compared to non-salt-treated SB fabric (**SB×3**) until 10 min of incubation, i.e., 18 TCID<sub>50</sub> (1 min) and 3.5 TCID<sub>50</sub> (10 min), with no virus detected after 15 min, indicating no possibility of viral infection. In the case of gentle press, the absence of virus detection (Figure 5.19a-ii) demonstrates the remarkable antimicrobial effect of the salt-coated three-stacked SB fabric compared to **SB×3**. For **SB×3**, viruses of 35 TCID<sub>50</sub>, 3.5 TCID<sub>50</sub>, and 0.07 TCID<sub>50</sub> were detected on the thumb after incubation for 1 min, 10 min, and 30 min, respectively.

In the case of the middle layer, when exposed to the virus under the same experimental conditions and assumptions as the SB fabric, MB fabric is expected to have a TCID<sub>50</sub> of  $5.3 \times 10^2$  (Figure 5.8b). Upon application of a strong press to **MB×1**, a gradual decrease in TCID<sub>50</sub> was observed due to translocation, mirroring the behavior observed in SB fabrics over time: 1 min ( $1.7 \times 10^2$  TCID<sub>50</sub>), 10 min (47.7 TCID<sub>50</sub>), and 30 min (26.5 TCID<sub>50</sub>). However, in a conventional 3-ply mask structure with an SB outer layer over the contaminated MB filter (**SB×1/MB×1**), translocation occurs at a one or two orders lower level of TCID<sub>50</sub> magnitude under strong pressing conditions: 10.6 TCID<sub>50</sub> in 1 min, 5.3 TCID<sub>50</sub> in 10 min, and 0.13 TCID<sub>50</sub> in 30 min. Surprisingly, when salt-coated stacked SB fabric was used as the outer layer (**SB<sub>NaCl</sub>×39/MB×1**), the TCID<sub>50</sub> was 0.42 after 1 min of incubation, significantly lower than **SB×1/MB×1**, and 0.04 after 10 min of incubation, followed by the absence of virus detection after 15 min. Similarly, after gentle pressing, no virus was detected in the case of **SB<sub>NaCl</sub>×39/MB×1** at all incubation time conditions. This indicates that **SB<sub>NaCl</sub>×39** offers significant potential to solve the problem of infection caused by contact transmission when used as an outer layer of a mask or mask cover.

It is reported that influenza virus, rhinovirus, and adenovirus have an infection rate of about 50% (HID<sub>50</sub>: 50% human infection dose) by aerosol inoculation at a dose of < 1 TCID<sub>50</sub> [362-365]. Our analysis is based on the estimated TCID<sub>50</sub> comparison due to a single event of contacting a contaminated mask and translocation of the virus through finger press, which requires more investigation for its connection to HID<sub>50</sub>. Moreover, it should be noted that predicting transmission due to contact during actual mask use is challenging due to extremely diverse and complex situations and its dependence on individual behavioral habits. Despite the need for further research, our work confirms that salt-coated fabric will help prevent disease transmission by contact.

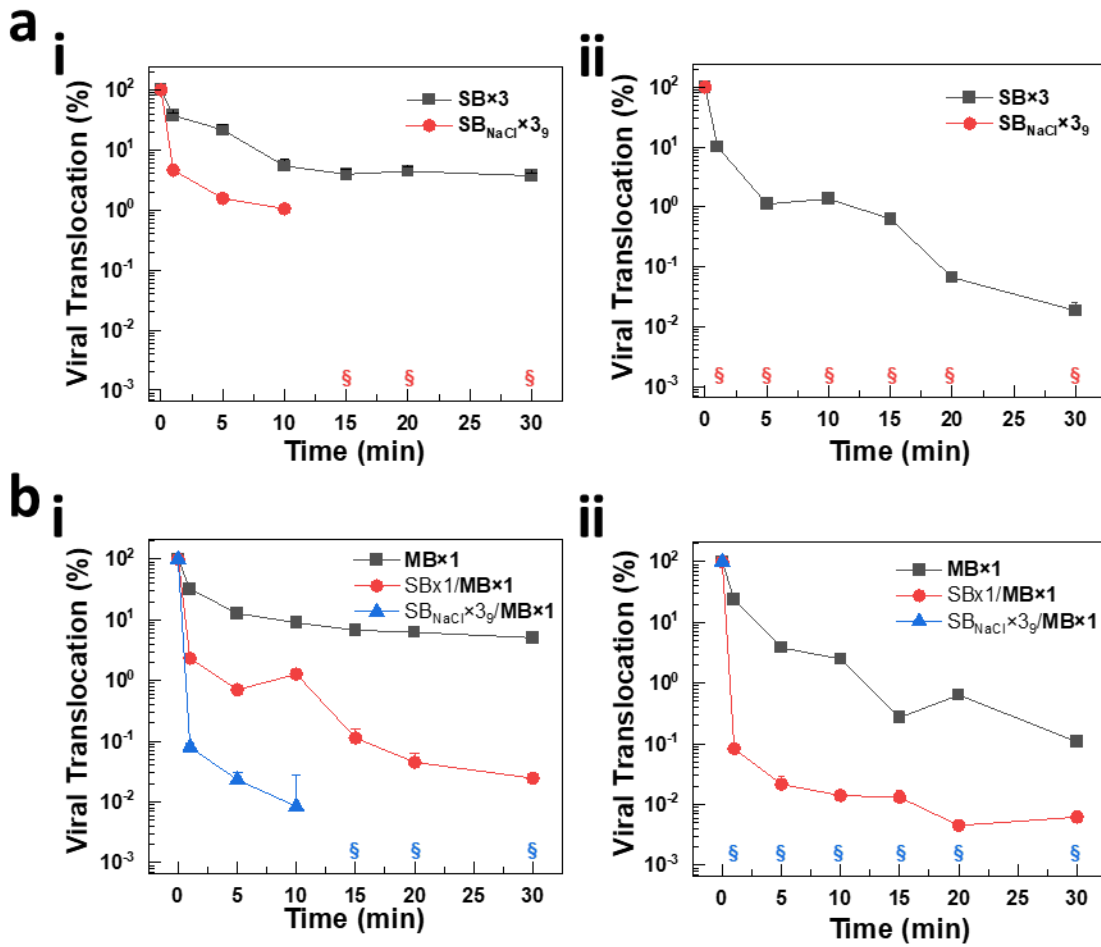


**Figure 5.19.** Viral translocation to fingers. Translocation of PR/34 associated with a finger pressing from (a) contaminated outermost layer (i.e., a stack of three SB fabrics w/ and w/o salt coating) and (b) contaminated MB middle layer (i.e., MB only, SB/MB, and salt-coated SB stack/MB) to a finger. (i) Strong and (ii) gentle pressing with the gloved thumb; the amount of the translocated virus was analyzed using real-time PCR targeting the HA gene. (n=3, mean ± SD). Relative: with respect to gene copy number of viruses sprayed on thumb sized fabric. Bold text indicates the contaminated layer. §: below detection limit.

## 5.4 Conclusions

In this study, we successfully demonstrated the efficacy of stacked salt-coated SB fabric in addressing critical challenges associated with mask performance. A stack of three salt-coated SB PP ( $\text{SB}_{\text{NaCl}\times 39}$ ) made of a SB fabric, often overlooked despite its role in forming the outermost layer of masks, significantly improved capturing efficiency for micron-sized contaminants. By strategically forming a layer of three stacked SB fabrics and applying salt coating, we achieved a balance between enhanced filtration efficiency for larger infectious droplets and maintained breathability, a crucial compromise in mask design. The salt-coated three-stacked SB fabric exhibited remarkable effectiveness in neutralizing both enveloped/non-enveloped viruses and spore-forming/non-spore-forming bacteria, with the antimicrobial effect scaling with the quantity of coated salt. Remarkably, its effectiveness against resilient pathogens like *C. difficile* and HRVs was significant, establishing its applicability as a universal antimicrobial technology. In the context of contact transmission, our experiments, utilizing three types of contaminant-containing droplets (fluorescent dyes, *K. pneumoniae*, and PR/34), highlighted the superior performance of the salt-coated three-stacked SB fabric compared to traditional SB or MB fabrics. Notably, a rapid and substantial reduction in bacterial/viral translocation percentage underscores the fabric's effectiveness in mitigating the contact transmission problem inherent in existing masks. This study not only substantiates the excellent antimicrobial and contact transmission prevention effects of the salt-coated three-stacked SB fabric but also underscores their practical application and performance in the development of antibacterial face masks and mask covers. Therefore, the proposed design and architecture of antimicrobial face mask and mask covering, based on the salt-coated stacked SB fabric presented in this study, are anticipated to enhance public health safety by effectively preventing the transmission of diseases carried through droplets.

# 6 Conclusions and future work

## 6.1 Conclusions

This thesis aims to identify, demonstrate, and optimize a novel method for improving global health by targeting pathogenic threats. We propose the use of salt-coated fabrics, which utilize the mechanism of salt recrystallization to physically inactivate pathogens upon contact with pathogen-laden aerosols. Our findings highlight the remarkable capabilities of salt-coated fabrics, including rapid and non-specific pathogen inactivation, reusability, and a notable reduction in contact transmission. Such properties are assumed to significantly reduce pathogen spread and contribute to the decrease in outbreak occurrences.

In Chapter 3, we conducted a comprehensive analysis of filter performance across a variety of fabric types, configurations, and environmental conditions, focusing on both salt-coated and bare fabrics. The study measured particle-size-dependent filtration efficiency, deepening our understanding of the underlying mechanisms driving the filtration capabilities of these materials. Our findings revealed that salt-coated fabrics, due to the absence of electrical charge, exhibited diminished filtration efficiency for particles smaller than  $0.3\ \mu\text{m}$  in size, when tested with 5% NaCl aerosols. However, this reduction in efficiency could be resolved by employing the salt-coated fabrics as either covers or outer layers in conjunction with surgical masks or N95 respirators, benefiting from the high-efficiency middle layer typically used in these setups. Moreover, the investigation also assessed the impact of fabric wetness on both filtration efficiency and breathability for salt-coated and bare fabrics. Notably, as wetness increased, the filtration efficiency of salt-coated fabrics improved—likely due to their hydrophilic nature facilitating the formation of a continuous water film around the fibers—while that of bare fabrics deteriorated. This decline in bare fabrics was linked to water interference

with their electret properties (statically charged fibers), which are crucial for capturing particles through electrostatic attraction. These experiments underscore the potential of salt-coated fabrics to maintain or enhance filtration efficiency under varying conditions of humidity and wetness, particularly when used as external layers. The comprehensive analysis affirms that salt-coated fabrics, when strategically employed, can significantly augment the overall filtration performance of protective respiratory devices.

In Chapter 4, we conducted a detailed mechanistic study aimed at elucidating the primary pathogen inactivation mechanisms associated with different types of salt-coated fabrics. The investigation focused on the time-dependent inactivation efficiency of these materials. The results were closely compared with the kinetics of salt recrystallization under similar conditions, revealing a significant correlation between the rapid antimicrobial action and the recrystallization process. Specifically, the inactivation occurred within less than 5 minutes for fabrics coated with NaCl and KCl, and between 5 to 15 minutes for those treated with K<sub>2</sub>SO<sub>4</sub>, which matches with their recrystallization behavior. Additionally, the study explored the potential roles of osmotic pressure and ionic effects in pathogen inactivation by employing various saline and sucrose solutions. However, these factors appeared to have minimal impact, contributing less than a 1 log reduction in pathogen levels, thereby reinforcing the hypothesis that salt recrystallization is the dominant mechanism behind the antimicrobial properties of these fabrics. Apart from the mechanistic study, the effects of transmission modes and mediums were analyzed. To this end, two distinct transmission modes—droplet and aerosol—and two mediums—artificial saliva and deionized water were used in pathogen inactivation tests. This comprehensive approach not only confirmed the significant and rapid inactivation capabilities of salt-coated fabrics but also highlighted their potential effectiveness across various environmental conditions and application scenarios. Through this extensive analysis, the research provides a

robust scientific foundation supporting the use of salt-coated fabrics as a viable method for enhancing microbial safety in public health applications. This study opens pathways for further research into optimizing the salt coatings and fabric materials to maximize health protection against a broad spectrum of microbial threats.

In Chapter 5, we explored the inactivation efficiency of salt-coated fabrics against more resilient pathogens, specifically non-enveloped viruses and spore-forming bacteria, which are typically more resistant to common antimicrobial treatments than their enveloped virus and non-spore-forming bacterial counterparts. Traditional antimicrobial efficiency tests for masks and other protective fabrics have predominantly focused on less resilient pathogens; however, the robust nature of non-enveloped viruses and spore-forming bacteria, due to their higher stability and resistance, necessitates their inclusion in comprehensive antimicrobial performance evaluations. To bridge this research gap, we conducted inactivation tests with those resilient pathogens using salt-coated fabrics. The testing revealed that salt-coated fabrics were remarkably effective in reducing the stability and viability of these pathogens, demonstrating a significant and rapid loss of viability within just 5 minutes of exposure for both non-enveloped viruses and spore-forming bacteria. This rapid inactivation suggests a potent antimicrobial action that could be critically advantageous in healthcare settings and other environments where quick decontamination of surfaces is desired. In addition to assessing pathogen inactivation, the study also examined the contact-based transmission efficiency of salt-coated fabrics compared to their bare counterparts. Interestingly, salt-coated fabrics exhibited drastically lower percentage of pathogen translocation. In conditions using salt-coated fabrics, no pathogen transfer was detected from the mask to the hand after less than 15 minutes of pathogen exposure, highlighting the effectiveness of salt coating in preventing the spread of infections through touch. These findings not only reinforce the importance of including more resilient pathogens in antimicrobial

testing but also highlight the potential of salt-coated fabrics to significantly enhance public health safety by reducing the risk of transmission.

Overall, the collective results from these studies underscore the innovative and multifaceted capabilities of salt-coated fabrics in addressing global health challenges by reducing the transmission of both common and resilient pathogens. Given the efficacy demonstrated in various test scenarios—from laboratory conditions simulating real-world environments to rigorous pathogen inactivation trials—the potential of salt-coated fabrics extends beyond traditional medical and personal protective equipment applications to include wide-ranging public health uses.

## **6.2 Future work**

Salt-coated fabrics have proven their efficacy in various studies targeting a broad spectrum of pathogens. To enhance our understanding of the pathogen inactivation mechanism of salt-coated fabrics, future work will include analyzing biomolecular structural changes (e.g., alternation and distortion in genes and lipid bilayers) in pathogens following exposure to salt-coated fabrics. These tests will be performed using both fabricated biomolecules and the actual molecular structures in pathogens. Genomes and proteins of interest can be fabricated using genetic engineering methods (e.g., recombinant DNA production, sequencing, and protein expression) and liposomes can be formulated using the methods such as thin-film hydration, reverse-phase evaporation, or solvent injection methods. Understanding these structural changes will not only reveal the mechanism behind the pathogen inactivation of salt-coated fabrics but will also be applicable to similar antimicrobial strategies that target the focus on the physical damages of pathogens. Furthermore, the functionalization of the middle MB layer and analysis of its filter performance should be conducted. Due to structural differences in the middle layer,

different coating strategies from those used in SB fabric coating should be adopted, based on Figure 1.5. The optimal coating strategy will prevent airway blockage by antimicrobial coatings to enhance breathability while still achieving high inactivation efficiency. Future work also includes the application of different coating formulas to modulate the fluid resistance of salt-coated fabrics. By enhancing water resistance, masks can prevent the penetration of pathogen-laden droplets and exposure to bodily fluids. Increasing oil resistance will broaden the applicability of these fabrics in industrial environments, where exposure to aerosols and organic compound vapors is a concern. As such, controlling the fluid resistance will allow for customization to meet specific needs and enhance protection against pathogens. Besides, by modulating the composition of salts in the saline solution, a humidity-resistant coating formulation can be developed. Depending on the types of salts, they exhibit different critical relative humidities (CRH) as described in Table 2.1. By combining salts with high inactivation efficiency and those with high critical relative humidity, a formulation resistant to high humidity can be achieved.

# Bibliography

1. Centers for Disease Control and Prevention. *Respiratory Infections*. 2024 [cited 2024 Jan 19]; Available from: <https://wwwnc.cdc.gov/travel/yellowbook/2024/posttravel-evaluation/respiratory-infections#:~:text=Causative%20agents%20include%20adenoviruses%2C%20coronaviruses,influenza%20virus%2C%20measles%2C%20mumps%2C>.
2. National Institutes of Health. *Pertussis*. [cited 2024 Jan 19]; Available from: <https://history.nih.gov/display/history/Pertussis>.
3. Kuchar, E., M. Karlikowska-Skwarnik, S. Han, and A. Nitsch-Osuch, *Pertussis: history of the disease and current prevention failure*. Pulmonary dysfunction and disease, 2016: p. 77-82.
4. Centers for Disease Control and Prevention. *History & Disease Patterns*. 2021 [cited 2024 Jan 19]; Available from: <https://www.cdc.gov/pneumonia/atypical/cpneumoniae/about/history.html>.
5. Centers for Disease Control and Prevention. *Haemophilus influenzae Disease (Including Hib)*. 2022 [cited 2024 Jan 19]; Available from: <https://www.cdc.gov/hidisease/index.html>.
6. Centers for Disease Control and Prevention. *Mycoplasma pneumoniae Infections*. 2022 [cited 2024 Jan 19]; Available from: <https://www.cdc.gov/pneumonia/atypical/mycoplasma/about/history-patterns.html>.
7. Kashyap, S. and M. Sarkar, *Mycoplasma pneumonia: Clinical features and management*. Lung India: Official Organ of Indian Chest Society, 2010. **27**(2): p. 75.
8. Zivich, P.N., J.D. Grabenstein, S.I. Becker-Dreps, and D.J. Weber, *Streptococcus pneumoniae outbreaks and implications for transmission and control: a systematic review*. Pneumonia, 2018. **10**: p. 1-15.
9. Brooks, L.R.K. and G.I. Mias, *Streptococcus pneumoniae's virulence and host immunity: aging, diagnostics, and prevention*. Frontiers in immunology, 2018. **9**: p. 1366.
10. Beveridge, W.I.B., *The chronicle of influenza epidemics*. History and philosophy of the life sciences, 1991: p. 223-234.
11. da Costa, V.G., M.L. Moreli, and M.V. Saivish, *The emergence of SARS, MERS and novel SARS-2 coronaviruses in the 21st century*. Archives of virology, 2020. **165**(7): p. 1517-1526.
12. World Health Organization. *Middle East respiratory syndrome coronavirus (MERS-CoV)*. [cited 2024 Jan 21]; Available from: [https://www.who.int/health-topics/middle-east-respiratory-syndrome-coronavirus-mers#tab=tab\\_1](https://www.who.int/health-topics/middle-east-respiratory-syndrome-coronavirus-mers#tab=tab_1).
13. Liang, S.T., L.T. Liang, and J.M. Rosen, *COVID-19: A comparison to the 1918 influenza and how we can defeat it*. 2021, Oxford University Press. p. 273-274.
14. Centers for Disease Control and Prevention. *Public Health Guidance for Community-Level Preparedness and Response to Severe Acute Respiratory Syndrome (SARS) Version 2/3*. 2005 [cited 2024 Jan 21]; Available from: <https://www.cdc.gov/sars/guidance/core/app1.html>.
15. Alimohamadi, Y., M. Taghdir, and M. Sepandi, *Estimate of the basic reproduction number for COVID-19: a systematic review and meta-analysis*. Journal of Preventive Medicine and Public Health, 2020. **53**(3): p. 151.
16. Eisenberg, J. *How scientists quantify the intensity of an outbreak like COVID-19*. 2020

- [cited 2024 Jan 21]; Available from: <https://sph.umich.edu/pursuit/2020posts/how-scientists-quantify-outbreaks.html>.
17. Vynnycky, E. and W.J. Edmunds, *Analyses of the 1957 (Asian) influenza pandemic in the United Kingdom and the impact of school closures*. *Epidemiology & Infection*, 2008. **136**(2): p. 166-179.
  18. Jackson, C., E. Vynnycky, and P. Mangtani, *Estimates of the transmissibility of the 1968 (Hong Kong) influenza pandemic: evidence of increased transmissibility between successive waves*. *American Journal of Epidemiology*, 2010. **171**(4): p. 465-478.
  19. White, L.F. and M. Pagano, *Transmissibility of the influenza virus in the 1918 pandemic*. *PLoS One*, 2008. **3**(1): p. e1498.
  20. Guerra, F.M., et al., *The basic reproduction number (R0) of measles: a systematic review*. *The Lancet Infectious Diseases*, 2017. **17**(12): p. e420-e428.
  21. Rota, P.A., et al., *Measles (Primer)*. *Nature Reviews: Disease Primers*, 2016. **2**(1).
  22. Zhou, H., et al., *A review of SARS-CoV2: compared with SARS-CoV and MERS-CoV*. *Frontiers in medicine*, 2021. **8**: p. 628370.
  23. Krammer, F., et al., *Influenza*. *Nature Reviews Disease Primers*, 2018. **4**(1): p. 3.
  24. Van den Hoogen, B.G., et al., *A newly discovered human pneumovirus isolated from young children with respiratory tract disease*. *Nature medicine*, 2001. **7**(6): p. 719-724.
  25. Williams, J.V., et al., *Human metapneumovirus and lower respiratory tract disease in otherwise healthy infants and children*. *New England Journal of Medicine*, 2004. **350**(5): p. 443-450.
  26. Perry, R.T. and N.A. Halsey, *The clinical significance of measles: a review*. *The Journal of infectious diseases*, 2004. **189**(Supplement\_1): p. S4-S16.
  27. Moss, W.J. and D.E. Griffin, *Measles*. *Lancet*, 2012. **379**(9811): p. 153-64.
  28. Rubin, S., et al., *Molecular biology, pathogenesis and pathology of mumps virus*. *The Journal of pathology*, 2015. **235**(2): p. 242-252.
  29. Hviid, A., S. Rubin, and K. Mühlemann, *Mumps*. *The Lancet*, 2008. **371**(9616): p. 932-944.
  30. Jacobs, S.E., D.M. Lamson, K. St. George, and T.J. Walsh, *Human rhinoviruses*. *Clinical microbiology reviews*, 2013. **26**(1): p. 135-162.
  31. Palmenberg, A.C., et al., *Sequencing and analyses of all known human rhinovirus genomes reveal structure and evolution*. *Science*, 2009. **324**(5923): p. 55-59.
  32. Centers for Disease Control and Prevention. *Blastomycosis in Minnesota, USA, 1999–2018*. 2020 [cited 2024 Jan 22]; Available from: [https://wwwnc.cdc.gov/eid/article/26/5/19-1074\\_article](https://wwwnc.cdc.gov/eid/article/26/5/19-1074_article).
  33. Crum, N.F., *Coccidioidomycosis: A contemporary review*. *Infectious Diseases and Therapy*, 2022. **11**(2): p. 713-742.
  34. Chen, S.C.A., et al., *Clinical manifestations of Cryptococcus gattii infection: determinants of neurological sequelae and death*. *Clinical infectious diseases*, 2012. **55**(6): p. 789-798.
  35. Wheat, J., et al., *Practice guidelines for the management of patients with histoplasmosis*. *Clinical Infectious Diseases*, 2000. **30**(4): p. 688-695.
  36. Centers for Disease Control and Prevention. *Paracoccidioidomycosis*. 2021 [cited 2024 Jan 22]; Available from: <https://www.cdc.gov/fungal/diseases/other/paracoccidioidomycosis.html>.
  37. Mahajan, M., *Talaromyces marneffeii*. *Emerging Infectious Diseases*, 2021. **27**(9): p. 2278.
  38. Seung, K.J., S. Keshavjee, and M.L. Rich, *Multidrug-resistant tuberculosis and extensively drug-resistant tuberculosis*. *Cold Spring Harbor perspectives in medicine*, 2015. **5**(9).
  39. Lempens, P., et al., *Isoniazid resistance levels of Mycobacterium tuberculosis can largely be predicted by high-confidence resistance-conferring mutations*. *Scientific reports*, 2018.

- 8(1): p. 3246.
40. Portelli, S., et al., *Prediction of rifampicin resistance beyond the RRDR using structure-based machine learning approaches*. Scientific reports, 2020. **10**(1): p. 18120.
  41. Lemos, A.C.M. and E.D. Matos, *Multidrug-resistant tuberculosis*. The Brazilian Journal of Infectious Diseases, 2013. **17**(2): p. 239-246.
  42. Henrichfreise, B., I. Wiegand, W. Pfister, and B. Wiedemann, *Resistance mechanisms of multidrug-resistant Pseudomonas aeruginosa strains from Germany and correlation with hypermutation*. Antimicrobial agents and chemotherapy, 2007. **51**(11): p. 4062-4070.
  43. Losito, A.R., F. Raffaelli, P. Del Giacomo, and M. Tumbarello, *New drugs for the treatment of Pseudomonas aeruginosa infections with limited treatment options: a narrative review*. Antibiotics, 2022. **11**(5): p. 579.
  44. Domínguez, L.M., et al., *Antiviral resistance in influenza viruses*. Cellular and Molecular Biology, 2023. **69**(13): p. 16-23.
  45. Deyde, V.M., et al., *Surveillance of resistance to adamantanes among influenza A (H3N2) and A (H1N1) viruses isolated worldwide*. The Journal of infectious diseases, 2007. **196**(2): p. 249-257.
  46. Ison, M.G., *Clinical use of approved influenza antivirals: therapy and prophylaxis*. Influenza and other respiratory viruses, 2013. **7**: p. 7-13.
  47. van der Vries, E. and M.G. Ison, *Antiviral resistance in influenza viruses: clinical and epidemiological aspects*. Antimicrobial Drug Resistance: Clinical and Epidemiological Aspects, Volume 2, 2017: p. 1165-1183.
  48. Matrosovich, M.N., et al., *Neuraminidase is important for the initiation of influenza virus infection in human airway epithelium*. Journal of virology, 2004. **78**(22): p. 12665-12667.
  49. Food and Drug Administration. *FDA Approves First Oral Antiviral for Treatment of COVID-19 in Adults*. 2023 [cited 2024 Jan 24]; Available from: <https://www.fda.gov/news-events/press-announcements/fda-approves-first-oral-antiviral-treatment-covid-19-adults>.
  50. Food and Drug Administration. *FDA Approves First Treatment for COVID-19*. 2020 [cited 2024 Jan 24]; Available from: <https://www.fda.gov/news-events/press-announcements/fda-approves-first-treatment-covid-19>.
  51. Food and Drug Administration. *Coronavirus (COVID-19) Update: FDA Authorizes Additional Oral Antiviral for Treatment of COVID-19 in Certain Adults*. 2021 [cited 2024 Jan 24]; Available from: <https://www.fda.gov/news-events/press-announcements/coronavirus-covid-19-update-fda-authorizes-additional-oral-antiviral-treatment-covid-19-certain>.
  52. Stevens, L.J., et al., *Mutations in the SARS-CoV-2 RNA-dependent RNA polymerase confer resistance to remdesivir by distinct mechanisms*. Science translational medicine, 2022. **14**(656): p. eabo0718.
  53. Iketani, S., et al., *Multiple pathways for SARS-CoV-2 resistance to nirmatrelvir*. Nature, 2023. **613**(7944): p. 558-564.
  54. Duan, Y., et al., *Molecular mechanisms of SARS-CoV-2 resistance to nirmatrelvir*. Nature, 2023. **622**(7982): p. 376-382.
  55. Sanderson, T., et al., *A molnupiravir-associated mutational signature in global SARS-CoV-2 genomes*. Nature, 2023. **623**(7987): p. 594-600.
  56. Strizki, J.M., et al., *Molnupiravir maintains antiviral activity against SARS-CoV-2 variants and exhibits a high barrier to the development of resistance*. Antimicrobial Agents and Chemotherapy, 2023: p. e00953-23.
  57. Monk, B.C., et al., *Fungal Lanosterol 14 $\alpha$ -demethylase: A target for next-generation*

- antifungal design*. Biochimica et Biophysica Acta (BBA)-Proteins and Proteomics, 2020. **1868**(3): p. 140206.
58. Rhodes, J., et al., *Population genomics confirms acquisition of drug-resistant Aspergillus fumigatus infection by humans from the environment*. Nature microbiology, 2022. **7**(5): p. 663-674.
  59. Centers for Disease Control and Prevention. *Antimicrobial-Resistant Aspergillus*. 2023 [cited 2024 Jan 26]; Available from: <https://www.cdc.gov/fungal/diseases/aspergillosis/antifungal-resistant.html#:~:text=Azole%2DResistant%20Aspergillus%20Fumigatus&text=That%20means%20the%20germs%20are,invasive%20mold%20infections%20in%20people>.
  60. Seyedmousavi, S., et al., *The role of azoles in the management of azole-resistant aspergillosis: from the bench to the bedside*. Drug Resistance Updates, 2014. **17**(3): p. 37-50.
  61. Pappas, P.G., et al., *Invasive candidiasis*. Nature Reviews Disease Primers, 2018. **4**(1): p. 1-20.
  62. Hirayama, T., et al., *Echinocandin resistance in Candida auris occurs in the murine gastrointestinal tract due to FKS1 mutations*. Antimicrobial Agents and Chemotherapy, 2023. **67**(4): p. e01243-22.
  63. Sabol, K. and T. Gumbo, *Anidulafungin in the treatment of invasive fungal infections*. Therapeutics and clinical risk management, 2008. **4**(1): p. 71-78.
  64. Coia, J.E., et al., *Guidance on the use of respiratory and facial protection equipment*. Journal of hospital Infection, 2013. **85**(3): p. 170-182.
  65. Patterson, B. and R. Wood, *Is cough really necessary for TB transmission?* Tuberculosis, 2019. **117**: p. 31-35.
  66. Zhou, M. and J. Zou, *A dynamical overview of droplets in the transmission of respiratory infectious diseases*. Physics of Fluids, 2021. **33**(3).
  67. Křištof, O., P. Bulejko, and T. Svěrák, *Experimental study on spray breakup in turbulent atomization using a spiral nozzle*. Processes, 2019. **7**(12): p. 911.
  68. Troitskaya, Y., et al., *Bag-breakup fragmentation as the dominant mechanism of sea-spray production in high winds*. Scientific reports, 2017. **7**(1): p. 1614.
  69. Soni, S.K., P. Kumar, and P. Kolhe. *High speed visualization of the bio derived fuel droplet deformation & breakup in continuous air flows*.
  70. Obenauf, D.G., et al. *Effect of reduced surface tension on size and velocity distributions of ethanol-water drop fragments formed via multi-mode and sheet-thinning breakup*.
  71. Paolicchi, P., A. Cellino, P. Farinella, and V. Zappala, *A semiempirical model of catastrophic breakup processes*. Icarus, 1989. **77**(1): p. 187-212.
  72. Tang, J.W., et al., *Factors involved in the aerosol transmission of infection and control of ventilation in healthcare premises*. Journal of Hospital Infection, 2006. **64**(2): p. 100-114.
  73. Kotay, S.M., et al., *Droplet-rather than aerosol-mediated dispersion is the primary mechanism of bacterial transmission from contaminated hand-washing sink traps*. Applied and environmental microbiology, 2019. **85**(2): p. e01997-18.
  74. Lin, K. and L.C. Marr, *Humidity-dependent decay of viruses, but not bacteria, in aerosols and droplets follows disinfection kinetics*. Environmental Science & Technology, 2019. **54**(2): p. 1024-1032.
  75. Firquet, S., et al., *Survival of enveloped and non-enveloped viruses on inanimate surfaces*. Microbes and environments, 2015. **30**(2): p. 140-144.
  76. Batt, S.M., D.E. Minnikin, and G.S. Besra, *The thick waxy coat of mycobacteria, a protective layer against antibiotics and the host's immune system*. Biochemical Journal,

2020. **477**(10): p. 1983-2006.
77. Lowen, A.C. and J. Steel, *Roles of humidity and temperature in shaping influenza seasonality*. Journal of virology, 2014. **88**(14): p. 7692-7695.
  78. Ikäheimo, T.M., et al., *A decrease in temperature and humidity precedes human rhinovirus infections in a cold climate*. Viruses, 2016. **8**(9): p. 244.
  79. Coates, S.J., M.D.P. Davis, and L.K. Andersen, *Temperature and humidity affect the incidence of hand, foot, and mouth disease: a systematic review of the literature—a report from the International Society of Dermatology Climate Change Committee*. International journal of dermatology, 2019. **58**(4): p. 388-399.
  80. Chang, H.-L., et al., *The association between enterovirus 71 infections and meteorological parameters in Taiwan*. 2012.
  81. Schwartz, D.J., et al., *Positively selected FimH residues enhance virulence during urinary tract infection by altering FimH conformation*. Proceedings of the National Academy of Sciences, 2013. **110**(39): p. 15530-15537.
  82. Schröder, A., et al., *Staphylococcus aureus fibronectin binding protein-A induces motile attachment sites and complex actin remodeling in living endothelial cells*. Molecular biology of the cell, 2006. **17**(12): p. 5198-5210.
  83. Doohan, D., et al., *Helicobacter pylori BabA–SabA key roles in the adherence phase: The synergic mechanism for successful colonization and disease development*. Toxins, 2021. **13**(7): p. 485.
  84. Muenzner, P., M. Naumann, T.F. Meyer, and S.D. Gray-Owen, *Pathogenic Neisseria trigger expression of their carcinoembryonic antigen-related cellular adhesion molecule 1 (CEACAM1; previously CD66a) receptor on primary endothelial cells by activating the immediate early response transcription factor, nuclear factor- $\kappa$ B*. Journal of Biological Chemistry, 2001. **276**(26): p. 24331-24340.
  85. Virgin, H.W., *The virome in mammalian physiology and disease*. Cell, 2014. **157**(1): p. 142-150.
  86. Zhao, C. and J. Pu, *Influence of host sialic acid receptors structure on the host specificity of influenza viruses*. Viruses, 2022. **14**(10): p. 2141.
  87. Leung, H.S.Y., et al., *Entry of influenza A Virus with a  $\alpha$ 2, 6-linked sialic acid binding preference requires host fibronectin*. Journal of virology, 2012. **86**(19): p. 10704-10713.
  88. Smith, L.K., et al., *Direct interaction of HIV gp120 with neuronal CXCR4 and CCR5 receptors induces cofilin-actin rod pathology via a cellular prion protein-and NOX-dependent mechanism*. PLoS One, 2021. **16**(3): p. e0248309.
  89. Lian, M., K. Hueffer, and M.M. Weltzin, *Interactions between the rabies virus and nicotinic acetylcholine receptors: A potential role in rabies virus induced behavior modifications*. Heliyon, 2022. **8**(9).
  90. Hoyer, L.L. and E. Cota, *Candida albicans agglutinin-like sequence (Als) family vignettes: a review of Als protein structure and function*. Frontiers in microbiology, 2016. **7**: p. 179464.
  91. Oh, S.-H., et al., *Agglutinin-like sequence (ALS) genes in the Candida parapsilosis species complex: blurring the boundaries between gene families that encode cell-wall proteins*. Frontiers in microbiology, 2019. **10**: p. 453139.
  92. Yauch, L.E., M.K. Mansour, and S.M. Levitz, *Receptor-mediated clearance of Cryptococcus neoformans capsular polysaccharide in vivo*. Infection and immunity, 2005. **73**(12): p. 8429-8432.
  93. Le Mauff, F. and D.C. Sheppard, *Understanding Aspergillus fumigatus galactosaminogalactan biosynthesis: A few questions remain*. The Cell Surface, 2023. **9**: p.

- 100095.
94. Brown, P., et al., “*It seems impossible that it’s been made so quickly*”: a qualitative investigation of concerns about the speed of COVID-19 vaccine development and how these may be overcome. *Human Vaccines & Immunotherapeutics*, 2022. **18**(1): p. 2004808.
  95. Smith, K.A., *Louis Pasteur, the father of immunology?* *Frontiers in immunology*, 2012. **3**: p. 68.
  96. Trovato, M., et al., *Viral emerging diseases: challenges in developing vaccination strategies*. *Frontiers in immunology*, 2020. **11**: p. 2130.
  97. Bellamkonda, N., et al., *Immune Response to SARS-CoV-2 Vaccines*. 2022: Biomedicines.
  98. Kutzler, M.A. and D.B. Weiner, *DNA vaccines: ready for prime time?* *Nature Reviews Genetics*, 2008. **9**(10): p. 776-788.
  99. Zhang, C., G. Maruggi, H. Shan, and J. Li, *Advances in mRNA vaccines for infectious diseases*. *Frontiers in immunology*, 2019: p. 594.
  100. V’kovski, P., et al., *Coronavirus biology and replication: implications for SARS-CoV-2*. *Nature Reviews Microbiology*, 2021. **19**(3): p. 155-170.
  101. Robert-Guroff, M., *Replicating and non-replicating viral vectors for vaccine development*. *Current opinion in biotechnology*, 2007. **18**(6): p. 546-556.
  102. Liu, M.A., *DNA vaccines: a review*. *J Intern Med*, 2003. **253**(4): p. 402-10.
  103. Pollard, A.J. and E.M. Bijker, *A guide to vaccinology: from basic principles to new developments*. *Nature Reviews Immunology*, 2021. **21**(2): p. 83-100.
  104. Berger, A., *Th1 and Th2 responses: what are they?* *Bmj*, 2000. **321**(7258): p. 424.
  105. Yanagawa, Y., K. Iwabuchi, and K. Onoé, *Co-operative action of interleukin-10 and interferon- $\gamma$  to regulate dendritic cell functions*. *Immunology*, 2009. **127**(3): p. 345-353.
  106. Nakamura, T., et al., *The role of major histocompatibility complex in organ transplantation-donor specific anti-major histocompatibility complex antibodies analysis goes to the next stage*. *International journal of molecular sciences*, 2019. **20**(18): p. 4544.
  107. Ritz, S.A., *The Immune System in Health and Disease*. 2004, Academic Press. p. 393-416.
  108. Lloyd, J., P. Lydon, R. Ouhichi, and M. Zaffran, *Reducing the loss of vaccines from accidental freezing in the cold chain: the experience of continuous temperature monitoring in Tunisia*. *Vaccine*, 2015. **33**(7): p. 902-907.
  109. Criscuolo, E., et al., *Alternative methods of vaccine delivery: an overview of edible and intradermal vaccines*. *Journal of Immunology Research*, 2019. **2019**.
  110. World Health Organization. *COVID-19 vaccination: supply and logistics guidance*. 2021 [cited 2023 Jan 13]; Available from: <https://www.who.int/publications/i/item/who-2019-ncov-vaccine-deployment-logistics-2021-1>.
  111. Crommelin, D.J.A., et al., *Addressing the cold reality of mRNA vaccine stability*. *Journal of Pharmaceutical Sciences*, 2021. **110**(3): p. 997-1001.
  112. Centers for Disease Control and Prevention. *Vaccine Administration*. 2023 [cited 2023 Feb 05]; Available from: <https://www.cdc.gov/vaccines/hcp/acip-recs/general-recs/administration.html>.
  113. Deisenhammer, S., K. Radon, D. Nowak, and J. Reichert, *Needlestick injuries during medical training*. *Journal of hospital infection*, 2006. **63**(3): p. 263-267.
  114. Krammer, F., *SARS-CoV-2 vaccines in development*. *Nature*, 2020. **586**(7830): p. 516-527.
  115. Park, J.H. and H.K. Lee, *Delivery routes for COVID-19 vaccines*. *Vaccines*, 2021. **9**(5): p. 524.
  116. An, X., et al., *Single-dose intranasal vaccination elicits systemic and mucosal immunity against SARS-CoV-2*. *Iscience*, 2021. **24**(9): p. 103037.
  117. Ma, Y., et al., *Vaccine delivery to the oral cavity using coated microneedles induces*

- systemic and mucosal immunity*. *Pharmaceutical research*, 2014. **31**: p. 2393-2403.
118. Mudie, D.M., G.L. Amidon, and G.E. Amidon, *Physiological parameters for oral delivery and in vitro testing*. *Molecular Pharmaceutics*, 2010. **7**(5): p. 1388-1405.
  119. Zhu Q, T.J., Zhang G, Cunningham T, Wang Z, Waters RC, Kirk J, Eppler B, Klinman DM, Sui Y, Gagnon S, *Large intestine-targeted, nanoparticle-releasing oral vaccine to control genitoretal viral infection*. *Nature medicine*, 2012. **18**(8): p. 1291-1296.
  120. Le, T., B. Aguilar, J.L. Mangal, and A.P. Acharya, *Oral drug delivery for immunoengineering*. *Bioengineering & Translational Medicine*, 2022. **7**(1): p. e10243.
  121. Ahadian, S., et al., *Micro and nanoscale technologies in oral drug delivery*. *Advanced Drug Delivery Reviews*, 2020. **157**: p. 37-62.
  122. Coffey, J.W., G.D. Gaiha, and G. Traverso, *Oral biologic delivery: advances toward oral subunit, DNA, and mRNA vaccines and the potential for mass vaccination during pandemics*. *Annual Review of Pharmacology and Toxicology*, 2021. **61**(1): p. 517-540.
  123. de Santa Barbara, P., G.R. van den Brink, and D.J. Roberts, *Development and differentiation of the intestinal epithelium*. *Cellular and Molecular Life Sciences CMLS*, 2003. **60**(7): p. 1322-1332.
  124. Roopenian, D.C. and S. Akilesh, *FcRn: the neonatal Fc receptor comes of age*. *Nature Reviews Immunology*, 2007. **7**(9): p. 715-725.
  125. Yang, S. and M. Yu, *Role of goblet cells in intestinal barrier and mucosal immunity*. *J Inflamm Res*, 2021. **14**: p. 3171-3183.
  126. Jung, C., J.-P. Hugot, and F. Barreau, *Peyer's patches: the immune sensors of the intestine*. *International Journal of Inflammation*, 2010. **2010**: p. 823710.
  127. Homayun, B., X. Lin, and H.-J. Choi *Challenges and Recent Progress in Oral Drug Delivery Systems for Biopharmaceuticals*. *Pharmaceutics*, 2019. **11**, DOI: 10.3390/pharmaceutics11030129.
  128. Ramirez, J.E.V., L.A. Sharpe, and N.A. Peppas, *Current state and challenges in developing oral vaccines*. *Advanced drug delivery reviews*, 2017. **114**: p. 116-131.
  129. De Smet, R., L. Allais, and C.A. Cuvelier, *Recent advances in oral vaccine development: Yeast-derived  $\beta$ -glucan particles*. *Human vaccines & immunotherapeutics*, 2014. **10**(5): p. 1309-1318.
  130. Partidos, C.D., *Intranasal vaccines: forthcoming challenges*. *Pharmaceutical Science & Technology Today*, 2000. **3**(8): p. 273-281.
  131. Xu, H., L. Cai, S. Hufnagel, and Z. Cui, *Intranasal vaccine: Factors to consider in research and development*. *International Journal of Pharmaceutics*, 2021. **609**: p. 121180.
  132. Takaki, H., S. Ichimiya, M. Matsumoto, and T. Seya, *Mucosal immune response in nasal-associated lymphoid tissue upon intranasal administration by adjuvants*. *Journal of Innate Immunity*, 2018. **10**(5-6): p. 515-521.
  133. Scherließ, R., *Nasal formulations for drug administration and characterization of nasal preparations in drug delivery*. *Therapeutic Delivery*, 2020. **11**(3): p. 183-191.
  134. Ramvikas, M., M. Arumugam, S.R. Chakrabarti, and K.S. Jaganathan, *Nasal vaccine delivery*, in *Micro and nanotechnology in vaccine development*. 2017, Elsevier. p. 279-301.
  135. Jadhav, K.R., et al., *Nasal drug delivery system-factors affecting and applications*. *Current drug therapy*, 2007. **2**(1): p. 27-38.
  136. Tirucherai, G.S., I. Pezron, and A.K. Mitra, *Novel approaches to nasal delivery of peptides and proteins*. *STP pharma sciences*, 2002. **12**(1): p. 3-12.
  137. Marx, D., G. Williams, and M. Birkhoff, *Intranasal drug administration—an attractive delivery route for some drugs*. *Drug Discov Dev*, 2015: p. 299-320.
  138. Upadhyay, S., et al., *Intranasal drug delivery system-A glimpse to become maestro*. *Journal*

- of applied pharmaceutical science, 2011(Issue): p. 34-44.
139. Han, K., O.E. Woghiren, and R. Priefer, *Surface tension examination of various liquid oral, nasal, and ophthalmic dosage forms*. Chemistry Central Journal, 2016. **10**(1): p. 1-5.
  140. Gao, M., X. Shen, and S. Mao, *Factors influencing drug deposition in the nasal cavity upon delivery via nasal sprays*. Journal of Pharmaceutical Investigation, 2020. **50**: p. 251-259.
  141. Food and Drug Administration. *FluMist Quadrivalent*. 2023 [cited 2023 Apr 24]; Available from: <https://www.fda.gov/vaccines-blood-biologics/vaccines/flumist-quadrivalent>.
  142. Gockel, C.M., S. Bao, and K.W. Beagley, *Transcutaneous immunization induces mucosal and systemic immunity: a potent method for targeting immunity to the female reproductive tract*. Molecular immunology, 2000. **37**(9): p. 537-544.
  143. Karande, P. and S. Mitragotri, *Transcutaneous immunization: an overview of advantages, disease targets, vaccines, and delivery technologies*. Annual review of chemical and biomolecular engineering, 2010. **1**: p. 175-201.
  144. Hettinga, J. and R. Carlisle, *Vaccination into the dermal compartment: techniques, challenges, and prospects*. Vaccines, 2020. **8**(3): p. 534.
  145. Menon, I., et al., *Microneedles: a new generation vaccine delivery system*. Micromachines, 2021. **12**(4): p. 435.
  146. Alimardani, V., et al., *Microneedle arrays combined with nanomedicine approaches for transdermal delivery of therapeutics*. Journal of Clinical Medicine, 2021. **10**(2): p. 181.
  147. Wang, F.-Y., Y. Chen, Y.-Y. Huang, and C.-M. Cheng, *Transdermal drug delivery systems for fighting common viral infectious diseases*. Drug Delivery and Translational Research, 2021. **11**(4): p. 1498-1508.
  148. Cárcamo-Martínez, Á., et al., *Hollow microneedles: A perspective in biomedical applications*. International journal of pharmaceutics, 2021. **599**: p. 120455.
  149. Prausnitz, M.R., *Engineering microneedle patches for vaccination and drug delivery to skin*. Annual review of chemical and biomolecular engineering, 2017. **8**: p. 177-200.
  150. Tariq, N., M.W. Ashraf, and S. Tayyaba, *A review on solid microneedles for biomedical applications*. Journal of Pharmaceutical Innovation, 2022. **17**(4): p. 1464-1483.
  151. Jung, J.H. and S.G. Jin, *Microneedle for transdermal drug delivery: current trends and fabrication*. Journal of pharmaceutical investigation, 2021: p. 1-15.
  152. Aldawood, F.K., A. Andar, and S. Desai, *A comprehensive review of microneedles: Types, materials, processes, characterizations and applications*. Polymers, 2021. **13**(16): p. 2815.
  153. He, X., et al., *Microneedle system for transdermal drug and vaccine delivery: devices, safety, and prospects*. Dose-Response, 2019. **17**(4): p. 1559325819878585.
  154. Leone, M., J. Mönkäre, J.A. Bouwstra, and G. Kersten, *Dissolving microneedle patches for dermal vaccination*. Pharmaceutical research, 2017. **34**: p. 2223-2240.
  155. Sartawi, Z., C. Blackshields, and W. Faisal, *Dissolving microneedles: Applications and growing therapeutic potential*. Journal of Controlled Release, 2022. **348**: p. 186-205.
  156. Turner, J.G., L.R. White, P. Estrela, and H.S. Leese, *Hydrogel-forming microneedles: current advancements and future trends*. Macromolecular Bioscience, 2021. **21**(2): p. 2000307.
  157. Dardano, P., et al., *A photolithographic approach to polymeric microneedles array fabrication*. Materials, 2015. **8**(12): p. 8661-8673.
  158. Jin, Z., et al., *Application of microneedle-based vaccines in biosecurity*. Journal of Biosafety and Biosecurity, 2022. **4**(1): p. 75-83.
  159. Donnelly, R.F., et al., *Hydrogel-forming microneedles prepared from "super swelling" polymers combined with lyophilised wafers for transdermal drug delivery*. PloS one, 2014.

- 9(10): p. e111547.
160. Salter, S., *Reinventing cloth masks in the face of pandemics*. Risk Analysis, 2021. **41**(5): p. 731-744.
  161. Pan, J., C. Harb, W. Leng, and L.C. Marr, *Inward and outward effectiveness of cloth masks, a surgical mask, and a face shield*. Aerosol Science and Technology, 2021. **55**(6): p. 718-733.
  162. Benson, S.M., D.A. Novak, and M.J. Ogg, *Proper use of surgical N95 respirators and surgical masks in the OR*. AORN journal, 2013. **97**(4): p. 457-470.
  163. Udawadia, Z.F. and R.S. Raju, *The N-95 mask: Invaluable ally in the battle against the COVID-19 pandemic*. Lung India: Official Organ of Indian Chest Society, 2020. **37**(4): p. 323.
  164. Rodriguez-Martinez, C.E., M.P. Sossa-Briceño, and J.A. Cortés-Luna, *Decontamination and reuse of N95 filtering facemask respirators: a systematic review of the literature*. American journal of infection control, 2020.
  165. Bartoszko, J.J., M.A.M. Farooqi, W. Alhazzani, and M. Loeb, *Medical masks vs N95 respirators for preventing COVID-19 in healthcare workers: A systematic review and meta-analysis of randomized trials*. Influenza and other respiratory viruses, 2020. **14**(4): p. 365-373.
  166. Mizukoshi, A., C. Nakama, J. Okumura, and K. Azuma, *Assessing the risk of COVID-19 from multiple pathways of exposure to SARS-CoV-2: Modeling in health-care settings and effectiveness of nonpharmaceutical interventions*. Environment international, 2021. **147**: p. 106338.
  167. Eikenberry, S.E., et al., *To mask or not to mask: Modeling the potential for face mask use by the general public to curtail the COVID-19 pandemic*. Infectious disease modelling, 2020. **5**: p. 293-308.
  168. Centers for Disease Control and Prevention, *Morbidity and mortality weekly report*. 2021.
  169. Adjodah, D., et al., *Association between COVID-19 outcomes and mask mandates, adherence, and attitudes*. PloS one, 2021. **16**(6): p. e0252315.
  170. Fadare, O.O. and E.D. Okoffo, *Covid-19 face masks: A potential source of microplastic fibers in the environment*. The Science of the total environment, 2020. **737**: p. 140279.
  171. Larsen, G.S., et al., *Polymer, Additives, and Processing Effects on N95 Filter Performance*. ACS Applied Polymer Materials, 2021. **3**(2): p. 1022-1031.
  172. Maddah, H.A., *Polypropylene as a promising plastic: A review*. American Journal of Polymer Science, 2016. **6**(1): p. 1-11.
  173. Fjeld, R.A. and T.M. Owens, *The effect of particle charge on penetration in an electret filter*. IEEE Transactions on Industry Applications, 1988. **24**(4): p. 725-731.
  174. Wang, Q., B. Maze, H.V. Tafreshi, and B. Pourdeyhimi, *A case study of simulating submicron aerosol filtration via lightweight spun-bonded filter media*. Chemical Engineering Science, 2006. **61**(15): p. 4871-4883.
  175. Soltani, I. and C.W. Macosko, *Influence of rheology and surface properties on morphology of nanofibers derived from islands-in-the-sea meltblown nonwovens*. Polymer, 2018. **145**: p. 21-30.
  176. Hossain, E., et al., *Recharging and rejuvenation of decontaminated N95 masks*. Physics of Fluids, 2020. **32**(9): p. 093304.
  177. Lowen, A.C. and J. Steel, *Roles of humidity and temperature in shaping influenza seasonality*. Journal of Virology, 2014. **88**(14): p. 7692-5.
  178. Kwon, T., N.N. Gaudreault, and J.A. Richt, *Environmental stability of SARS-CoV-2 on different types of surfaces under indoor and seasonal climate conditions*. Pathogens, 2021.

- 10(2): p. 227.
179. Dehbandi, R. and M.A. Zazouli, *Stability of SARS-CoV-2 in different environmental conditions*. Lancet Microbe, 2020. **1**(4): p. e145.
  180. Rahman, J., J. Mumin, and B. Fakhruddin, *How frequently do we touch facial T-zone: a systematic review*. Annals of Global Health, 2020. **86**(1).
  181. Fikenzler, S., et al., *Effects of surgical and FFP2/N95 face masks on cardiopulmonary exercise capacity*. Clinical Research in Cardiology, 2020. **109**(12): p. 1522-1530.
  182. Chughtai, A.A., et al., *Contamination by respiratory viruses on outer surface of medical masks used by hospital healthcare workers*. BMC Infectious Diseases, 2019. **19**(1): p. 1-8.
  183. Shukla, S., R. Khan, A. Saxena, and S. Sekar, *Microplastics from face masks: A potential hazard post Covid-19 pandemic*. Chemosphere, 2022. **302**: p. 134805.
  184. Lee, Y., J. Cho, J. Sohn, and C. Kim, *Health Effects of Microplastic Exposures: Current Issues and Perspectives in South Korea*. Yonsei Medical Journal, 2023. **64**(5): p. 301.
  185. Liao, L., et al., *Can N95 respirators be reused after disinfection? How many times?* ACS nano, 2020. **14**(5): p. 6348-6356.
  186. Lehner, N.D.M., J.T. Crane, M.P. Mottet, and M.E. Fitzgerald, *Biohazards: Safety Practices, Operations and Containment Facilities*, in *Planning and Designing Research Animal Facilities*. 2009, Elsevier. p. 347-363.
  187. World Health Organization. *Decontamination and reprocessing of medical devices for health-care facilities*. 2016 [cited 2016 September 5]; Available from: <https://www.who.int/publications/i/item/9789241549851>.
  188. Ou, Q., et al., *Evaluation of decontamination methods for commercial and alternative respirator and mask materials—view from filtration aspect*. Journal of aerosol science, 2020. **150**: p. 105609.
  189. Bernard, L., et al., *Controlled heat and humidity-based treatment for the reuse of personal protective equipment: A pragmatic proof-of-concept to address the mass shortage of surgical masks and N95/FFP2 respirators and to prevent the SARS-CoV2 transmission*. Frontiers in Medicine 2020. **7**: p. 584036.
  190. Occupational Safety Health Administration. *Enforcement guidance on decontamination of filtering facepiece respirators in healthcare during the coronavirus disease 2019 (COVID-19) pandemic*. [cited 2020 April 24]; Available from: <https://www.osha.gov/laws-regs/standardinterpretations/2020-04-24>.
  191. Pascoe, M., et al., *Dry heat and microwave-generated steam protocols for the rapid decontamination of respiratory personal protective equipment in response to COVID-19-related shortages*. Journal of Hospital Infection, 2020. **106**(1): p. 10-19.
  192. Xiang, Y., Q. Song, and W. Gu, *Decontamination of surgical face masks and N95 respirators by dry heat pasteurization for one hour at 70 C*. American journal of infection control, 2020. **48**(8): p. 880-882.
  193. Safety, O. and H. Administration, *Enforcement guidance on decontamination of filtering facepiece respirators in healthcare during the coronavirus disease 2019 (COVID-19) pandemic*. April 24, 2020).
  194. Lin, T.-H., et al., *Filter quality of electret masks in filtering 14.6–594 nm aerosol particles: Effects of five decontamination methods*. PloS one, 2017. **12**(10): p. e0186217.
  195. Salter, W., et al., *Analysis of residual chemicals on filtering facepiece respirators after decontamination*. Journal of occupational and environmental hygiene, 2010. **7**(8): p. 437-445.
  196. Bergman, M.S., et al., *Evaluation of multiple (3-cycle) decontamination processing for filtering facepiece respirators*. Journal of Engineered Fibers and Fabrics

- Fabrics 2010. **5**(4): p. 155892501000500405.
197. Garcia-Haro, M., et al., *Decontamination of filtering facepiece respirators using a low-temperature-steam–2%-formaldehyde sterilization process during a pandemic: a safe alternative for re-use*. Journal of Hospital Infection, 2021. **108**: p. 113-119.
  198. Cai, C. and E.L. Floyd, *Effects of sterilization with hydrogen peroxide and chlorine dioxide on the filtration efficiency of N95, KN95, and surgical face masks*. JAMA network open, 2020. **3**(6): p. e2012099-e2012099.
  199. John, A.R., et al., *Scalable in-hospital decontamination of N95 filtering face-piece respirator with a peracetic acid room disinfection system*. Infection Control & Hospital Epidemiology 2020: p. 1-10.
  200. Bałazy, A., et al., *Do N95 respirators provide 95% protection level against airborne viruses, and how adequate are surgical masks?* American journal of infection control, 2006. **34**(2): p. 51-57.
  201. Grinshpun, S.A., M. Yermakov, and M. Khodoun, *Autoclave sterilization and ethanol treatment of re-used surgical masks and N95 respirators during COVID-19: impact on their performance and integrity*. Journal of Hospital Infection, 2020. **105**(4): p. 608-614.
  202. Jatta, M., et al., *N95 reprocessing by low temperature sterilization with 59% vaporized hydrogen peroxide during the 2020 COVID-19 pandemic*. American Journal of Infection Control, 2021. **49**(1): p. 8-14.
  203. Ludwig-Begall, L.F., et al., *The use of germicidal ultraviolet light, vaporized hydrogen peroxide and dry heat to decontaminate face masks and filtering respirators contaminated with a SARS-CoV-2 surrogate virus*. 2020. **106**(3): p. 577-584.
  204. Asadi, S., et al., *Efficacy of masks and face coverings in controlling outward aerosol particle emission from expiratory activities*. Scientific reports, 2020. **10**(1): p. 1-13.
  205. Cramer, A., et al., *Disposable N95 masks pass qualitative fit-test but have decreased filtration efficiency after cobalt-60 gamma irradiation*. MedRxiv, 2020.
  206. Kumar, A., et al., *Effect of gamma sterilization on filtering efficiency of various respiratory face-masks*. 2020.
  207. Rubio-Romero, J.C., M. del Carmen Pardo-Ferreira, J.A. Torrecilla-García, and S. Calero-Castro, *Disposable masks: Disinfection and sterilization for reuse, and non-certified manufacturing, in the face of shortages during the COVID-19 pandemic*. Safety science, 2020. **129**: p. 104830.
  208. Viscusi, D.J., M.S. Bergman, B.C. Eimer, and R.E. Shaffer, *Evaluation of five decontamination methods for filtering facepiece respirators*. Annals of occupational hygiene, 2009. **53**(8): p. 815-827.
  209. Rubio-Romero, J.C., M. del Carmen Pardo-Ferreira, J.A. Torrecilla-García, and S. Calero-Castro, *Disposable masks: Disinfection and sterilization for reuse, and non-certified manufacturing, in the face of shortages during the COVID-19 pandemic*. Safety science, 2020. **129**: p. 104830.
  210. Montazer, M. and Z.K. Nia, *Conductive nylon fabric through in situ synthesis of nano-silver: Preparation and characterization*. Materials Science and Engineering: C, 2015. **56**: p. 341-347.
  211. Lore, M.B., et al., *Effectiveness of three decontamination treatments against influenza virus applied to filtering facepiece respirators*. Annals of occupational hygiene, 2012. **56**(1): p. 92-101.
  212. Azam, A., et al., *Antimicrobial activity of metal oxide nanoparticles against Gram-positive and Gram-negative bacteria: a comparative study*. International journal of nanomedicine,

- 2012: p. 6003-6009.
213. Gautam, S., et al., *Transition metal-based nanoparticles as potential antimicrobial agents: recent advancements, mechanistic, challenges, and future prospects*. Discover Nano, 2023. **18**(1): p. 1-20.
  214. Bruna, T., F. Maldonado-Bravo, P. Jara, and N. Caro, *Silver nanoparticles and their antibacterial applications*. International Journal of Molecular Sciences, 2021. **22**(13): p. 7202.
  215. Naqvi, Q.-u.-A., et al., *Size-dependent inhibition of bacterial growth by chemically engineered spherical ZnO nanoparticles*. Journal of biological physics, 2019. **45**: p. 147-159.
  216. Sajid, M., et al., *Impact of nanoparticles on human and environment: review of toxicity factors, exposures, control strategies, and future prospects*. Environmental Science and Pollution Research, 2015. **22**: p. 4122-4143.
  217. Yoo, J.-H., *Review of disinfection and sterilization—back to the basics*. Infection & chemotherapy, 2018. **50**(2): p. 101.
  218. Qiu, Y., et al., *Disinfection efficacy of sodium hypochlorite and glutaraldehyde and their effects on the dimensional stability and surface properties of dental impressions: a systematic review*. PeerJ, 2023. **11**: p. e14868.
  219. Yim, J.-H., et al., *Effectiveness of calcium hypochlorite, quaternary ammonium compounds, and sodium hypochlorite in eliminating vegetative cells and spores of Bacillus anthracis surrogate*. Journal of Veterinary Science, 2021. **22**(1).
  220. Tan, E.L. and N.H. Johari, *Comparative in vitro evaluation of the antimicrobial activities of povidone-iodine and other commercially available antiseptics against clinically relevant pathogens*. GMS Hygiene and Infection Control, 2021. **16**.
  221. Rengasamy, S., E. Fisher, and R.E. Shaffer, *Evaluation of the survivability of MS2 viral aerosols deposited on filtering face piece respirator samples incorporating antimicrobial technologies*. American journal of infection control, 2010. **38**(1): p. 9-17.
  222. Lei, J., et al., *The antimicrobial peptides and their potential clinical applications*. American journal of translational research, 2019. **11**(7): p. 3919.
  223. Huan, Y., Q. Kong, H. Mou, and H. Yi, *Antimicrobial peptides: classification, design, application and research progress in multiple fields*. Frontiers in microbiology, 2020. **11**: p. 582779.
  224. Boman, H.G., *Antibacterial peptides: basic facts and emerging concepts*. Journal of internal medicine, 2003. **254**(3): p. 197-215.
  225. Fernández de Ullivarri, M., S. Arbulu, E. Garcia-Gutierrez, and P.D. Cotter, *Antifungal peptides as therapeutic agents*. Frontiers in Cellular and Infection Microbiology, 2020. **10**: p. 105.
  226. Vilas Boas, L.C.P., et al., *Antiviral peptides as promising therapeutic drugs*. Cellular and Molecular Life Sciences, 2019. **76**: p. 3525-3542.
  227. Guarnieri, A., et al., *Antimicrobial of chitosan from different developmental stages of the bioconverter insect Hermetia illucens*. Scientific Reports, 2022. **12**(1): p. 8084.
  228. Morena, A.G., et al., *Antibacterial properties and mechanisms of action of sonoenzymatically synthesized lignin-based nanoparticles*. ACS Applied Materials & Interfaces, 2022. **14**(33): p. 37270-37279.
  229. Borlinghaus, J., et al., *Alliin: chemistry and biological properties*. Molecules, 2014. **19**(8): p. 12591-12618.
  230. Phadataré, A.G., V. Viswanathan, and A. Mukne, *Novel strategies for optimized delivery of select components of Allium sativum*. Pharmacognosy Research, 2014. **6**(4): p. 334.

231. Martins, A.F., et al., *Antimicrobial activity of chitosan derivatives containing N-quaternized moieties in its backbone: a review*. International Journal of Molecular Sciences, 2014. **15**(11): p. 20800-20832.
232. Alzagameem, A., et al., *Antimicrobial activity of lignin and lignin-derived cellulose and chitosan composites against selected pathogenic and spoilage microorganisms*. Polymers, 2019. **11**(4): p. 670.
233. Kumar, P., P. Huo, R. Zhang, and B. Liu, *Antibacterial properties of graphene-based nanomaterials*. Nanomaterials, 2019. **9**(5): p. 737.
234. Sadare, O.O., C.N. Frances, and M.O. Daramola, *Antimicrobial (Antibacterial) Properties and Other Miscellaneous Applications of Carbon Nanotubes (CNTs)*, in *Handbook of Carbon Nanotubes*. 2021, Springer. p. 1-29.
235. Abedi-Gaballu, F., et al., *PAMAM dendrimers as efficient drug and gene delivery nanosystems for cancer therapy*. Applied materials today, 2018. **12**: p. 177-190.
236. Madani, S.Y., A. Mandel, and A.M. Seifalian, *A concise review of carbon nanotube's toxicology*. Nano reviews, 2013. **4**(1): p. 21521.
237. Ou, L., et al., *Toxicity of graphene-family nanoparticles: a general review of the origins and mechanisms*. Particle and fibre toxicology, 2016. **13**: p. 1-24.
238. Janaszewska, A., et al., *Cytotoxicity of dendrimers*. Biomolecules, 2019. **9**(8): p. 330.
239. Boyce, J.M., *Modern technologies for improving cleaning and disinfection of environmental surfaces in hospitals*. Antimicrobial Resistance & Infection Control, 2016. **5**(1): p. 1-10.
240. Hooper, D.C., *Mechanisms of action of antimicrobials: focus on fluoroquinolones*. Clinical Infectious Diseases, 2001. **32**(Supplement\_1): p. S9-S15.
241. Yu, M., et al., *Recent advances in needleless electrospinning of ultrathin fibers: from academia to industrial production*. Macromolecular Materials and Engineering, 2017. **302**(7): p. 1700002.
242. Haider, A., S. Haider, and I.-K. Kang, *A comprehensive review summarizing the effect of electrospinning parameters and potential applications of nanofibers in biomedical and biotechnology*. Arabian Journal of Chemistry, 2018. **11**(8): p. 1165-1188.
243. Tseng, C.-C., Z.-M. Pan, and C.-H. Chang, *Application of a quaternary ammonium agent on surgical face masks before use for pre-decontamination of nosocomial infection-related bioaerosols*. Aerosol Science and Technology, 2016. **50**(3): p. 199-210.
244. Adlhart, C., et al., *Surface modifications for antimicrobial effects in the healthcare setting: A critical overview*. Journal of Hospital Infection, 2018. **99**(3): p. 239-249.
245. Si, Y., et al., *Daylight-driven rechargeable antibacterial and antiviral nanofibrous membranes for bioprotective applications*. Science advances, 2018. **4**(3): p. eaar5931.
246. Kumaran, S., E. Oh, S. Han, and H.J. Choi, *Photopolymerizable, universal antimicrobial coating to produce high-performing, multifunctional face masks*. Nano Letters, 2021. **21**(12): p. 5422-5429.
247. Government of Canada, *COVID-19 mask use: Types of masks and respirators*. 2022.
248. National Institute for Occupational Safety and Health, *NIOSH 42CFR84: Respiratory Protective Devices*, U.S.D.o.H.a.H. Services, Editor. 1995: Washington, DC.
249. Standardization Administration of the People's Republic of China, *GB 2626: Respiratory protection - Non-powered air-purifying particle respirator*. 2006, SAC: Beijing, China.
250. European Committee for Standardization, *EN 149: Respiratory protective devices - Filtering half masks to protect against particles - Requirements, testing, marking*. 2009, CEN: Brussels, Belgium.
251. Ministry of Food and Drug Safety, *Notice of MFDS 2020-6: 보건용 마스크의 기준*

- 규격에 대한 가이드라인. 2020, Ministry of Food and Drug Safety: Cheong-Ju, Korea.
252. ASTM International, *ASTM F2100-19e1: Standard Specification for Performance of Materials Used in Medical Face Masks*. 2019, ASTM International: West Conshohocken, PA.
  253. European Committee for Standardization, *EN 14683: Medical face masks - Requirements and test methods*. 2019, CEN: Brussels, Belgium.
  254. Standardization Administration of the People's Republic of China, *YY 0469: Surgical mask*. 2011, SAC: Beijing, China.
  255. Canadian Centre for Occupational Health and Safety. *Personal Protective Equipment*. 2024.
  256. ASTM International, *ASTM F2101: Standard Test Method for Evaluating the Bacterial Filtration Efficiency (BFE) of Medical Face Mask Materials, Using a Biological Aerosol of Staphylococcus aureus*. . 2019, ASTM International: West Conshohocken, PA.
  257. Jennekens, M.H.G., *The importance of critical relative humidity—temperature relationship on design of rotary dryers for fertilizers*. Fertilizer research, 1987. **12**: p. 175-184.
  258. Rockland, L.B., *Saturated salt solutions for static control of relative humidity between 5° and 40° C*. Analytical Chemistry, 1960. **32**(10): p. 1375-1376.
  259. Rubino, I., et al., *Study of the pathogen inactivation mechanism in salt-coated Filters*. ACS Applied Materials & Interfaces, 2021. **13**(14): p. 16084-16096.
  260. Payne, S., *Introduction to RNA viruses*. Viruses, 2017: p. 97.
  261. Alberts, B., *Molecular biology of the cell*. 2017: Garland science.
  262. Sambrook, J., E.F. Fritsch, and T. Maniatis, *Molecular cloning: a laboratory manual*. 1989: Cold spring harbor laboratory press.
  263. Thermo Fisher Scientific, *High Capacity cDNA Reverse Transcription Kits (Publication No. 4375222)*. 2016.
  264. Sa, B., *The MIQE guidelines: minimum information for publication of quantitative real-time PCR experiments*. Clinical Chemistry, 2009. **55**: p. 4611-622.
  265. Applied Biosystems, *User Guide: SYBR Green Master Mix*. 2011.
  266. James, C. and S. Natalie, *Microbiology. A laboratory manual*. 2014, Pearson Education.
  267. Kangro, H.O. and B.W.J. Mahy, *Virology methods manual*. 1996: Elsevier.
  268. Smith, P.K.e., et al., *Measurement of protein using bicinchoninic acid*. Analytical biochemistry, 1985. **150**(1): p. 76-85.
  269. Lei, C., J. Yang, J. Hu, and X. Sun, *On the calculation of TCID 50 for quantitation of virus infectivity*. Virologica Sinica, 2021. **36**: p. 141-144.
  270. Webster, R.G., et al., *Evolution and ecology of influenza A viruses*. Microbiological reviews, 1992. **56**(1): p. 152-179.
  271. Crosby, A.W., *America's forgotten pandemic: the influenza of 1918*. 2003: Cambridge University Press.
  272. Doung-Ngern, P., et al., *Case-control study of use of personal protective measures and risk for SARS-CoV 2 infection, Thailand*. Emerging infectious diseases, 2020. **26**(11): p. 2607.
  273. Wang, Y., et al., *Reduction of secondary transmission of SARS-CoV-2 in households by face mask use, disinfection and social distancing: a cohort study in Beijing, China*. BMJ global health, 2020. **5**(5): p. e002794.
  274. Payne, D.C., et al., *SARS-CoV-2 infections and serologic responses from a sample of US Navy service members—USS Theodore Roosevelt, April 2020*. Morbidity and Mortality Weekly Report, 2020. **69**(23): p. 714.
  275. Lepelletier, D., et al., *What face mask for what use in the context of the COVID-19 pandemic? The French guidelines*. Journal of Hospital Infection, 2020. **105**(3): p. 414-418.
  276. Kumaran, S., E. Oh, S. Han, and H.-J. Choi, *Photopolymerizable, universal antimicrobial*

- coating to produce high-performing, multifunctional face masks*. Nano Letters, 2021. **21**(12): p. 5422-5429.
277. National Institute for Occupational Safety and Health, *NIOSH 42CFR84: Respiratory Protective Devices*. 1995, U.S. Department of Health and Human Services: Washington, DC.
  278. European Committee for Standardisation, *EN 149: Respiratory protective devices - Filtering half masks to protect against particles - Requirements, testing, marking*. 2009, CEN: Brussels, Belgium.
  279. European Committee for Standardization, *EN 14683: Medical face masks – Requirements and test methods*. 2019, CEN: Brussels, Belgium.
  280. Standardization Administration of the People's Republic of China, *GB 2626-2006: Respiratory protective equipment – Non-powered air-purifying particle respirator*. 2006, SAC: Beijing, China.
  281. China, S.A.o.t.P.s.R.o., *YY 0469: surgical mask*. 2011, SAC: Beijing, China.
  282. Han, S., et al., *Engineering of materials for respiratory protection: salt-coated antimicrobial fabrics for their application in respiratory devices*. Accounts of Materials Research, 2022. **3**(3): p. 297-308.
  283. Chen, C.-C. and K. Willeke, *Aerosol penetration through surgical masks*. American journal of infection control, 1992. **20**(4): p. 177-184.
  284. Konda, A., et al., *Aerosol filtration efficiency of common fabrics used in respiratory cloth masks*. ACS nano, 2020. **14**(5): p. 6339-6347.
  285. Orton, C.M., et al., *A comparison of respiratory particle emission rates at rest and while speaking or exercising*. Communications Medicine, 2022. **2**(1): p. 44.
  286. Xie, X., Y. Li, H. Sun, and L. Liu, *Exhaled droplets due to talking and coughing*. Journal of the Royal Society Interface, 2009. **6**(suppl\_6): p. S703-S714.
  287. Lindsley, W.G., et al., *Quantity and size distribution of cough-generated aerosol particles produced by influenza patients during and after illness*. Journal of occupational and environmental hygiene, 2012. **9**(7): p. 443-449.
  288. Asadi, S., et al., *Efficacy of masks and face coverings in controlling outward aerosol particle emission from expiratory activities*. Scientific reports, 2020. **10**(1): p. 1-13.
  289. Mansour, E., et al., *Measurement of temperature and relative humidity in exhaled breath*. Sensors and Actuators B: Chemical, 2020. **304**: p. 127371.
  290. Courtney, J.M. and A. Bax, *Hydrating the respiratory tract: An alternative explanation why masks lower severity of COVID-19*. Biophysical journal, 2021. **120**(6): p. 994-1000.
  291. Lee, J. and J. Kim, *Material properties influencing the charge decay of electret filters and their impact on filtration performance*. Polymers, 2020. **12**(3): p. 721.
  292. Grillet, A.M., et al., *COVID-19 global pandemic planning: Performance and electret charge of N95 respirators after recommended decontamination methods*. Experimental Biology and Medicine, 2021. **246**(6): p. 740-748.
  293. Quan, F.-S., et al., *Universal and reusable virus deactivation system for respiratory protection*. Scientific reports, 2017. **7**(1): p. 39956.
  294. Rubino, I., et al., *Salt coatings functionalize inert membranes into high-performing filters against infectious respiratory diseases*. Scientific reports, 2020. **10**(1): p. 13875.
  295. Louten, J., *Virus structure and classification*. Essential human virology, 2016: p. 19.
  296. Kabir, A.M.R., et al., *Drag force on micron-sized objects with different surface morphologies in a flow with a small Reynolds number*. Polymer Journal, 2015. **47**(8): p. 564-570.
  297. Deng, D., et al., *Hydrophobic meshes for oil spill recovery devices*. ACS applied materials

- & interfaces, 2013. **5**(3): p. 774-781.
298. Coia, J., et al., *Guidance on the use of respiratory and facial protection equipment*. J Hosp Infect, 2013. **85**(3): p. 170-182.
  299. Bałazy, A., et al., *Do N95 respirators provide 95% protection level against airborne viruses, and how adequate are surgical masks?* Am J Infect Control, 2006. **34**(2): p. 51-57.
  300. Bunyan, D., L. Ritchie, D. Jenkins, and J.E. Coia, *Respiratory and facial protection: a critical review of recent literature*. J Hosp Infect, 2013. **85**(3): p. 165-9.
  301. Loeb, M., et al., *Surgical mask vs N95 respirator for preventing influenza among health care workers: a randomized trial*. JAMA, 2009. **302**(17): p. 1865-1871.
  302. Rubino, I. and H.J. Choi, *Respiratory protection against pandemic and epidemic diseases*. Trends Biotechnol, 2017. **35**(10): p. 907-910.
  303. Salter, W.B., et al., *Analysis of residual chemicals on filtering facepiece respirators after decontamination*. J Occup Environ Hyg, 2010. **7**(8): p. 437-45.
  304. Hamzavi, I.H., et al., *Ultraviolet germicidal irradiation: Possible method for respirator disinfection to facilitate reuse during the COVID-19 pandemic*. J Am Acad Dermatol, 2020. **82**(6): p. 1511-1512.
  305. Rubino, I., et al., *Salt coatings functionalize inert membranes into high-performing filters against infectious respiratory diseases*. Sci Rep, 2020. **10**(1): p. 13875.
  306. Quan, F.S., et al., *Universal and reusable virus deactivation system for respiratory protection*. Sci. Rep., 2017. **7**(1): p. 39956.
  307. Robinson, M.T., *The crystal structures of  $\beta$ -K<sub>2</sub>SO<sub>4</sub> and  $\beta$ -K<sub>2</sub>PO<sub>3</sub>F*. J Phys Chem, 1958. **62**(8): p. 925-928.
  308. Choi, H.J., et al., *Stability of whole inactivated influenza virus vaccine during coating onto metal microneedles*. J Control Release, 2013. **166**(2): p. 159-71.
  309. Choi, H.J., et al., *Effect of osmotic pressure on the stability of whole inactivated influenza vaccine for coating on microneedles*. PLoS One, 2015. **10**(7): p. e0134431.
  310. Baldwin, R.L., *How Hofmeister ion interactions affect protein stability*. Biophys J, 1996. **71**(4): p. 2056-2063.
  311. Cevc, G. and H. Richardsen, *Lipid vesicles and membrane fusion*. Adv Drug Deliv Rev, 1999. **38**(3): p. 207-232.
  312. Sarig, S., A. Glasner, J. Epstein, and N. Eidelman, *Growth of potassium chloride crystals*. J Cryst Growth, 1977. **39**(2): p. 255-266.
  313. Kardum, J.P., A. Sander, and A. Glasnoviæ, *Batch crystallization of KCl: The influence of the cooling and mixing rate on the granulometric properties of obtained crystals*. Chem Biochem Eng Q, 2005. **19**(1): p. 39-48.
  314. Mullin, J.W. and C. Gaska, *Potassium sulfate crystal growth rates in aqueous solution*. J Chem Eng Data, 1973. **18**(2): p. 217-220.
  315. Mullin, J. and C. Gaska, *The growth and dissolution of potassium sulphate crystals in a fluidized bed crystallizer*. Can J Chem Eng, 1969. **47**(5): p. 483-489.
  316. Garside, J., C. Gaska, and J. Mullin, *Crystal growth rate studies with potassium sulphate in a fluidized bed crystallizer*. J Cryst Growth, 1972. **13**: p. 510-516.
  317. Al-Jibbouri, S. and J. Ulrich, *The influence of impurities on crystallization kinetics of sodium chloride*. Cryst Res Technol, 2001. **36**(12): p. 1365-1375.
  318. Rodriguez-Clemente, R., *Crystal growth kinetics of sodium chloride from solution*, in *Industrial Crystallization*. 1976, Springer. p. 187-199.
  319. Zhao, J., et al., *The mass transfer process and the growth rate of NaCl crystal growth by evaporation based on temporal phase evaluation*. Opt Lasers Eng, 2012. **50**(4): p. 540-546.
  320. Mullin, J., *Industrial techniques and equipment*. Crystallization (Fourth Edition),

- Butterworth-Heinemann, Oxford, 2001: p. 315-402.
321. Hidalgo, A.F. and C. Orr Jr, *Homogeneous nucleation of sodium chloride solutions*. Ind Eng Chem Res, 1968. **7**(1): p. 79-83.
  322. Nývlt, J., *Kinetics of nucleation in solutions*. J Cryst Growth, 1968. **3**: p. 377-383.
  323. Leech, G., et al., *Mask wearing in community settings reduces SARS-CoV-2 transmission*. Proceedings of the National Academy of Sciences, 2022. **119**(23): p. e2119266119.
  324. Food and Drug Administration. *N95 Respirators, surgical masks, face masks, and barrier face coverings*. 2023 [cited 2023 Dec 30]; Available from: <https://www.fda.gov/medical-devices/personal-protective-equipment-infection-control/n95-respirators-surgical-masks-face-masks-and-barrier-face-coverings>.
  325. Sorci, M., et al., *Virucidal N95 respirator face masks via ultrathin surface-grafted quaternary ammonium polymer coatings*. ACS applied materials & interfaces, 2022. **14**(22): p. 25135-25146.
  326. Demir, B., et al., *N-halamine-modified antimicrobial polypropylene nonwoven fabrics for use against airborne bacteria*. ACS applied materials & interfaces, 2015. **7**(3): p. 1752-1757.
  327. Cen, L., K.G. Neoh, and E.T. Kang, *Antibacterial activity of cloth functionalized with N-alkylated poly (4-vinylpyridine)*. Journal of Biomedical Materials Research Part A: An Official Journal of The Society for Biomaterials, The Japanese Society for Biomaterials, and The Australian Society for Biomaterials and the Korean Society for Biomaterials, 2004. **71**(1): p. 70-80.
  328. McKenney, P.T., A. Driks, and P. Eichenberger, *The Bacillus subtilis endospore: assembly and functions of the multilayered coat*. Nature Reviews Microbiology, 2013. **11**(1): p. 33-44.
  329. Andryukov, B.G., A.A. Karpenko, and I.N. Lyapun, *Learning from nature: Bacterial spores as a target for current technologies in medicine*. Современные технологии в медицине, 2020. **12**(3 (eng)): p. 105-122.
  330. Zeng, L., et al., *Environmental stability and transmissibility of enveloped viruses at varied animate and inanimate interfaces*. Environment & Health, 2023. **1**(1): p. 15-31.
  331. Lin, Q., et al., *Sanitizing agents for virus inactivation and disinfection*. View, 2020. **1**(2): p. e16.
  332. Vasickova, P., I. Pavlik, M. Verani, and A. Carducci, *Issues concerning survival of viruses on surfaces*. Food and Environmental Virology, 2010. **2**: p. 24-34.
  333. Best, E.L., W.N. Fawley, P. Parnell, and M.H. Wilcox, *The potential for airborne dispersal of Clostridium difficile from symptomatic patients*. Clinical Infectious Diseases, 2010. **50**(11): p. 1450-1457.
  334. Venkataraman, D., E. Shabani, and J.H. Park, *Advancement of nonwoven fabrics in personal protective equipment*. Materials, 2023. **16**(11): p. 3964.
  335. Gupta, V.B. and V.K. Kothari, *Manufactured fibre technology*. 1997: Springer Science & Business Media.
  336. Hutten, I.M., *Handbook of nonwoven filter media*. 2007: Elsevier.
  337. Han, Z., et al., *How do three-layer surgical masks prevent SARS-CoV-2 aerosol transmission?* Separation and Purification Technology, 2023. **314**: p. 123574.
  338. Yim, W., et al., *KN95 and N95 respirators retain filtration efficiency despite a loss of dipole charge during decontamination*. ACS applied materials & interfaces, 2020. **12**(49): p. 54473-54480.
  339. Ju, J.T.J., L.N. Boisvert, and Y.Y. Zuo, *Face masks against COVID-19: Standards, efficacy, testing and decontamination methods*. Advances in Colloid and Interface Science,

2021. **292**: p. 102435.
340. Choi, H., et al., *Current understanding of the surface contamination and contact transmission of SARS-CoV-2 in healthcare settings*. Environmental chemistry letters, 2021. **19**: p. 1935-1944.
341. Otter, J.A., S. Yezli, and G.L. French, *The role played by contaminated surfaces in the transmission of nosocomial pathogens*. Infection Control & Hospital Epidemiology, 2011. **32**(7): p. 687-699.
342. Russotto, V., A. Cortegiani, S.M. Raineri, and A. Giarratano, *Bacterial contamination of inanimate surfaces and equipment in the intensive care unit*. Journal of intensive care, 2015. **3**(1): p. 1-8.
343. Nightingale, M., M. Mody, A. Rickard, and M. Cassone, *Bacterial contamination on used face masks in healthcare personnel*. Antimicrobial Stewardship & Healthcare Epidemiology, 2022. **2**(S1): p. s86-s87.
344. Delanghe, L., et al., *Cotton and surgical face masks in community settings: Bacterial contamination and face mask hygiene*. Frontiers in medicine, 2021: p. 1477.
345. Fimlaid, K.A., et al., *Global analysis of the sporulation pathway of Clostridium difficile*. PLoS genetics, 2013. **9**(8): p. e1003660.
346. American Type Culture Collection. *Human rhinovirus 16*. [cited 2023 Nov 27]; Available from: <https://www.atcc.org/products/vr-283>.
347. World Health Organization. *Serological detection of avian influenza A (H7N9) infections by microneutralization assay 2013* [cited 2023 Dec 15]; Available from: [https://www.who.int/publications/m/item/serological-detection-of-avian-influenza-a\(h7n9\)-infections-by-microneutralization-assay](https://www.who.int/publications/m/item/serological-detection-of-avian-influenza-a(h7n9)-infections-by-microneutralization-assay).
348. Oh, E., et al., *Highly effective salt-activated alcohol-based disinfectants with enhanced antimicrobial activity*. ACS nano, 2023. **17**(18): p. 17811-17825.
349. PALAS. *PMFT 1000 / PMFT 1000 M operating manual*. 2021 [cited 2023 Oct 26]; Available from: <https://www.palas.de/en/>.
350. National Institute for Occupational Safety and Health, *Determination of particulate filter efficiency level for N95 series filters against solid particulates for non-powdered, air-purifying respirators standard testing procedure 2019*.
351. Charvet, A., et al., *Impact of washing cycles on the performances of face masks*. Journal of Aerosol Science, 2022. **160**: p. 105914.
352. European Union, *EN 14683+C1 Medical face masks – Requirements and test methods*. 2018.
353. ASTM F2101-19e1, *Standard Test Method for Evaluating the Bacterial Filtration Efficiency of Medical Face Mask Materials, Using a Biological Aerosol of Staphylococcus aureus*. 2019.
354. ASTM F2100-19e1, *Standard Specification for Performance of Materials Used in Medical Face Masks*. 2019.
355. Rineh, A., et al., *Clostridium difficile infection: molecular pathogenesis and novel therapeutics*. Expert review of anti-infective therapy, 2014. **12**(1): p. 131-150.
356. MacLeod-Glover, N. and C. Sadowski, *Efficacy of cleaning products for C difficile: Environmental strategies to reduce the spread of Clostridium difficile-associated diarrhea in geriatric rehabilitation*. Canadian Family Physician, 2010. **56**(5): p. 417-423.
357. Cunliffe, A.J., et al., *How do we determine the efficacy of an antibacterial surface? A review of standardised antibacterial material testing methods*. Antibiotics, 2021. **10**(9): p. 1069.
358. The Environmental Protection Agency. *Disinfectants for Emerging Viral Pathogens (EVPs)*:

- List Q*. 2023 [cited 2024 Jan 15]; Available from: <https://www.epa.gov/pesticide-registration/disinfectants-emerging-viral-pathogens-evps-list-q>.
359. The Environmental Protection Agency. *List K: Antimicrobial Products Registered with EPA for Claims Against Clostridium difficile Spores*. 2023 [cited 2024 Jan 15]; Available from: <https://www.epa.gov/pesticide-registration/list-k-antimicrobial-products-registered-epa-claims-against-clostridium>.
360. Gaeckle, N.T., et al., *Aerosol generation from the respiratory tract with various modes of oxygen delivery*. American Journal of Respiratory and Critical Care Medicine, 2020. **202**(8): p. 1115-1124.
361. Jones, R.M. and D. Rempel, *Standards for surgical respirators and masks: relevance for protecting healthcare workers and the public during pandemics*. Annals of work exposures and health, 2021. **65**(5): p. 495-504.
362. Yezli, S. and J.A. Otter, *Minimum infective dose of the major human respiratory and enteric viruses transmitted through food and the environment*. Food and Environmental Virology, 2011. **3**(1): p. 1-30.
363. Couch, R.B., et al., *Effect of route of inoculation on experimental respiratory viral disease in volunteers and evidence for airborne transmission*. Bacteriol Rev, 1966. **30**(3): p. 517-29.
364. Alford, R.H., J.A. Kasel, P.J. Gerone, and V. Knight, *Human influenza resulting from aerosol inhalation*. Proc Soc Exp Biol Med, 1966. **122**(3): p. 800-4.
365. Weber, T.P. and N.I. Stilianakis, *Inactivation of influenza A viruses in the environment and modes of transmission: a critical review*. J Infect, 2008. **57**(5): p. 361-73.